RATE AND STRAIN GRADIENT EFFECTS ON CREEP-FATIGUE CRACK GROWTH IN NICKEL-BASE SUPERALLOYS

by

Joshua D. Pribe

A Dissertation

Submitted to the Faculty of Purdue University

In Partial Fulfillment of the Requirements for the degree of

Doctor of Philosophy

School of Mechanical Engineering

West Lafayette, Indiana

August 2021

THE PURDUE UNIVERSITY GRADUATE SCHOOL
STATEMENT OF COMMITTEE APPROVAL

Dr. Thomas Siegmund, Chair

School of Mechanical Engineering

Dr. Ganesh Subbarayan

School of Mechanical Engineering

Dr. Farshid Sadeghi

School of Mechanical Engineering

Dr. Michael D. Sangid

School of Aeronautics and Astronautics

Dr. Jamie J. Kruzic

UNSW Sydney School of Mechanical and Manufacturing Engineering

Approved by:

Dr. Nicole L. Key

ACKNOWLEDGMENTS

I would first like to thank Professor Thomas Siegmund, my advisor during my time at Purdue. I greatly appreciate his guidance, enthusiasm, and especially encouragement to discover and pursue my own interests, both during my PhD research and for my future career. I am also grateful to Professor Jamie Kruzic, Professor Ganesh Subbarayan, Professor Michael Sangid, and Professor Farshid Sadeghi for serving on my committee. Their questions and suggestions helped me to think more deeply about the research questions underlying my work and helped me to grow as a student and researcher. I also thank Professor Kruzic for hosting me during my two-month stay at UNSW Sydney and for sharing his expertise and perspectives on research.

Teaching was an important part of my experience at Purdue, and I am grateful to Professors Chuck Krousgrill, Marcial Gonzalez, Klod Kokini, Kejie Zhao, Beth Hess, and Jim Jones for their mentorship and encouragement. Support from Professor Krousgrill and Professor Hess was especially helpful as I navigated the challenges of teaching a class online in Summer 2020.

I would like to thank Dylan Addison and Halsey Ostergaard, whose creep-fatigue crack growth experiments helped inspire much of the work in this thesis. Halsey's support and friendship during my time in Sydney are much appreciated as well. I also thank my groupmates, officemates, and friends at Purdue for many good conversations over the past five years.

Support for my research from the Department of Energy National Energy Technology Laboratory and Nuclear Energy University Program, the Australia-Americas PhD Research Internship Program, the Purdue School of Mechanical Engineering, and the Indiana Consortium for Simulation-based Engineering of Materials and Structures is greatly appreciated.

Finally, I would like to thank my parents, Dan and Susy, and my sister, Sarah. Even when the COVID-19 pandemic kept us apart, they were always happy to share their love, support, and encouragement.

TABLE OF CONTENTS

LIST OF TABLES

LIST OF FIGURES

ABSTRACT

An important challenge in predicting fatigue and creep crack growth is describing crack growth rates under transient conditions. Transient conditions occur when similitude is violated at the crack tip due to the applied loads or material behavior. Crack growth models like the Paris law, valid for homogeneous materials under constant-amplitude cyclic loading or sustained loading, no longer apply. Transient crack growth rates are strongly influenced by changes in plastic deformation at the crack tip. Activation of time-dependent damage and viscoplastic deformation at high temperatures further complicates the problem.

This thesis advances knowledge and predictive capabilities for transient creep and fatigue crack growth in metals, with specific applications to two technologically-relevant nickel-base superalloys. Finite element computations of crack growth following overloads and in multilayered materials are conducted. Crack extension is an outcome of the boundary value problem through an irreversible cohesive zone model and its interaction with plasticity and viscoplasticity in the bulk material.

First, fatigue crack growth in rate-independent materials is analyzed. The plasticity formulation considers both plastic strain and gradients of plastic strain, which produce hardening beyond that predicted by classical plasticity models. The computations demonstrate that hardening due to plastic strain gradients plays a significant role in transient fatigue crack growth following overloads. Fatigue crack growth transients associated with material inhomogeneity are studied through the case of a crack growing toward interfaces between plastically dissimilar materials. Interactions between the interface strength and the yield strength mismatch are found to govern crack growth rates near the interface. Hardening due to plastic strain gradients is important for finding the critical conditions associated with crack bifurcation at an interface and penetration through an interlayer.

Subsequently, crack growth in rate-dependent materials is analyzed. For materials characterized by power-law viscoplasticity, fatigue crack growth rates following overloads are found to depend strongly on the material rate sensitivity. The computations predict a transition from acceleration- to retardation-dominated post-overload crack growth as the rate sensitivity decreases. The predicted post-overload crack growth rates show good agree-

ment with high-temperature experimentally-measured trends for Alloy 617, a solid solution strengthened nickel-base superalloy proposed for use in next-generation nuclear power plants. The results demonstrate why Alloy 617 behaves in a relatively brittle manner following overloads despite being characterized as a creep-ductile material. Crack growth is also studied in materials where rate dependence is captured through time-dependent damage and dislocation storage and dynamic recovery processes. This approach is relevant for high-strength creep-brittle materials, in which the viscoplastic zone grows with the advancing crack. The computations predict crack growth retardation for several loading waveforms containing overloads. The amount of retardation depends strongly on the overload ratio and subsequent unloading ahead of the crack tip. The predicted post-overload crack extension shows good agreement with high-temperature experimentally-measured trends for Alloy 718, a precipitation-hardened nickel-base superalloy used in turbine engines and power generation applications. The results demonstrate why Alloy 718 behaves in a ductile manner following overloads, despite being characterized as a creep-brittle material.

1. INTRODUCTION

1.1 Motivation

Fatigue crack growth is a critical failure mechanism for metallic components that must be considered in any application involving cyclic loading. One approach to designing against fatigue is a damage-tolerant design philosophy. Damage-tolerant design is based on predicting the remaining fatigue life of a component given an initial flaw size [1], [2]. The flaw size is typically inferred from a nondestructive evaluation procedure, and fracture mechanics concepts are used to calculate the number of cycles required for the flaw to grow to a critical size [1]. This approach can also be used to set inspection intervals given the detection threshold of the testing procedure. Despite advances in both fracture mechanics and nondestructive evaluation, a majority of in-service failures occur due to fatigue [2], [3]. High temperatures on the order of half the melting point of a material exacerbate the problem by activating various time-dependent mechanisms during crack growth [4]. This includes both viscoplastic deformation and damage mechanisms such as creep void growth, dynamic embrittlement, and grain boundary oxidation [5]. Time-dependent damage mechanisms can cause crack growth during constant, sustained loading as well as cyclic loading.

An important concern in damage-tolerant design is that crack growth rates in response to realistic load spectra must be considered in order to accurately predict the life of engineering components [2]. This requires consideration of various load transients, such as overloads (OLs) and hold times at multiple load levels. Studies of variable-amplitude loading in rate-independent materials indicate that crack growth in these situations is closely associated with crack-tip plasticity [6], [7]. Changes in the plastic zone during variable-amplitude loading induce residual stresses that affect subsequent crack growth under constant-amplitude loading [1]. Fatigue crack growth transients also occur in inhomogeneous material systems subjected to constant-amplitude loading [8]. Here, the plastic zone and the crack-tip fields are disturbed due to interactions with interfaces and materials with differing properties. Predicting crack growth rates under transient conditions requires cycle-by-cycle analysis of crack-tip plasticity and the active damage mechanisms ahead of the crack tip.

This thesis is specifically motivated by experiments involving each of these crack growth transients on two technologically-relevant nickel-base superalloys, Alloy 617 and Alloy 718. Alloy 617 is the leading candidate material for use in the intermediate heat exchanger (IHX) of the very high temperature reactor (VHTR) [9]. This material was also recently approved for high-temperature nuclear applications under Section III of the ASME Boiler and Pressure Vessel code [10]. The VHTR design is a Generation IV nuclear reactor concept that envisions IHX outlet temperatures in excess of 800°C [9], [11]. This exceeds the solvus temperature of γ' precipitates, so Alloy 617 is exclusively solid solution strengthened at temperatures of interest [12]. An important requirement for next-generation reactor designs is load-following capabilities [13]. Load-following requirements arise from increasing use of renewable energy sources like wind and solar, which typically provide intermittent power [14]. Reactor components are therefore subjected to cyclic and time-dependent loads associated with daily power variations. As a result, these components cannot be designed to provide only base-load power, and crack growth under transient loads must be understood for safe operation [15].

Experiments demonstrate that Alloy 617 behaves in a ductile manner during crack growth under constant sustained loads and constant-amplitude cyclic loading. Time-dependent crack growth rates under sustained loading have been successfully correlated with the C^* parameter [15], [16]. This indicates that widespread viscoplastic deformation occurs during creep crack growth, and Alloy 617 can be described as a creep-ductile material [5], [15], [17]. Similarly, during constant-amplitude cyclic loading, crack growth occurs by a cyclic viscoplasticity mechanism [15]. Evidence for this mechanism includes the transgranular crack path (Figure 1.1a) and fatigue striations on the fracture surface (Figure 1.1b) [18]. Time-dependent creep void growth only contributes to crack extension at high loads and low loading frequencies, Figure 1.1c [15]. However, experiments with transient loads produce unexpected results for what is perceived as a ductile material. A single OL does not affect crack growth rates, within the noise of the experimental measurements. Blocks of multiple OLs result in net retardation at low loads and net acceleration at high loads, [18], [19]. Cases where OLs do not produce crack growth retardation are more typical of brittle materials [20]. Therefore, there is a contradiction: Alloy 617 behaves like a ductile material under sustained loading

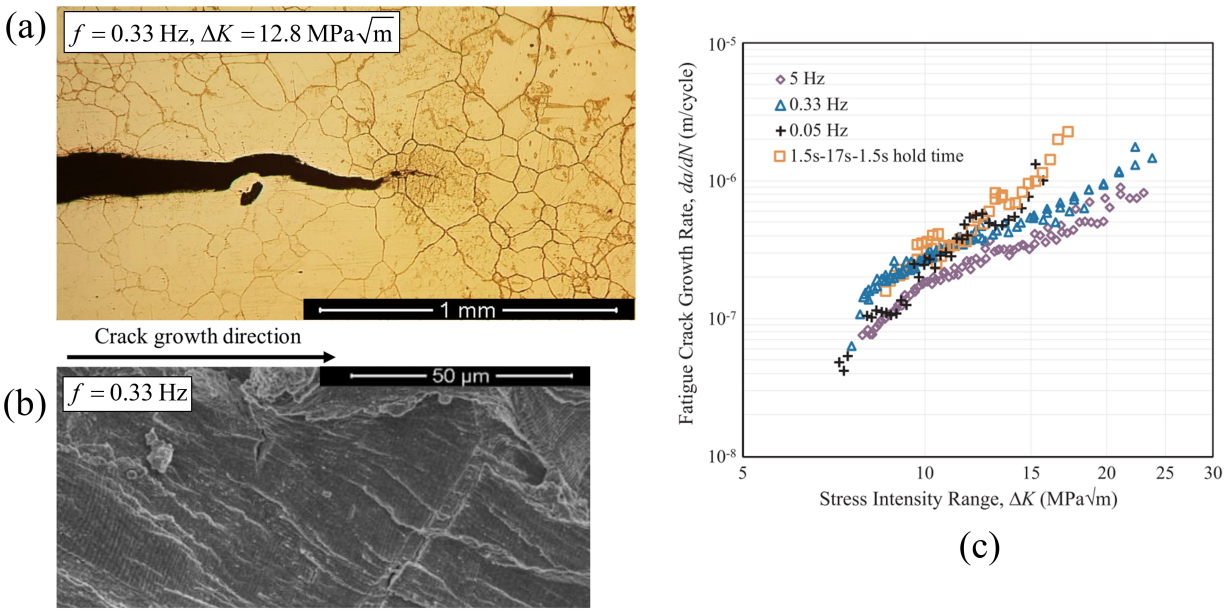

Figure 1.1. Crack morphology and crack growth rates for Alloy 617 fatigue crack growth specimens tested at 800°C. (a) Optical micrograph of the etched crack profile and (b) SEM micrograph of the fracture surface of a specimen subjected to cyclic loading with a frequency of 0.33 Hz, showing a transgranular crack path and fatigue striations. Used with permission from [18]. (c) Steady state fatigue crack growth rates for different load frequencies and a hold-time waveform, showing that crack growth rates are nearly frequency independent up to $\Delta K \approx 11.5$ MPa$\sqrt{\text{m}}$. Used with permission from [15].

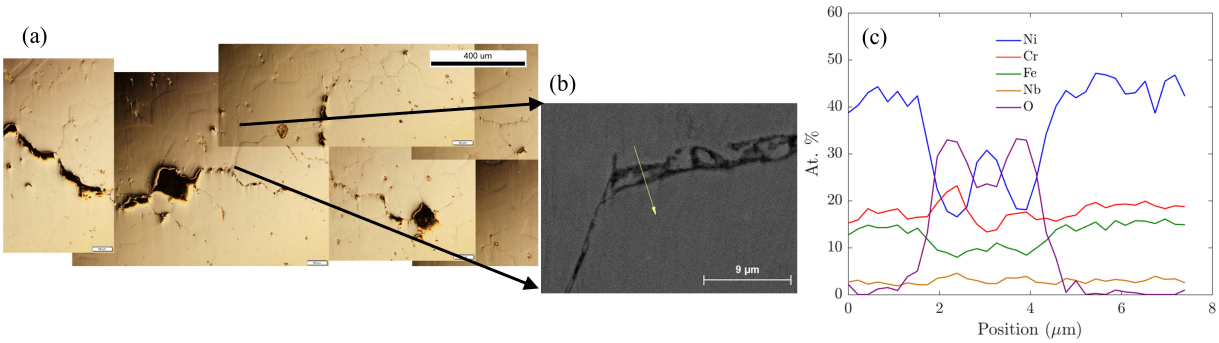

Figure 1.2. Crack morphology for Alloy 718 crack growth specimen subjected to sustained loading at 650°C. (a) Optical micrograph and (b) SEM micrograph of a segment of the crack profile, showing an intergranular crack path. (c) EDS line scan along the arrow in (b), demonstrating oxidation on the grain boundary. Crack growth experiment conducted by H. E. Ostergaard; original images generated for this thesis.

and constant-amplitude cyclic loading, but it behaves like a brittle material under transient loads.

Alloy 718 and its derivatives are used in a variety of applications at temperatures up to 650°C due to a good combination of creep resistance, strength, and toughness [21], [22]. Below this temperature, strengthening in Alloy 718 derives primarily from precipitation hardening with the coherent γ'' and γ' phases that can be sheared by dislocations [23], [24]. Common applications of Alloy 718 include nuclear reactor components and both land-based and aircraft gas turbine engines [21], [23], [25]. In addition to the load-following requirements associated with future operation of nuclear power plants, load transients also must be considered in turbine engine applications [26]. In the case of aircraft, load transients may arise from hold times at multiple load levels during a takeoff-cruise-landing cycle, thermal transients during engine start-up, and load excursions due to hard landings or turbulence [25]–[27].

Alloy 718 is classified as a creep-brittle material based on its crack growth behavior under sustained loads at 650°C [5], [28]. Creep-brittle behavior is associated with a small viscoplastic zone that grows together with the advancing crack and higher crack growth rates than in creep-ductile materials [5]. In polycrystalline Alloy 718 and similar materials, high crack growth rates are driven by environmental attack on grain boundaries ahead of the crack

tip [29]. Due to its high strength and creep resistance, Alloy 718 can sustain high stresses ahead of the crack tip that activate a stress-assisted oxygen diffusion or oxidation mechanism [30], [31]. The environmentally-driven damage leads to brittle intergranular crack growth under sustained loading and low-frequency cyclic loading [29], [32]. Figure 1.2 demonstrates brittle intergranular crack growth and grain boundary oxidation for a polycrystalline Alloy 718 crack growth specimen subjected to sustained loading at 650°C. However, experiments demonstrate that OLs during both cyclic and sustained loading at 650°C cause crack growth retardation for all load cases that have been investigated [30], [33], [34]. Post-OL retardation is characteristic of ductile materials [20]. These results create the opposite contradiction as with Alloy 617: Alloy 718 is described as brittle during steady-state crack growth, but it behaves in a more ductile way under transient loads.

Alloy 718 is also being studied for use with additive manufacturing processes to accelerate production of complex components and circumvent machining challenges [21]. In experiments investigating crack extension in additive manufactured Alloy 718 at 650°C, crack growth transients have been observed even under constant-amplitude cyclic loading. In this case, transients are associated with the microstructure and material properties ahead of the crack tip. Figure 1.3 shows an example of the crack path in a compact tension specimen where the initial mode I crack growth direction was perpendicular to the build direction. As shown in Figure 1.3b, the crack path consists of different segments: a mainly transgranular path in the initial mode I crack growth direction, and an intergranular path along oxidized grain boundaries nearly perpendicular to this direction. Similar to the case of OLs, crack extension depends on a cycle-by-cycle evolution of the crack-tip fields. Here, competition between transgranular fatigue crack growth and crack deflection along the weakened grain boundaries determines both the crack path and crack growth rates. The overall result is deflection of the crack downward from the initial mode I direction, seen in Figure 1.3a. These characteristics of crack extension are similar to both fatigue crack growth and monotonic fracture in inhomogeneous and highly-textured elastic-plastic materials containing weak interfaces [8], [35]–[37].

These motivating experiments all relate back to two fundamental problems in fatigue crack growth: crack growth following an OL and crack growth in the vicinity of an interface

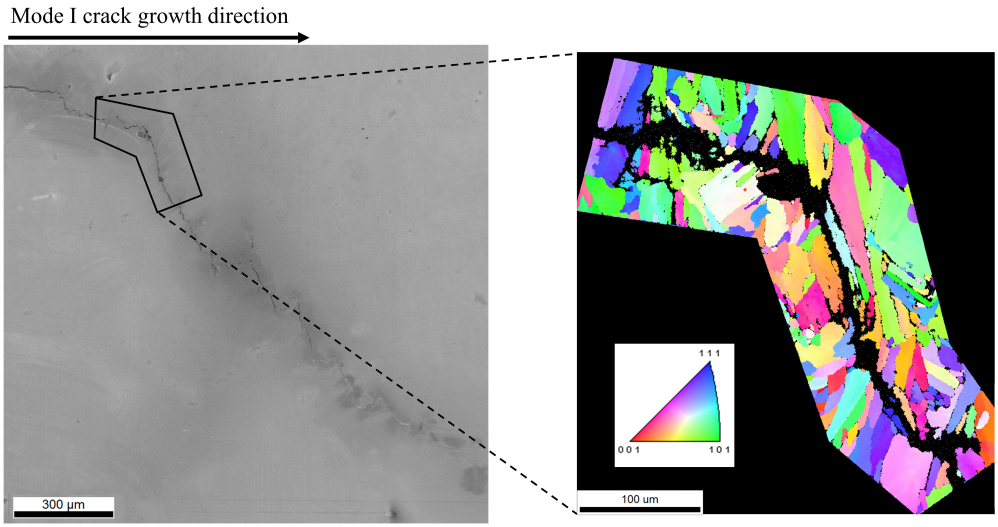

Figure 1.3. Crack path in an additive manufactured Alloy 718 specimen subjected to cyclic loading at 650°C. (a) SEM micrograph of the crack path in an additive manufactured Alloy 718 specimen showing significant deviation from the mode I crack growth direction. (b) Inverse pole figure, generated using EBSD, of a segment of the crack path, demonstrating transgranular crack growth in the initial mode I direction and crack deflection along oxidized grain boundaries nearly perpendicular to this direction. Crack growth experiment conducted by H. E. Ostergaard; original images generated for this thesis.

between dissimilar materials. As noted previously, experiments in rate-independent materials demonstrate how disturbances of crack-tip plastic deformation are critical for understanding and predicting crack growth rates in these scenarios. The overarching objective of this thesis is then to provide new understanding of how crack-tip plastic and viscoplastic deformation interacts with the damage process to determine transient crack growth rates in these fundamental problems and in the specific experiments on Alloy 617 and Alloy 718. This objective is first addressed through consideration of plastic strain gradients in fatigue crack growth. In regions of highly inhomogeneous plastic deformation, such as the crack-tip plastic zone, plastic strain gradients lead to the development of geometrically-necessary dislocations [38]–[40]. Hardening due to geometrically-necessary dislocations cannot be predicted by classical plasticity models [41], and its influence on transient fatigue crack growth has not been investigated in detail. The objective is also addressed through consideration of rate-dependent viscoplastic deformation and time-dependent damage. Each of these mechanisms contributes to time-dependent crack growth observed in experiments at high temperatures. As indicated by the contradictions in the motivating experiments, the characteristics of material behavior that govern crack growth following load transients in rate-dependent materials are not well understood.

The remainder of this chapter provides an overview of the scientific background, research contribution, and organization of this thesis. A brief literature review of rate-independent and rate-dependent fatigue and creep crack growth is included. Gaps in understanding are identified for crack extension under transient loads and in inhomogeneous materials. Specific research questions are then proposed, together with a description of the general modeling approach to address these questions. Detailed introductions to each topic can be found at the beginning of subsequent chapters.

1.2 Fatigue crack growth in rate-independent materials

Most descriptions of rate-independent fatigue crack growth follow from the pioneering work of Paris and Erdogan [42]. The Paris law relates the cyclic fatigue crack growth rate $\mathrm{d}a/\mathrm{d}N$ to the stress intensity factor range ΔK through a power law:

$$\frac{\mathrm{d}a}{\mathrm{d}N} = A_p \left(\Delta K\right)^{M_p}, \tag{1.1}$$

where the prefactor A_p and exponent M_p are determined through experiments. The Paris law equation is applicable for crack growth under constant-amplitude loading and small-scale yielding. Under these conditions, the concept of similitude applies: the crack-tip plastic zone is embedded inside a region where the elastic stress and strain fields are determined by the stress intensity factor. As a result, crack-tip conditions are uniquely related to the remote loading parameter ΔK [1].

Modifications are necessary when crack growth transients occur. The reason is that transients are associated with a local violation of similitude near the crack tip. The steady-state crack-tip fields are disturbed due to changes in the plastic zone. The crack-tip fields thereby change as the crack grows and can no longer be described by a remote loading parameter alone. Overloads, for example, are the most well-studied source of load transients. Overloads have consistently been found to cause subsequent crack growth retardation in rate-independent ductile metals [6]. Explanations for post-OL retardation are based on crack growth through the OL plastic zone, Figure 1.4, which induces compressive residual stresses near the crack tip.

Widely-used analytical models for retardation that describe crack growth through the OL plastic zone include those of Wheeler [43] and Willenborg [44]. The Wheeler model uses an empirical retardation parameter to correct the crack growth rates while the crack and the plastic zone during subsequent cycles are within the OL plastic zone. The retardation parameter is based on the OL plastic zone size and a shaping exponent fit to OL experiments [2]. The Willenborg model proposes a residual stress intensity factor K_R calculated based on

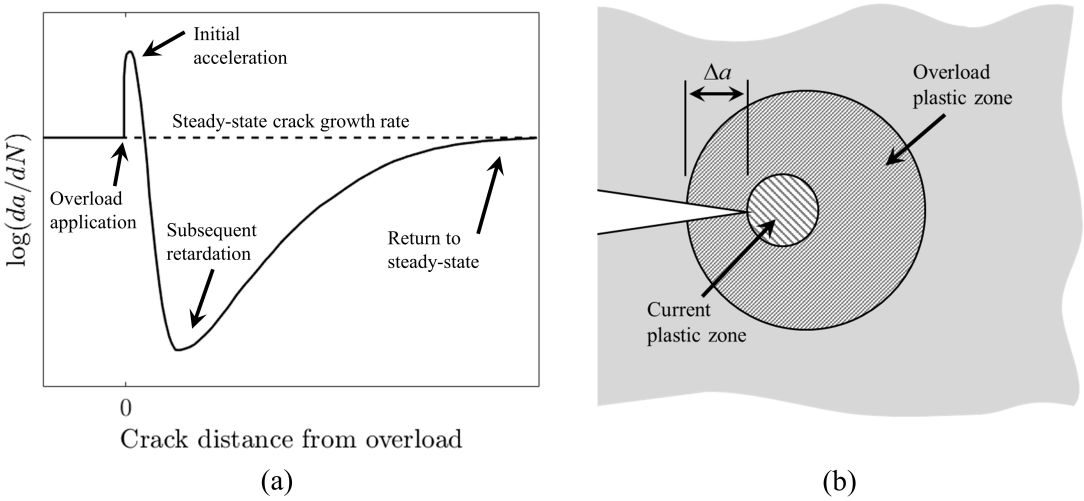

Figure 1.4. (a) Schematic of typical crack growth rates ($\mathrm{d}a/\mathrm{d}N$) following an OL in rate-independent materials. (b) Schematic of crack extension through the OL plastic zone. Adapted from [1], [43].

an assumed relationship with crack growth through the OL plastic zone [1], [44], [45]. The residual stress intensity factor is typically calculated using the equation

$$K_R = K_{\mathrm{OL}}\sqrt{1 - \frac{\Delta a}{r_{\mathrm{OL}}}} - K_{\mathrm{max}}, \tag{1.2}$$

where K_{OL} is the maximum stress intensity factor during the OL cycle, Δa is the crack extension after the OL, r_{OL} is the OL plastic zone size, and K_{max} is the maximum stress intensity factor during cyclic after the OL [45]. The value of K_R is in turn used to determine an effective load ratio or stress intensity factor range. To achieve a better fit with experimental data, modifications to this approach often introduce a scaling factor to Eq. (1.2) or use a fitting exponent in the relationship between K_R and the effective load ratio [26], [46]–[48]. Modifications to the Willenborg and Wheeler models are also necessary to account for the acceleration that occurs immediately after an OL, as well as the crack growth rates resulting from more complex load sequences [46], [49], [50].

Another explanation for post-OL behavior is based on the concept of plasticity-induced crack closure. Following the pioneering work of Elber [51], a large number of studies have investigated this phenomenon from both an experimental and modeling perspective [52].

The crack closure approach postulates that, after an OL, the crack remains closed behind the current crack tip during a larger portion of each load cycle due to the compressive residual stresses in the OL plastic zone. Crack closure in turn reduces the effective stress intensity range at the crack tip by increasing the effective minimum stress intensity factor from the applied $K_{\min}$ to K_{op}, the stress intensity when the crack opens [1]. Experiments have generally confirmed that significant plasticity-induced crack closure occurs following OLs and that this is associated with crack growth retardation [7], [53]–[55]. Numerical studies have used strip-yield models or finite element computations to quantify crack closure and investigate the influence of loading parameters and the plasticity formulation [52], [56]–[60]. These studies indicate that the crack opening loads depend strongly on the details of crack-tip plastic deformation.

Crack-tip plasticity is also highly relevant to fatigue crack growth near interfaces in inhomogeneous materials. Two configurations in which a fatigue crack grows perpendicularly towards one or more interfaces are of particular interest in this work. The first is a bi-material, in which plastically-dissimilar materials are bonded at an interface. The second is a multilayered material consisting of a high-yield-strength matrix and a low-yield-strength interlayer. In these cases, similitude is violated when the plastic zone interacts with an interface and the material on the other side. A yield strength mismatch between material on either side of the interface changes the shape and size of the plastic zone as the crack approaches the interface [8]. Material separation along the interface itself can also lead to crack deflection or arrest [8], [35], [61].

Similar to OLs, changes in crack growth rates near the interface(s) are typically explained through modifications to the effective crack driving force. The modifications are based on the changes in plastic deformation and subsequent stress redistribution that occur across the interface [8], [62]–[64]. This approach has successfully described crack growth rates in cases where the crack penetrates one or more interfaces with minimal debonding along the interfaces themselves [8], [36]. However, these models are more challenging to apply when multiple cracks may be actively growing: the original crack and cracks along the interface(s) [65]. Models based only on calculating the effective crack driving force also cannot identify

the critical conditions for crack deflection into the interface. Here, interactions occur between the growth of each crack and the inhomogeneous plastic deformation across the interface.

These observations indicate that advances in plasticity modeling can help to understand crack extension following OLs and near interfaces in inhomogeneous materials. These advances can in turn enhance both fatigue life predictions under complex load spectra and design of fracture-resistant materials. To this end, this thesis addresses two gaps associated with transient fatigue crack growth in rate-independent materials. First, the role of plastic strain gradients in transient fatigue crack growth and associated phenomena like crack closure is unknown. Second, interactions between a yield strength mismatch and weak interfaces for fatigue crack growth in multilayer materials have not been investigated in detail.

1.3 Creep-fatigue crack growth in rate-dependent materials

Over the last several decades, the field of time-dependent fracture mechanics has developed to characterize subcritical crack extension at high temperatures [5]. Initial research focused on identifying crack-tip parameters for rate-dependent materials analogous to the stress intensity factor K and the J integral for rate-independent elastic-plastic materials [66]. The goal of this approach is to extend the concept of similitude to rate-dependent material behavior, such that crack-tip conditions can be described by a single parameter [67]. The appropriate parameter is generally calculated using a path-independent integral around the crack tip and, in some cases, using experimentally-measured load-displacement records [5].

For materials undergoing widespread viscoplastic or creep deformation, the C^* parameter, defined by Landes and Begley [68], characterizes the crack-tip fields for both stationary and growing cracks [67]. The C^* parameter can be calculated based on load-displacement data in an experiment and has been successfully used to correlate crack growth rates in cases of widespread creep [5]. In this case, the time-dependent crack growth rates $\mathrm{d}a/\mathrm{d}t$ are related to C^* through a power law:

$$\frac{\mathrm{d}a}{\mathrm{d}t} = A_c \left(C^*\right)^{M_c}, \tag{1.3}$$

where A_c and M_c are determined from experiments, similar to the Paris law for rate-independent fatigue crack growth. The $C(t)$ parameter, calculated using an integral on

a contour within the creep zone, generalizes C^* to situations without widespread creep and serves as the time-dependent analogue of the J integral [69]. The $C(t)$ integral is path-independent if the contour is within a region where the creep strain rate is much greater than the elastic strain rate. It is path independent everywhere under extensive creep conditions, where $C(t) = C^*$. The $C(t)$ parameter characterizes the stress and strain fields at the crack tip as the creep zone grows from a small-scale creep regime to a widespread creep regime. The crack-tip fields have the form of Hutchinson-Rice-Rosengren (HRR) fields defined for plastically-deforming materials [70], [71], but with amplitude given by $C(t)$ instead of J [72]. Since $C(t)$ cannot be measured experimentally, Saxena [73] introduced the C_t parameter, calculated based on the energy rate (or power) input to a specimen. The C_t parameter is proportional to the rate of expansion of the creep zone for a stationary crack and is equivalent to C^* for extensive creep conditions, but it is not equal to $C(t)$ in the small-scale and transition creep regime. [74].

Experimental studies of time-dependent crack growth rates led to two general classifications for metals at high temperatures based on material behavior and crack extension during sustained loading. Creep-ductile materials are characterized by widespread viscoplastic deformation that accompanies crack extension [5]. During steady-state crack growth, changes in the crack-tip fields due to crack extension are minimal, and the crack can be treated as stationary (i.e., the HRR-type fields calculated using the C^* parameter are valid for both stationary and growing cracks) [75]. During constant-amplitude cyclic loading of creep-ductile materials, the stress intensity factor range ΔK is still applicable, as long as the loading frequency meets conditions prescribed in ASTM E2760 [76]. Creep-brittle materials are characterized by confined viscoplastic deformation in a region near the crack tip [5]. The viscoplastic zone, in turn, advances with crack extension. Many studies have successfully correlated K and ΔK with crack growth under sustained loads and constant-amplitude cyclic loads, respectively [4], [32], [77], [78]. However, caution is required when the creep zone changes in size and shape during sustained loading, which can lead to a non-unique correlation with K and other parameters like C_t [79], [80]. Based on sustained-loading crack growth experiments at high temperatures, Alloy 617 meets the conditions for creep-ductile materials [15], [17], while Alloy 718 meets the conditions for creep-brittle materials [5], [28].

More work is needed to extend these ideas to cases with transient loading. For example, finite element computations by Yoon et al. [81] predicted a reduction in the effective C_t parameter during hold times following OLs. However, high-temperature experiments on a Cr-Mo steel using the same waveform led to increased crack growth rates after OLs, which was attributed to enhanced void nucleation and growth [81]. Some numerical studies using strip-yield [82], [83] and finite element [84] methods have investigated crack closure in rate-dependent materials but primarily under steady-state conditions. Overall, it is unknown how the concepts of creep-ductile and creep-brittle materials can be applied for crack growth under transient loads. A gap exists in predicting whether crack growth acceleration, retardation, or a close competition between the two will occur following OLs in rate-dependent materials. The contradictions observed in the experiments on Alloy 617 and Alloy 718 discussed in Section 1.1 provide compelling evidence that this gap is important to fill. The possibility of net acceleration following OLs in Alloy 617 is especially concerning because the retardation-based models developed for rate-independent ductile metals do not predict this behavior.

1.4 Research questions

This thesis first considers fatigue crack growth in rate-independent materials. This addresses the knowledge gap related to the role of plastic strain gradients in fatigue crack growth. This also addresses the gap related to interactions between a yield strength mismatch and weak interfaces in inhomogeneous materials.

The research questions addressed in this thesis for rate-independent fatigue crack growth are as follows:

1. What role do plastic strain gradients play in predictions of fatigue crack growth under constant-amplitude and transient loading?

2. How do the interface strength, yield strength mismatch, and plastic strain gradients control fatigue crack growth behavior in bi-materials?

3. In a multilayered material, how does the size of a layer relative to the crack-tip plastic zone influence crack extension?

Creep-fatigue crack growth in rate-dependent materials is considered next. This addresses the knowledge gap regarding situations where crack growth acceleration and retardation occur following OLs in rate-dependent materials. The specific cases of crack growth in Alloy 617 and Alloy 718 are investigated.

The research questions addressed in this thesis for rate-dependent creep-fatigue crack growth are as follows:

1. What is the influence of the material rate sensitivity on post-overload fatigue crack growth rates in creep-ductile materials like Alloy 617?

2. What damage, hardening, and recovery mechanisms are relevant to steady-state and transient crack growth in creep-brittle materials like Alloy 718?

3. What insights do the computations provide into experimental results for crack growth following OLs in Alloy 617 and Alloy 718?

4. For both Alloy 617 and Alloy 718, what role do plastic strain gradients play in steady-state and transient crack growth?

These questions were addressed using finite element computations. The computational model combined elastic-plastic or elastic-viscoplastic constitutive laws in the bulk material with an incremental cohesive zone formulation to describe material degradation and crack extension. The plasticity and viscoplasticity formulations accounted for hardening due to plastic strain gradients [38], [41], [85]. Damage evolution equations phenomenologically accounted for dissipative mechanisms associated with subcritical crack growth under cyclic and hold-time loading [86]–[89]. Crack extension was thereby an outcome of the model. This enabled the model to predict the evolution of the crack-tip fields and the transient crack growth rates associated with OLs and inhomogeneous materials. This approach also made it possible to identify how different aspects of crack-tip plasticity, particularly plastic strain gradients and rate dependence, influence crack extension and the crack-tip fields.

1.5 Structure of this thesis

Chapter 2 presents an overview of the constitutive models used in the finite element computations. This includes each of the model components: (i) strain gradient plasticity and viscoplasticity models used to describe irreversible deformation in the bulk material and (ii) the cohesive zone model, together with fatigue and time-dependent damage evolution equations, used to describe subcritical material degradation and crack extension.

Chapter 3 presents a numerical study of crack growth following OLs in rate-independent materials. Particular emphasis is placed on the evolution of the crack-tip fields and crack growth rates after an OL. It is demonstrated that hardening due to plastic strain gradients is significant in the OL plastic zone. This hardening plays an important role in the residual stresses at the crack tip and the subsequent crack growth rates predicted by the model.

Chapter 4 presents a numerical study of crack growth in inhomogeneous multilayered materials with weak interfaces. Configurations investigated in the model include a bi-material, with each constituent having a different yield strength, and a high-yield-strength material containing a low-yield-strength interlayer. Hardening due to plastic strain gradients is shown to influence crack growth rates when the crack-tip plastic zone begins interacting with the interfaces.

Chapter 5 presents computations of crack growth in rate-dependent materials subjected to cyclic loading. Here, the bulk material was characterized by a power-law viscoplasticity formulation, which is typical of Alloy 617. The computations investigated fatigue crack growth rates following a single OL and a block of multiple OLs. Results from a parametric study demonstrate the crucial role of the material rate sensitivity, or creep exponent, in determining whether retardation occurs following OLs. The model was subsequently calibrated to experimentally-measured steady-state fatigue crack growth rates for Alloy 617 at 800°C from [15]. Predictions of crack extension following OLs agree with trends in experiments on Alloy 617 [18].

Chapter 6 presents computations of crack growth using a more complex viscoplasticity model that accounts for hardening and dynamic recovery based on dislocation storage and annihilation mechanisms. Time- and stress-dependent damage was considered as the main

crack growth mechanism. This approach is relevant for creep-brittle materials like Alloy 718. The model was calibrated using experimentally-measured crack growth rates under constant-amplitude and sustained loading on Alloy 718 at 650°C from [90]. The computations predicted crack growth retardation for three loading waveforms containing OLs, with a strong dependence on the OL ratio. Predictions of crack extension following OLs agree with trends in experiments on Alloy 718 [30], [33], [47].

Finally, Chapter 7 summarizes the main contributions of this thesis. The research questions identified in Section 1.4 are addressed based on the results presented in Chapters 3–6. General conclusions are also discussed.

2. PROBLEM FORMULATION AND CONSTITUTIVE MODELS

The boundary value problems analyzed in this thesis considered a solid containing internal cohesive interfaces. Problem solutions were obtained using two-dimensional plane strain finite element computations. For quasi-static deformation with body forces neglected, the principle of virtual work for a model containing internal cohesive surfaces is

$$\int_V \boldsymbol{s} : \delta \boldsymbol{F} \mathrm{d}V - \int_{S_{\mathrm{int}}} \boldsymbol{T}_{\mathrm{CZ}} \cdot \delta \boldsymbol{\Delta} \mathrm{d}S = \int_{S_{\mathrm{ext}}} \boldsymbol{T}_{\mathrm{e}} \cdot \delta \boldsymbol{u} \mathrm{d}S, \tag{2.1}$$

where $\boldsymbol{s}$ is the nominal stress tensor, $\boldsymbol{F}$ is the deformation gradient, V is the volume of the solid, $\boldsymbol{T}_{\mathrm{CZ}}$ is the traction vector on the cohesive surfaces, $\boldsymbol{\Delta}$ is the separation vector (or displacement jump) across the cohesive surfaces, $\boldsymbol{T}_{\mathrm{e}}$ is the traction vector on external surfaces, $\boldsymbol{u}$ is the displacement vector, and S_{int} and S_{ext} are the interfacial and external surfaces, respectively. The traction and separation vectors $\boldsymbol{T}_{\mathrm{CZ}}$ and $\boldsymbol{\Delta}$ are decomposed into normal and tangential components with respect to the cohesive surface: $\boldsymbol{T}_{\mathrm{CZ}} = T_n \hat{\boldsymbol{n}} + T_t \hat{\boldsymbol{t}}$ and $\boldsymbol{\Delta} = \Delta_n \hat{\boldsymbol{n}} + \Delta_t \hat{\boldsymbol{t}}$. The first and second terms in Eq. (2.1) capture deformation in the solid and material separation on the cohesive surfaces, respectively. Separate constitutive relations characterize each of these mechanisms. In this thesis, strain gradient plasticity and viscoplasticity formulations were used for the solid material. An irreversible cohesive zone formulation was used for material separation. The remainder of this chapter describes each constitutive relation and provides background on their development and prior use.

2.1 Strain gradient plasticity and viscoplasticity

It is now well known that classical plasticity models provide an incomplete description of plastic deformation. These models typically consider hardening as a function of the plastic strain, which is associated with the development of statistically-stored dislocations (SSDs) [41]. Experiments have shown that plastic strain gradients, associated with geometrically necessary dislocations (GNDs), are important in the hardening response when there is significant nonuniform plastic deformation over a sufficiently small lengthscale, usually on the

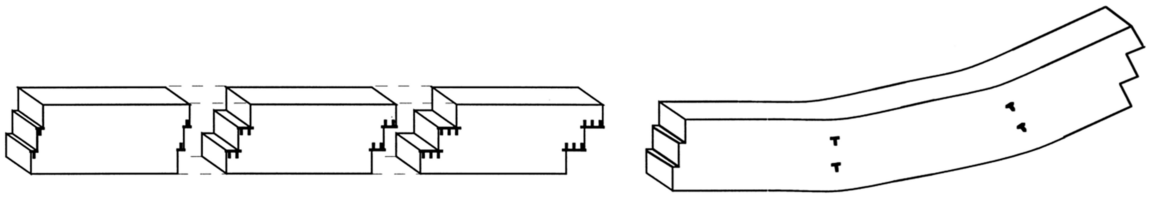

Figure 2.1. Depiction of inhomogeneous plastic deformation and development of geometrically necessary edge dislocations in order to maintain compatibility. Used with permission from [92].

order of microns [41], [91]. In these situations, GNDs arise to maintain deformation compatibility, as shown schematically in Figure 2.1 for a crystal undergoing single slip [91], [92]. The GNDs in turn serve as obstacles to mobile dislocations, leading to enhanced hardening beyond what is predicted by classical plasticity theories. Strain gradient plasticity models account for the hardening contribution from GNDs by introducing the plastic strain gradient and one or more intrinsic material lengthscales to the constitutive law [41]. These formulations generally fall into two classes. Higher-order theories (e.g. [93]) include the higher-order stress as the work conjugate to the plastic strain gradients. Lower-order theories (e.g., [85]) use an effective measure of the plastic strain gradient to alter the tangent modulus during plastic deformation, without including the higher-order stress.

Initial experiments demonstrated the importance of plastic strain gradients in nanoindentation [94] and torsion of thin wires [91]. These experiments demonstrated the trend that "smaller is harder" or "smaller is stronger": in situations where there is significant nonuniform deformation, a smaller specimen size or a smaller indentation depth leads to a higher flow stress or hardness due to the influence of GNDs. Plastic strain gradients have been shown to be relevant to crack-tip fields and crack growth under monotonic loading [38], [40], [95], [96]. The reason is the development of large plastic strain gradients in the crack-tip plastic zone. This leads to restricted plastic deformation relative to predictions from classical plasticity models.

In this thesis, the influence of plastic strain gradients and rate-dependent deformation on creep-fatigue crack growth rates and crack tip fields was evaluated using two strain gradient viscoplasticity formulations. The first is the conventional theory of mechanism-based

strain gradient viscoplasticity (CMSG-vp) of Huang et al. [85]. The rate-independent limit of this formulation, referred to as the CMSG model in [85], was also used in studies of rate-independent materials in this thesis. The second is the strain gradient Kocks-Mecking (SGKM) model developed by Nguyen et al. [97]. The SGKM model combines calculations of the GND density with a formulation based on the physical mechanisms of storage and dynamic recovery of SSDs. These models are described in the next two sections.

2.1.1 Conventional theory of mechanism-based strain gradient viscoplasticity

The CMSG-vp model is based on Taylor's dislocation theory [98]. This defines the flow stress in terms of the dislocation density ρ:

$$\sigma_{\text{flow}} = M\alpha\mu b\sqrt{\rho}, \tag{2.2}$$

where M is the Taylor factor, α is an empirical prefactor, μ is the shear modulus, and b is the Burgers vector magnitude. The total dislocation density is taken as the sum of the SSD and GND densities (ρ_{S} and ρ_{G}, respectively), such that $\rho = \rho_{\text{S}} + \rho_{\text{G}}$ [99]. The GND density is related to the effective viscoplastic strain gradient η^{vp}, a measure of the curvature of plastic deformation [100], by

$$\rho_{\text{G}} = \bar{r}\frac{\eta^{vp}}{b}, \tag{2.3}$$

where $\bar{r}$ is the Nye factor, equal to about 1.9 for face-centered cubic polycrystals [92]. An equation for ρ_{S} can be found by considering the case of uniaxial tension, in which $\eta^{p} = 0$ [85]. In this case, Eq. (2.2) can be rearranged to give

$$\rho_{\text{S}} = \left[\frac{\sigma_{\text{flow}}}{M\alpha\mu b}\right]^2, \tag{2.4}$$

where the flow stress can be written in terms of the viscoplastic strain through a strain hardening function $f\left(\varepsilon^{vp}\right)$, with $\sigma_{\text{flow}} = \sigma_0 f\left(\varepsilon^{vp}\right)$. Substituting Eq. (2.4) back into Eq. (2.2)

gives a general expression for the flow stress in terms of both the viscoplastic strain ε^{vp} and the effective viscoplastic strain gradient η^{vp}:

$$\sigma_{\text{flow}} = \sqrt{\sigma_0^2 f^2\left(\varepsilon^{vp}\right) + M^2 \bar{r} \alpha^2 \mu^2 b \eta^{vp}} = \sigma_0 \sqrt{f^2\left(\varepsilon^{vp}\right) + l \eta^{vp}}, \tag{2.5}$$

where l is an intrinsic material length that scales the influence of viscoplastic strain gradients. The intrinsic length is typically on the order of microns, which corresponds to the experimental lengthscale where size effects are observed [85]. As in [85] and other studies based on this approach [40], [101], a power-law hardening equation is used for f:

$$f\left(\varepsilon^{vp}\right) = \left(1 + \frac{E\varepsilon^{vp}}{\sigma_0}\right)^n, \tag{2.6}$$

where n is the strain hardening exponent and E is Young's modulus. Using analytical calculations based on models of GNDs for bending, torsion, and void growth, Fleck and Hutchinson [41] and Gao et al. [93] determined the effective viscoplastic strain gradient η^{vp} to be given by

$$\eta^{vp} = \sqrt{\frac{1}{4} \eta_{ijk}^{vp} \eta_{ijk}^{vp}}, \tag{2.7}$$

where

$$\eta_{ijk}^{vp} = \varepsilon_{ik,j}^{vp} + \varepsilon_{jk,i}^{vp} - \varepsilon_{ij,k}^{vp}. \tag{2.8}$$

These equations use the standard index notation, with derivatives denoted by a comma. The accumulated viscoplastic strain ε_{ij}^{vp} is the integral of the viscoplastic strain rate, i.e.

$$\varepsilon_{ij}^{vp} = \int \dot{\varepsilon}_{ij}^{vp} \mathrm{d}t, \quad \varepsilon^{vp} = \int \dot{\varepsilon}^{vp} \mathrm{d}t, \tag{2.9}$$

and $\dot{\varepsilon}^{vp}$ is the von Mises effective viscoplastic strain rate.

A power law viscoplasticity equation relates the effective viscoplastic strain rate to the effective stress:

$$\dot{\varepsilon}^{vp} = \dot{\varepsilon}_0 \left(\frac{\bar{\sigma}}{\sigma_{\text{flow}}}\right)^m, \tag{2.10}$$

where $\dot{\varepsilon}_0$ is a reference strain rate, $\bar{\sigma}$ is the von Mises effective stress, and m is the creep exponent. This type of model is also often expressed in terms of the strain rate sensitivity, $1/m$, such that the model is highly rate sensitive for small m. The model reduces to a Norton secondary creep law for strain hardening exponent $n = 0$.

A rate-independent plasticity formulation is approximated by setting m to a large value and replacing the reference strain rate $\dot{\varepsilon}_0$ with the von Mises effective strain rate, $\dot{\bar{\varepsilon}}$. This recovers the original rate-independent CMSG model of Huang et al. [85], where the effective plastic strain rate $\dot{\varepsilon}^p$ is given by

$$\dot{\varepsilon}^p = \dot{\bar{\varepsilon}} \left(\frac{\bar{\sigma}}{\sigma_{\text{flow}}} \right)^m . \tag{2.11}$$

Approximating rate independence using Eq. (2.11) provides an advantage over models that incorporate plastic strain gradients into conventional rate-independent plasticity models: by relating the strain rate to the stress instead of the stress rate, hardening due to plastic strain gradients can be incorporated with minimal changes to the model framework [85]. Strain gradient plasticity formulations based on standard rate-independent plasticity require calculation of the higher-order stress and the subsequent use of higher-order boundary conditions [41], [93]. For the rate-independent fatigue crack growth computations in this thesis, a value of $m = 75.0$ was found to provide sufficiently rate-independent behavior without introducing numerical difficulties.

The CMSG-vp model was implemented using a UMAT subroutine in Abaqus [102], based on the original CMSG implementation of [85], [103], which was used for the rate-independent computations in this thesis. The implementation used a standard predictor-corrector algorithm, and the viscoplastic strain increment was found using Newton-Raphson iterations in each time step. Details of the numerical implementation are given in Appendix A.

2.1.2 Strain gradient Kocks-Mecking viscoplasticity formulation

The SGKM formulation is based on the work of Kocks, Mecking, and Estrin [104]–[107]. This approach describes viscoplastic deformation using the dislocation density as an internal variable capturing the current microstructural state. The evolution of the SSD density is described using physically-based laws for dislocation accumulation and annihilation [106],

[108]. Nguyen et al. [97] developed the SGKM model by extending the Kocks-Mecking approach to account for GNDs. The SGKM model uses the viscoplastic constitutive law in Eq. (2.10), with the flow stress σ_{flow} determined as a function of the dislocation density. Equation (2.10) is typically referred to as the *kinetic equation* in this context, as it relates the rate of plastic strain to the stress and the current material state [106].

The flow stress in the SGKM formulation is given by

$$\sigma_{\text{flow}} = \sigma_0 + M\alpha\mu b\sqrt{\rho_{\text{S}} + \rho_{\text{G}}}. \tag{2.12}$$

Here, σ_0 is the initial yield stress accounting for pre-existing strengthening mechanisms, particularly second-phase particles (mainly γ'' in the case of Alloy 718) [106]. The second term accounts for strengthening associated with dislocations. As before, the evolution of the GND density is given by Eq. (2.3), with the effective viscoplastic strain gradient calculated from Eqs. (2.8) and (2.7).

Strain hardening is associated with an increase in the SSD density. Changes in the SSD density result from the competition between dislocation storage and dynamic recovery [108]. Mathematically, the evolution of the SSD density with respect to the viscoplastic strain is

$$\frac{\mathrm{d}\rho_{\text{S}}}{\mathrm{d}\varepsilon^{vp}} = \frac{\mathrm{d}\rho_{\text{S}}^{+}}{\mathrm{d}\varepsilon^{vp}} - \frac{\mathrm{d}\rho_{\text{S}}^{-}}{\mathrm{d}\varepsilon^{vp}}. \tag{2.13}$$

The first term on the right-hand side of Eq. (2.13) represents SSD storage, associated with dislocations becoming immobilized at obstacles, described by the following equation:

$$\frac{\mathrm{d}\rho_{\text{S}}^{+}}{\mathrm{d}\varepsilon^{vp}} = \frac{M}{b\Lambda}, \tag{2.14}$$

where Λ is the mean free path of mobile dislocations. When mobile dislocations are immobilized by forest dislocations, Λ is proportional to $1/\sqrt{\rho}$ [108]. The storage term is then given by

$$\frac{\mathrm{d}\rho_{\text{S}}^{+}}{\mathrm{d}\varepsilon^{vp}} = Mk_1\sqrt{\rho}, \tag{2.15}$$

where k_1 is a constant. Since both SSDs and GNDs can serve as obstacles to mobile dislocations, the total dislocation density is used in Eq. (2.15) (i.e., $\rho = \rho_S + \rho_G$) [109].

The second term on the right-hand side of Eq. (2.13) describes SSD annihilation due to dynamic recovery, a thermally-activated process associated with dislocation climb at high temperatures [106]. This term is given by

$$\frac{\mathrm{d}\rho_S^-}{\mathrm{d}\varepsilon^{vp}} = M k_2 \rho_S \tag{2.16}$$

where k_2 is a parameter describing the rate sensitivity of the dynamic recovery process [106]. Estrin and Mecking [110] suggest that k_2 is given by

$$k_2 = k_{20} \left(\frac{\dot{\varepsilon}^{vp}}{\dot{\varepsilon}_0} \right)^{-1/n}, \tag{2.17}$$

where k_{20} is a constant, $\dot{\varepsilon}_0$ is the reference strain rate from the kinetic equation, and n is a rate sensitivity exponent. The form of Eq. (2.17) is based on observations that the flow stress increases up to a saturation stress during the hardening process [110]. The SSD density alone is used in Eq. (2.16) since GNDs are fully described by Eq. (2.3) and do not participate in the annihilation process [109]. Also, dynamic recovery is the main source of rate dependence in this formulation, as typically $m \gg n$ [106], [107], [110]. Using Eqs. (2.15) and (2.16), the expression for the evolution of the SSD density (Eq. (2.13)) becomes

$$\frac{\mathrm{d}\rho_S}{\mathrm{d}\varepsilon^{vp}} = M \left(k_1 \sqrt{\rho} - k_2 \rho_S \right). \tag{2.18}$$

The SGKM model was implemented using a UMAT subroutine in Abaqus [102], based in part on the original implementation of Nguyen et al. [97]. Here, two state variables must be updated in each time step: the viscoplastic strain increment $\Delta\varepsilon^{vp}$ and the SSD density increment $\Delta\rho_S$. To achieve this, the SSD density increment was written in terms of the viscoplastic strain increment, and the viscoplastic strain increment was found using Newton-Raphson iteration. Details of the numerical implementation are given in Appendix B.

2.2 Material separation

The computations in this thesis captured material separation using an irreversible cohesive zone model (CZM). The CZM approach follows from the work of Barenblatt and Dugdale [111], [112], who developed what is typically referred to as a process-zone or strip-yield model to describe the stress distribution ahead of a crack tip [1]. Needleman [113], [114] implemented a cohesive constitutive law within a finite element model. The cohesive constitutive law relates material separation to cohesive tractions resisting separation on the crack surfaces. As separation proceeds, the traction increases until it reaches a peak and then smoothly falls, reaching zero when complete separation occurs [113]. The traction-separation law describes the material separation process using two parameters: the cohesive strength (i.e., the maximum traction) and the work of fracture or cohesive energy per unit area. The traction-separation law was embedded in zero-thickness cohesive elements placed along an interface between two materials or ahead of a crack tip. This eliminates the singularity at the crack tip, while also enabling computations to predict fracture as an outcome of the model even when there is not an initial crack.

Tvergaard and Hutchinson applied this concept to ductile fracture [115], [116]. Here, the traction-separation law is intended to model the void growth and coalescence process, which occurs together with plastic deformation in the bulk material. Subsequently, CZMs have been used in numerous finite element computations involving fracture and interface separation, with a variety of constitutive laws describing the bulk material and fracture mechanisms embedded within the CZM description [117].

The CZM approach has been extended to fatigue crack growth by introducing either unloading-reloading hysteresis or an evolving damage variable into the traction-separation law [118]. Either of these approaches adds irreversibility to the CZM. For example, Nguyen et al. [119] developed a model that used different unloading and reloading stiffnesses for the CZM under cyclic loading. The reloading stiffness was assumed to gradually decay as a function of the crack opening displacement rate. The more common approach has been to introduce a damage variable, which degrades the traction-separation law until load-carrying capacity is lost at a critical value of the damage [118]. The damage evolution equation is

typically a function of the separation increment and the current traction at a point in the cohesive zone, based on the concepts of damage mechanics [86], [88], [89], [120]–[123].

Multiple damage mechanisms can be considered in the development of damage evolution equations for an irreversible CZM. For example, Bouvard et al. [88] combined fatigue and creep damage evolution equations to describe subcritical crack growth in a single crystal nickel-base superalloy. A simple summation of the creep and fatigue damage was found to adequately fit experimental crack growth rate data in load regimes where both damage mechanisms were active. Sun el al. [89] followed a similar approach, with the addition of an environmental damage term associated with oxidation. Failure was assumed to occur when either the combined creep-fatigue damage or the environmental damage reached a critical value. The model was successfully fit to crack growth experiments on IN100. This approach has also been extended to address crack growth due to oxygen-enhanced gain boundary sliding [124].

The CZM approach with damage evolution was chosen in this thesis based on two key advantages it provides. First, using a CZM formulation within an incremental finite element model enables the computations to predict crack growth for arbitrary loading waveforms. This enables a detailed analysis of the crack growth rates and the crack-tip fields following various types of transient loading. Second, the CZM can be combined with any choice of problem geometry and constitutive law for the bulk material. The computations can thereby quantify how different characteristics of viscoplastic deformation and material inhomogeneity influence the crack growth rates.

2.2.1 Irreversible cohesive zone model

The traction-separation relationship is based on the potential function proposed by Xu and Needleman [125]. The normal and tangential traction-separation laws are given by

$$T_n = \sigma_{\max,0}\,(1-D)\,\mathrm{e}\exp\left(-\frac{\Delta_n}{\delta_0}\right)\frac{\Delta_n}{\delta_0}\left\{1-q\left[1-\exp\left(-\frac{\Delta_t^2}{\delta_0^2}\right)\right]\right\} \tag{2.19}$$

$$T_t = 2\sigma_{\max,0}\,(1-D)\,\mathrm{e}q\frac{\Delta_t}{\delta_0}\left(1+\frac{\Delta_n}{\delta_0}\right)\exp\left(-\frac{\Delta_n}{\delta_0}\right)\exp\left(-\frac{\Delta_t^2}{\delta_0^2}\right), \tag{2.20}$$

where $\sigma_{\max,0}$ is the cohesive strength, δ_0 is a characteristic separation, D is a damage variable, $\mathrm{e} = \exp(1)$, $q = \phi_{n,0}/\phi_{t,0}$, and $\phi_{n,0}$ and $\phi_{t,0}$ are the cohesive energies for pure normal and pure tangential separation, respectively. The cohesive strengths in normal and shear are related by $\tau_{\max,0} = \sigma_{\max,0} q\sqrt{2\mathrm{e}}$. The normal and shear cohesive energies are given by

$$\phi_{n,0} = \sigma_{\max,0}\delta_0 \mathrm{e} \tag{2.21}$$

$$\phi_{t,0} = q\sigma_{\max,0}\delta_0 \mathrm{e}. \tag{2.22}$$

Here, the parameter q was chosen as $q = 1/\sqrt{2\mathrm{e}}$ such that $\tau_{\max,0} = \sigma_{\max,0}$ [125]. In the context of crack extension, the normal components are associated with mode I fracture, and the tangential components are associated with mode II (shear) fracture.

For normal separation, unloading occurs toward the origin [126]. For tangential separation, unloading occurs with the current stiffness of the tangential traction-separation law [126]. When contact occurs between the cohesive surfaces, the normal traction is negative, and no damage accumulation occurs. In this situation, the traction-separation law is modified with a penalty stiffness $A = 30$ [87] such that the normal traction is given by

$$T_n\left(\Delta_n\right) = A\sigma_{\max,0} \exp\left(1 - \frac{\Delta_n}{\delta_0}\right)\left(\frac{\Delta_n}{\delta_0}\right). \tag{2.23}$$

Subcritical crack growth is captured through the evolution of the damage variable D. A cohesive element is considered to have failed when $D = 1.0$. Damage is defined on an averaged-per-element basis [86]. For materials where rate-independent fatigue damage is relevant, the damage evolution equation introduced by Roe and Siegmund [86] was used:

$$\dot{D} = \frac{|\dot{\bar{\Delta}}|}{\delta_\Sigma}\left\langle \frac{\bar{T}/\left(1-D\right) - \sigma_f}{\sigma_{\max,0}} \right\rangle \mathrm{H}\left(\bar{\Delta}_{\mathrm{acc}} - \delta_0\right), \quad \bar{\Delta}_{\mathrm{acc}} = \int |\dot{\bar{\Delta}}| dt \tag{2.24}$$

where $\bar{\Delta}_{\mathrm{acc}}$ is the accumulated separation, $\langle\rangle$ are Macauley brackets, and H is the Heaviside function. The characteristic fatigue separation δ_Σ scales the increment in effective separation while the cohesive zone endurance limit σ_f sets the traction below which no damage accumulation occurs [86]. Damage does not set in until the accumulated separation exceeds

a threshold, chosen as δ_0 [86], [87]. During an increment in a finite element computation, the fatigue damage increment is proportional to the separation increment and weighted by the current traction. In Chapter 5, a modified version of this equation was used:

$$\dot{D} = \frac{|\dot{\bar{\Delta}}|}{C_f} \left\langle \bar{T} - \sigma_f \right\rangle, \tag{2.25}$$

where C_f is a reference damage energy with units of stress-length or energy per unit area and, as before, σ_f is a threshold below which damage does not accumulate. This removes the explicit coupling between the cohesive strength and the damage evolution equation, leaving a single parameter C_f in the denominator of this equation. The parameter C_f is similar to reference energy release rate terms that serve as scaling parameters in damage laws coupled with elasticity and plasticity in the bulk material [127]. The parameters C_f and σ_f are used to calibrate the model to experimentally-measured crack growth rates.

For rate-dependent materials where time-dependent damage is relevant, a Kachanov-Rabotnov-type damage evolution equation was used [88], [128]. Here, the damage evolution is given by

$$\dot{D} = \left\langle \frac{\bar{T}/\left(1-D\right) - T_c}{C_c} \right\rangle^r, \tag{2.26}$$

where T_c is a threshold traction below which damage does not accumulate and r is a damage exponent. The parameter C_c is similar to the reference damage energy in Eq. (2.25), but it has units of [stress]·[time]$^{1/r}$. These parameters are used to calibrate the model to experimentally-measured crack growth rates. The time-dependent damage is proportional to the current traction, such that damage accumulation increases with long hold times at high stresses.

The effective traction and separation, $\bar{T}$ and $\bar{\Delta}$, used in the damage evolution equations are given by

$$\bar{T} = \sqrt{T_n^2 + T_t^2} \tag{2.27}$$

$$\bar{\Delta} = \sqrt{\Delta_n^2 + \Delta_t^2} \tag{2.28}$$

such that the normal and tangential components are given equal weight for the current choice of $q = 1/\sqrt{2\mathrm{e}}$.

Under pure mode I conditions, the tangential traction and separation are zero. Therefore, the traction-separation law simplifies to

$$T_n = \sigma_{\max,0}\,(1-D)\exp\left(1-\frac{\Delta_n}{\delta_0}\right)\left(\frac{\Delta_n}{\delta_0}\right). \tag{2.29}$$

The effective traction and separation used in the damage evolution equations are also equivalent to the normal traction and separation. This is the case for all studies presented here except for crack growth along interfaces in Chapter 4.

The UEL subroutine [102] implementation of the irreversible CZM by Roe and Siegmund [86] was used throughout this thesis. The subroutine was modified to incorporate the time-dependent damage evolution equation, Eq. (2.26).

3. PLASTIC STRAIN GRADIENTS AND TRANSIENT FATIGUE CRACK GROWTH

A version of this chapter has been previously published in *International Journal of Fatigue* [129]: J.D. Pribe, T. Siegmund, V. Tomar, J.J. Kruzic, "Plastic strain gradients and transient fatigue crack growth: A computational study," *Int J Fatigue*, vol. 120, pp. 283-293, 2019. DOI:10.1016/j.ijfatigue.2018.11.020.

3.1 Introduction

A key question in fatigue failure is how crack growth rates change in response to variable amplitude loads, where no steady state solutions exist for the fatigue crack growth problem. As a result, transients in fatigue crack growth require a detailed, often cycle-by-cycle analysis of the problem [6], [54]. The use of cohesive zone models for fatigue crack growth has been shown to be highly relevant in such studies and has provided detailed insight into transient crack growth problems [87], [118], [119], [130]–[132]. As noted in Chapter 1, the description of plastic deformation during crack growth transients is also extremely important for predicting the crack growth rates. To this end, this study investigates the influence of hardening due to plastic strain gradients on crack extension following OLs.

Strong plastic strain gradients can develop in the plastic zone ahead of a crack tip, particularly under plane strain conditions [133]. Numerical studies of cracked bodies subjected to monotonic loading have shown that GNDs associated with plastic strain gradients reduce crack-tip blunting and produce a region ahead of the crack tip with significantly higher stress than that predicted by either the classical HRR fields or computations with classical plasticity models [95], [134]. As a result, strain gradient plasticity models predict lower fracture toughness for both sharp and initially blunted cracks [135].

In the context of fatigue, Sevillano [136] derived an analytical model for the intrinsic stress intensity threshold for fatigue crack growth based on the strain gradient in the crack-tip plastic zone. An overview of experimental results indicated that plastic strain gradients explained the existence of this intrinsic threshold, on which crack closure effects are superim-

posed in experimentally measured thresholds. Brinckmann and Siegmund [137] found that plastic strain gradients reduce crack closure in constant amplitude loading, which led to a slightly increased steady-state growth rate in a numerical study using strain gradient plasticity model based on dislocation densities. Computations using a cohesive zone model coupled to the GND density predicted the delayed retardation phenomenon following an OL [138], well-known from numerous fatigue crack growth experiments [51], [54], [139]. Regions of enhanced and reduced GND densities in the computations corresponded to the OL-induced acceleration and retardation, respectively. Results in [138] were limited, however, due in part to numerical difficulties that arose outside of a small range of applied loads.

Experiments also provide evidence for the relevance of plastic strain gradients in fatigue crack growth. Electron backscatter diffraction measurements have been used by several researchers to infer grain misorientations and GND densities ahead of a fatigue crack [140]–[142]. These studies have generally observed GNDs at distances ahead of the crack close to classical estimates of the plastic zone size. Using X-ray microdiffraction, the authors in [143] observed large GND densities, along with small voids and cracks, near the surface of a fatigue crack subjected to an OL. However, the relative role of GNDs in comparison to SSDs remains an open question for both steady-state and transient fatigue crack growth. Further investigation is thus warranted to quantify the changes in crack tip fields and cyclic deformation predicted by strain gradient plasticity models relative to classical plasticity. This will in turn determine whether plastic strain gradients must be accounted for in practical fatigue assessments.

This study addresses the hypothesis that lengthscale effects in plasticity would not affect predicted steady-state fatigue crack growth rates but would alter predicted crack growth rates when the crack is subjected to load transients, such as an OL. This hypothesis is motivated by the fact that steady-state fatigue crack growth is known to be essentially microstructure insensitive and can be described by linear elastic fracture mechanics under small-scale yielding conditions. On the other hand, the extent of retardation due to an OL depends on the well-known mechanisms of plasticity-induced crack closure and compressive residual stress ahead of the crack tip, both of which are closely tied to the crack-tip plastic zone size and plastic strain magnitudes [44], [51], [144]. These quantities will be influenced by

plastic strain gradient hardening in the large monotonic plastic zone resulting from the OL. Furthermore, it has been argued that post-OL crack growth is governed by near-threshold micromechanisms [139], which, as noted previously, have been connected to GNDs at the crack tip and in the plastic zone.

The computational model used in this study combined a first-order strain gradient plasticity formulation [85] with an irreversible cohesive zone model [86]. Crack growth rates, the evolution of cohesive zone tractions and separations, and plasticity in terms of strains and strain gradients in the bulk material are considered for both constant-amplitude loading and the transient period following a single OL. The effects of plastic strain gradients are then elucidated by analyzing the crack-tip stress, strain, and strain gradient fields.

3.2 Model description

Mode I cyclic loading under plane strain conditions was applied via a boundary layer model [57], modified by the introduction of cohesive elements. In this approach, an initially sharp crack and the domain of crack extension are enclosed in a circular domain. Displacements corresponding to the asymptotic crack-tip solution were imposed on the boundary, which remains elastic and surrounds the crack-tip plastic zone. This assumes that the condition of small-scale yielding is fulfilled. Given a prescribed mode I stress intensity factor K_I, the boundary displacements $u(t)$ are determined from the Williams expansion [145] as

$$u_x(t,r,\theta) = K_I(t)\frac{1+\nu}{E}\sqrt{\frac{r}{2\pi}}\cos\left(\frac{\theta}{2}\right)(3-4\nu-\cos\theta)\,, \tag{3.1}$$

$$u_y(t,r,\theta) = K_I(t)\frac{1+\nu}{E}\sqrt{\frac{r}{2\pi}}\sin\left(\frac{\theta}{2}\right)(3-4\nu-\cos\theta)\,, \tag{3.2}$$

where E is Young's modulus, ν is Poisson's ratio, and r and θ are the radial and angular coordinates, with the initial crack tip as the origin. A triangular waveform was prescribed for the mode I stress intensity factor in order to simulate cyclic loading.

The finite element mesh used in this study is shown in Figure 3.1. The displacement boundary conditions were applied on the outer nodes, as shown in Figure 3.1a. Due to

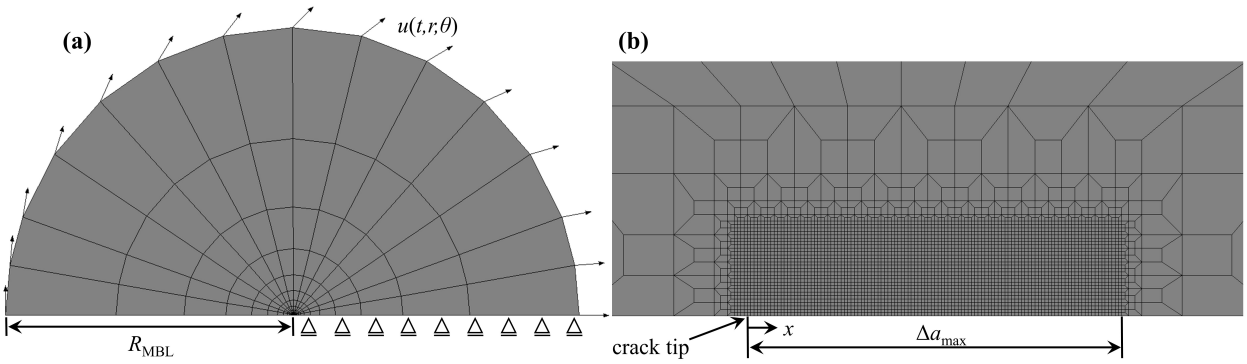

Figure 3.1. (a) Global and (b) crack-tip mesh in the modified boundary layer model.

symmetry in mode I loading, a half-model was considered. The continuum consisted of 3892 linear plane strain elements and 123 cohesive zone elements along the symmetry line. The cohesive elements shared their top nodes with the adjacent solid elements. The bottom nodes were along the symmetry line, so their vertical displacements were fixed at zero. Due to symmetry, the horizontal displacements of the top and bottom nodes were tied pairwise, such that pure mode I conditions were present and the tangential traction and separation in the cohesive zone were zero. A structured quadrilateral mesh was used near the crack tip, extending in the crack growth direction. The MBL model radius (R_{MBL}) is 10,000 times larger than the minimum element size.

The rate-independent CMSG model described in Section 2.1.1, with $m = 75.0$ in Eq. (2.11) was used to describe the bulk material. The irreversible CZM with fatigue damage given by Eq. (2.24) in Section 2.2.1 was used to describe material separation ahead of the initial crack tip. Since pure mode I conditions were active, the traction-separation law was given by Eq. (2.29).

3.2.1 Model parameters

A model material was considered in order to provide general understanding of the role of plastic strain gradients in fatigue crack growth. The material properties are based on the work of Wang and Siegmund [87], [126]. For all computations, Young's modulus and Poisson's ratio were $E = 100$ GPa and $\nu = 0.34$, respectively. The reference stress σ_0 was taken as the

initial yield strength σ_Y and set to $\sigma_Y = 0.0025E = 250$ MPa, with an isotropic hardening exponent of $n = 0.1$. Two intrinsic material length values were considered: $l = 0$ (predicts strain hardening only) and $l = 10$ μm (strain hardening and strain gradient hardening). This is an approximate upper bound on the value of l based on previous CMSG-based studies [39], [85].

Previous studies of fatigue crack growth have linked the ratio of the cohesive strength to the yield strength, $\sigma_{\max,0}/\sigma_Y$, with the plastic dissipation in the bulk material during crack extension [126], [131], [132], [137], [146]. Two values of this ratio were considered: $\sigma_{\max,0}/\sigma_Y = 4.0$ and $\sigma_{\max,0}/\sigma_Y = 4.5$. These correspond to cohesive energies of $\phi_0 = 20.0$ J/m^2 and $\phi_0 = 25.0$ J/m^2 for constant characteristic separation $\delta_0 = 7.36$ nm. These two cases were used to investigate the effect of plastic strain gradients relative to the amount of crack-tip plasticity. The cohesive zone endurance limit and characteristic fatigue separation were chosen as $\sigma_f/\sigma_{\max,0} = 0.25$ and $\delta_\Sigma/\delta_0 = 4.0$, following previous studies of fatigue crack growth in the Paris regime [87], [137]. The implications of these parameter choices are considered further in the Discussion.

A reference stress intensity factor K_0 is defined from the linear elastic fracture mechanics relation between the energy release rate and mode I stress intensity:

$$K_0 = \sqrt{\frac{E\phi_0}{1-\nu^2}}. \tag{3.3}$$

For $\phi_0 = 20.0$ J/m^2 and 25.0 J/m^2, $K_0 = 1.50$ MPa$\sqrt{\text{m}}$ and 1.68 MPa$\sqrt{\text{m}}$, respectively. The maximum applied stress intensity factor $K_{\max}$ and stress intensity range ΔK are related to the plane strain monotonic and cyclic plastic zone sizes R_p and R_c, respectively [147]:

$$R_p = \frac{1}{3\pi}\left(\frac{K_{\max}}{\sigma_Y}\right)^2 \tag{3.4}$$

$$R_c = \frac{1}{3\pi}\left(\frac{\Delta K}{2\sigma_Y}\right)^2. \tag{3.5}$$

All computations presented here were completed under small-scale yielding conditions, with R_{MBL} on the order of $100R_p$ or greater. The smallest element size in the structured quadri-

lateral mesh, equal to the minimum incremental crack advance, was $2.5\delta_0$, while crack extension was restricted to the structured mesh region, resulting in a maximum crack extension of $\Delta a_{\max} = 275\delta_0$. Results are depicted for crack extension up to only $\Delta a = 250\delta_0$ since this ensures the crack-tip plastic zone also remains contained in the refined mesh region.

3.3 Results

First, steady-state crack growth is considered. Figure 3.2 shows the dependence of the predicted normalized crack growth rate $\mathrm{d}(a/\delta_0)/\mathrm{d}N$ on the normalized applied stress intensity factor range $\Delta K/K_0$ for combinations of the intrinsic material length l, load ratio R, and initial cohesive strength $\sigma_{\max,0}$. In all cases, a Paris Law-type response emerges from the model, i.e., the predicted response can be described by the equation $\mathrm{d}\left(a/\delta_0\right)/\mathrm{d}N = A\left(\Delta K/K_0\right)^{M_p}$.

The exponent M_p characterizes the slope of the lines in Figure 3.2. Table 3.1 summarizes the predicted M_p values for each combination of $\sigma_{\max,0}/\sigma_Y$, R, and l. The exponent is quite insensitive to the value of l, with small changes in the predicted steady-state crack growth rate only becoming apparent for high values of ΔK with $\sigma_{\max,0}/\sigma_Y = 4.5$. This produces differences in the predicted value of M_p on the order of 10^{-2}. Changing the load ratio R shifts the data with respect to $\Delta K/K_0$ and slightly reduces the exponent M_p as well. This behavior is seen in experiments [2] and in other numerical studies with cohesive zone models [122].

Constant-amplitude loading interrupted by a single OL is now considered. Each computation was conducted with load ratio $R = 0.1$ and consisted of the following steps. First, constant-amplitude loading was applied with $\Delta K/K_0 = 0.28$, 0.35, or 0.40. The OL was applied in the cycle after the crack extension exceeded $\Delta a/\delta_0 = 75$, such that steady-state conditions developed prior to the OL. The OL ratio was $K_{\max,\mathrm{OL}}/K_{\max} = 1.73$, where $K_{\max,\mathrm{OL}}$ is the maximum applied stress intensity factor during the OL. This corresponds to applied energy release rate ratio $G_{\max,\mathrm{OL}}/G_{\max} = 3.0$.

Figure 3.3 shows the predicted crack extension for the computations with a single OL and different steady-state $\Delta K/K_0$ values. Predictions for both $l = 0$ and $l = 10$ μm are

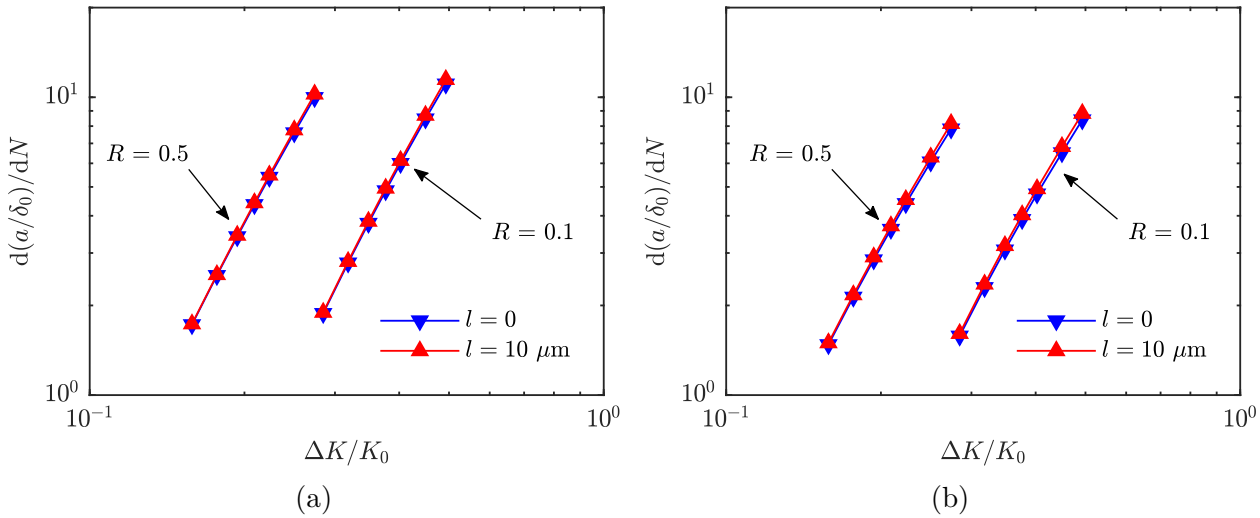

Figure 3.2. Dependence of the normalized crack growth rate on the normalized stress intensity range for (a) $\sigma_{\max,0}/\sigma_Y = 4.0$ and (b) $\sigma_{\max,0}/\sigma_Y = 4.5$.

Table 3.1. Paris law exponents.

$\sigma_{\max,0}/\sigma_Y$	R	l (μm)	M_p
4.0	0.1	0	3.23
		10	3.27
	0.5	0	3.19
		10	3.23
4.5	0.1	0	3.03
		10	3.09
	0.5	0	3.03
		10	3.08

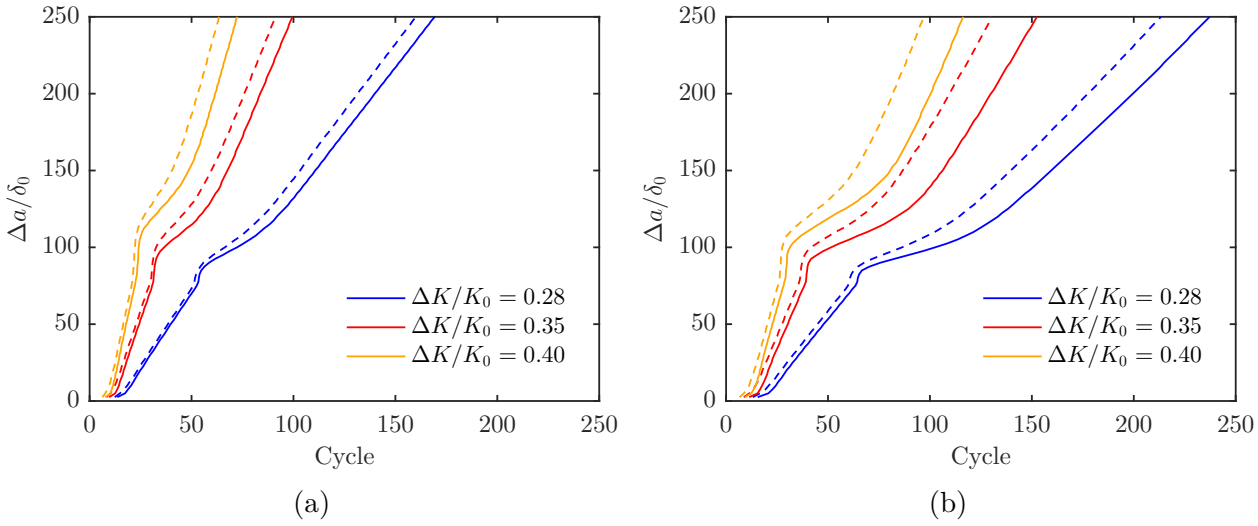

Figure 3.3. Crack extension with a single OL for $l = 0$ (solid lines) and $l = 10$ μm (dashed lines) with cohesive strength (a) $\sigma_{\max,0}/\sigma_Y = 4.0$ and (b) $\sigma_{\max,0}/\sigma_Y = 4.5$. The load ratio is $R = 0.1$, with several cases of steady-state $\Delta K/K_0$.

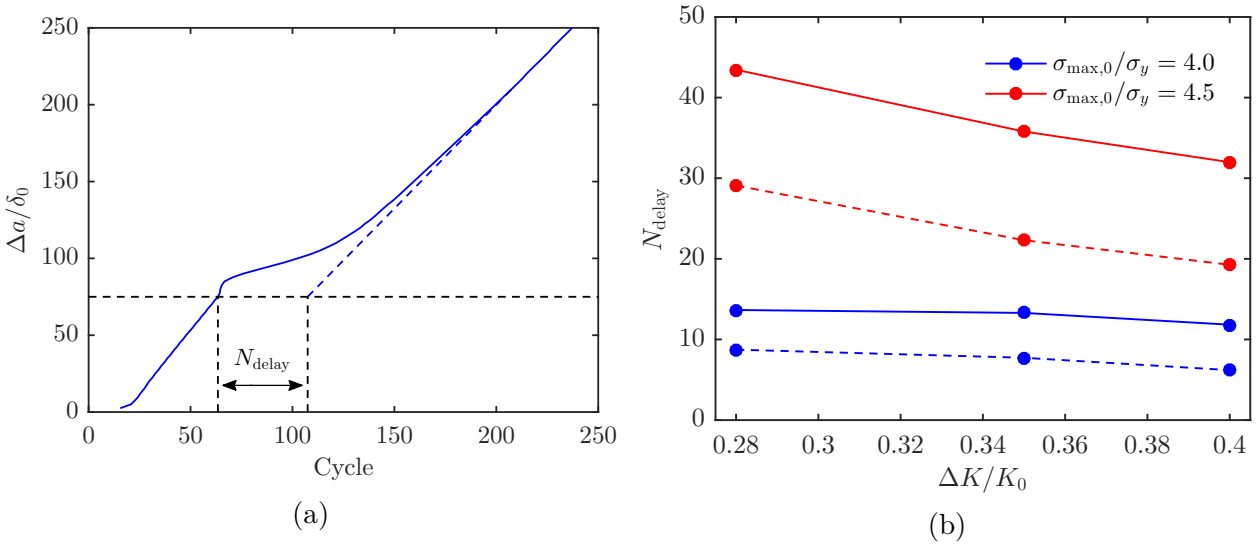

Figure 3.4. (a) Sample calculation of number of delay cycles. (b) Number of delay cycles for $l = 0$ (solid lines) and $l = 10$ μm (dashed lines).

shown. All computations predict a brief transient period while crack growth begins from the initial crack tip, followed by steady-state crack growth where the crack growth rate is insensitive to the value of l. During the OL, the computations predict a brief acceleration followed by crack growth retardation in the following cycles. For large crack extensions, the crack growth rate is predicted to nearly return to the original steady-state value. The slightly lower crack growth rate for longer crack lengths is a known feature of the modified boundary layer model [87], as the assumptions behind Eq. (3.1) and (3.2), i.e. that the displacements correspond to a constant ΔK, begin to be violated. In the present computations, the crack grows through the entire OL plastic zone, allowing for analysis of the region where the OL most significantly affects crack growth rates.

The importance of plastic strain gradients becomes clear in the post-OL crack growth transients, where the computations predict less severe retardation for $l = 10$ μm than for $l = 0$. The retardation was measured using the number of delay cycles N_{delay}, defined as the number of cycles required to traverse the OL-affected region relative to a crack under only constant-amplitude loading [53], [54]. The value of N_{delay} was calculated by applying a linear fit to the region of crack extension far beyond the OL and extrapolating back to the crack length when the OL was applied, as depicted in Figure 3.4a. The number of delay

cycles for computations with $l = 0$ and $l = 10$ μm for each $\sigma_{\max,0}/\sigma_Y$ and several values of $\Delta K/K_0$ is shown in Figure 3.4b. The predicted N_{delay} is always smaller for $l = 10$ μm, with the effect becoming stronger for higher cohesive strength. Although N_{delay} becomes smaller at higher values of $\Delta K/K_0$, the difference between the predicted values for $l = 0$ and $l = 10$ μm remains very nearly constant.

The severity of retardation can be further examined through the crack growth rates, shown in Figure 3.5 for $\Delta K/K_0 = 0.35$, relative to the number of cycles and the crack extension. Figure 3.5a shows that, for $l = 10$ μm, the model predicts a higher minimum fatigue crack growth rate than for $l = 0$ for both values of cohesive strength. Figure 3.5b provides information about the spatial extent of crack retardation after the OL. Following the peak, the model predicts that the crack growth rate almost immediately falls to the minimum value for $l = 0$ while the crack growth rate for $l = 10$ μm remains elevated for the first few elements after the OL is applied. However, the maximum extent of the OL-affected region is not significantly affected by the value of l. The OL-affected region ends at about $\Delta a/\delta_0 = 175$ for all cases, with the higher cohesive strength ($\sigma_{\max,0}/\sigma_Y = 4.5$) leading to a small increase. Thus, for $l = 10$ μm, the model predicts a higher minimum crack growth rate and a lower number of delay cycles, but a similar maximum extent of the OL-affected region, relative to $l = 0$.

The transient processes in the cohesive zone and in the bulk plastic deformation give insight into the role of plastic strain gradients in post-OL crack growth. In the following results, these processes are analyzed using the computations with $\Delta K/K_0 = 0.35$ as a representative case. Figures 3.6 and 3.7 show a comparison between the steady-state and post-OL traction distributions for $\sigma_{\max,0}/\sigma_Y = 4.0$ and $\sigma_{\max,0}/\sigma_Y = 4.5$, respectively. In each case, the steady-state traction distributions are nearly independent of the value of l, with the main difference being a small amount of crack closure—indicated by negative traction—for $l = 0$ and $\sigma_{\max,0}/\sigma_Y = 4.5$. This occurs only at the minimum applied load, meaning that the crack remains open for nearly the entire cycle. During and after the OL cycle, the model predicts higher tractions and therefore more damage accumulation, along with a lower magnitude of crack closure for $l = 10$ μm. This is most pronounced in the region

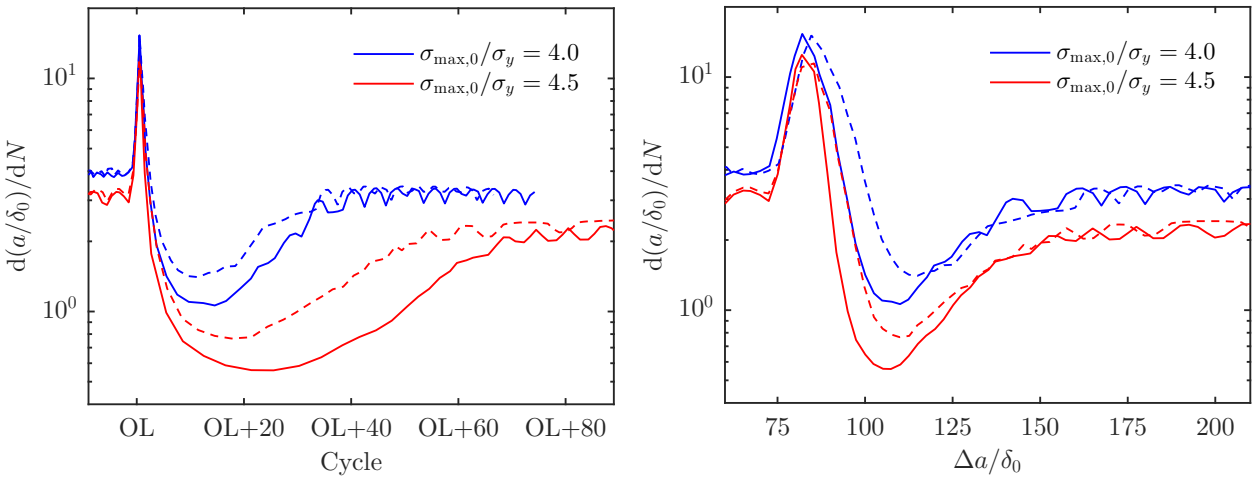

Figure 3.5. Dependence of normalized crack growth rates for $l = 0$ (solid lines) and $l = 10$ μm (dashed lines) on (a) cycles after the OL cycle and (b) normalized crack extension. The load ratio is $R = 0.1$, with $\Delta K/K_0 = 0.35$.

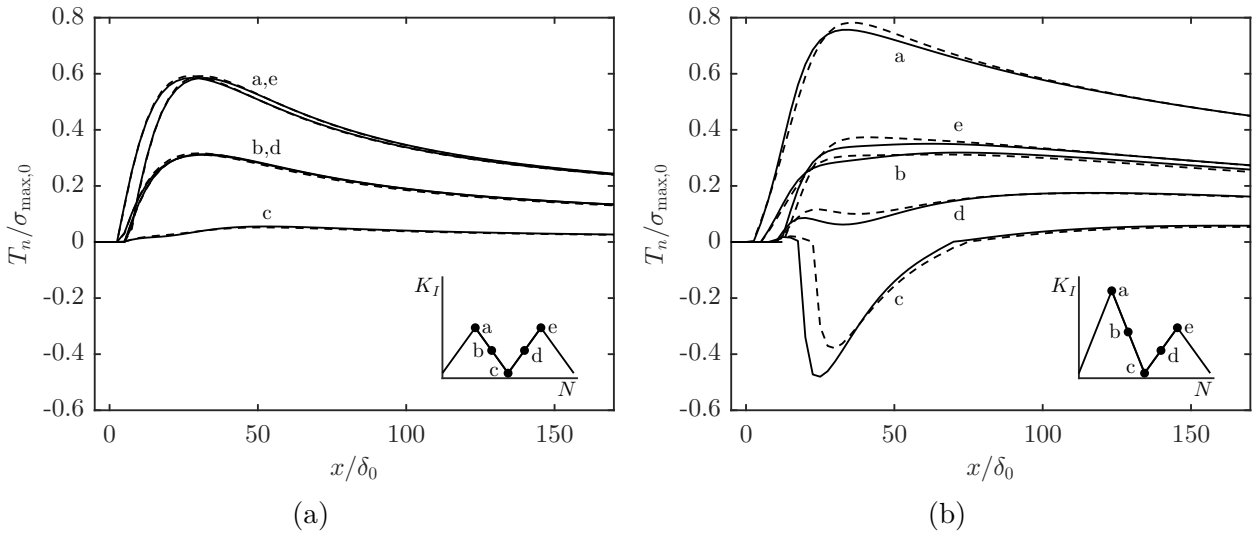

Figure 3.6. Traction distribution in the cohesive zone for $l = 0$ (solid lines) and $l = 10$ μm (dashed lines) during (a) steady-state crack growth and (b) the OL cycle. The load ratio is $R = 0.1$, with $\Delta K/K_0 = 0.35$ and $\sigma_{\max,0}/\sigma_Y = 4.0$. The insets depict the points at which the traction distribution is shown. $x = 0$ corresponds to $D = 1.0$ for point "a".

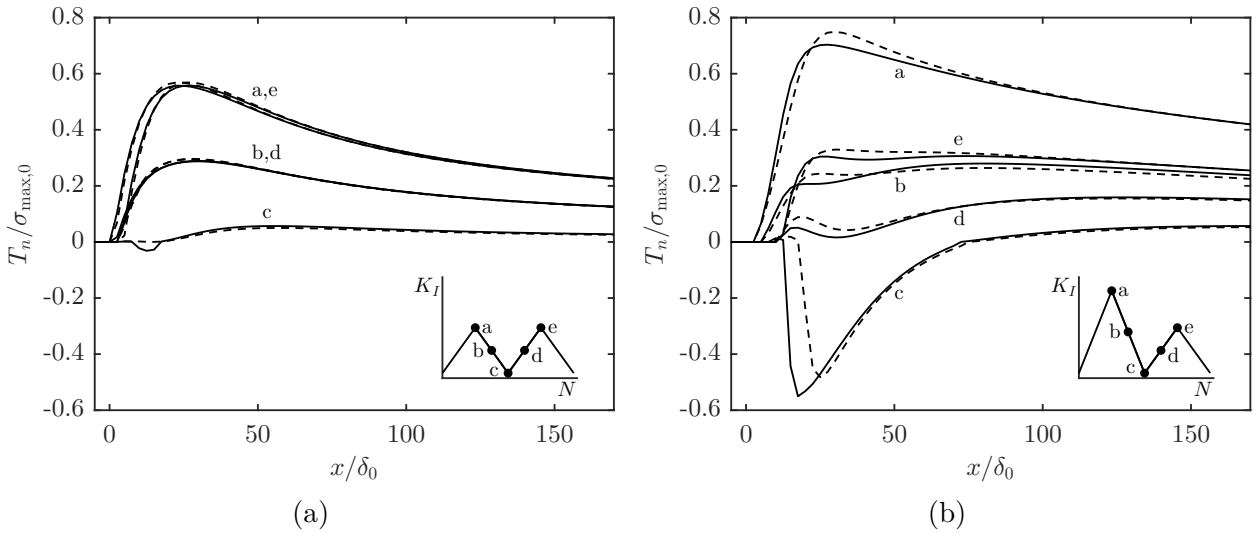

Figure 3.7. Traction distribution in the cohesive zone for $l = 0$ (solid lines) and $l = 10$ μm (dashed lines) during (a) steady-state crack growth and (b) the OL cycle. The load ratio is $R = 0.1$, with $\Delta K/K_0 = 0.35$ and $\sigma_{\max,0}/\sigma_Y = 4.5$. The insets depict the points at which the traction distribution is shown. $x = 0$ corresponds to $D = 1.0$ for point "a".

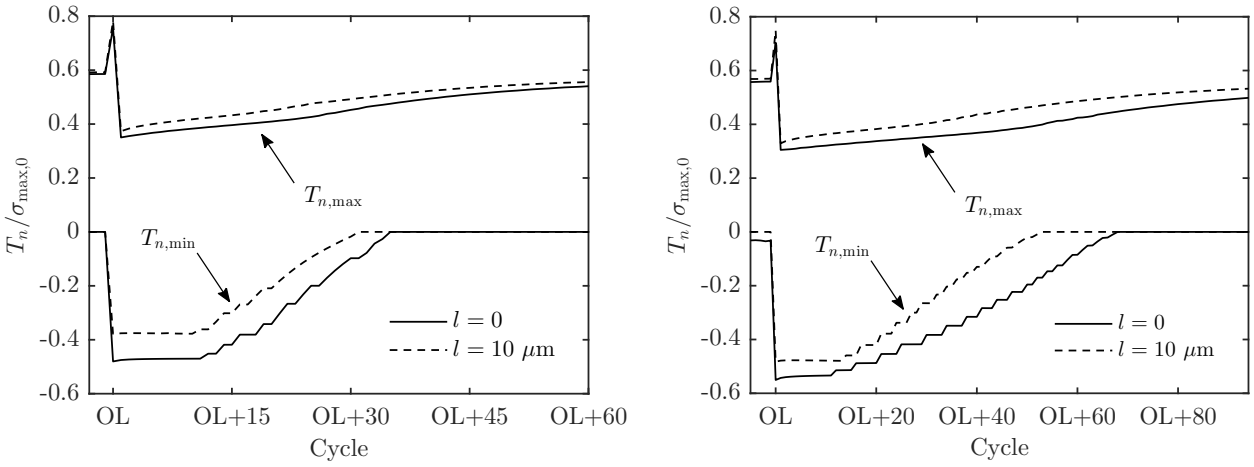

Figure 3.8. Maximum and minimum traction in the cohesive zone for each cycle relative to the OL with (a) $\sigma_{\max,0}/\sigma_Y = 4.0$ and (b) $\sigma_{\max,0}/\sigma_Y = 4.5$. The load ratio is $R = 0.1$, with $\Delta K/K_0 = 0.35$.

where compressive tractions occur at minimum load, which corresponds to the OL-affected region where crack growth rates are significantly reduced.

The evolution of cohesive zone tractions in the OL-affected region is summarized using the values of the maximum and minimum traction in the cohesive zone in each cycle, Figure 3.8. For a given cycle, this corresponds to the maximum traction at point "a" and the minimum traction at point "c" as depicted in Figures 3.6 and 3.7. The region of interest is restricted to the cohesive zone ahead of $D = 1.0$ in order to gain insight into the material separation process. The maximum traction provides a measure of K_{tip}, the effective maximum stress intensity at the crack tip, suggested by Willenborg et al. [44] as the controlling parameter for retardation following an OL. The minimum traction is a measure for the magnitude of crack closure, which is associated with K_{op}, the stress intensity factor required to open the crack [51], [131]. After the OL, for $l = 10$ μm, the model predicts higher maximum and minimum traction in each cycle. The predicted level of crack closure is therefore reduced when plastic strain gradients are accounted for, while the crack-tip stress intensity is increased. This effect persists for a larger number of cycles for the higher cohesive strength value due to the lower crack growth rates. The increased tractions are associated with a reduction in compressive

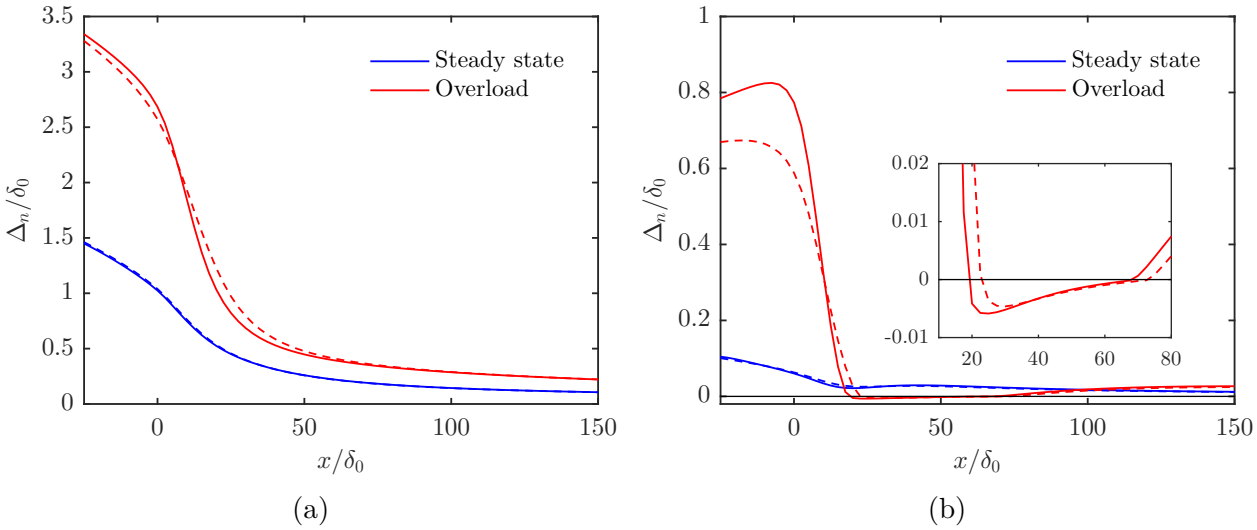

Figure 3.9. Normalized separation distribution in the cohesive zone for $l = 0$ (solid lines) and $l = 10$ μm (dashed lines) at (a) maximum applied load and (b) minimum applied load. The load ratio is $R = 0.1$, with $\Delta K/K_0 = 0.35$ and $\sigma_{\max,0}/\sigma_Y = 4.0$. The inset in (b) shows a zoom of the region where the cohesive surfaces are in contact, and $x = 0$ corresponds to $D = 1.0$.

residual stresses induced by the OL and correspond to the higher minimum crack growth rate seen for $l = 10$ μm.

Figure 3.9 shows representative separation distributions for steady-state crack growth and the OL cycle. Plastic strain gradients have virtually no effect on the separation during steady-state crack growth. At maximum load in the OL cycle for $l = 10$ μm, the model predicts elevated separation in the cohesive zone compared to $l = 0$, which leads to additional damage accumulation. At minimum load, the crack faces are in contact ahead of the location where $D = 1.0$. The length of the region where closure occurs is quite independent of the value of l, while the magnitude of closure is reduced for $l = 10$ μm. The predicted separation behind the crack tip is also lower for $l = 10$ μm at both maximum and minimum load in the OL cycle. This is consistent with previously reported computations with cracks in monotonically loaded structures where strain gradient plasticity models predict less blunting than classical plasticity models [134], [148].

Figures 3.10a and 3.10b show the spatial distribution of the accumulated plastic strain in the structured-mesh region for each value of l. The outer contour, at $\varepsilon^p = 0.001$, marks

the edge of the plastic zone. Initially, a steady-state plastic zone forms as the crack grows at a constant rate. The OL then induces an increase in the plastic zone size and maximum plastic strain magnitude, which is mostly ahead of the location where $D = 1.0$ at the start of the OL cycle. No further crack-tip plasticity is generated for 40 cycles and 36 cycles after the OL for $l = 0$ and $l = 10$ μm, respectively, as the most significant crack growth retardation occurs. At the crack extension shown in Figure 3.10, $\Delta a/\delta_0 = 245$, the steady-state plastic zone has re-formed. This occurs at 66 cycles and 59 cycles after the OL for $l = 0$ and $l = 10$ μm, respectively. While the plastic zone sizes in the steady state and at the OL for each value of l are quite similar, the maximum plastic strain magnitude in the OL plastic zone is reduced by a factor of about 1.6 for $l = 10$ μm relative to $l = 0$. This reduced plastic strain magnitude in the bulk means that more separation occurs in the cohesive zone following the OL, leading to enhanced damage accumulation. This is responsible for the higher minimum crack growth rate and the reduced number of cycles required for the steady-state plastic zone to re-develop for $l = 10$ μm.

Figure 3.10c shows the spatial distribution of plastic strain gradients for $l = 10$ μm. Similar to the plastic strain, the plastic strain gradients reach a steady-state distribution until the OL induces an instantaneous increase in the plastic strain gradient magnitude. The regions where plastic strain gradients are highest correspond to regions of restricted plastic deformation in Figure 3.10b relative to Figure 3.10a. In the OL-affected region, the maximum value of η^p is 82 mm^{-1}, while the maximum value of η^p during steady-state crack growth is 24 mm^{-1}. A more quantitative description of the role of plastic strain gradients in the hardening response is based on Eq. (2.5). If isotropic hardening is neglected (i.e. the strain hardening exponent n is set to 0), the flow stress associated with strain gradient hardening alone, $\sigma^{\text{SG}}_{\text{flow}}$, is

$$\frac{\sigma^{\text{SG}}_{\text{flow}}}{\sigma_Y} = \sqrt{1 + l\eta^p}. \tag{3.6}$$

The outer contour in Figure 3.10c corresponds to $\sigma^{\text{SG}}_{\text{flow}}/\sigma_Y = 1.05$. During steady-state crack growth, the largest value of $\sigma^{\text{SG}}_{\text{flow}}/\sigma_Y$ is about 1.11. However, in the OL-affected region, the largest value of $\sigma^{\text{SG}}_{\text{flow}}/\sigma_Y$ is about 1.35.

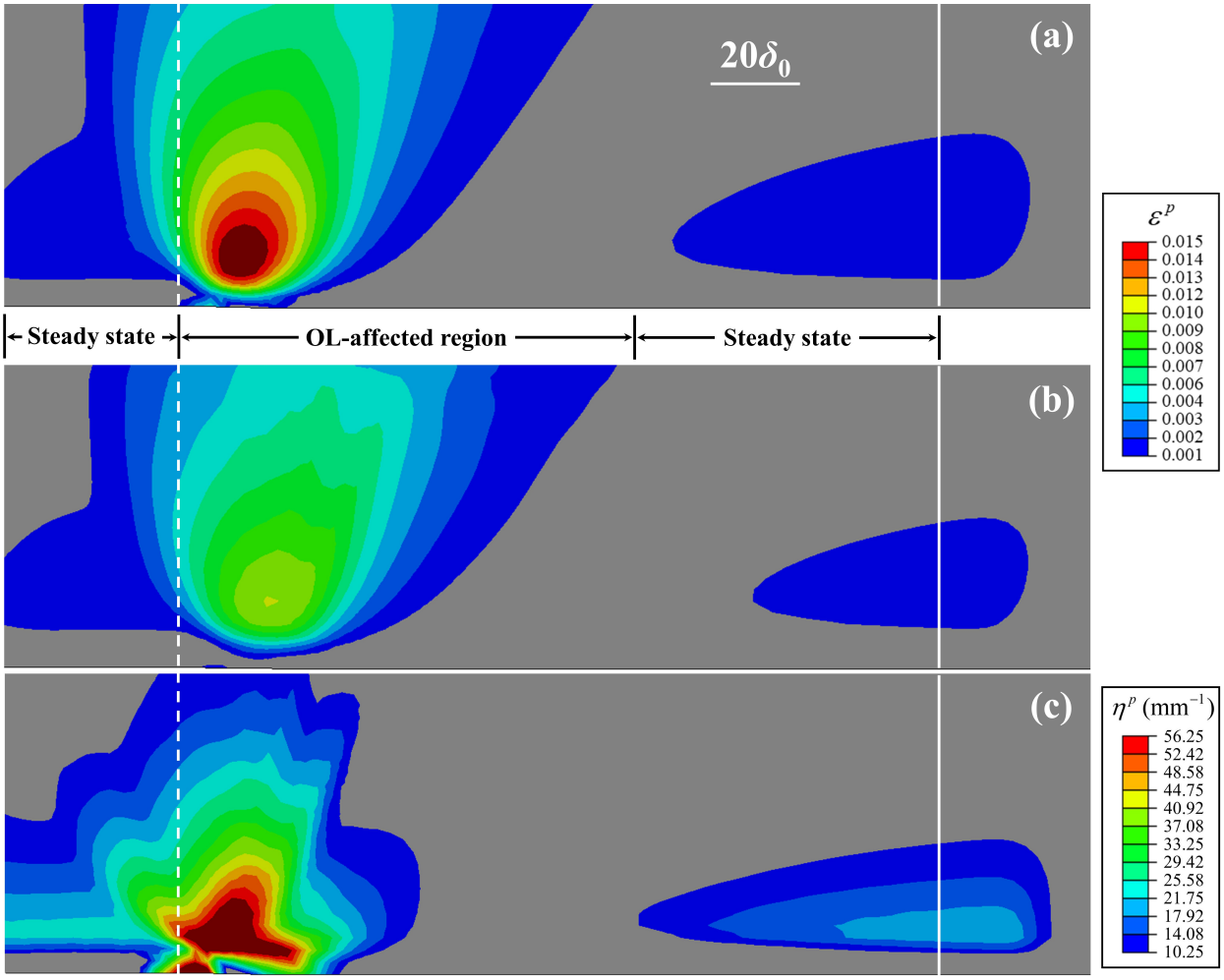

Figure 3.10. (a) Accumulated plastic strain (ε^p) contours for $l = 0$; (b) Accumulated plastic strain (ε^p) contours for $l = 10$ μm; and (c) Plastic strain gradient (η^p) contours for $l = 10$ μm. The superimposed solid lines mark the current crack extension ($\Delta a/\delta_0 = 245$) while the dashed lines mark the crack extension at the start of the OL cycle ($\Delta a/\delta_0 = 75$). The load ratio is $R = 0.1$, with $\Delta K/K_0 = 0.35$ and $\sigma_{\max,0}/\sigma_Y = 4.0$.

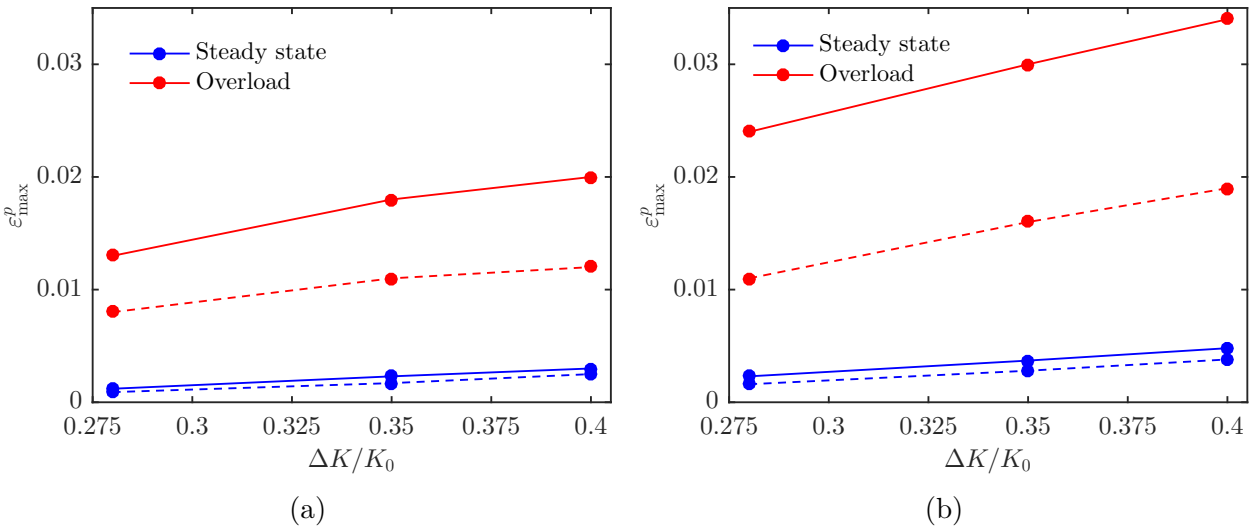

Figure 3.11. Maximum accumulated plastic strain in the steady-state and OL plastic zones for computations with (a) $\sigma_{\max,0}/\sigma_Y = 4.0$ and (b) $\sigma_{\max,0}/\sigma_Y = 4.5$. Solid lines are for $l = 0$; dashed lines are for $l = 10$ μm.

Two measures that allow for comparisons across values of l, $\sigma_{\max,0}/\sigma_Y$, and steady-state $\Delta K/K_0$ are now defined. Figure 3.11 shows the maximum plastic strain magnitude in the steady-state and OL plastic zones for each computation. For $l = 10$ μm, the model predicts significantly reduced plastic strains in the OL plastic zone for all cases, with the effect becoming more significant for the higher cohesive strength. This leads to more deformation in the cohesive zone and corresponds to the higher separation, traction, and crack growth rates seen previously for $l = 10$ μm. While the absolute magnitude of the plastic strain increases with increasing $\Delta K/K_0$, the relative effect of increasing l does not significantly change. The plastic strain in the steady-state plastic zone is also fairly insensitive to l.

Figure 3.12 shows the length of the cohesive zone that is closed at minimum load in the cycles following the OL for each computation, denoted by L_{closure}. While this quantity increases with increasing cohesive strength and stress intensity range, it shows only a small dependence on the value of l. In fact, L_{closure} differs between each value of l by a maximum of one element length. This is consistent with evidence from the crack growth rate, traction and separation distributions, and plastic zone size that the maximum extent of the OL-affected region does not depend on l.

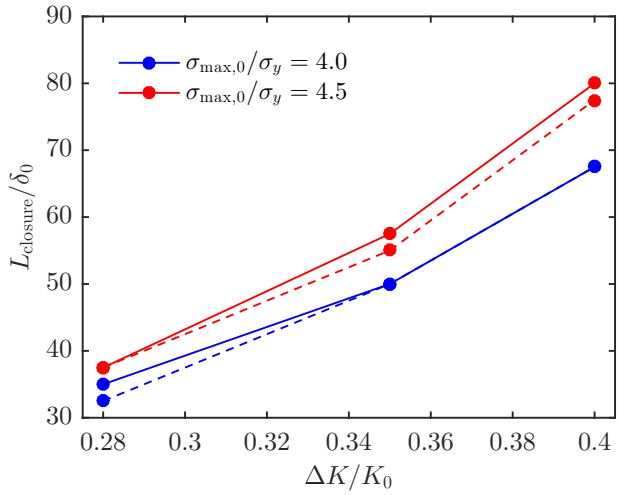

Figure 3.12. Length of the region where crack closure occurs following the OL. Solid lines are for $l = 0$; dashed lines are for $l = 10$ μm.

3.4 Discussion

The computations presented here show that hardening due to plastic strain gradients significantly affects numerical predictions of fatigue crack growth following an OL. Due to restricted plastic deformation in the OL plastic zone, there is increased dissipation in the cohesive zone. This is seen in the elevated values of traction and separation predicted for $l = 10$ μm that persist throughout the OL-affected region and lead to higher crack growth rates relative to $l = 0$. The relative increase in crack growth rates is amplified for computations with a higher cohesive strength, which is associated with more crack-tip plasticity. Changing the applied load does not significantly alter the model predictions for $l = 10$ μm relative to $l = 0$. The computations thus support the hypothesis that plastic strain gradient hardening is important in transient fatigue crack growth situations but does not significantly affect steady-state fatigue crack growth.

The irreversible cohesive zone model implemented in this study assumes that fatigue crack growth is a stress- and deformation-dependent process. The damage evolution law depends on scaled measures of both traction and separation, which is seen in discrete dislocation models of fatigue crack growth [149], other studies using cohesive zone models [118], and analytical models that include both ΔK and $K_{\max}$ in the crack growth law [150]. The $K_{\max}$ dependence is associated with ductile damage in metals, such as micro- and nano-voids ahead of the crack tip, which have produced dimpled damage zones corresponding to the region where acceleration occurs after an OL [20], [151]. The current study indicates that plastic strain gradients aid in understanding this process, as they promote the higher stresses required to activate ductile damage mechanisms during the OL cycle. This leads to elevated crack growth rates over a larger region relative to computations with $l = 0$, as observed in Figure 3.5b. This is similar to arguments for strain gradient hardening as the mechanism by which the stress ahead of cracks in monotonic loading situations can reach the high values required for cleavage cracking, even in ductile materials undergoing significant plastic deformation [38], [40], [134], [152].

A key finding is that plastic strain gradients do not alter the OL plastic zone size, but are critical in predicting the plastic strain magnitude and distribution in the OL plastic

zone. Along with the predicted tractions shown in Figure 3.8, this indicates that plastic strain gradients should be considered in predictions of K_{tip} and K_{op}. These parameters are associated with experimental observations of crack retardation [44], [51], [54] and finite element studies of crack extension [133], [153], [154]. To determine K_{op}, the time step at which the cohesive zone separation became positive (i.e. the crack opened) at all points ahead of $D = 1.0$ was recorded for each cycle after the OL. The applied stress intensity factor at this time step was then determined, which corresponds to an estimate of K_{op}. Although the precise value of K_{op} determined through this process is dependent on the time incrementation, trends with respect to the plastic strain gradient effects can still be observed. For each loading case in this study, the model predicts K_{op} for $l = 10$ μm is 20% to 30% less than for $l = 0$ in the region of maximum crack growth retardation. For example, with $\Delta K/K_0 = 0.35$ and $\sigma_{\text{max},0}/\sigma_Y = 4.5$, $K_{\text{op}}/K_{\text{max}} = 0.5$ for $l = 0$ while $K_{\text{op}}/K_{\text{max}} = 0.4$ for $l = 10$ μm at the minimum post-OL crack growth rate. This indicates that plastic strain gradient hardening has a meaningful effect on post-OL crack closure through its role in the plastic strain distribution.

As a consequence of this analysis, a useful conceptual question emerges: can the effect of plastic strain gradients following the OL be replicated by increasing the bulk yield strength relative to the cohesive strength? The predicted crack growth rates in Figure 3.13 indicate that the answer to this question is *no*—that is, the effect of plastic strain gradients is unique. Here, two additional computations were conducted with higher bulk yield strengths ($\sigma_Y =$ 260 MPa and $\sigma_Y = 270$ MPa) and no strain gradient hardening. The cohesive strength was fixed at 1125 MPa. While increasing the initial yield strength can capture either the minimum crack growth rate or the number of cycles in the OL-affected region predicted by the strain gradient plasticity model, it cannot capture both. This is because hardening due to plastic strain gradients is highly localized at the crack tip, where the most extreme gradients appear as seen in Figure 3.10c. The role of this localized hardening in predicted crack growth rates cannot be captured by simply recalibrating the parameters of the classical plasticity model or the cohesive zone.

It should be noted that the magnitude of the predicted steady-state crack growth rates in this study is on the order of 10^{-8} to 10^{-7} m/cycle, which corresponds to the lower end

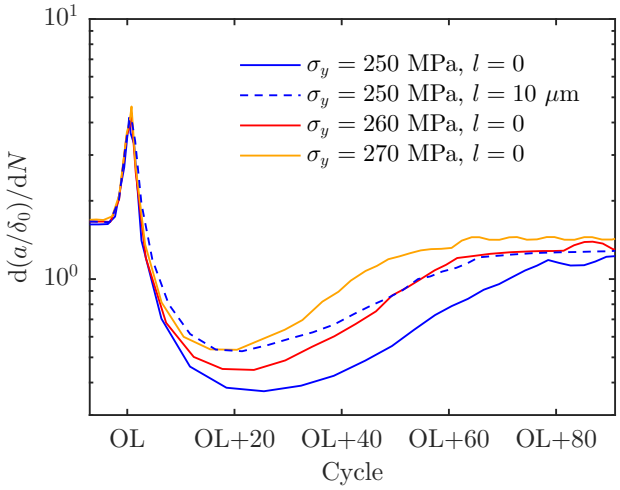

Figure 3.13. Predictions of the crack growth rate for $l = 10$ μm compared with predictions for $l = 0$ with varied initial yield strength. The load ratio is $R = 0.1$, with $\Delta K/K_0 = 0.28$.

of the Paris law regime. The applied ΔK values necessary to achieve these crack growth rates for the model material considered here are similar to those found in discrete dislocation studies but are an order of magnitude below those of typical alloys [2], [155], [156]. This is due to the choice of cohesive zone damage parameters (σ_f, $\sigma_{\max,0}$, and δ_Σ), which allow for computations of the Paris law regime and of the response to load transients with reasonable computational expense. Extensions of the current study could involve calibrating these parameters to a specific fatigue threshold and crack growth rates. Such computations would face significantly increased cost: the finite element mesh must be small enough—on the order of the size used here and in strain gradient plasticity-based studies of fracture [39], [152], [157]—to resolve plastic strain gradients and the active cohesive zone, while the crack extension and number of cycles required to achieve a stabilized plastic wake scales with the increasing plastic zone size [154]. Possible roadmaps for this type of study are discussed for cohesive zone models in [122] and in the context of discrete dislocation models of fatigue crack growth in [155].

Further extensions of this study could consider large-scale plasticity or small cracks, in which plastic strain gradients may indeed be important even in constant-amplitude loading. In addition, the isotropic hardening law used here is expected to give acceptable results for growing cracks, but the model could be extended to kinematic hardening, which would be necessary for considering crack initiation.

3.5 Conclusions

This study investigated steady-state fatigue crack growth and transient crack growth after an OL using an irreversible cohesive zone model. The computations compared predictions of crack extension and the crack-tip fields for a strain gradient plasticity model and a classical plasticity model. This made it possible to identify situations where hardening due to plastic strain gradients plays an important role in fatigue crack growth. Key conclusions include the following:

- The Paris law response for steady-state fatigue crack growth predicted by the strain gradient plasticity model is virtually the same as that predicted by the classical plasticity model.

- Hardening due to plastic strain gradients significantly restricts plastic deformation in the OL plastic zone. This is associated with less compressive residual stress and reduced crack closure compared with the classical plasticity model.

- The strain gradient plasticity model predicts a higher minimum crack growth rate following the OL and less overall retardation. However, the extent of the OL-affected region in terms of crack extension is nearly the same as in the classical plasticity model.

- Classical plasticity alone is sufficient for analyzing steady-state fatigue crack growth in the small-scale yielding problem considered here. However, the computations with strain gradient plasticity indicate that classical plasticity models underpredict transient crack growth rates following OLs.

4. FATIGUE CRACK GROWTH ACROSS INTERFACES

A version of this chapter has been previously published in *Engineering Fracture Mechanics* [158]: J.D. Pribe, T. Siegmund, J.J. Kruzic, "The roles of yield strength mismatch, interface strength, and plastic strain gradients in fatigue crack growth across interfaces," *Eng Fract Mech*, vol. 235, pp. 107072, 2020. DOI:10.1016/j.engfracmech.2020.107072.

4.1 Introduction

An important question in predicting fatigue crack growth is how cracks behave in the vicinity of heterogeneities. Introducing inhomogeneities by design holds promise for increasing the toughness of materials. An example is the use of laminates, in which sheets of the same or different materials are bonded together, and the design of metals with preferential grain orientations or morphologies [159], [160]. Increased toughness is achieved in these materials by deflecting cracks at or near the interfaces, or by sufficiently reducing the crack driving force such that it arrests at the interface. Advances in predicting crack behavior near interfaces can therefore contribute greatly to the design and analysis of fracture- and fatigue-resistant materials. However, from an analysis perspective, predicting the crack path and growth rate becomes challenging as the steady state crack-tip process zone is disturbed by elastic or plastic property mismatches near the interfaces.

In elastic materials, the main factors that govern whether a crack will penetrate or deflect into an interface are the properties of the interface itself and the degree of mismatch in the elastic properties on either side of the interface. Based on an energy release rate analysis, He and Hutchinson [161] showed that, for identical elastic materials on either side of the interface, the toughness of the matrix material must be at least four times the interface toughness to cause crack deflection at a perpendicular interface. An elastic modulus mismatch or the presence of residual stresses can significantly relax this requirement [162]–[164]. Mixed mode effects also need to be considered on the interface, where combined mode I and mode II loading are present [163].

In elastic-plastic materials, a yield strength mismatch can also affect the crack path when the plastic zone interacts with the interface and the adjacent bulk material [35], [165]. Fur-

thermore, the transient crack growth rates as the crack approaches the interface, in addition to the penetration versus deflection behavior, are of interest in fatigue crack growth. The situation in the current study involves a crack growing perpendicularly toward an interface between a plastically soft (i.e. low yield strength) material and a plastically hard (i.e. high yield strength) material. When the plastic zone approaches the interface, small-scale yielding is locally violated since the plastic zone size and the distance from the crack to the interface are on the same order of magnitude. As a result, self-similarity is no longer valid. Concepts like Paris' law therefore cannot be directly applied even when the overall specimen dimensions are sufficient to satisfy the global small-scale yielding assumption. Extensive experiments investigating this situation [8], [35], [36], [61], [166], [167] have produced the following key observations: (1) crack growth rate retardation occurs near the interface for a crack growing from a soft material to a hard material; (2) acceleration occurs near the interface for a crack growing from a hard material to a soft material; and (3) the crack can arrest and deflect into the interface if the interface is sufficiently weak.

These results can be conceptually understood based on shielding and anti-shielding mechanisms as the crack interacts with the interface. As explained by Sugimura et al. [168], stress redistribution across the interface is key. For a crack growing from a soft material to a hard material, load transfer to the hard material reduces the stress near the crack tip, thereby reducing the effective driving force (a shielding effect). For a crack growing from a hard material to a soft material, load shedding due to plastic deformation in the soft material increases the stress near the crack tip, thereby increasing the effective driving force (an anti-shielding effect). These effects may be superimposed with damage and material separation along the interface itself, which will also shield the crack [61].

Modeling efforts for fatigue cracks in plastically mismatched materials have focused extensively on quantifying the shielding or anti-shielding due to the difference in yield strength. This is typically accomplished by calculating the J integral on a contour near the crack tip that does not cross the interface. This local crack-tip driving force is then compared with the global applied J to determine the extent of shielding or anti-shielding, while each value can be converted to a stress intensity range based on standard linear elastic fracture mechanics [168]. Riemelmoser and Pippan [63] showed that the local J is proportional to the

crack-tip opening displacement and therefore describes the crack-tip plastic strains, as in homogeneous materials.

The near-tip J can also be understood as the superposition of the applied J and a "material inhomogeneity term" found by calculating J on a contour around the interface itself [63], [64]. This idea has been extended by Kolednik and co-workers based on the concept of configurational or material forces [64], [65], [169], [170]. Here, the material inhomogeneity term is interpreted as an additional driving force on the crack that can be positive or negative, thereby producing an anti-shielding or shielding effect, respectively. In the context of fatigue crack growth, the main objective of this approach is to determine the conditions under which the computed crack-tip driving force falls below the fatigue crack growth threshold. This would occur near a soft-to-hard interface, where the shielding effect due to the yield strength mismatch is strong [36], [65]. However, these models based on the J integral and its extensions have difficulty in cases where the crack may deflect into the interface, or where the interface sustains damage and provides additional shielding to the crack [65]. Furthermore, these models cannot capture the transient evolution of crack tip fields as the crack approaches the interface without also using a node release criterion to advance the crack tip [171].

To capture transient crack growth and possible deflection of the crack at an interface, a model framework is needed where deformation in the bulk material and degradation ahead of the crack tip determine fatigue crack growth as an outcome of the model. To this end, the CZM approach is used to describe material degradation for both the main crack and the interface crack. This approach allows for analysis of the competition between cracks penetrating through the interface and deflecting at the interface, as crack advance is an outcome of the boundary value problem. CZMs have successfully been used in conjunction with various constitutive constitutive laws in the bulk material, including elastic [163], [172], elastic-plastic [126], [165], and discrete dislocation [173] formulations, to investigate crack extension near material interfaces under both monotonic and cyclic loading.

This study uses a strain gradient plasticity model to describe the bulk material. In the context of cracks interacting with interfaces, significant plastic strain gradients can arise due to constraint of the plastic zone by the interface. Such constraint can have a significant effect on the fatigue crack growth behavior in these cases [174]. This effect has been investigated

in monotonic fracture by Messner et al. [37]. These authors used a gradient-enhanced crystal plasticity model to analyze crack-tip fields near grain boundaries in an Al-Li alloy. Their results showed large GND densities near a grain boundary between a compliant grain (containing the crack front) and a stiff grain. This outcome indicated that the stress enhancement from GNDs could help drive delamination along the grain boundary [37].

The current study addresses two situations involving fatigue cracks in plastically inhomogeneous materials: a crack growing toward a single perpendicular interface between plastically mismatched materials, and a crack in a multilayer material where a plastically soft interlayer is surrounded by a plastically hard matrix. There are three key research questions. (1) What regimes of behavior arise in terms of crack acceleration, retardation, and deflection as a function of interface strength and yield strength mismatch between the two materials? (2) For the interlayer configuration, how does the size of the interlayer relative to the crack-tip plastic zone and cohesive zone influence crack extension? (3) For all cases, how are the crack extension predictions enhanced by accounting for plastic strain gradients? These questions are addressed through a detailed parametric study.

4.2 Model description

The computations in this study used a symmetric, plane strain boundary layer model modified by the introduction of cohesive zone elements, similar to Chapter 3. The global and near-tip finite element meshes are shown in Figure 4.1 for the case of fatigue crack growth toward a bi-material interface. The model domains on either side of the bi-material interface were prescribed to have different yield strengths, shown schematically as "Material 1" and "Material 2" in Figure 4.1. A half model was considered, and symmetry was employed about the crack plane. As a result, an interface implicitly exists in the bottom half of the model as well. This is physically reasonable based on experimental observations of cracks bifurcating at bi-material interfaces [8]. Global small-scale yielding conditions are assumed in this approach, but, as noted previously, small-scale yielding is violated locally when the crack-tip plastic zone interacts with the interface.

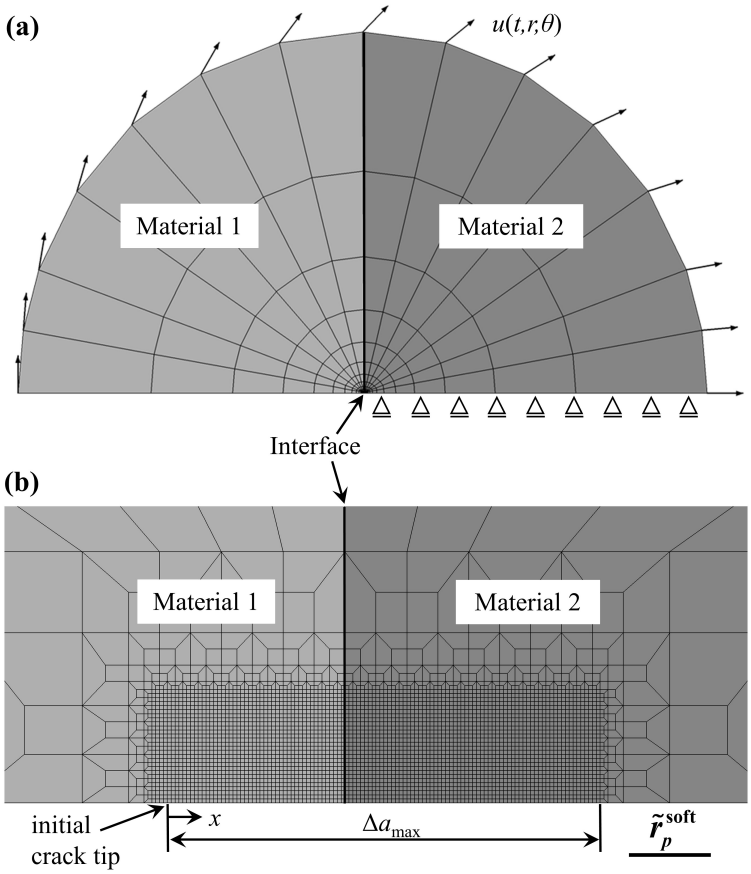

Figure 4.1. Finite element mesh for the bi-material computations. Different yield strengths were assigned for Materials 1 and 2, and cohesive zone elements were placed along the symmetry line and the interface. (a) Global mesh with displacement boundary conditions. (b) Refined mesh at the crack tip. The scale $\tilde{r}_p^{\text{soft}}$ is defined in Section 4.2.1.

The finite element model consisted of 3892 linear plane strain elements, 123 cohesive elements along the symmetry line (representing the main crack), and 44 cohesive elements along the bi-material interface. The cohesive elements on the main crack shared their top nodes with the adjacent row of solid elements. The bottom nodes coincided with the symmetry line, so their vertical displacements were fixed at zero. Symmetry also required that the horizontal displacements of the top and bottom nodes of the cohesive elements were pairwise tied to each other, preventing tangential separation on the main crack. Pure mode I conditions were therefore present on the main crack. Cohesive elements on the interface shared one row of nodes with the adjacent elements in Material 1 and one row of nodes with the adjacent elements in Material 2. Mixed mode conditions were present on the interface, so both normal and tangential separation were relevant. Modifications to the geometry in order to simulate fatigue crack growth in multilayer materials are described in Section 4.4. Crack face contact conditions were operational between newly formed crack faces. No contact conditions were present along the initial crack faces. Numerical experiments indicate that accounting for contact along the initial crack faces has negligible effect on the computational results.

The rate-independent CMSG model described in Section 2.1.1, with $m = 75.0$ in Eq. (2.11) was used to describe the bulk material. The irreversible CZM with fatigue damage given by Eq. (2.24) in Section 2.2.1 was used to describe material separation ahead of the initial crack tip and along the interface. Both the normal and tangential traction and separation were nonzero along the interface due to the mixed-mode conditions. Only the normal traction was nonzero for the main crack, which was under pure mode I conditions.

4.2.1 Model parameters

The material properties are based on the work of Wang and Siegmund [126], who considered a property set relevant to aluminum multilayer structures. As in Chapter 3, the reference stress σ_0 was taken as the initial yield strength σ_Y in each material. The bulk material properties of each material were taken as constant, with the exception of the yield strength σ_Y and the intrinsic length scale l. The elastic properties were $E = 100$ GPa and

$\nu = 0.34$, and the strain hardening exponent was $n = 0.1$. In the soft material, the yield strength was fixed at $\sigma_Y^{\text{soft}} = 250$ MPa, while the yield strength of the hard material was varied in the range $1.0 \leq \sigma_Y^{\text{hard}}/\sigma_Y^{\text{soft}} \leq 2.0$.

Setting the intrinsic length $l^{\text{soft}} = 0$ reproduces a classical plasticity model. Results for this case are compared with computations using $l^{\text{soft}} = 10$ μm, which represents a typical upper bound on values of this parameter [85]. Since the hard and soft materials have identical properties, except for the yield strength, the intrinsic length of the hard material was calculated from

$$l^{\text{hard}} = l^{\text{soft}} \left(\sigma_Y^{\text{soft}}/\sigma_Y^{\text{hard}}\right)^2. \tag{4.1}$$

In the cohesive zone, $\sigma_{\max,0}/\sigma_Y = 4.0$ for both the soft and the hard materials, with cohesive energies of $\phi_{n,0}^{\text{soft}} = 20.0$ J/m^2 and 20.0 J/m^2 $\leq \phi_{n,0}^{\text{hard}} \leq 40.0$ J/m^2 for constant characteristic separation $\delta_0 = 7.36$ nm [126]. The interface cohesive strength was varied in the range $0.7 \leq \sigma_{\max,0}^{\text{int}}/\sigma_{\max,0}^{\text{soft}} \leq 1.0$. These bounds represent a relatively weak interface, where the crack tends to deflect, and a relatively strong interface, where the crack tends to penetrate through to the second material. Similar to previous studies with irreversible CZMs, the damage evolution parameters were held constant at $\delta_\Sigma = 4.0\delta_0$ and $\sigma_f = 0.25\sigma_{\max,0}$ [126], [175].

In all cases, the load ratio was $R = 0.0$, and the applied energy release rate range was $\Delta G/\phi_0^{\text{soft}} = 0.2$. As a result, the maximum applied energy release rate in a cycle was also $G_{\max}/\phi_0 = 0.2$. Converged results were obtained with 20 load steps per half cycle.

For comparison purposes, fatigue crack growth computations were performed with a homogeneous material. In each computation, the yield strength was increased from the reference value $\sigma_Y = \sigma_Y^{\text{soft}} = 250$ MPa. The magnitude of the applied load was the same for all the computations. Figure 4.2 shows the predicted crack extension for each case. For yield strengths higher than the reference value, the model predicts that the steady-state crack growth rate decreases. This is representative of an idealized material where a relationship exists between the crack extension Δa and the cyclic crack-tip opening displacement ΔCTOD [176]. Also, plastic strain gradients do not significantly affect the predicted steady-state crack growth.

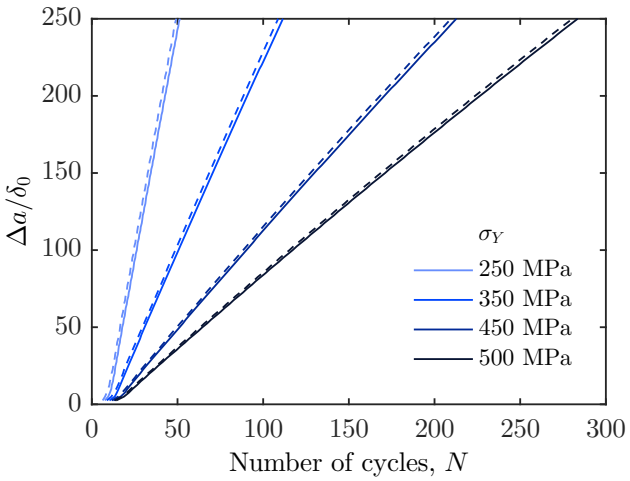

Figure 4.2. Crack extension in a homogeneous material for varied values of the yield strength with $l = 0$ (solid lines) and $l = 10$ μm (dashed lines).

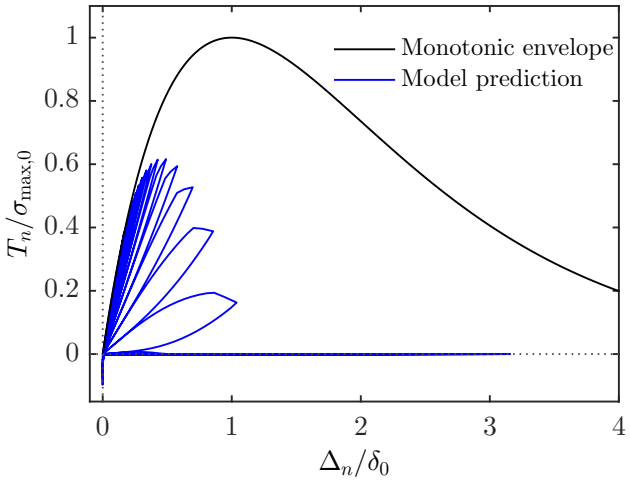

Figure 4.3. Evolution of the traction-separation response for a typical element in the cohesive zone. The monotonic cohesive envelope is shown for reference.

Figure 4.3 shows the typical evolution of the normal traction-separation response in a cohesive element during steady-state crack growth with $\sigma_Y = \sigma_Y^{\text{soft}} = 250$ MPa. The monotonic cohesive envelope, with $\Delta_t = 0$, is included for reference. The maximum traction never reaches the initial cohesive strength. As damage evolution occurs, the highest traction reached in each cycle reduces until the element loses all load-carrying capacity. Since the predicted Δ_n remains below δ_0 throughout the computation, the portion of the monotonic cohesive envelope for separations beyond δ_0 does not significantly affect the response in the fatigue damage model.

Finally, a reference plastic zone size is introduced. A classical estimate for the plastic zone size for global small-scale yielding and plane strain conditions is $r_p = EG_{\max}/\left[3\pi\left(1-\nu^2\right)\sigma_Y^2\right]$ [176]. During steady-state fatigue crack growth, the degradation of the cohesive strength limits the stresses that can be attained ahead of the crack tip in the model. This in turn limits the size of the forward plastic zone to a fraction of r_p. An initial estimate for this reduced plastic zone size is $0.5r_p$ [87]. Consequently, a modified plastic zone size estimate is introduced as

$$\tilde{r}_p = \frac{1}{6\pi}\frac{E}{(1-\nu^2)}\frac{G_{\max}}{\sigma_Y^2}. \tag{4.2}$$

Since the soft material has yield strength $\sigma_Y^{\text{soft}} = 250$ MPa for all computations, $\tilde{r}_p^{\text{soft}}$ is used as a reference plastic zone size. Since $G_{\max} = 0.2\phi_0^{\text{soft}}$ for all computations, the reference plastic zone size is $\tilde{r}_p^{\text{soft}} \approx 52.2\delta_0$. For the bi-material configuration, the distance from the initial crack tip to the interface was $110\delta_0$ or about $2.1\tilde{r}_p^{\text{soft}}$, which was sufficient for the steady-state plastic zone to develop before interacting with the interface.

4.3 Results for fatigue crack growth across and into a bi-material interface

The interface strength and the yield strength mismatch between each material are the key variables considered here for a crack growing toward a single interface. The interaction of the crack-tip fields with the interface can lead to acceleration or retardation of the crack, while the crack may also deflect into the interface. Furthermore, computations accounting for and neglecting plastic strain gradients are compared to determine their influence on the crack path and crack growth rates. Variations of the interface strength are considered first, followed by variations of the yield strength mismatch.

Several figures in this section depict the crack extension Δa. Since there may be multiple cracks in the model, a definition for this parameter is required. For the main crack, Δa is the location of the crack tip relative to the initial crack tip. For the interface crack, Δa^{int} is the location of the crack tip relative to the center line of the model.

4.3.1 Role of interface strength

The following computations consider the highest yield strength mismatch $\sigma_Y^{\text{hard}}/\sigma_Y^{\text{soft}} = 2.0$, with varied values of the interface strength $\sigma_{\max,0}^{\text{int}}/\sigma_{\max,0}^{\text{soft}}$. The case of a crack initially in the soft material and growing toward the hard material is considered first. Figure 4.4 shows two bounding cases and an intermediate case for the interface strength.

For a weak interface ($\sigma_{\max,0}^{\text{int}}/\sigma_{\max,0}^{\text{soft}} = 0.7$), the crack growth rate falls as the crack approaches the interface from the soft material, Figure 4.4a. This occurs when the cohesive zone and plastic zone begin to interact with the interface and the material on the opposing side. The crack then deflects into the interface, Figure 4.4b. In this case, accounting for

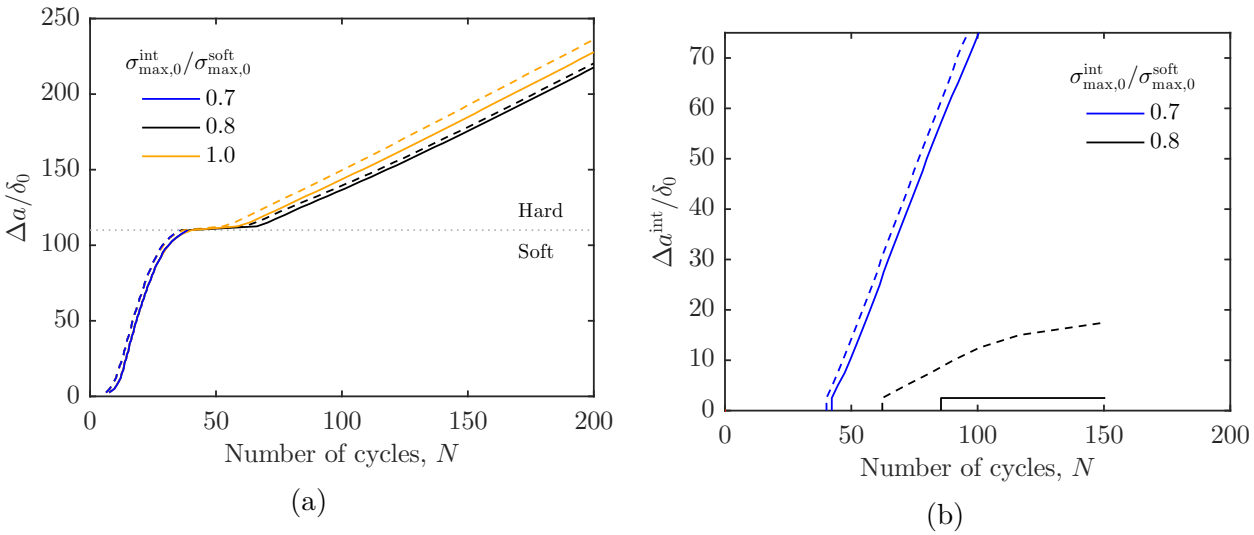

Figure 4.4. Crack extension for the soft-to-hard case with $\sigma_Y^{\text{hard}}/\sigma_Y^{\text{soft}} = 2.0$ and varied values of the interface strength $\sigma^{\text{int}}_{\text{max},0}/\sigma^{\text{soft}}_{\text{max},0}$ for $l^{\text{soft}} = 0$ (solid lines) and $l^{\text{soft}} = 10$ μm (dashed lines). (a) Main crack. (b) Interface crack. There is no interface crack growth for $\sigma^{\text{int}}_{\text{max},0}/\sigma^{\text{soft}}_{\text{max},0} = 1.0$.

plastic strain gradients (i.e. setting $l^{\text{soft}} = 10$ μm) does not significantly affect the model predictions after crack growth initiates.

For a strong interface ($\sigma^{\text{int}}_{\text{max},0}/\sigma^{\text{soft}}_{\text{max},0} = 1.0$), the crack growth rate similarly falls as the crack approaches the interface, indicating that this initial retardation is mainly controlled by the yield strength mismatch rather than the interface strength. Then, the crack penetrates into the hard material and returns to a steady-state crack growth regime. No crack extension along the interface occurs, Figure 4.4b. Here, accounting for plastic strain gradients mainly influences the number of cycles required for crack extension to begin in the hard material once the crack reaches the interface.

Finally, for the intermediate case $\sigma^{\text{int}}_{\text{max},0}/\sigma^{\text{soft}}_{\text{max},0} = 0.8$, the main crack again penetrates the interface. Compared to the strong interface, a small amount of additional shielding is provided by energy dissipation along the interface, thereby increasing the number of cycles required to penetrate into the hard material. This is more significant for $l^{\text{soft}} = 10$ μm, where the model predicts some crack branching, while the classical plasticity model predicts that only the first element along the interface fails, Figure 4.4b. The equivalent plastic strain distribution shown in Figure 4.5 provides more insight into these results. When accounting

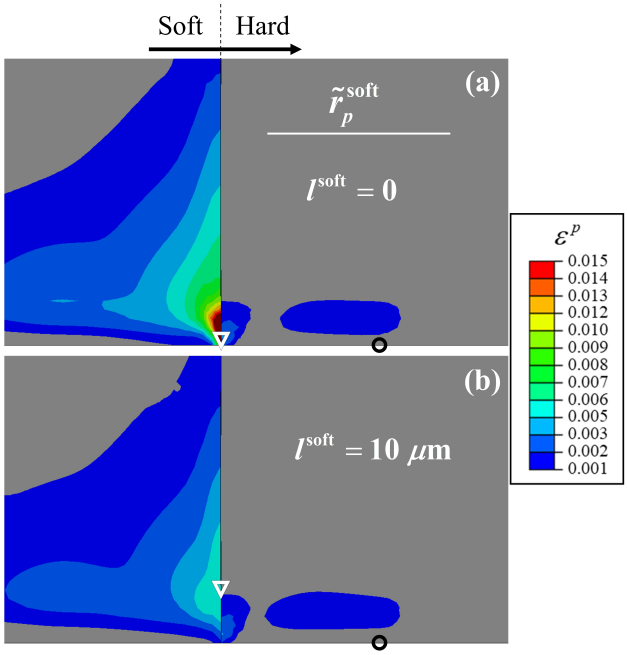

Figure 4.5. Equivalent plastic strain (ε^p) contours for the soft-to-hard case with $\sigma_Y^{hard}/\sigma_Y^{soft} = 2.0$ and $\sigma_{max,0}^{int}/\sigma_{max,0}^{soft} = 0.8$. Both plots have the same amount of main crack extension ($\Delta a/\delta_0 = 155$). (a) $l^{soft} = 0$, at $N = 125$ cycles. (b) $l^{soft} = 10\ \mu$m, at $N = 121$ cycles. Open circles mark the main crack tip, and open triangles mark the interface crack tip.

for plastic strain gradients, the model predicts restricted plastic strains near the interface. This leads to reduced shielding of the *interface crack* compared to the classical plasticity model. As a result, enough damage accumulates for the interface crack to initiate and grow before the main crack has significantly penetrated into the hard material. On the other hand, the plastic zone size does not change, and there is not sufficient plastic deformation in the hard material for plastic strain gradients to have a significant effect.

Two measures are now defined to summarize and compare results for different interface strengths. First, the maximum normalized crack extension along the interface, a_{max}^{int}/δ_0, indicates the extent of crack deflection and the role of the interface in shielding the main crack. This quantity is reported for computations where some interface crack growth occurs, but the main crack penetrates into the hard material and continues to grow. Second, Figure 4.6 defines the normalized delay cycles. This quantity, equal to $(N_1 + \Delta N)/N_1$ with N_1 and ΔN defined in Figure 4.6, compares the model predictions described in this section to a simple

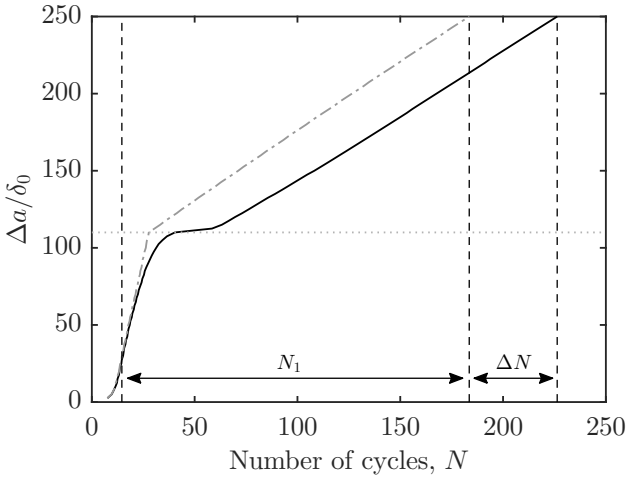

Figure 4.6. Definition of the quantities N_1 and ΔN used to calculate the normalized delay cycles.

superposition of the steady-state crack growth rates in each material. This superposition of crack growth rates ignores interactions between the crack-tip plastic zone and cohesive zone and the interface. The normalized delay cycles therefore quantifies how much crack growth life is gained or lost due to shielding or anti-shielding as the crack approaches the interface. If the normalized delay cycles exceeds 1.0, then the interface provides a net shielding effect.

Figure 4.7 shows $a^{\text{int}}_{\text{max}}/\delta_0$ and the normalized delay cycles as a function of interface strength. Above $\sigma^{\text{int}}_{\text{max},0}/\sigma^{\text{soft}}_{\text{max},0} = 0.800$, accounting for plastic strain gradients decreases the predicted normalized delay cycles. This is due to the increased separation and damage accumulation in the cohesive zone along the main crack near the interface, while no interface crack growth is triggered. Between $\sigma^{\text{int}}_{\text{max},0}/\sigma^{\text{soft}}_{\text{max},0} = 0.765$ and 0.800, there is a transition where interface crack growth occurs ($a^{\text{int}}_{\text{max}}/\delta_0 > 0$), but the main crack penetrates into the hard material and the interface crack arrests. For $l^{\text{soft}} = 10$ μm, the model predicts this transition region begins at a slightly higher interface strength, due to the reduced shielding of the interface crack. The transition also corresponds to the normalized delay cycles predictions for $l^{\text{soft}} = 10$ μm increasing over those for $l^{\text{soft}} = 0$. Here, the additional interface crack growth decreases the driving force on the main crack.

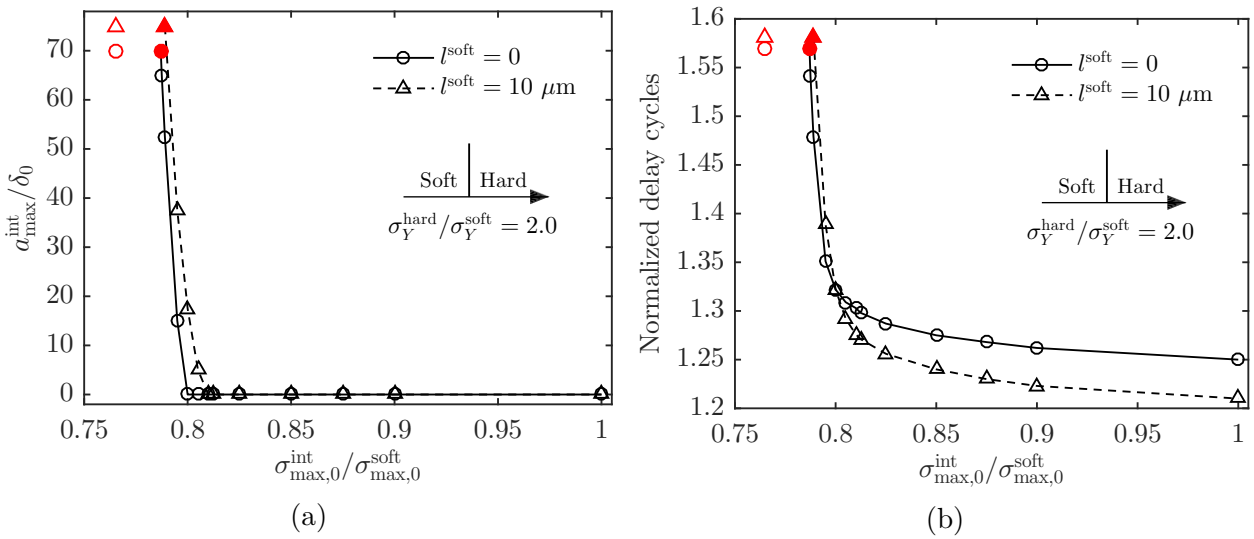

Figure 4.7. (a) Interface crack growth and (b) normalized delay cycles for crack growth from the soft to the hard material, in dependence of the interface strength. At interface strengths below the open red symbols, the main crack deflects into the interface and does not enter the hard material. Between the open and filled red symbols, the main crack and interface crack both are actively growing at the end of the computations.

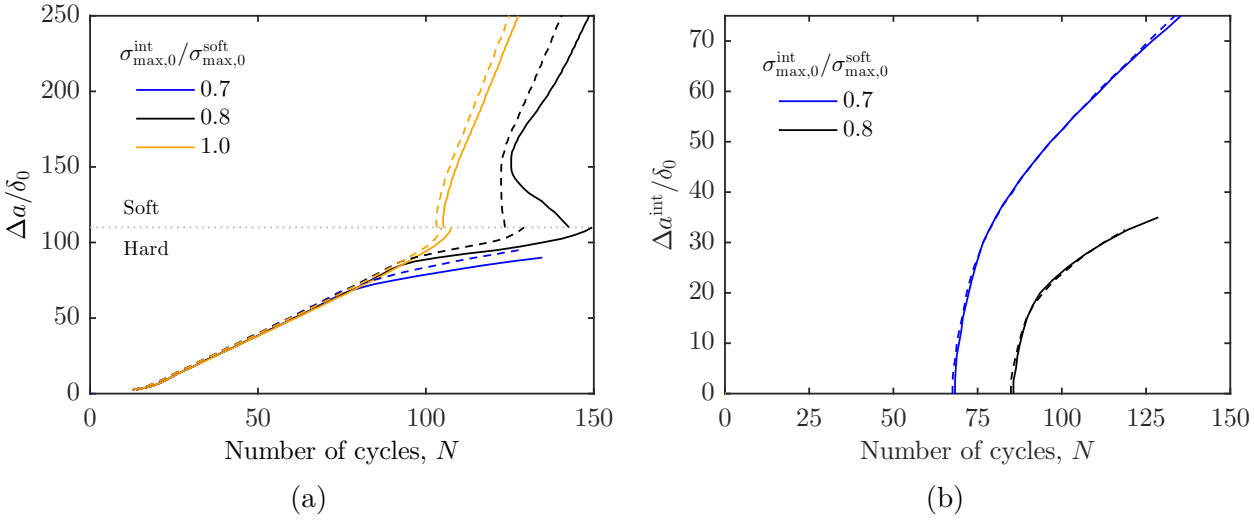

Figure 4.8. Crack extension for the hard-to-soft case with $\sigma_Y^{\text{hard}}/\sigma_Y^{\text{soft}} = 2.0$ and varied values of the interface strength $\sigma^{\text{int}}_{\text{max},0}/\sigma^{\text{soft}}_{\text{max},0}$ for $l^{\text{soft}} = 0$ (solid lines) and $l^{\text{soft}} = 10$ μm (dashed lines). (a) Main crack. (b) Interface crack. There is no interface crack growth for $\sigma^{\text{int}}_{\text{max},0}/\sigma^{\text{soft}}_{\text{max},0} = 1.0$.

Between $\sigma^{\text{int}}_{\text{max},0}/\sigma^{\text{soft}}_{\text{max},0} = 0.765$ and 0.787 for $l^{\text{soft}} = 0$ and between $\sigma^{\text{int}}_{\text{max},0}/\sigma^{\text{soft}}_{\text{max},0} = 0.765$ and 0.789 for $l^{\text{soft}} = 10$ μm, there is a regime where the crack penetrates through the interface and begins to grow in the hard material, but the interface crack reaches the end of the fine-meshed region before it is clear which crack will be dominant. This regime is bounded by the open and filled red symbols in Figure 4.7. Fully resolving this situation would require further computations using a full fracture mechanics specimen, as the mode I displacement boundary conditions on the boundary layer model become invalid for large amounts of interface crack growth. At interface strengths below $\sigma^{\text{int}}_{\text{max},0}/\sigma^{\text{soft}}_{\text{max},0} = 0.765$, there is no crack growth in the hard material. The estimated bounds between these regimes are obtained by incrementally approaching each bound with discrete computations at each interface strength.

For crack growth from the hard to soft material, Figure 4.8 shows two bounding cases and an intermediate case of interface strength. For the highest interface strength, the crack accelerates when the plastic zone and cohesive zone begin to interact with the interface and the adjacent soft material. The crack penetrates into the soft material and quickly returns to a steady-state regime. Plastic strain gradients do not play a significant role, and no interface crack growth occurs.

For the lowest interface strength, the main crack arrests and deflects along the interface. Unlike the soft-to-hard case, the interface crack begins to grow while the main crack is still some distance away. This produces a shielding effect, causing significant retardation of the main crack. The beginning of this retardation coincides with the beginning of crack extension along the interface. The model predicts less retardation for $l^{\text{soft}} = 10$ μm, while interface crack growth predictions are not affected, and the main crack still ultimately arrests.

For the intermediate strength ($\sigma^{\text{int}}_{\text{max},0}/\sigma^{\text{soft}}_{\text{max},0} = 0.8$), the main crack and the interface crack compete. Interface crack growth begins while the main crack is still in the hard material, causing retardation similar to the lowest interface strength. However, the main crack continues to grow and accelerates close to the interface, similar to the highest interface strength. At the same time, plastic deformation occurs in the soft material, and a secondary crack initiates near $\Delta a/\delta_0 = 150$. There are now two active cracks along the main crack line: the crack in the hard material, which continues to grow toward the interface; and the crack in the soft material, which simultaneously grows back toward the interface and further in the soft material. Plastic strain gradients have the strongest effect when the crack reinitiates in the soft material. This is due to the suppressed plastic deformation in the soft material compared with the classical plasticity model, which reduces shielding of the main crack.

Values of $\Delta a^{\text{int}}_{\text{max}}/\delta_0$ and the normalized delay cycles are used to summarize the data in Figure 4.9. For the highest interface strengths, the normalized delay cycles is less than 1. This indicates that the anti-shielding from the yield strength mismatch dominates over shielding from the weak interface. The transition region where the crack partially deflects but still penetrates through the interface occurs between $\sigma^{\text{int}}_{\text{max},0}/\sigma^{\text{soft}}_{\text{max},0} = 0.900$ and 0.738. This region is significantly larger than for the soft-to-hard case—some interface crack growth occurs for all but the strongest interface. Plastic strain gradients do not play a significant role in the interface crack growth, but do lead to a lower predicted normalized delay cycles when the crack penetrates to the soft material. The interface crack and main crack both actively grow between 0.738 and 0.730, while the crack fully deflects into the interface below $\sigma^{\text{int}}_{\text{max},0}/\sigma^{\text{soft}}_{\text{max},0} = 0.730$ for both $l^{\text{soft}} = 0$ and $l^{\text{soft}} = 10$ μm.

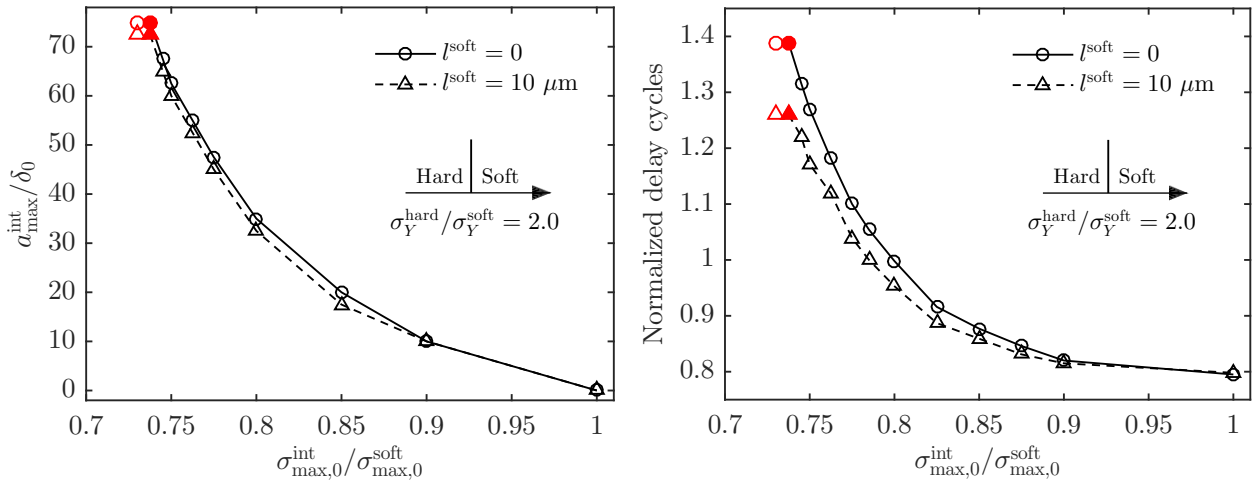

Figure 4.9. (a) Interface crack growth and (b) normalized delay cycles for crack growth from the hard to the soft material, in dependence of the interface strength. At interface strengths below the open red symbols, the crack deflects into the interface and does not enter the soft material. Between the open and filled red symbols, the main crack and interface crack both are both actively growing at the end of the computations.

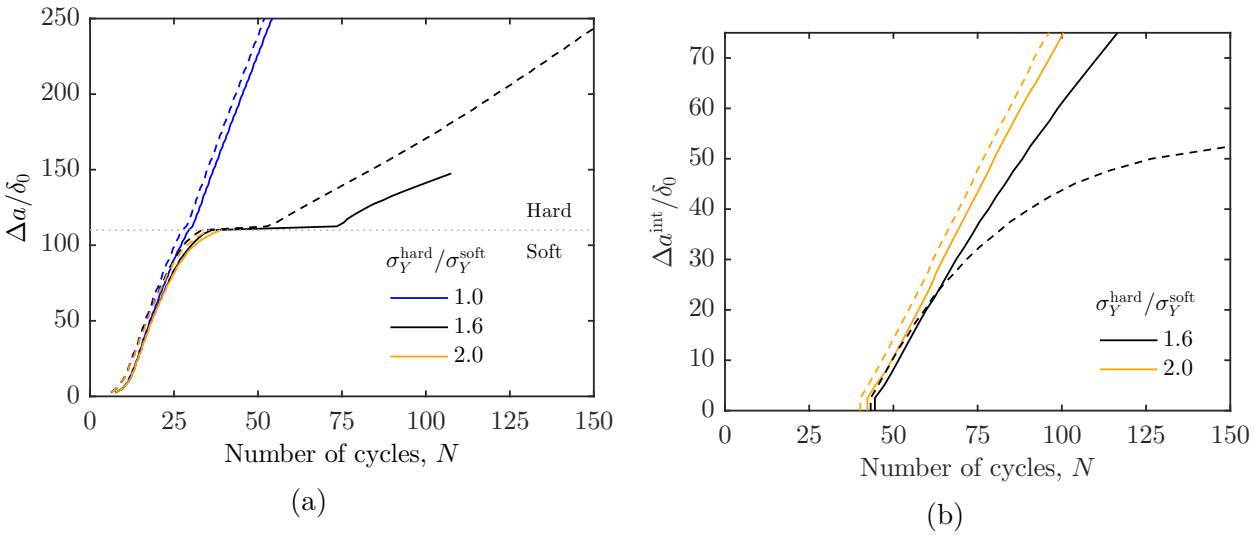

Figure 4.10. Crack extension for the soft-to-hard case with $\sigma^{\text{int}}_{\text{max},0}/\sigma^{\text{soft}}_{\text{max},0} = 0.7$ and varied values of the yield strength mismatch $\sigma_Y^{\text{hard}}/\sigma_Y^{\text{soft}}$ for $l^{\text{soft}} = 0$ (solid lines) and $l^{\text{soft}} = 10$ μm (dashed lines). (a) Main crack. (b) Interface crack. There is no interface crack growth for $\sigma_Y^{\text{hard}}/\sigma_Y^{\text{soft}} = 1.0$.

4.3.2 Role of yield strength mismatch

This section investigates whether deflection still occurs for smaller yield strength mismatches. In the following computations, $1.0 < \sigma_Y^{\text{hard}}/\sigma_Y^{\text{soft}} < 2.0$ while the interface strength was fixed at $\sigma^{\text{int}}_{\text{max},0}/\sigma^{\text{soft}}_{\text{max},0} = 0.7$. Based on the previous results, this represents a relatively weak interface and causes crack deflection at $\sigma_Y^{\text{hard}}/\sigma_Y^{\text{soft}} = 2.0$. The soft-to-hard case is analyzed first.

Figure 4.10 shows crack extension for three values of the yield strength mismatch. When the materials have equal yield strength ($\sigma_Y^{\text{hard}}/\sigma_Y^{\text{soft}} = 1.0$), there is no interface crack growth, and the weak interface has virtually no effect on the main crack. For $\sigma_Y^{\text{hard}}/\sigma_Y^{\text{soft}} = 2.0$, the crack deflects into the interface. This shows that the property mismatch plays an important role in amplifying the effects of the interface. As before, in these bounding cases, accounting for plastic strain gradients does not significantly affect the predictions.

The transition regime and the role of plastic strain gradients are demonstrated in the results for the intermediate case of $\sigma_Y^{\text{hard}}/\sigma_Y^{\text{soft}} = 1.6$. For $l^{\text{soft}} = 0$, the model predicts that the interface crack and the main crack are in competition, as both continue to grow until

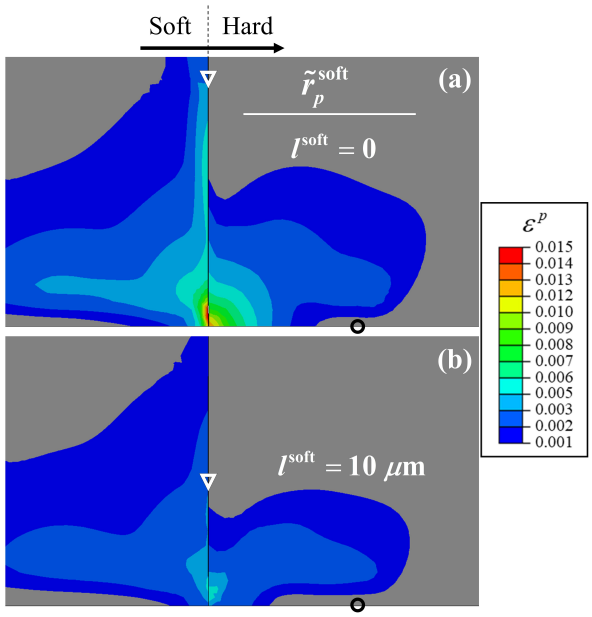

Figure 4.11. Equivalent plastic strain contours for the soft-to-hard case with $\sigma^{int}_{max,0}/\sigma^{soft}_{max,0} = 0.7$ and $\sigma^{hard}_Y/\sigma^{soft}_Y = 1.6$. Both plots have the same amount of main crack extension ($\Delta a/\delta_0 = 155$). (a) $l^{soft} = 0$, at $N = 118$ cycles. (b) $l^{soft} = 10\ \mu$m, at $N = 88$ cycles. Open circles mark the main crack tip, and open triangles mark the interface crack tip.

the interface crack reaches the maximum allowable extension. However, for $l^{soft} = 10\ \mu$m, the model predicts that the main crack dominates despite some branching into the interface. The equivalent plastic strain contours in Figure 4.11 provide further insight on this behavior. In contrast to Figure 4.5, there is sufficient plastic deformation in the hard material for plastic strain gradients to become significant. This mitigates shielding of the main crack, promoting penetration through the interface and leading to the behavior seen in Figure 4.10. The plastic zone size is somewhat smaller in the region where the main crack reinitiates in the hard material when accounting for plastic strain gradients.

The results are summarized in Figure 4.12. No interface crack growth occurs below $\sigma^{hard}_Y/\sigma^{soft}_Y = 1.40$, although the yield strength mismatch does provide some shielding, demonstrated through the higher normalized delay cycles. The transition where the main crack penetrates through the hard material despite some interface crack growth is between $\sigma^{hard}_Y/\sigma^{soft}_Y = 1.40$ and 1.58 for $l^{soft} = 0$ and between $\sigma^{hard}_Y/\sigma^{soft}_Y = 1.48$ and 1.61 for $l^{soft} = 10\ \mu$m. In contrast to the predictions for varied interface strengths, the model

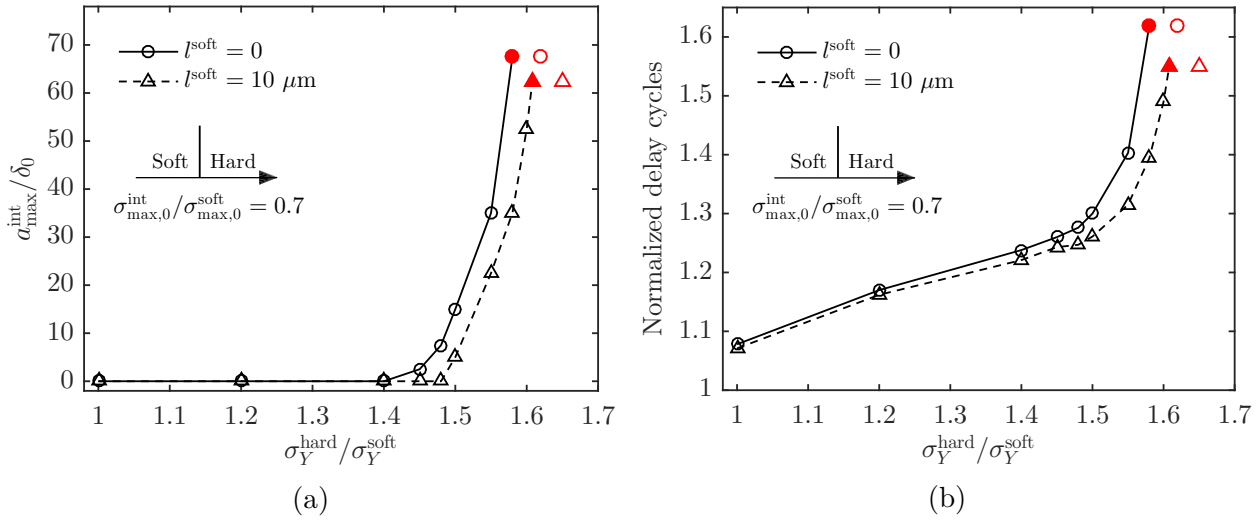

Figure 4.12. (a) Interface crack growth and (b) normalized delay cycles for crack growth from the soft to the hard material, in dependence of the yield strength mismatch. At yield strength mismatches above the red open symbols, the main crack deflects into the interface and does not enter the soft material. Between the open and filled red symbols, the main crack and interface crack both are actively growing at the end of the computations.

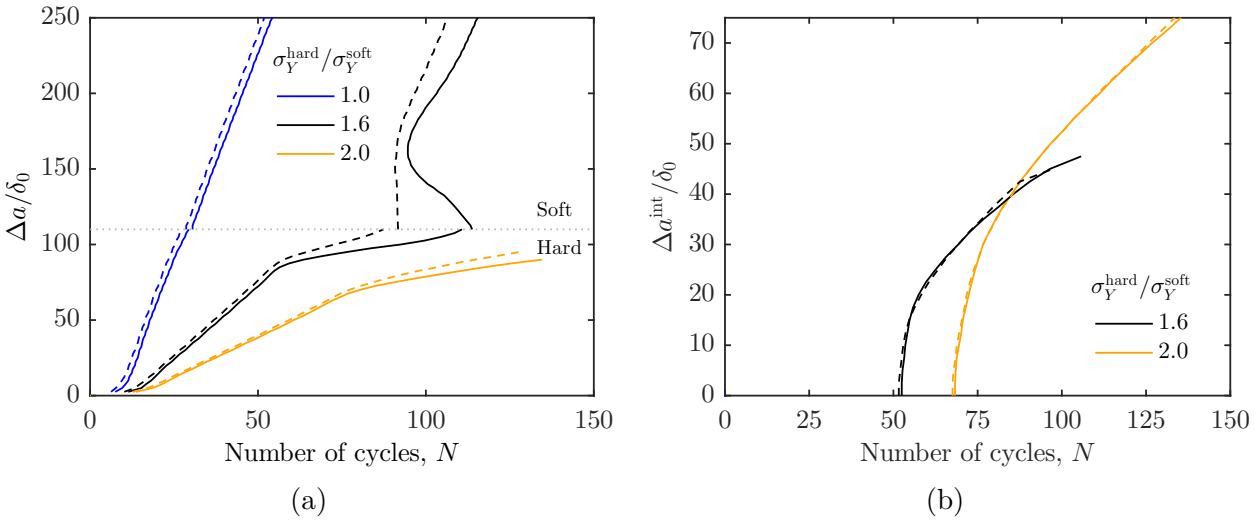

Figure 4.13. Crack extension for the hard-to-soft case with $\sigma^{\text{int}}_{\text{max},0}/\sigma^{\text{soft}}_{\text{max},0} = 0.7$ and varied values of the yield strength mismatch $\sigma_Y^{\text{hard}}/\sigma_Y^{\text{soft}}$ for $l^{\text{soft}} = 0$ (solid lines) and $l^{\text{soft}} = 10$ μm (dashed lines). (a) Main crack. (b) Interface crack. There is no interface crack growth for $\sigma_Y^{\text{hard}}/\sigma_Y^{\text{soft}} = 1.0$.

predicts less interface crack growth for $l^{\text{soft}} = 10$ μm in this transition region. This is due to the reduced shielding in the hard material discussed previously and shown in Figure 4.11. Similarly, accounting for plastic strain gradients leads to a reduced normalized delay cycles in the transition region, as indicated in Figure 4.12b. Both the interface and main cracks are actively growing at the end of the computations between $\sigma_Y^{\text{hard}}/\sigma_Y^{\text{soft}} = 1.58$ and 1.62 for $l^{\text{soft}} = 0$ and between $\sigma_Y^{\text{hard}}/\sigma_Y^{\text{soft}} = 1.61$ and 1.67 for $l^{\text{soft}} = 10$ μm.

Finally, Figure 4.13 shows crack extension for varied yield strength mismatch in the hard-to-soft case. As before, for the largest yield strength mismatches, the crack deflects into the interface, and retardation of the main crack coincides with the start of interface crack growth. For $\sigma_Y^{\text{hard}}/\sigma_Y^{\text{soft}} = 1.6$ and other intermediate cases, some interface crack growth occurs, while the main crack re-initiates remote from the interface in the soft material. Accounting for plastic strain gradients tends to accelerate this reinitiation process.

A new trend appears for the normalized delay cycles in Figure 4.14b. Increasing $\sigma_Y^{\text{hard}}/\sigma_Y^{\text{soft}}$ above 1.0 initially reduces the normalized delay cycles. Here, the anti-shielding associated with the hard-to-soft transition tends to accelerate the main crack when the active plastic zone and cohesive zone cross the interface. This effect becomes stronger as the yield

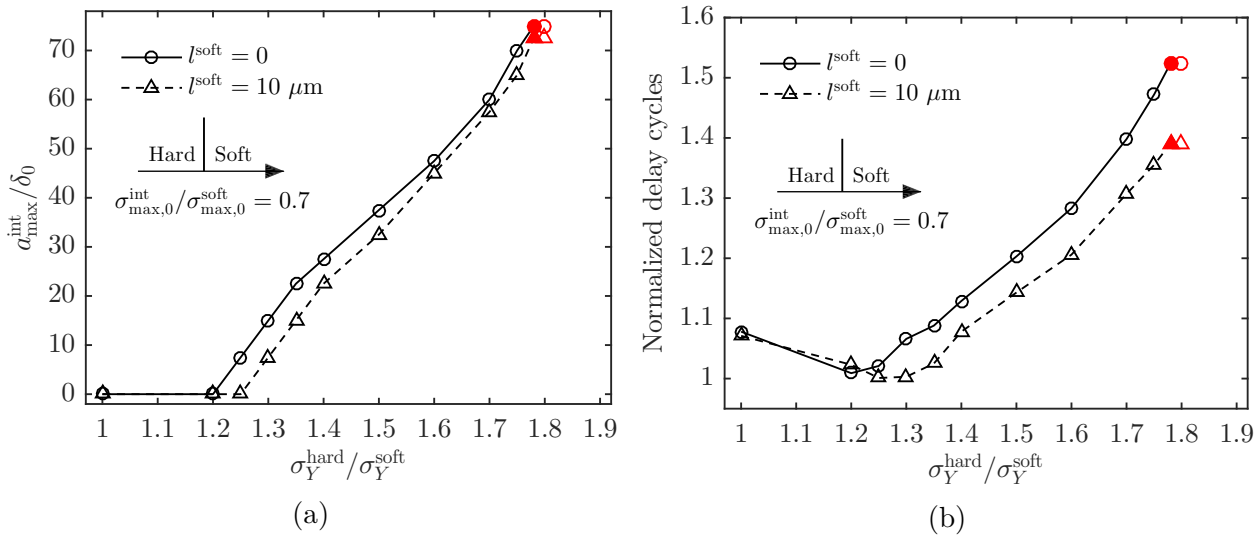

Figure 4.14. Interface crack growth and normalized delay cycles for crack growth from the hard to the soft material, in dependence of the yield strength mismatch. At yield strength mismatches above the red open symbols, the main crack deflects into the interface and does not enter the soft material. Between the open and filled red symbols, the main crack and interface crack both are actively growing at the end of the computations.

strength mismatch increases, up to $\sigma_Y^{\text{hard}}/\sigma_Y^{\text{soft}} = 1.20$ for $l^{\text{soft}} = 0$ and $\sigma_Y^{\text{hard}}/\sigma_Y^{\text{soft}} = 1.25$ for $l^{\text{soft}} = 10$ μm. Accounting for plastic strain gradients extends the region where anti-shielding dominates due to restricted plastic deformation in the soft material promoting penetration through the interface. Beyond this point, the yield strength mismatch amplifies the shielding effect of the weak interface, as discussed for the soft-to-hard case. The regime where both the interface and main cracks actively grow is small, between $\sigma_Y^{\text{hard}}/\sigma_Y^{\text{soft}} = 1.78$ and 1.80, while the crack fully deflects into the interface beyond $\sigma_Y^{\text{hard}}/\sigma_Y^{\text{soft}} = 1.80$ for both $l^{\text{soft}} = 0$ and $l^{\text{soft}} = 10$ μm.

4.4 Results for fatigue crack growth across multilayers

The model is now applied to a material system consisting of a plastically hard matrix surrounding a plastically soft interlayer. In this scenario, the crack may interact with both a hard-to-soft and a soft-to-hard interface, potentially producing a complex superposition of shielding and anti-shielding effects from each interface should the crack-tip fields span the interlayer [177], [178]. The maximum crack growth rate reduction is expected to occur near the soft-to-hard interface due to the combined shielding from the yield strength mismatch and the weak interface. However, the question remains of whether interaction effects due to the presence of two interfaces alter the crack extension predictions.

The global boundary layer geometry with mode I displacements applied to the boundary as described in Section 4.2 was again used in the computations. The near-crack-tip mesh is shown in Figure 4.15 for two interlayer thicknesses ($120\delta_0$ and $40\delta_0$) that lead to different predictions of crack growth rates and crack paths. Cohesive elements were placed along the main crack front and along both interfaces.

Here, the yield strength mismatch was fixed at $\sigma_Y^{\text{hard}}/\sigma_Y^{\text{soft}} = 2.0$, which produced the most significant effects on crack growth for the case of a bi-material interface. As in the bi-material computations, σ_Y^{soft} was fixed at 250 MPa. Therefore, $\sigma_Y^{\text{hard}} = 500$ MPa for all computations in this section. Both interfaces had the same cohesive strength, allowing the crack to penetrate through or deflect into either interface. The same load conditions ($\Delta G/\phi_0^{\text{soft}} = 0.2$ and

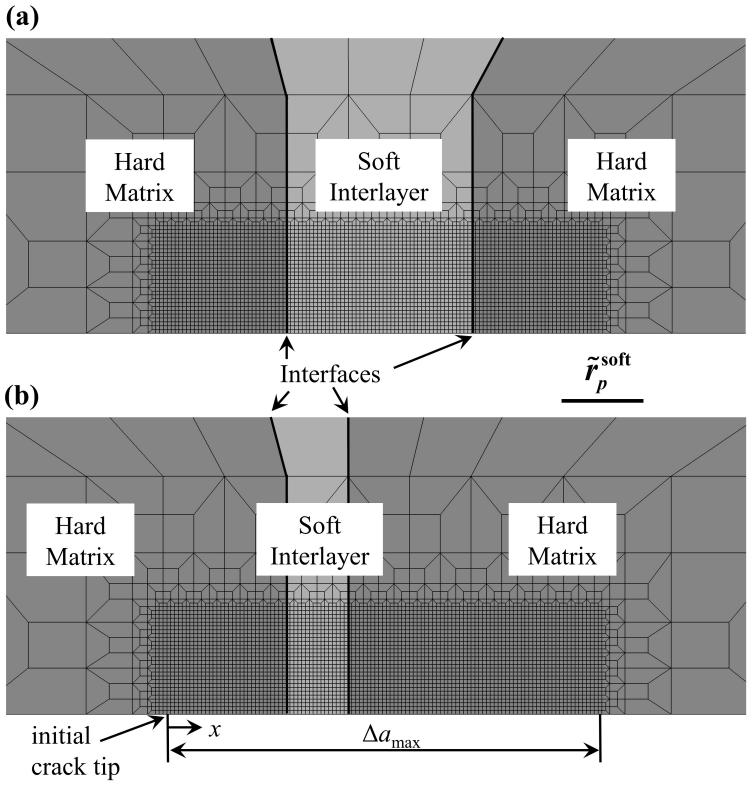

Figure 4.15. Finite element mesh for the interlayer computations. The matrix was taken as the hard material ($\sigma_Y^{\text{hard}} = 500$ MPa), and the interlayer was taken as the soft material ($\sigma_Y^{\text{soft}} = 250$ MPa). The computations considered two different interlayer thicknesses: (a) $120\delta_0$ and (b) $40\delta_0$.

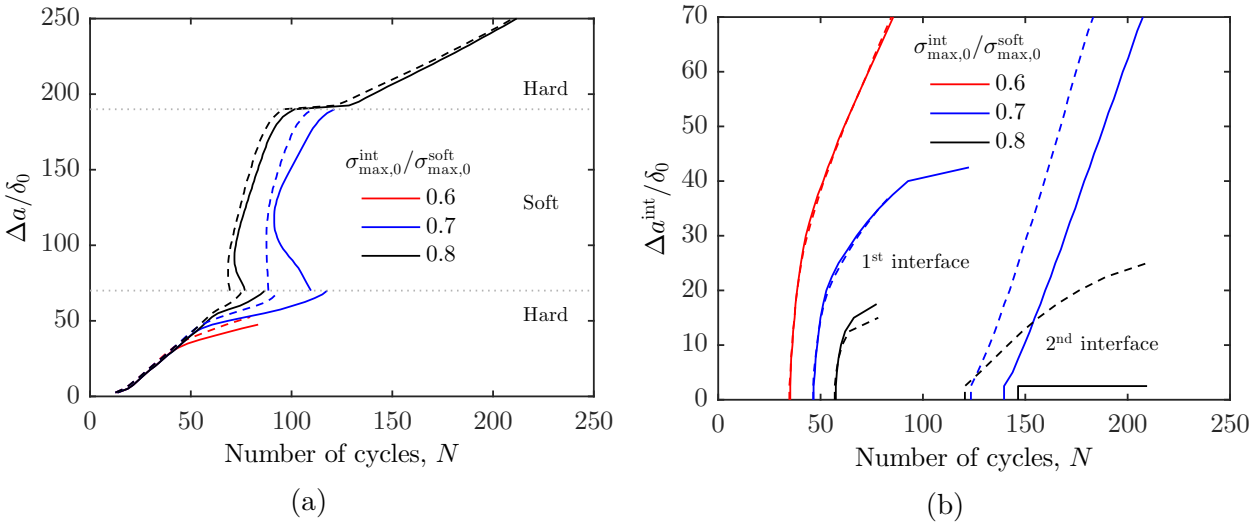

Figure 4.16. Crack extension predictions for fatigue crack growth through a soft interlayer with thickness $120\delta_0$. Solid lines are $l^{\text{soft}} = 0$; dashed lines are $l^{\text{soft}} = 10$ μm. (a) Main crack. (b) Interface cracks.

$R = 0.0$) as in the previous section were applied. The role of plastic strain gradients was again investigated through computations with $l^{\text{soft}} = 0$ and with $l^{\text{soft}} = 10$ μm.

The reference plastic zone size in the soft material is the same as the previous section, $\tilde{r_p}^{\text{soft}} \approx 52.2\delta_0$. With $\sigma_Y^{\text{hard}}/\sigma_Y^{\text{soft}} = 2.0$, the reference plastic zone size in the hard material is $\tilde{r}_p^{\text{hard}} = 0.25\tilde{r}_p^{\text{soft}} \approx 13.0\delta_0$. The distance from the initial crack tip to the first interface was $70\delta_0$, or about $5.3\tilde{r}_p^{\text{hard}}$ and $1.3\tilde{r}_p^{\text{soft}}$. This was sufficient for the steady-state plastic zone to develop in the hard material before interacting with the interface.

Figure 4.16 shows three representative crack extension predictions for the larger interlayer thickness, both accounting for and neglecting plastic strain gradients. For $\sigma^{\text{int}}_{\text{max},0}/\sigma^{\text{soft}}_{\text{max},0} = 0.8$, the response at each interface can be directly related with the bi-material computations. At the hard-to-soft interface, the yield strength mismatch causes anti-shielding, while a small amount of interface crack growth shields the crack. The crack reinitiates some distance into the soft material and continues to grow. As in the bi-material computations, hardening due to plastic strain gradients triggers some crack growth along the soft-to-hard interface, although the main crack still penetrates the interface.

For $\sigma^{\text{int}}_{\text{max},0}/\sigma^{\text{soft}}_{\text{max},0} = 0.7$, the main crack penetrates through the hard-to-soft interface, unlike the bi-material computations. This appears to be related to constraint of the active cohe-

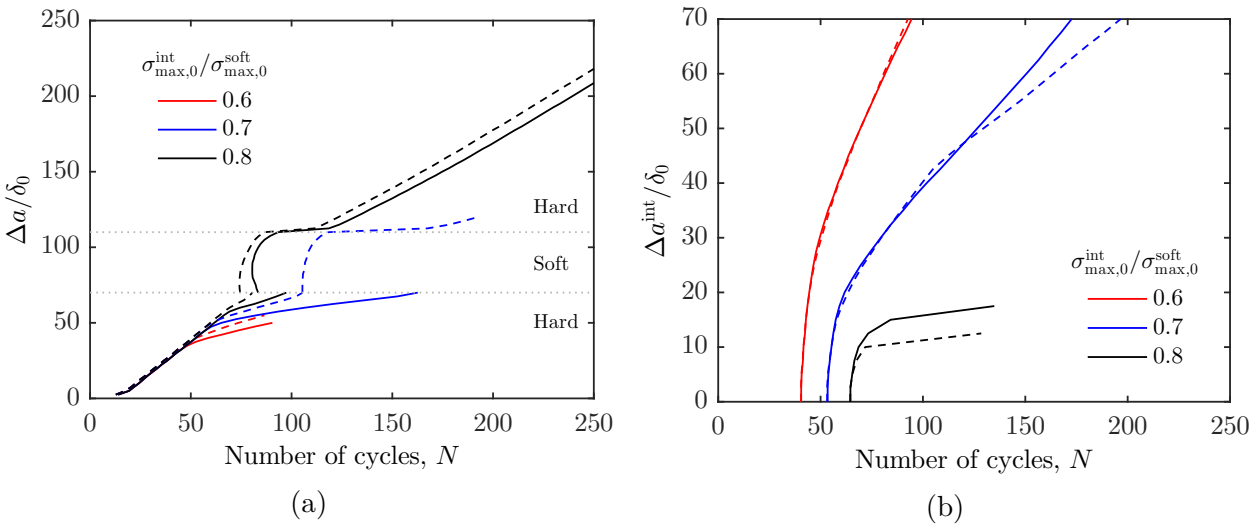

Figure 4.17. Crack extension predictions for fatigue crack growth through a soft interlayer with thickness $40\delta_0$. Solid lines are $l^{\text{soft}} = 0$; dashed lines are $l^{\text{soft}} = 10$ μm. (a) Main crack. (b) Interface crack. In all cases, the model predicts crack growth along the first interface but not the second.

sive zone in the interlayer as the secondary crack initiates. Otherwise, the response from the bi-material computations is recovered at the soft-to-hard interface, where the crack deflects. Plastic strain gradients mainly influence the model predictions as the crack re-initiates and begins growing in the soft material. At lower interface strengths (e.g. $\sigma^{\text{int}}_{\text{max},0}/\sigma^{\text{soft}}_{\text{max},0} = 0.6$), deflection occurs at the first interface, with plastic strain gradients playing a minimal role in the predictions.

Figure 4.17 shows the crack extension predictions for the smaller interlayer thickness. Shielding and anti-shielding due to the yield strength mismatch at the first and second interfaces, respectively, is again evident for $\sigma^{\text{int}}_{\text{max},0}/\sigma^{\text{soft}}_{\text{max},0} = 0.8$. For the weakest interfaces, such as $\sigma^{\text{int}}_{\text{max},0}/\sigma^{\text{soft}}_{\text{max},0} = 0.6$, the response is also comparable to the thick interlayer, as the crack deflects into the hard-to-soft interface.

For $\sigma^{\text{int}}_{\text{max},0}/\sigma^{\text{soft}}_{\text{max},0} = 0.7$, the model predicts that the main crack arrests at the first interface when plastic strain gradients are neglected. However, when accounting for plastic strain gradients, the model predicts a competition between the main crack and the first interface crack. The main crack penetrates the first interface, causing a clear retardation in the growth of the interface crack around $N = 100$ cycles. The main crack penetrates through

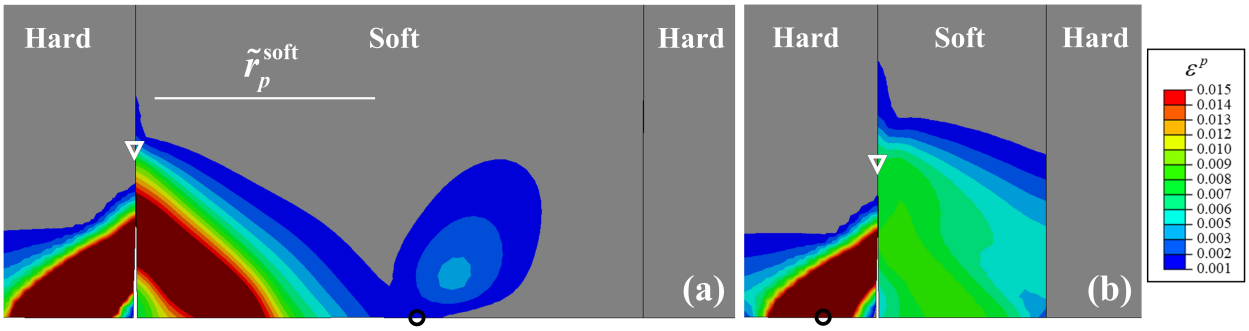

Figure 4.18. Equivalent plastic strain (ε^p) contours for fatigue crack growth through a soft interlayer with $l^{\text{soft}} = 0$ and $\sigma^{\text{int}}_{\text{max},0}/\sigma^{\text{soft}}_{\text{max},0} = 0.7$. (a) Thick interlayer, where plastic zone can fully develop after the crack penetrates the first interface, at $\Delta a/\delta_0 = 137.5$ and $N = 95$ cycles. (b) Thin interlayer, where plastic zone spreads across the interlayer while the crack is still in the hard matrix, at $\Delta a/\delta_0 = 57.5$ and $N = 101$ cycles. Open circles mark the main crack tip, and open triangles mark the first interface crack tip.

the second interface as well just before the first interface crack reaches the end of the fine-meshed region. Interestingly, there is no crack extension at the second interface—crack deflection only occurs into the first interface.

These predictions at $\sigma^{\text{int}}_{\text{max},0}/\sigma^{\text{soft}}_{\text{max},0} = 0.7$ can be associated with constraint of the plastic zone in the interlayer. Figures 4.18 and 4.19 show equivalent plastic strain contours with $l^{\text{soft}} = 0$ and $l^{\text{soft}} = 10$ μm, respectively, for each interlayer thickness. For the larger thickness, the plastic zone can fully develop after the crack has penetrated through the first interface. The soft-to-hard interface then behaves quite similarly to the case of a bi-material, with the arrest of the main crack. For the smaller thickness, the plastic zone has already spread across the entire interlayer before the crack crosses the first interface. Here, plastic strain gradients develop throughout the interlayer, reducing shielding of the main crack and causing it to penetrate through the interlayer when hardening due to plastic strain gradients is accounted for.

4.5 Discussion

The key outcomes for the bi-material computations are the maximum interface crack growth and the normalized delay cycles, in Figures 4.7, 4.9, 4.12, and 4.14. The maximum

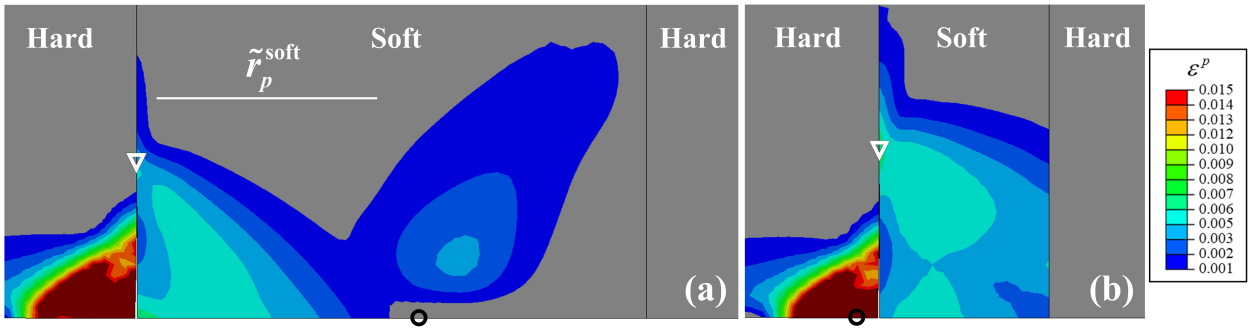

Figure 4.19. Equivalent plastic strain (ε^p) contours for fatigue crack growth through a soft interlayer with $l^{\text{soft}} = 10$ μm and $\sigma^{\text{int}}_{\text{max},0}/\sigma^{\text{soft}}_{\text{max},0} = 0.7$. (a) Thick interlayer, where plastic zone can fully develop after the crack penetrates the first interface, at $\Delta a/\delta_0 = 137.5\delta_0$ and $N = 91$ cycles. (b) Thin interlayer, where plastic zone spreads across the interlayer while the crack is still in the hard matrix, at $\Delta a/\delta_0 = 65$ and $N = 101$ cycles. Open circles mark the main crack tip, and open triangles mark the first interface crack tip.

interface crack growth essentially measures the contribution of the interface to shielding the main crack. More interface crack growth leads to a reduced driving force on the main crack as it interacts with the interface. The normalized delay cycles then represent this interface shielding combined with the shielding or antishielding due to the yield strength mismatch. The yield strength mismatch alters the crack-tip fields near the interface, regardless of the interface strength. This leads to transient evolution of the crack growth rates that cannot be captured by considering each material in isolation. Furthermore, the results indicate that the strength mismatch is key in causing crack deflection—a weak interface alone is not sufficient.

The yield strength mismatch and interface strength both can be varied to produce three regimes of behavior: penetration without any interface crack growth, deflection into the interface, and competing crack growth between the main crack and the interface. Hardening due to plastic strain gradients is key to understanding the transition between these regimes. In most cases, the classical plasticity model overestimates shielding of the main crack relative to the strain gradient plasticity model. However, there are distinct differences depending on both the properties and the direction of crack growth (i.e. hard-to-soft or soft-to-hard). Key examples are in Figure 4.7 and Figure 4.14, which show results for the soft-to-hard case in dependence of the interface strength and hard-to-soft case in dependence of the yield strength mismatch, respectively.

Figure 4.7 shows that plastic strain gradients influence the transition between bifurcation and penetration at the interface when there is a large strength mismatch. Due to the lower yield strength, there is more plastic deformation in the soft material than in the hard material, and this plastic deformation is constrained due to the interface, introducing significant plastic strain gradients. For large interface strengths, hardening due to these gradients is not as important, as the interface crack does not grow. However, when the interface is sufficiently weak, this hardening triggers interface crack growth, which inhibits growth of the main crack. This is reflected in the sudden increase in the normalized delay cycles for $l^{\text{soft}} = 10$ μm relative to $l^{\text{soft}} = 0$ around $\sigma^{\text{int}}_{\text{max},0}/\sigma^{\text{soft}}_{\text{max},0} = 0.8$. The transition regime where this occurs is quite small, however, and may be manifested experimentally as a sudden transition from penetration to bifurcation at a critical interface strength.

Meanwhile, Figure 4.14 shows the competition between interface shielding and anti-shielding due to the hard-to-soft material mismatch. When there is no yield strength mismatch, the weak interface provides a small shielding effect, leading to normalized delay cycles greater than 1.0 but without any interface crack growth. A small yield strength mismatch (e.g. $\sigma_Y^{\text{hard}}/\sigma_Y^{\text{soft}} = 1.2$) induces anti-shielding, which reduces the normalized delay cycles. Plastic strain gradients again become important in the soft material, this time in the process of reinitiation remote from the interface, as shown in Figure 4.13a. This leads to a further reduction in the normalized delay cycles and slightly inhibits interface crack growth since the main crack leaves the vicinity of the interface sooner. As the yield strength mismatch is further increased, however, interface shielding becomes dominant, and the crack bifurcates. These findings are similar to the results obtained by Parmigiani and Thouless [163] for a purely elastic bi-material with a weak interface and an elastic modulus mismatch. Using cohesive zones for both the main crack and the interface crack, they found a clear preference for penetration through the interface when both materials had the same stiffness. However, subjecting the crack to a stiff-to-compliant or compliant-to-stiff transition across the interface tended to cause deflection.

Further computations with different applied loads have been conducted. These computations predict the same regimes of behavior as for $\Delta G/\phi_0 = 0.2$. The influence of plastic strain gradients becomes less significant at lower load magnitudes and more significant at higher load magnitudes.

Applying the model to the case of a plastically soft interlayer showed that, for high interface strengths and large interlayers where the crack tip plastic zone can fully develop Figure 4.19, crack extension can essentially be predicted by separately analyzing the soft-to-hard and hard-to-soft cases studied previously. However, this is not the case for weak interfaces and small interlayers, where the plastic zone is constrained. Here, the crack interacts with both interfaces. Plastic strain gradients become important, as they develop at both interfaces and promote penetration into the soft interlayer.

For the current study, the cohesive zone parameters were set to values that allowed for the computations to be completed with reasonable computational expense. The ratio $\sigma_{\max,0}/\sigma_Y = 4.0$ for both hard and soft materials was chosen based on previous work show-

ing that this ratio introduced a relevant plastic zone size [87], [126], [179]. For lower ratios, plasticity essentially vanishes, and for higher ratios, plasticity is amplified. We have investigated this influence in the context of overloads in our previous work [129]. Meanwhile, the crack growth resistance of the interface was defined relative to the reference soft material through the ratio $\sigma^{\text{int}}_{\text{max},0}/\sigma^{\text{soft}}_{\text{max},0}$. The choice of cohesive zone parameters allowed for the detailed parametric study and identification of regimes of behavior as the crack approached the interface. Therefore, while this study could be enhanced by calibrating the parameters to provide quantitative predictions for material systems of interest, the current results provide a roadmap for interpreting results in terms of crack penetration, bifurcation, and the competition between the two.

Challenges remain to identify correct fatigue cohesive zone parameters for metallic materials. The damage-based formulation used in this study captures salient aspects of fatigue, including Paris-law type behavior for constant-amplitude loading and R-ratio dependence [86], [88], [129]. While we interpret the cohesive strength $\sigma_{\text{max},0}$ as scaling the amount of plastic deformation that accompanies crack growth in the fatigue cohesive zone model, alternate approaches are possible. For example, one could attempt to infer the values of $\sigma_{\text{max},0}$ and the other fatigue cohesive zone parameters from a particular physical mechanism of interest. This idea has been investigated using discrete dislocation computations together with a CZM based on the cleavage mechanism [149], [180]. Further, for the situations investigated in this study, the mixed-mode behavior of the interface and its failure mechanisms would also need to be considered. The current model assumed that $\tau^{\text{int}}_{\text{max},0} = \sigma^{\text{int}}_{\text{max},0}$, which helped maintain a reasonable parameter space. The relationship between these parameters would need to be investigated in more detail for applying the model to a particular material system. The appropriate definition and parameterization of mixed-mode cohesive laws is also the subject of active research (see e.g., [181]).

This study could also be enhanced by considering residual stresses in either or both constituents. Experiments have shown that a small thermal expansion mismatch can significantly affect crack growth rates, which is supported by energy-based modeling approaches [8], [162], [169]. This would be especially important for additive-manufactured materials, where significant residual stresses arise due to thermal gradients.

Extensions of this approach to small cracks or the near-threshold regime are also possible. The results here are qualitatively similar to the observed retardation of a crack approaching a grain boundary followed by reinitiation of the crack in a subsequent grain, possibly at a location remote from the grain boundary and the initial crack [62], [182], [183]. Other extensions include applying the fatigue cohesive zone formulation within the extended finite element method or other approaches that allow for arbitrary crack paths [184]–[186]. This would allow the model to capture the behavior seen in some experiments where the crack path changes in the soft material as the crack approaches the interface [8], [166], [167].

The strain gradient plasticity theory used in this study (CMSG) is a lower-order theory, which has been shown to match the results of higher-order theories outside of a thin boundary layer of the solid [85]. However, use of a higher-order theory would allow the model to capture dislocation pileups at the interface between the two materials [187]. In some situations, such as crack growth across a grain boundary between two misoriented grains, dislocation pileups may be key to understanding the crack growth response [37]. The model could also be extended to incorporate a kinematic hardening law, which would be important in studies of crack initiation. This includes further analysis of cases where the main crack reinitiates beyond the interface, as observed here in some of the hard-to-soft bi-material cases. The isotropic hardening law used here is expected to give acceptable results for growing cracks, when each material point sees a limited cyclic load due to crack advance.

4.6 Conclusions

Using an irreversible cohesive zone model and a strain gradient plasticity formulation, this numerical study addressed the competition between shielding and anti-shielding mechanisms for a fatigue crack approaching an interface between materials with different yield strengths. Applying the model to the case of a crack growing through a soft interlayer surrounded by a hard matrix showed the conditions under which interaction effects between interfaces are important. The key conclusions are as follows:

- The model predicts that a soft-to-hard transition and a hard-to-soft transition provide shielding and anti-shielding, respectively, as the crack approaches the interface.

- A weak interface always shields the crack and can cause the crack to bifurcate. This shielding is enhanced by increasing the yield strength mismatch.
- Hardening due to plastic strain gradients is important for finding the critical values of the yield strength mismatch and interface strength that cause a crack to transition from penetration to bifurcation at an interface.
- When a soft interlayer is used to toughen a material, interaction effects must be considered when the interfaces are weak and the crack-tip plastic zone spreads across the interlayer. Plastic strain gradients are important in promoting penetration through the interlayer in this configuration.
- While steady-state fatigue crack growth in elastic-plastic materials can accurately be predicted using classical plasticity models, plastic strain gradients become important for understanding crack growth transients.

5. HIGH-TEMPERATURE FATIGUE CRACK GROWTH UNDER TRANSIENT OVERLOADING: APPLICATION TO ALLOY 617

A version of this chapter is under minor revisions for publication in *International Journal of Fracture* [19]: J.D. Pribe, D.A. Addison, T. Siegmund, J.J. Kruzic, "High-temperature fatigue crack growth under transient overloading: Application to Alloy 617," *Int J Fract*, Under minor revisions.

5.1 Introduction

Structural components in power generation applications are required to maintain their strength and toughness at high temperatures. To qualify materials for these applications, their behavior under both constant and time-varying loads must be understood. This is a particular concern for the very high temperature reactor (VHTR) design, where the intermediate heat exchanger is expected to sustain significantly higher temperatures than in current reactors [9], [11]. The need for load-following capabilities introduces fatigue concerns due to cyclic loading and the possibility of load transients, such as overloads and waveforms with hold times at multiple load levels [13]. Therefore, understanding the behavior of VHTR candidate materials under high-temperature transient loads is important for predicting their service lifetime.

Numerous experimental studies have assessed crack growth under constant loads and constant-amplitude cyclic loading in structural metals at high temperatures. These studies have generally focused on correlating crack growth rates with a loading parameter, such as K_I, C^*, or C_t (typically ΔK or $(C_t)_{\text{avg}}$ for fatigue), and establishing conditions under which each parameter is valid [16], [79], [188]–[190]. Analytical and numerical models initially connected these parameters to the crack-tip fields associated with both stationary [69], [72], [74], [191], [192] and growing cracks [193]–[195].

Models were subsequently developed to predict crack extension based on the influence of fatigue, creep, the environment, and their interactions. Several phenomenological models

posit damage accumulation laws for cycle-dependent fatigue damage and time-dependent creep damage based on concepts from damage mechanics [120], [196], [197]. Interactions are modeled through linear or nonlinear summation of each damage source [198]. These approaches have been incorporated into finite element computations through three main approaches: cohesive zone models [88], [89], coupled elastic-viscoplastic-damage laws for the continuum stress-strain behavior [196], [199], [200], or crack growth criteria based on a critical condition being attained ahead of the crack tip [201], [202]. Mechanistic models, based on the relevant crack extension mechanism(s) in particular alloys, have also been incorporated into finite element models. Examples include grain boundary cavitation [203], [204] and oxidation [124], [205], [206].

Numerical models have also been applied to investigate issues specific to cyclic loading, particularly crack closure. For example, using finite element computations, Sehitoglu and Sun [84] found that the crack opening stress during cyclic loading depends strongly on hold time and the creep constitutive parameters. Longer hold times and higher rate sensitivity produced lower crack opening loads, indicating a reduction in crack closure. Potirniche [82] recently found similar results using a strip-yield model. In particular, creep deformation induced by longer hold times during cyclic loading was found to reduce plasticity-induced crack closure. This led to increased crack growth rates during the cyclic part of the load waveform.

Crack growth due to waveforms containing load transients has been investigated in detail at temperatures where rate dependence is negligible. Rate-independent ductile metals almost uniformly demonstrate crack growth retardation following overloads (OLs), the most common type of load transient. Retardation is associated with crack growth through the OL plastic zone, which shields the crack and reduces the effective crack-tip stress intensity factor range [7]. However, debate continues over the relative importance of mechanisms like crack closure behind the crack tip and compressive residual stresses ahead of the crack tip [51], [144], [207].

A review of experiments on high-temperature transient OLs shows a range of response characteristics depending on the material and the applied loads. For example, several experiments have focused on OLs in Alloy 718 and its variants, a family of precipitation-hardened

nickel-base superalloys typically used in applications up to 650°C. These experiments have generally shown post-OL retardation for cyclic loading similar to the low-temperature, rate-independent case. [25], [34], [47]. Overloads applied prior to hold times have been shown to attenuate and in some cases completely eliminate the detrimental effect of the hold time on crack extension [27], [30], [33]. Overloads during cyclic loading also caused crack growth retardation in the similar precipitation-hardened alloy IN100 [208], [209]. On the other hand, in a recent study of crack growth at two different temperatures in IN100 under cyclic loading, Adair et al. [210] found that the presence or absence of retardation depends on the OL ratio. High OL ratios (2.0× and 1.6×) always caused crack growth retardation. However, a lower OL ratio (1.3×) caused acceleration for tests at 649°C and retardation for tests at 316°C. The authors argued that increased oxidation embrittlement at 649°C caused the crack to quickly grow through the smaller plastic zone from the 1.3× OL without a significant retardation effect. Yoon et al. [81] performed high-temperature creep-fatigue crack growth tests on 1.25Cr-0.5Mo steel with waveforms containing a hold time at maximum load. These authors investigated the effect of applying an OL prior to each hold time. The results showed that time-dependent crack growth rates were higher in the experiments with OLs compared to experiments without OLs. Based on microscopic observations, this was attributed to microcavity nucleation triggered by higher crack-tip stresses during the OL.

In general, these results indicate that more study is needed to predict how crack growth rates are affected by load transients at high temperatures. Furthermore, nearly all studies of OLs in nickel-base superalloys have considered precipitation-hardened alloys used in turbine engines. The candidate materials for the intermediate heat exchanger in the VHTR design, including Alloy 617, are solid solution strengthened at temperatures of interest [9], [211]. Knowledge about the response of these materials to load transients is therefore particularly limited. The current study addresses this gap by analyzing fatigue crack growth following OLs in such materials by applying numerical modeling to experiments on Alloy 617.

The OL experiments on Alloy 617 that inspired this work showed several key characteristics that contrast with its characterization as a creep-ductile material [18], [19]. First, when a single OL with an OL ratio of 1.25 was applied, the crack growth rate was indistinguishable from the baseline Paris Law growth rate within the noise of electrical potential difference

measurements. Second, experiments with blocks of 20 OLs included three main observations: (1) a small amount of overall crack growth retardation occurs at low applied loads; (2) this transitions towards an acceleration-dominated response at higher loads; and (3) the retardation is more pronounced for experiments with a higher OL ratio. The experimentally measured crack extension is illustrated in Figure 5.1 and Figure 5.2 for OL ratios of 1.25 and 1.5, respectively. To help assess the post-OL acceleration and retardation, constant-amplitude crack growth predictions are also included. These were found by integrating the Paris Law relationship from [15] for the constant-amplitude data over the range of crack extension shown in each figure. The figures show crack extension from 25 μm before the OL block to 175 μm after the OL block. The range of cycles begins 200 cycles before the OL block.

The model approach used in this study to investigate OLs in Alloy 617 and similar materials consists of separate constitutive laws describing viscoplastic deformation and material degradation ahead of the crack tip. Crack extension was thereby an outcome of the model, which allows for analysis of transient crack growth rates during and after the OLs [119], [129]. A power law viscoplasticity model was used for deformation in the bulk material, while a cohesive zone model (CZM) was used to describe subcritical material degradation. A phenomenological damage evolution equation coupled with the CZM captured damage due to fatigue. The model approach was based on characteristics observed in experiments on Alloy 617 at 800°: it exhibits power law creep behavior at this temperature [12], and crack extension under cyclic loading is fully transgranular and shows fatigue striations on the fracture surface [15]. The overall approach is similar to that of Bouvard et al. [88], who studied high-temperature creep-fatigue crack growth in a single-crystal nickel-base superalloy.

The computations in this study are used to address three research questions:

- What is the influence of the material rate sensitivity (or creep exponent) on post-OL fatigue crack growth rates, for both a single OL and a block of multiple OLs?
- How do the CZM parameters governing damage evolution affect the crack growth trends with respect to the material rate sensitivity?

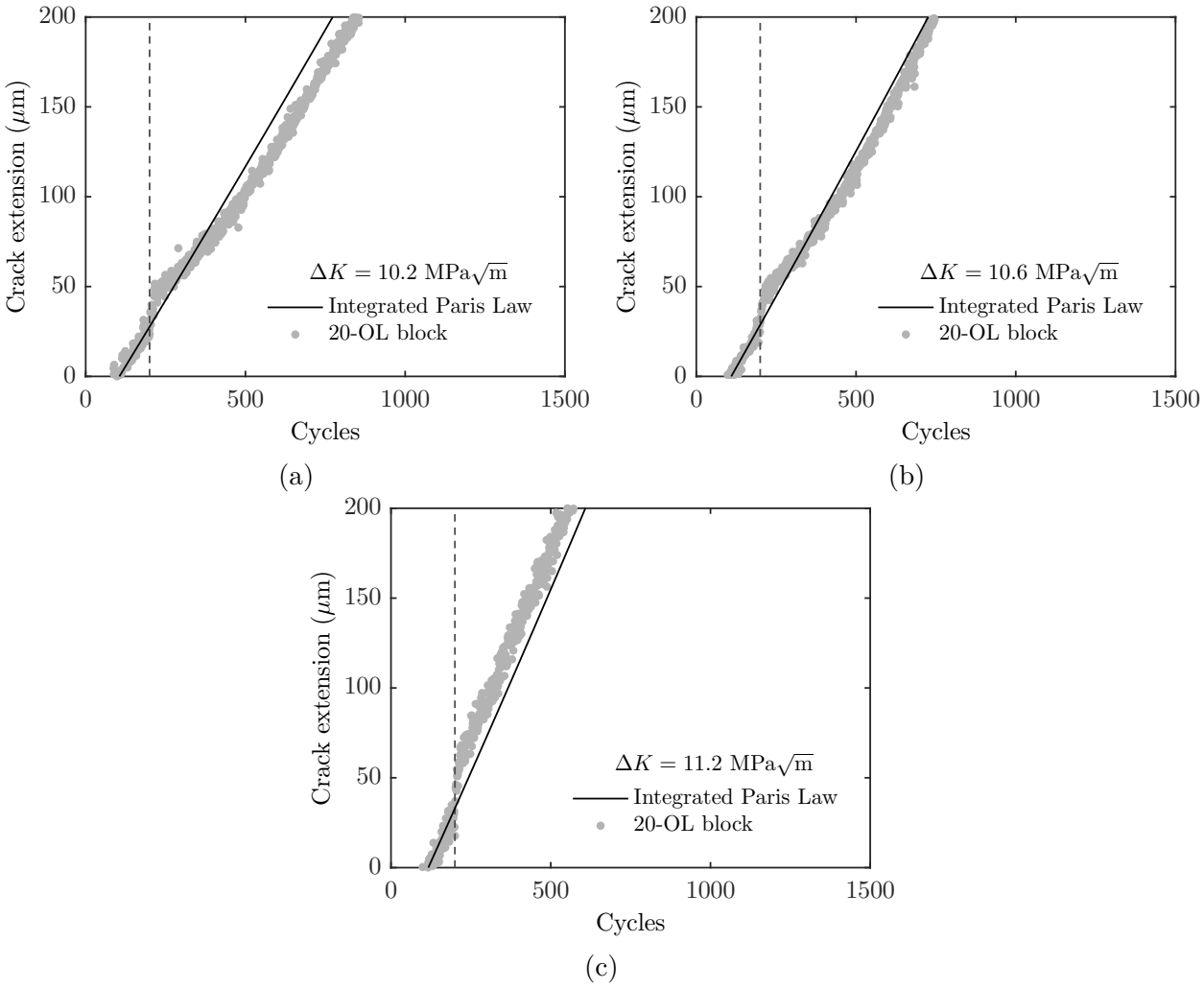

Figure 5.1. Crack extension from experiments with blocks of 20 OLs at OL ratio 1.25. The dashed line indicates the cycle where the OL block begins. The predicted crack extension based on the constant-amplitude loading experiments is included for comparison. Results are shown for three different baseline stress intensity factors prior to the OLs: (a) $\Delta K = 10.2$ MPa$\sqrt{\text{m}}$ (b) $\Delta K = 10.6$ MPa$\sqrt{\text{m}}$ (c) $\Delta K = 11.2$ MPa$\sqrt{\text{m}}$.

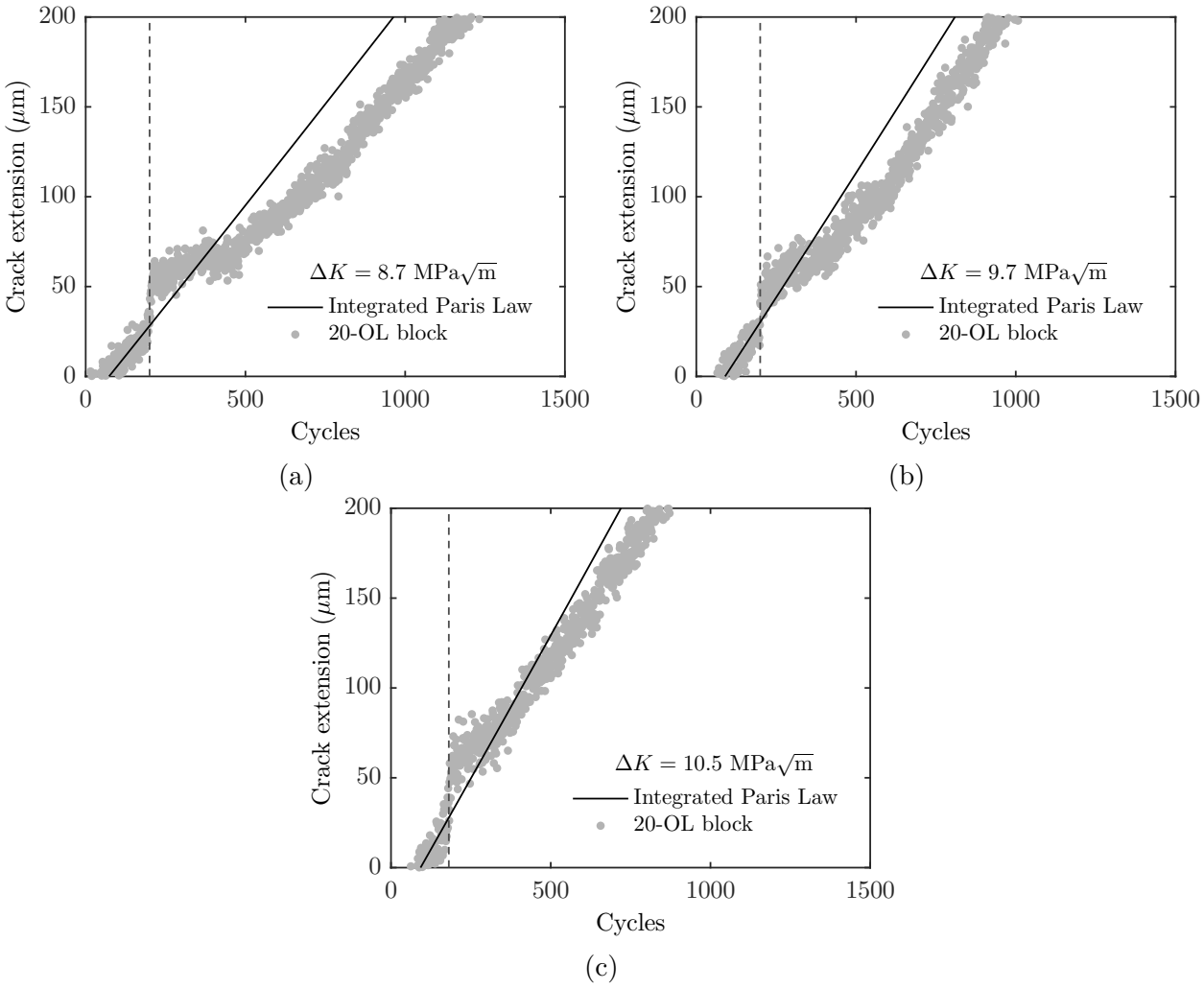

Figure 5.2. Crack extension from experiments with blocks of 20 OLs at overload ratio 1.5. The dashed line indicates the cycle where the OL block begins. The predicted crack extension based on the constant-amplitude loading experiments is included for comparison. Results are shown for three different baseline stress intensity factors prior to the OLs: (a) $\Delta K = 8.7$ MPa$\sqrt{\text{m}}$ (b) $\Delta K = 9.7$ MPa$\sqrt{\text{m}}$ (c) $\Delta K = 10.5$ MPa$\sqrt{\text{m}}$.

- How can the experimental results for Alloy 617 be understood in light of the model predictions?

To answer the first two questions, a parametric study was conducted using a finite element model of a creep-fatigue crack growth specimen. The predicted crack growth response and crack-tip fields are analyzed in detail for a typical range of material parameters for solid solution strengthened alloys. The model was then calibrated to the measured crack growth rates from constant-amplitude cyclic loading experiments on Alloy 617 at 800°C from [15] and applied to the experiments with OLs from [18]. The third research question was subsequently addressed through comparisons of the numerical and experimental results and interpretation of the results based on observations from the parametric study.

5.2 Model description

The computations used a compact tension (C(T)) specimen geometry, shown in Figure 5.3. This approach was used due to the possibility of widespread viscoplastic deformation ahead of the crack tip for materials with high rate sensitivity. Widespread viscoplastic deformation can preclude the use of simplified, boundary layer-type models. Symmetry was employed about the crack plane, allowing a half model to be used. A custom mesh generation tool written in Python was used to create the mesh for the C(T) specimen. The mesh generation tool first created the highly-structured mesh near the crack tip, with gradual coarsening of the mesh away from the crack tip. The tool then connected this crack-tip mesh with the mesh surrounding the hole in the C(T) specimen, which was created in Abaqus/CAE [102]. The refined crack-tip mesh was moved to the desired crack length, and the remainder of the C(T) specimen was uniformly filled in with elements out to the desired dimensions.

The finite element model consisted of 13759 linear plane strain elements in the bulk material and 224 cohesive elements along the crack line ahead of the initial crack tip. The cohesive elements shared their top nodes with the adjacent solid elements. The bottom nodes were along the symmetry line, so their vertical displacements were fixed at zero. Due to symmetry, the horizontal displacements of the top and bottom nodes were tied pairwise, such that pure mode I conditions were present. The refined mesh in the vicinity of the

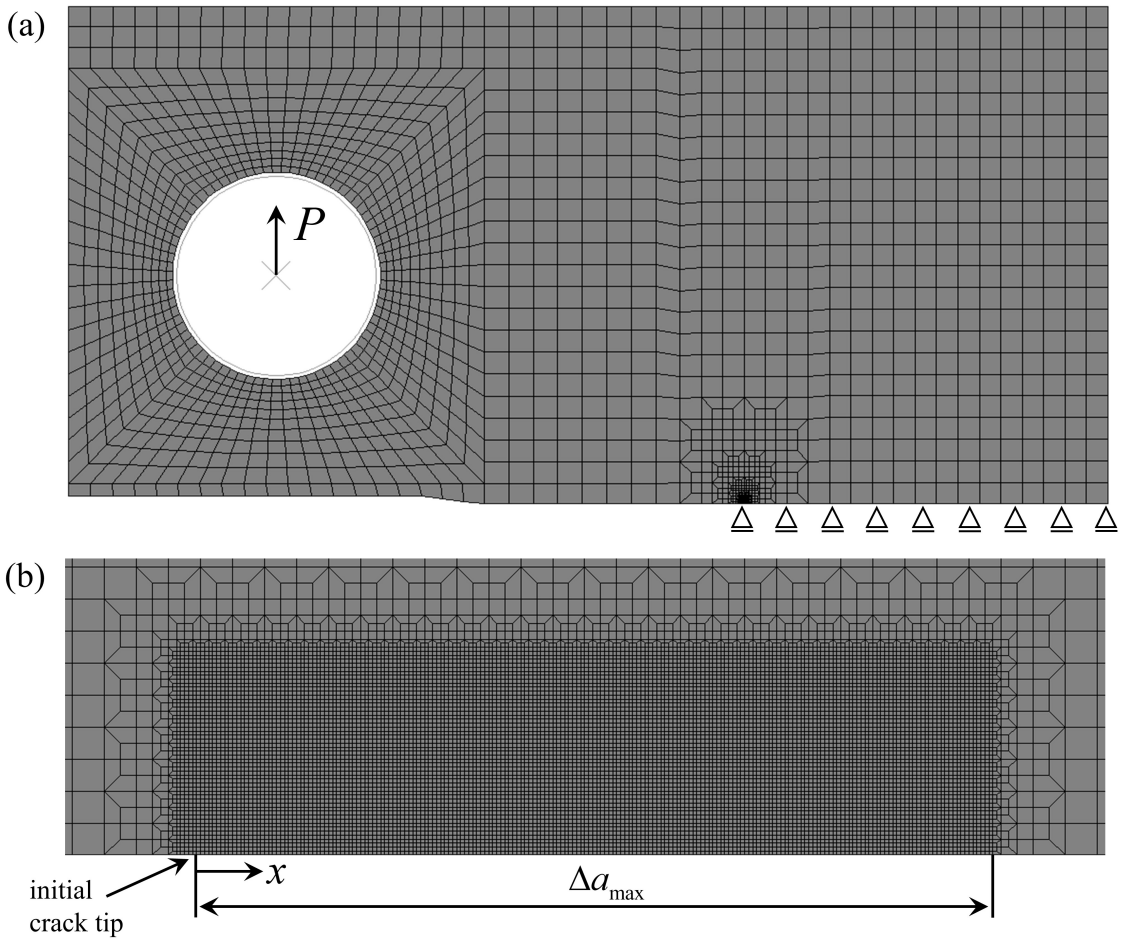

Figure 5.3. Finite element mesh for the compact tension specimen. (a) Global mesh including the load pin. (b) Refined mesh near the crack tip.

crack tip, shown in Figure 5.3b, had a minimum element size of 1.0 μm. This mesh size adequately resolved the active cohesive zone, and the predicted crack extension agreed with computations using an element size of 0.5 μm. To ensure details of post-OL crack extension and crack growth rates could be resolved and analyzed for all cases, larger element sizes were not considered for the refined-mesh region. Computations were terminated when the crack reached the end of the refined mesh region.

The load pin was modeled as a rigid cylinder, with frictionless surface-to-surface contact between the pin and the specimen. To replicate experimental conditions, loading was applied by imposing a force on the pin. The applied force is related to the stress intensity factor from the standard equation [76]

$$K(t) = \frac{P(t)}{\left(BB_N\right)^{1/2} W^{1/2}} f\left(a/W\right) \tag{5.1}$$

where $P(t)$ is the applied load as a function of time t, B is the specimen thickness, B_N is the net thickness for side-grooved specimens, a is the crack length, and W is the specimen width (measured from the force line to the rear surface of the specimen). For a C(T) specimen, the function $f\left(a/W\right)$ is given by

$$\begin{aligned} f\left(a/W\right) = &\left[\frac{2 + a/W}{\left(1 - a/W\right)^{3/2}}\right] \\ &\left[0.886 + 4.64\left(a/W\right) - 13.32\left(a/W\right)^2 + 14.72\left(a/W\right)^3 - 5.60\left(a/W\right)^4\right]. \end{aligned} \tag{5.2}$$

The CMSG-vp model described in Section 2.1.1 was used for the bulk material, and the irreversible CZM described in Section 2.2.1 was used for the cohesive elements. The material surrounding the load pin was treated as elastic. Motivated by the experiments showing cycle-dependent transgranular crack growth with fatigue striations at the loads of interest, only fatigue damage was considered. The modified fatigue damage evolution equation given in Eq. (2.25) was used here, such that the fatigue damage under pure normal separation is given by

$$\dot{D} = \frac{|\dot{\Delta}_n|}{C_f} \left\langle T_n - \sigma_f \right\rangle. \tag{5.3}$$

The parameters C_f and σ_f were used to calibrate the model to experimentally-measured fatigue crack growth rates for Alloy 617 at 800°C. Modifications to this approach to apply the model across different loading frequencies are investigated in Section 5.3.3.

5.2.1 Model parameters

The elastic and viscoplastic parameters were chosen based on the properties of Alloy 617 [9], [12], [212]. Young's modulus and Poisson's ratio were $E = 158600$ MPa and $\nu = 0.3$. The viscoplastic reference stress and reference strain rate were $\sigma_0 = 284$ MPa and $\dot{\varepsilon}_0 = 3.0 \times 10^{-4}$ s^{-1}. Two values of the strain hardening exponent were considered: $n = 0.0$, reducing the model to a Norton creep law, and $n = 0.1$, which would be relevant for materials with substantial primary creep [101]. Three values of the creep exponent were considered to assess its influence on the fatigue crack growth rates: $m = 3.0$, 5.0, and 7.0. These represent a typical range of values for solid solution strengthened materials [213]; this range of values was also considered by Reboul et al. [214] in a study of void growth in single crystals. To calibrate the model to crack growth data for Alloy 617, computations were conducted with $m = 5.6$ and $n = 0.0$. These values are based on creep tests [12], strain rate jump tests [9], and nanoindentation [212].

Similar to the CZMs developed for fatigue crack growth in Ni-base superalloys in [88], [89], the parameters $\sigma_{\max,0}$ and δ_0 were interpreted as setting the stiffness of the CZM in the context of fatigue crack growth. The values were set to $\sigma_{\max,0} = 10^4$ MPa and $\delta_0 = 0.002$ mm. These values ensured that the compliance in the CZM did not substantially affect the response in the bulk material before damage set in while allowing the model to resolve the active cohesive zone during crack extension.

The two parameters in the fatigue damage evolution law, Eq. (2.25), were varied parametrically to assess how the damage evolution interacted with rate sensitivity in the bulk material. Two values of each parameter were considered: $C_f = 3.0$ and 6.0 MPa $\cdot$ mm, and $\sigma_f = \sigma_0$ and $1.5\sigma_0$ ($\sigma_f = 284.0$ and 426.0 MPa). These parameters were subsequently calibrated to the fatigue crack growth test results for Alloy 617.

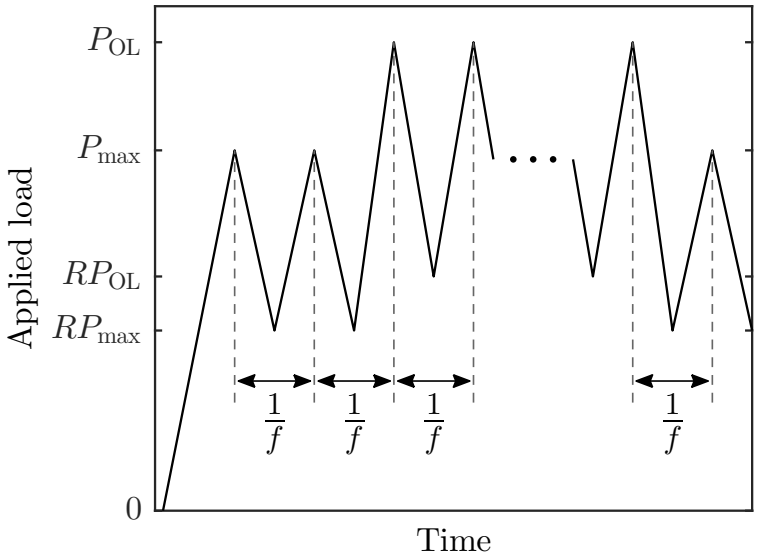

Figure 5.4. Schematic of the loading waveform for cyclic loading with OLs. The same loading frequency f was maintained during constant-amplitude loading and the OL(s).

The initial crack length for all computations was $a/W = 0.560$. A triangular waveform was used for all computations. Most of the computations used a load frequency of $f = 10^3\dot{\varepsilon}_0 = 0.3$ Hz, which is on the same order of magnitude as the load frequency in the experiments. To investigate the effect of load frequency on the results, $f = 10^2\dot{\varepsilon}_0 = 0.03$ Hz was also considered. The maximum applied load was $P_{max} = 1500$ N. With load ratio $R = 0.5$, this corresponds to a stress intensity factor range of $\Delta K = 11.75$ MPa$\sqrt{\text{m}}$. For computations with OL(s) in the parametric study, the OL ratio was $P_{max,OL}/P_{max} = 1.5$. The same load ratio was maintained during the OL cycles as well, such that the stress intensity factor range during the OLs was 1.5 times the baseline stress intensity factor range. The OL was always applied during the cycle after the crack extension reached a value of $\Delta a = 25$ µm. Computations with constant-amplitude loading (0 OLs), 1 OL, and a block of 10 OLs were considered in the parametric study. Different baseline stress intensity factor ranges and OL ratios were compared in connection with the experimental results for Alloy 617. Figure 5.4 shows the waveform used for the OLs in both the parametric study and the experiments. The same loading frequency f and load ratio R were maintained for all cycles.

5.3 Results

Results are first reported for the parametric study. The key outcome is the dependence of post-OL crack growth rates on the material rate sensitivity. The dependence of these results on the underlying CZM damage parameters is also investigated. Then, results are presented for the application to Alloy 617. Model predictions for post-OL crack growth rates are compared to the experiments, and the results are interpreted in light of the insights gained from the parametric study.

5.3.1 Parametric study

The first set of computations considered CZM damage parameters $C_f = 3.0$ MPa·m and $\sigma_f = \sigma_0$. Computations were conducted with constant-amplitude loading, a single OL, and a block of 10 OLs for each value of the creep exponent under consideration ($m = 3.0$, 5.0, and 7.0). Figure 5.5 shows the predicted crack extension for each case. For $m = 7.0$, crack growth following OLs is similar to the typical behavior of ductile metals in the rate-independent regime. For a single OL, there is a small amount of acceleration during the OL cycle, followed by substantial retardation. The result is an overall delay effect: the cycles required for the crack to grow through the fine-meshed region is larger for the single OL than for constant-amplitude loading. The 10-OL block causes more acceleration during the OLs as well as additional retardation in the subsequent cycles. The increased retardation is much more substantial: the total number of cycles required for the crack to grow through the fine-meshed region increases more for the OL block than for the single OL. For $m = 3.0$, the OLs accelerate crack extension, with the acceleration becoming more pronounced for the 10-OL block than a single OL. After the OL cycle(s), there is virtually no retardation. This response is more characteristic of relatively brittle materials. For $m = 5.0$, the acceleration and retardation are in close competition for both a single OL and the 10-OL block. The computations predicts that the number of cycles required for the crack to grow through the fine-meshed region in the model is nearly the same for zero, one, and 10 OLs. These results indicate a transition from retardation-dominated behavior at $m = 7.0$ (low rate sensitivity) to acceleration-dominated behavior at $m = 3.0$ (high rate sensitivity).

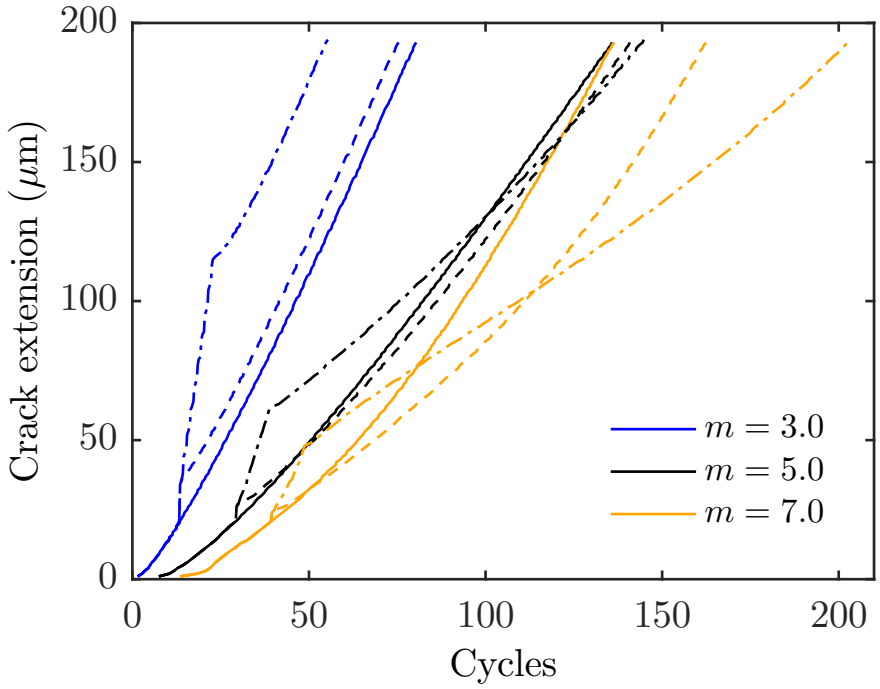

Figure 5.5. Predicted crack extension for computations with three different values of the creep exponent m, with constant-amplitude loading (solid lines), 1 OL (dashed lines), and 10 OLs (dash-dot lines). Retardation dominates after OLs for $m = 7.0$, while only acceleration occurs for $m = 3.0$.

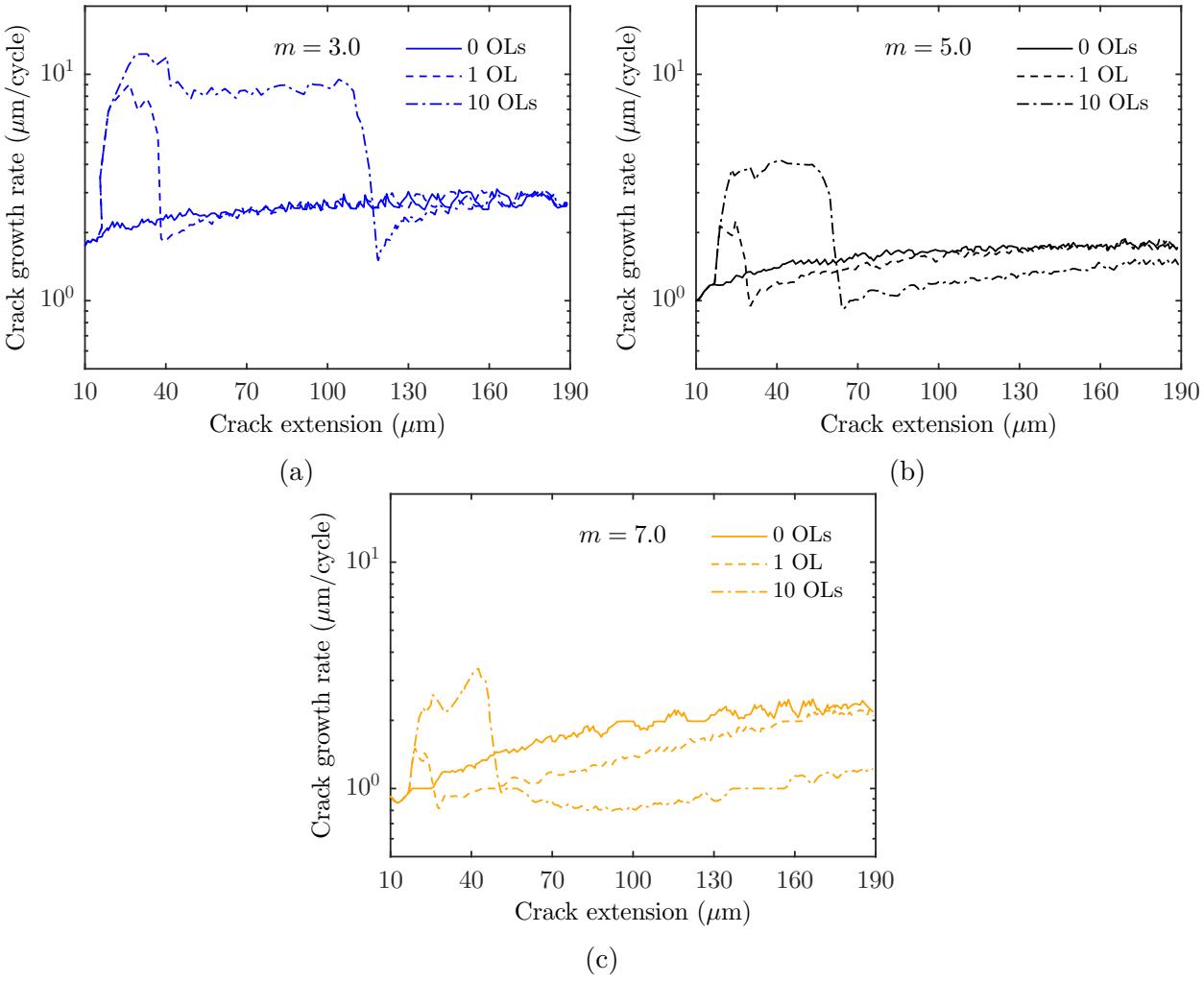

Figure 5.6. Predicted crack growth rates (log scale) for three values of the creep exponent m for constant-amplitude loading (zero OLs), 1 OL, and 10 OLs. (a) $m = 3.0$ (b) $m = 5.0$ (c) $m = 7.0$

Figure 5.6 shows the crack growth rates for each value of m and number of OLs. The evolution of the crack growth rates helps to quantify the size of the OL-affected region, where crack growth retardation occurs. Figure 5.6c shows a substantial reduction in crack growth rates after the OL cycle(s) for $m = 7.0$, again similar to ductile metals in the rate-independent regime. For one OL, the end of the OL-affected region approximately corresponds with the end of the fine-meshed region. Increasing the number of OLs slightly reduces the minimum post-OL crack growth rate, but the main effect is increasing the size of the OL-affected region. Crack growth rates are still significantly suppressed at the end of the fine-meshed region with the 10-OL block. Figure 5.6a indicates that a very small amount of retardation occurs for $m = 3.0$, but crack growth rates quickly return to steady state after the OL cycle(s). The crack growth rates for $m = 5.0$ again show the close competition between acceleration and retardation. There is a brief but significant acceleration during the OL cycle(s), followed by a region where crack growth rates are clearly reduced. As observed in Figure 5.5, the acceleration and retardation essentially cancel each other out for one OL, as there is only a small delay effect in the number of cycles. The 10-OL block widens the extent of the OL-affected region. Figure 5.6b shows that crack growth rates are still slightly suppressed at the end of the fine-meshed region for the OL block. Thus, the retardation would likely persist beyond the end of the computation, resulting in a larger delay effect than for a single OL. Overall, the OL-affected region is larger, and the minimum post-OL crack growth rate is lower for higher m.

The next question of interest is why the trends observed in the post-OL crack growth rates occur, particularly the transition from acceleration-dominated behavior for $m = 3.0$ to retardation-dominated behavior for $m = 7.0$. To this end, outputs from the model in both the cohesive zone and the bulk material are now analyzed.

Figure 5.7 shows the traction distribution in the cohesive zone at the maximum load for several cycles during the computations with 1 OL. To enable comparisons between each case, the traction is normalized by the peak value during the cycle immediately before the OL. For all cases, the peak traction increases during the OL cycle, while the peak traction decreases during the cycle after the OL. The decreased peak traction is associated with increased damage during the OL cycle. However, key differences arise in the shape of the

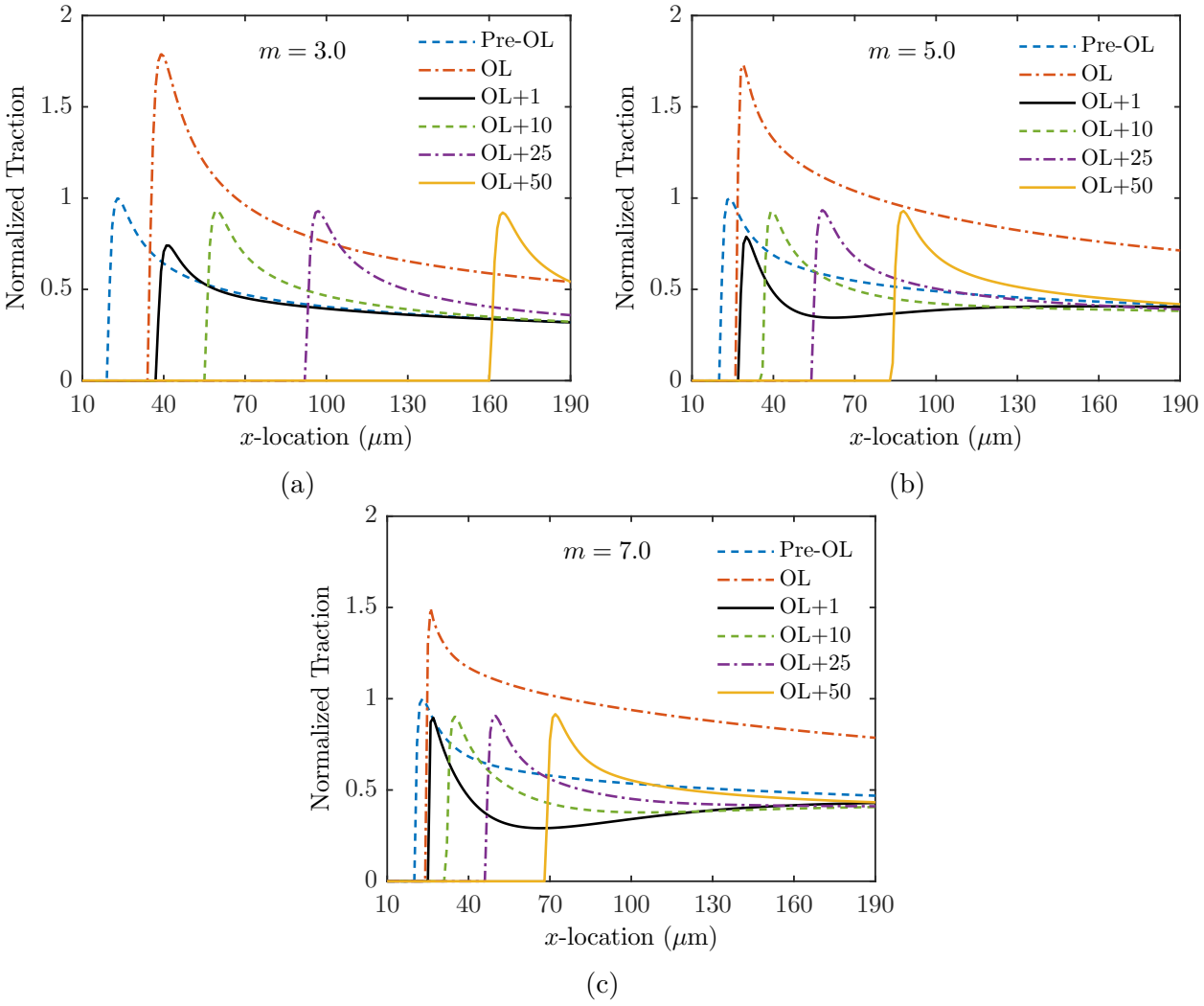

Figure 5.7. Predicted traction distributions for computations with 1 OL and for three values of the creep exponent: (a) $m = 3.0$ (b) $m = 5.0$ (c) $m = 7.0$. The traction distribution is shown at maximum load for six different cycles: constant-amplitude loading before the OL; the OL cycle; and 1, 10, 25, and 50 cycles after the OL. In each case, the traction is normalized by the peak traction during constant-amplitude loading prior the OL cycle.

traction distribution ahead of the crack tip during subsequent cycles. These differences are associated with the crack extension and crack growth rate trends observed in Figure 5.5 and Figure 5.6. For $m = 7.0$ (Figure 5.7c), the shape of the traction distribution after the OL deviates from the distribution during constant-amplitude loading. There is a region ahead of the crack tip where the traction is clearly suppressed, most clearly pronounced in the first cycle after the OL. The minimum traction is higher in subsequent cycles, but it remains suppressed ahead of the crack tip compared with the constant-amplitude distribution. This corresponds to reduced damage accumulation and subsequent crack growth retardation.

For $m = 3.0$ (Figure 5.7a), the only change in the traction distribution following the OL is the lower peak traction. There is no region ahead of the crack tip where the traction is clearly suppressed. The traction distribution immediately returns to the shape from constant-amplitude loading before the OL cycle. This corresponds to the minimal amount of crack growth retardation for $m = 3.0$. For $m = 5.0$ (Figure 5.7b), the response falls in between the other two cases. Unlike $m = 3.0$, there is a clear dip in the traction distribution following the OL, but it is less extensive than for $m = 7.0$. By the 50th cycle after the OL, the traction ahead of the crack tip returns to the shape observed during constant-amplitude loading. This corresponds to the smaller OL-affected region and lower number of cycles required to return to the steady-state crack growth rates compared to $m = 7.0$. Also, the length of the region with suppressed traction in the first cycle after the OL agrees closely with the length of the OL-affected region observed in Figure 5.6b. The crack growth rate returns to the steady-state value at a location of about 150 μm beyond the initial crack tip. This is close to the location where the traction in the "OL+1" cycle returns to the steady-state distribution from before the OL.

Figure 5.8 shows contours of the accumulated viscoplastic strain for each case in the 50th cycle after the OL. The key result is that a higher value of the creep exponent m correlates with higher local viscoplastic strains near the location of the crack tip when the OL was applied. For example, for $m = 7.0$, there is a region of clearly increased viscoplastic strain near the OL location. There is a modest increase in viscoplastic strain for $m = 5.0$ and virtually no evidence of the OL for $m = 3.0$. Together with Figure 5.7, this indicates that the traction distributions for $m = 7.0$ and $m = 5.0$ are disturbed by residual stress due to

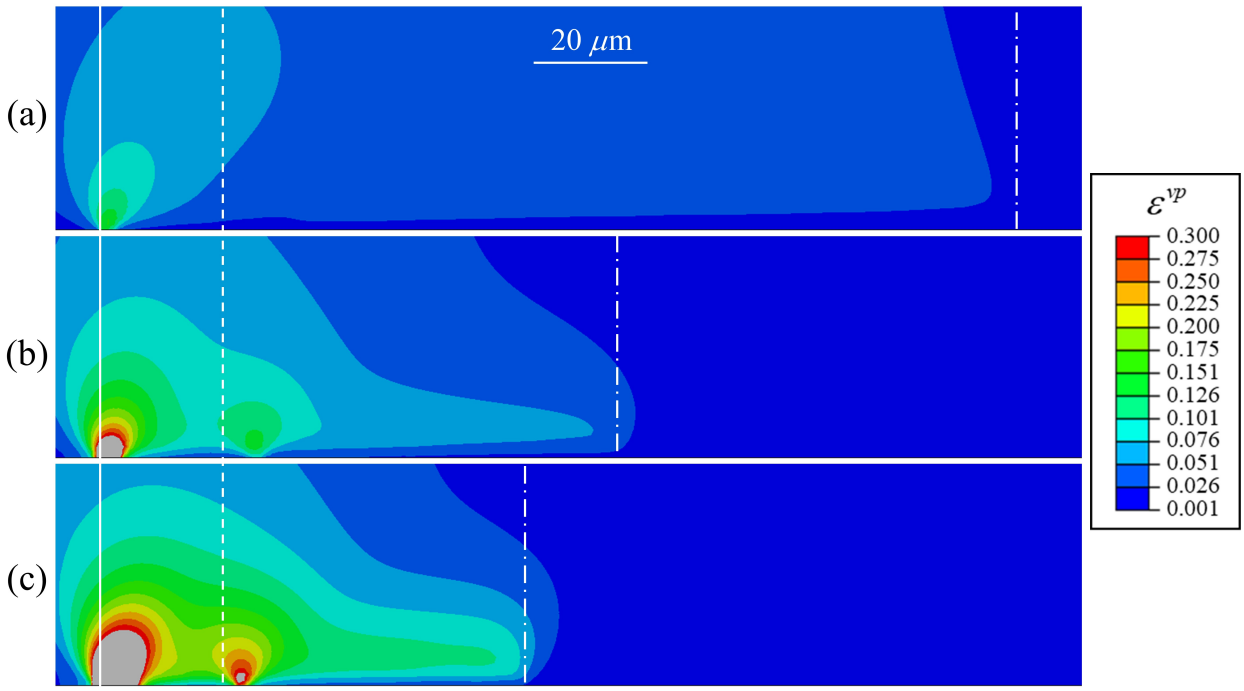

Figure 5.8. Contours of the accumulated viscoplastic strain ε^{vp} in the 50th cycle after the OL for computations with 1 OL and three values of the creep exponent: (a) $m = 3.0$ (b) $m = 5.0$ (c) $m = 7.0$. In all cases, contours are shown on the undeformed configuration. The solid white line marks the initial crack tip location. The dashed white line marks the location of the crack tip when the OL was applied. The dash-dot white line marks the current crack-tip location.

the increased crack-tip viscoplastic deformation during the OL. As a result, crack growth retardation occurs after the OL. This phenomenon is similar to what has been observed in rate-independent elastic-plastic materials in computations of fatigue crack growth including OLs [119], [129].

Next, the traction threshold σ_f and the reference damage energy C_f are varied to determine if these parameters influence the observed trends with respect to the creep exponent m. Figure 5.9 shows crack extension predictions for three parameter sets. The results from Figure 5.5 are repeated in Figure 5.9a to aid in comparisons between each case. Higher values of the reference damage energy C_f reduce the damage accumulation by the same factor at all locations in the CZM. Comparing Figure 5.9a ($C_f = 3.0$ MPa·mm) and Figure 5.9b ($C_f = 6.0$ MPa·mm) shows that doubling the value of C_f increases the number of cycles required for the crack to grow through the fine-meshed region for all values of m. In quasi-brittle materials, doubling C_f would increase this number of cycles and reduce the crack growth rates by exactly a factor of two. In that case, damage evolution is the only dissipative process [130]. Here, there is additional crack-tip viscoplastic deformation for the slower-growing cracks that reduces crack growth rates beyond a factor of two. Comparing Figure 5.9a and Figure 5.9b shows this is more significant for higher values of m, where there is also more crack-tip viscoplasticity as seen in Figure 5.8. In computations with OLs, the acceleration and retardation are both suppressed for all cases with $C_f = 6.0$ MPa·mm compared to the predictions for $C_f = 3.0$ MPa·mm. However, the trends with respect to m remain the same. The response is dominated by acceleration for $m = 3.0$, with a transition to retardation for $m = 7.0$.

Similarly, increasing the threshold σ_f reduces the crack growth rates for all cases. In this case, the length of the active cohesive zone is also reduced, as the region where damage evolution occurs extends a shorter distance ahead of the crack tip [88], [130]. As a result, the shape of the crack extension curves changes somewhat in Figure 5.9c ($\sigma_f = 1.5\sigma_0$) compared with Figure 5.9a ($\sigma_f = \sigma_0$). The computations with $\sigma_f = 1.5\sigma_0$ predict that a smaller amount of crack extension is required to reach a steady-state crack growth rate for constant-amplitude loading. As with the C_f parameter, however, the post-overload trends with respect to m are not affected.

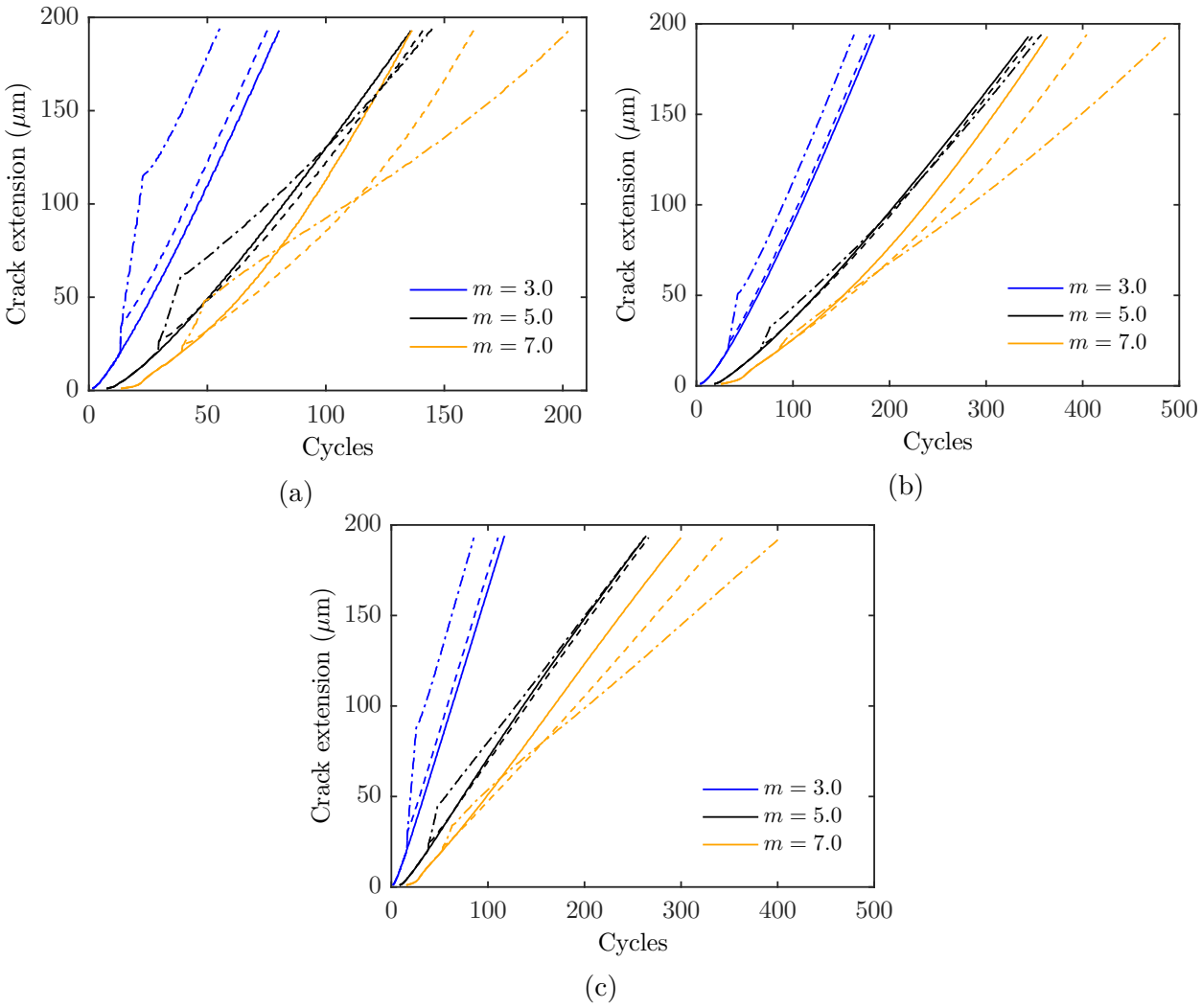

Figure 5.9. Predicted crack extension for computations with different combinations of CZM damage parameters: (a) $C_f = 3.0$ MPa·mm and $\sigma_f = \sigma_0$ (repeated from Figure 5.5) (b) $C_f = 6.0$ MPa·mm and $\sigma_f = \sigma_0$ (c) $C_f = 3.0$ MPa·mm and $\sigma_f = 1.5\sigma_0$. The figures include constant-amplitude loading (solid lines), 1 OL (dashed lines), and 10 OLs (dash-dot lines) with three different values of the creep exponent m.

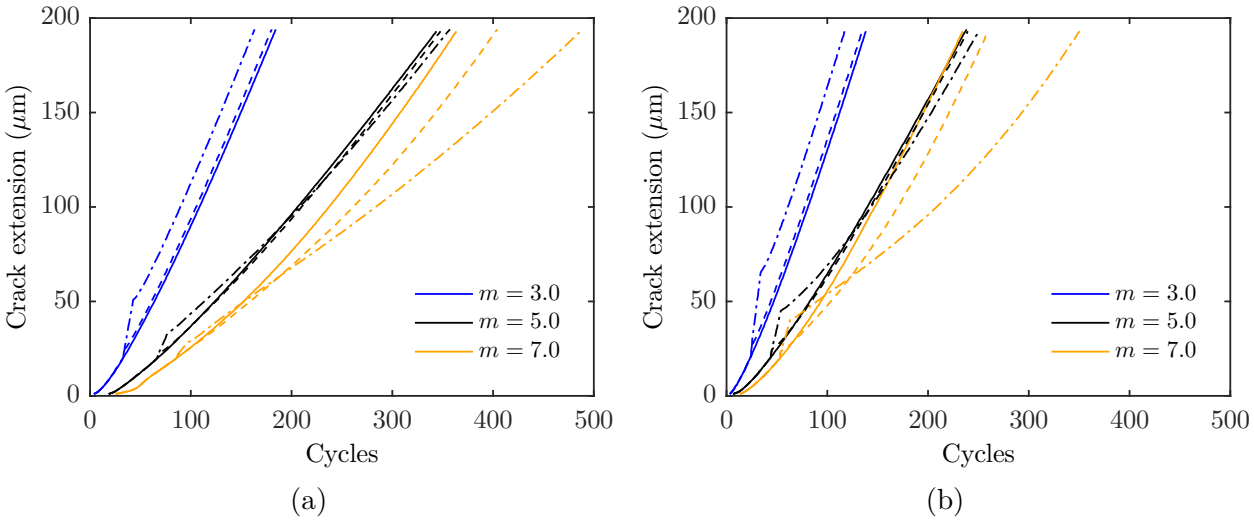

Figure 5.10. Predicted crack extension for computations with different values of the strain hardening exponent N: (a) $N = 0.0$ (repeated from Figure 5.9b) (b) $N = 0.1$. The figures include constant-amplitude loading (solid lines), 1 OL (dashed lines), and 10 OLs (dash-dot lines) with three different values of the creep exponent m.

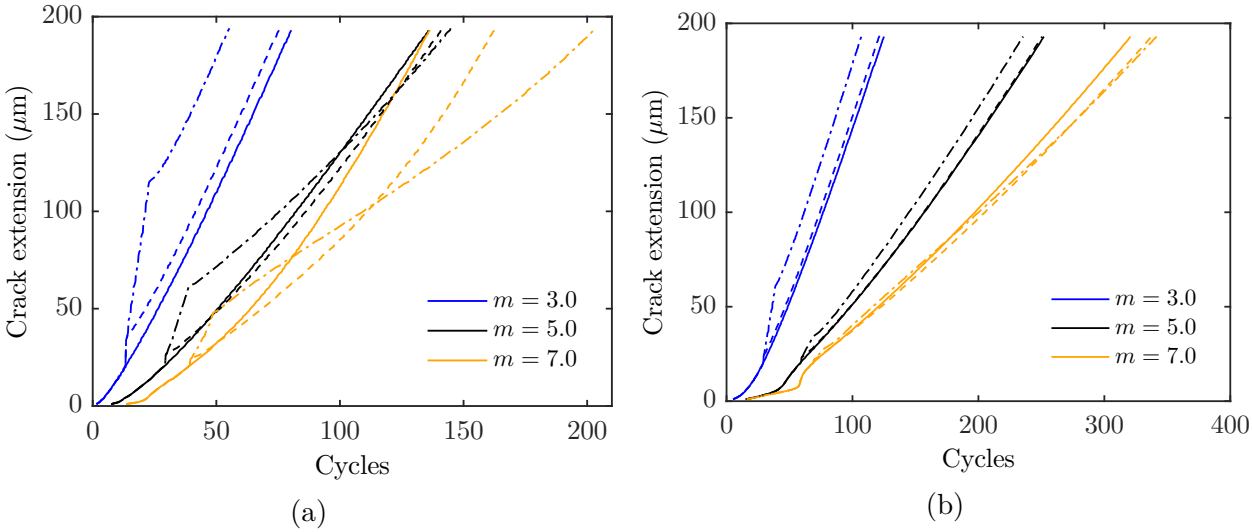

Figure 5.11. Predicted crack extension for computations with different loading frequencies: (a) $f = 10^3\dot{\varepsilon}_0 = 0.3$ Hz (repeated from Figure 5.5) (b) $f = 10^2\dot{\varepsilon}_0 = 0.03$ Hz. The figures include constant-amplitude loading (solid lines), 1 OL (dashed lines), and 10 OLs (dash-dot lines) with three different values of the creep exponent m.

Figure 5.10 shows the effect of including strain hardening in the material definition, which is relevant for materials that exhibit substantial primary creep. Crack extension predictions are compared for strain hardening exponents $n = 0.0$ and $n = 0.1$ with damage parameters $C_f = 6.0$ MPa·mm and $\sigma_f = \sigma_0$. Crack growth rates are higher overall for $n = 0.1$ due to a reduction of crack-tip shielding from viscoplastic deformation in the bulk material. However, this does not affect the trend of the post-overload crack growth rates either. The dominance of acceleration or retardation depends only on the creep exponent m.

Finally, Figure 5.11 shows the influence of the load frequency on crack extension. Unlike the other parameters that have been considered, decreasing the load frequency alters the creep exponent value at which the transition between acceleration and retardation-dominant behavior occurs. Although the trend towards retardation at higher m remains the same, net acceleration clearly occurs for $m = 5.0$ at the lower load frequency of $f = 0.03$ Hz. Aside from the damage parameters and the load frequency, the magnitude of the applied load is the other main factor governing the crack growth rates. The influence of the load magnitude is investigated in the next section through comparisons to the experiments.

5.3.2 Application to Alloy 617

The model was calibrated to the experimentally-measured crack growth rates for Alloy 617 under constant-amplitude loading at 800°C and a loading frequency of $f = 0.33$ Hz reported in [15]. Figure 5.12 shows the cyclic crack growth rates $\mathrm{d}a/\mathrm{d}N$ as a function of stress intensity factor range ΔK for the constant-amplitude loading experiments. The results follow the typical Paris law relationship [42]:

$$\frac{\mathrm{d}a}{\mathrm{d}N} = A_p \left(\Delta K\right)^{M_p}, \tag{5.4}$$

with exponent $M_p = 1.85$. Computations at stress intensity factor ranges of $\Delta K = 9.20$, 11.75, and 14.10 MPa$\sqrt{\mathrm{m}}$ were used to calibrate the model. The traction threshold σ_f was chosen such that the predicted slope of the da/dN versus ΔK curve agreed with the experiments. The reference damage energy C_f was chosen such that the numerical values of the crack growth rates aligned with the experiments. This procedure resulted in values of $\sigma_f = 100$ MPa and $C_f = 20.0$ MPa·m. Values of the bulk material parameters are given in Section 5.2.1. Predicted crack growth rates for the calibrated model are shown in Figure 5.12 together with the experimentally-measured crack growth rates.

Computations with a single OL and a block of 20 OLs were conducted using the calibrated model. Baseline stress intensity factor ranges of $\Delta K = 9.20$, 11.75, and 14.10 MPa$\sqrt{\mathrm{m}}$ were used in the computations. Both OL ratios from the experiments were considered. Recall that a single OL did not produce any measureable effects. Overload blocks produced retardation at low loads and acceleration at high loads, with the retardation being more pronounced at a higher OL ratio.

Figure 5.13 and Figure 5.14 show the predicted crack extension and cyclic crack growth rates for each OL ratio and baseline ΔK. Particularly for an OL ratio of 1.25 the predicted crack extension for a single OL is nearly the same as for constant-amplitude loading. Acceleration and retardation are both virtually absent. This agrees with the single-OL experiment. For the blocks of 20 OLs the crack extension predictions show net retardation for $\Delta K = 9.20$ MPa$\sqrt{\mathrm{m}}$, particularly for OL ratio 1.5. The retardation becomes less significant for higher

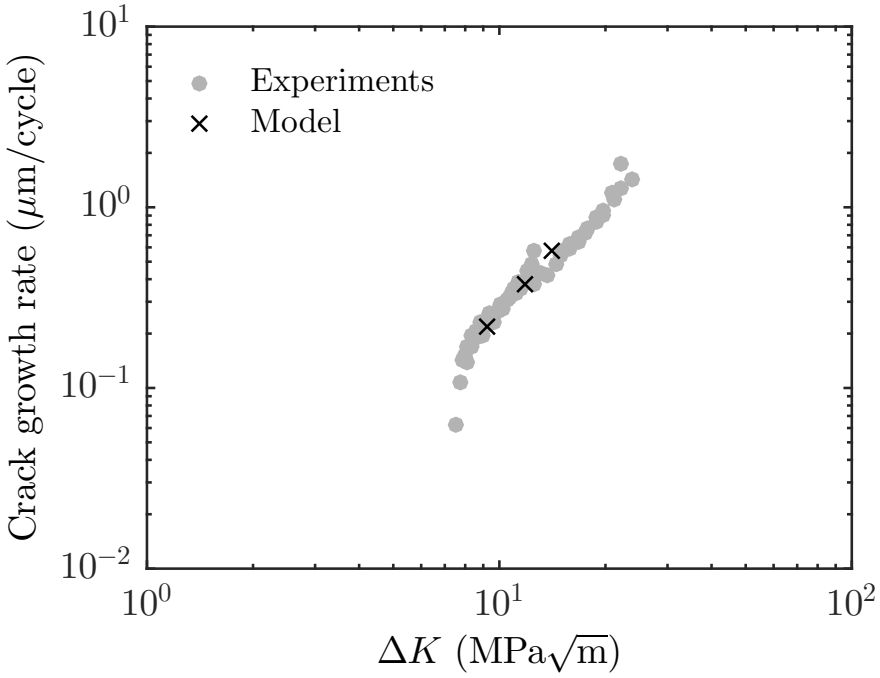

Figure 5.12. Cyclic crack growth rates as a function of stress intensity factor range (double-log scale) for a triangular loading waveform with load frequency $f = 0.33$ Hz. Results are shown for crack growth experiments and for the calibrated model.

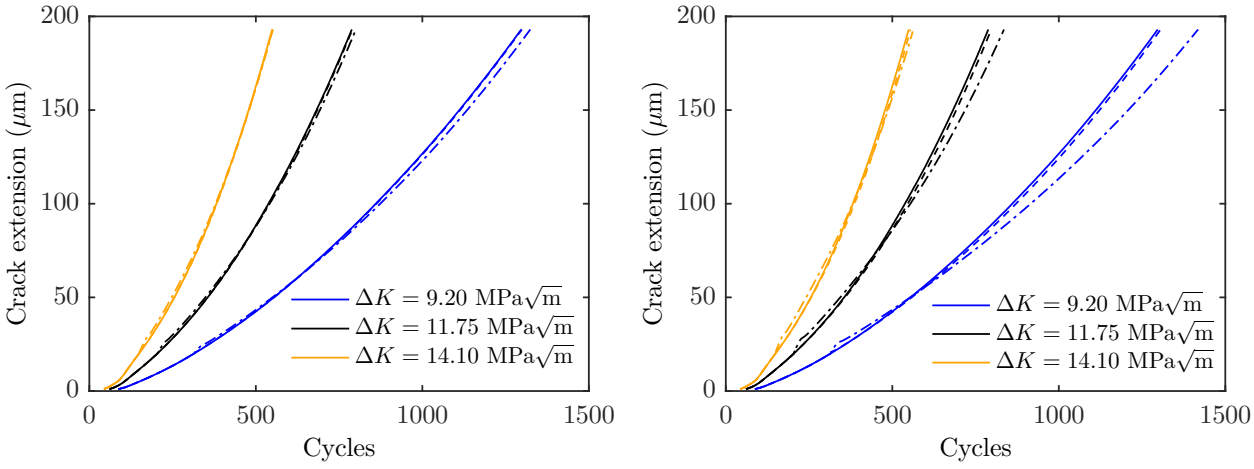

Figure 5.13. Predicted crack extension for computations with the calibrated model for OL ratios of (a) 1.25 and (b) 1.5. The figures include constant-amplitude loading (solid lines), 1 OL (dashed lines), and 20 OLs (dash-dot lines) at three different baseline stress intensity factor ranges.

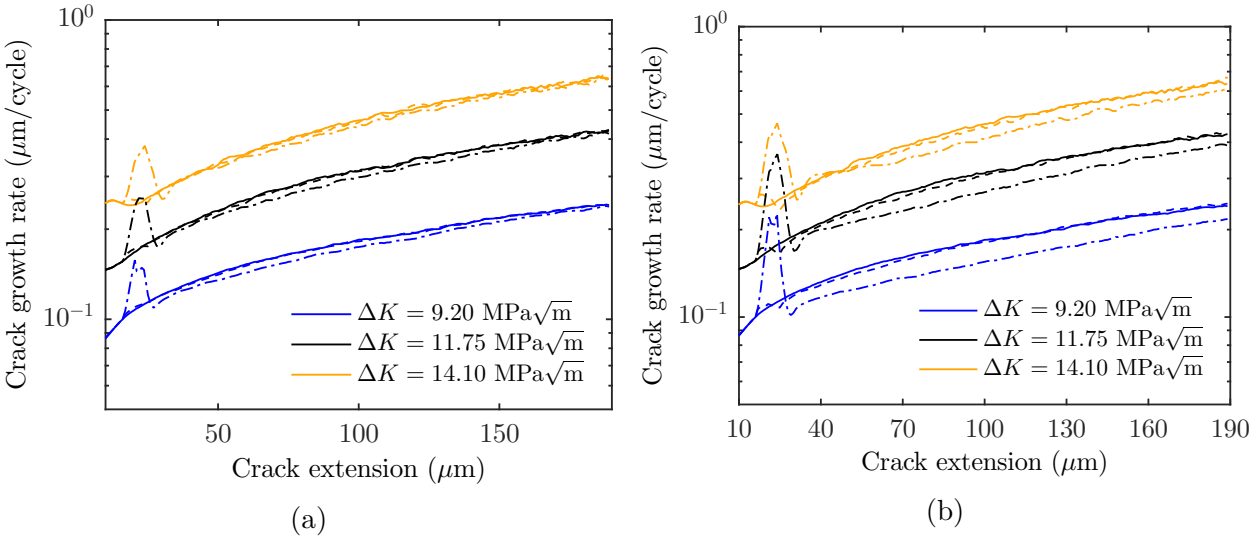

Figure 5.14. Predicted crack growth rates for computations with the calibrated model for OL ratios of (a) 1.25 and (b) 1.5. The figures include constant-amplitude loading (solid lines), 1 OL (dashed lines), and 20 OLs (dash-dot lines) at three different baseline stress intensity factor ranges.

baseline loads and essentially disappears at $\Delta K = 14.10$ MPa$\sqrt{\text{m}}$, with the acceleration and retardation cancelling each other out. The same trend was observed in the experiments with OL blocks shown in Figure 5.1 and Figure 5.2. However, the predicted retardation immediately after the OLs is less severe than in the experiments, while the model appears to overpredict the length of the OL-affected region in terms of both cycles and crack extension.

5.3.3 Plastic strain gradients and cyclic loading at different frequencies

The role of plastic strain gradients was investigated for the calibrated model by setting the intrinsic material length to $l = 4.5$ μm, the value inferred from nanoindentation experiments at 800°C on Alloy 617 [212]. Computations were conducted with constant-amplitude loading and a block of 20 OLs at each OL ratio of interest (i.e., 1.25 and 1.5) using the calibrated CZM. Results are shown in Figure 5.15 comparing the computations incorporating plastic strain gradients to the original computations without strain gradient hardening shown in Figure 5.13. These results demonstrate that hardening due to plastic strain gradients does not significantly affect steady-state or post-OL crack growth. Essentially, for this material, the OL effect is already insignificant enough that accounting for the increased hardening

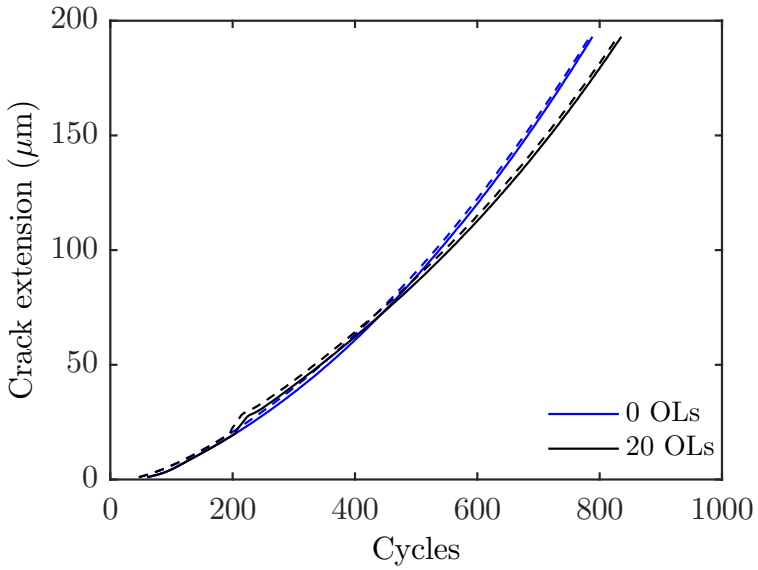

Figure 5.15. Predicted crack extension with the calibrated model for $\Delta K = 11.75$ MPa$\sqrt{\text{m}}$ and OL ratio 1.5. Solid lines are for $l = 0$ (shown previously in Figure 5.13b). Dashed lines are for $l = 4.5$ μm.

close to the crack tip due to plastic strain gradients does not affect the model predictions. This contrasts with the results in Chapter 3 for the rate-independent material.

Another interesting observation is that, as shown in Figure 5.11, the model predicts much lower constant-amplitude crack growth rates for the same applied load when the frequency is reduced. However, the experiments by [15] show that the relationship between constant-amplitude crack growth rates and the stress intensity factor range is nearly independent of load frequency up to about $\Delta K \approx 11.5$ MPa$\sqrt{\text{m}}$ or $K_{\max} \approx 23.0$ MPa$\sqrt{\text{m}}$. It was therefore hypothesized that incorporating the same rate-dependence from the viscoplasticity formulation into the damage evolution equation could account for this discrepancy. This is based on the idea that crack growth at loads of interest below $K_{\max} \approx 23.0$ MPa$\sqrt{\text{m}}$ is associated with the cyclic viscoplasticity.

To demonstrate the concept, this was done in an approximate manner using the following approach. First, the maximum effective stress ahead of the crack tip during crack growth was extracted from computations at $\Delta K = 11.75$ MPa$\sqrt{\text{m}}$ and each frequency of interest: $f = 0.33$, 0.05, and 5.0 Hz. The stresses are denoted as $\bar{\sigma}_{0.33}$, $\bar{\sigma}_{0.05}$, and $\bar{\sigma}_{5.0}$, respectively.

The stress from computations with $f = 0.33$ Hz was used as a reference case to calculate a ratio for each frequency:

$$R_{0.05} = \left(\frac{\bar{\sigma}_{0.05}}{\bar{\sigma}_{0.33}}\right)^{5.6}, \quad R_{5.0} = \left(\frac{\bar{\sigma}_{5.0}}{\bar{\sigma}_{0.33}}\right)^{5.6}. \tag{5.5}$$

These ratios represent the influence of the material rate sensitivity on the computations at each frequency. The ratios were found to be $R_{0.05} \approx 0.75$ and $R_{5.0} \approx 1.6$. To incorporate this rate dependence into the CZM, the reference damage energy was scaled by this parameter. With the calibrated model for $f = 0.33$ Hz using $C_f = 20.0$ MPa·mm, the reference damage energies for the other two frequencies were

$$C_{f,0.05} = R_{0.05}C_f = 15.0 \text{ MPa} \cdot \text{mm}, \quad C_{f,5.0} = R_{5.0}C_f = 32.0 \text{ MPa} \cdot \text{mm}. \tag{5.6}$$

Figure 5.16 shows the predicted crack growth rates from the revised model, together with the experimental data from [15]. The predicted crack growth rates no longer depend strongly on the load frequency. The model therefore still overpredicts the crack growth rates for $f = 5.0$ Hz somewhat, but it does support the hypothesis that incorporating rate dependence into the CZM can remove the frequency dependence of the model predictions. For the $f = 0.05$ Hz results, two further observations are relevant. First, the experiments observed significant void growth and coalescence above $\Delta K \approx 11.5$ MPa $\sqrt{\text{m}}$ for $f = 0.05$ Hz and loading waveforms containing a hold time [15]. The highest stress intensity factor considered in the computations clearly exceeds this level ($\Delta K = 14.10$ MPa$\sqrt{\text{m}}$). The modified model does predict a slightly higher crack growth rate for $f = 0.05$ Hz at this load level, but void growth should be also be considered at this point. Second, based on the conditions laid out in ASTM E2760 [76], the stress intensity factor becomes ineffective for characterizing fatigue crack growth below $f \approx 0.125$ Hz for this material [15]. This calls into question the correlation with ΔK for $f = 0.05$ Hz. To investigate this further, additional computations were conducted at a different crack length but the same applied ΔK. Figure 5.17 shows the predicted crack growth rates for the original calibrated model with $C_f = 20$ MPa·mm, $\Delta K = 9.2$ MPa$\sqrt{\text{m}}$, $a/W = 0.560$ and 0.485, and $f = 0.33$ Hz and

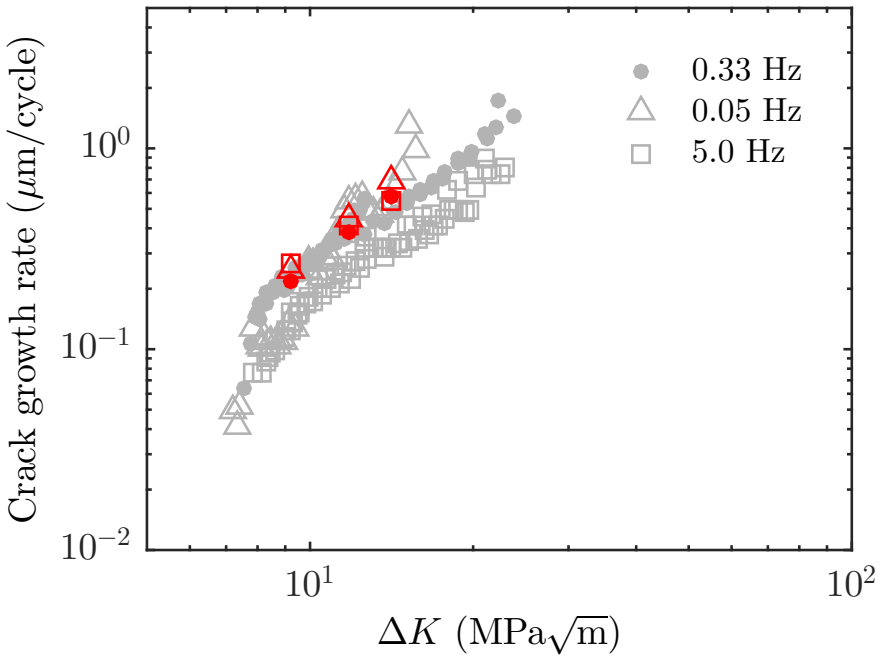

Figure 5.16. Cyclic crack growth rates as a function of stress intensity factor range (double-log scale) for a triangular loading waveform with load frequencies $f = 0.33$, 0.05, and 5.0 Hz. Experimental results are in grey, and predictions from the modified model are in red.

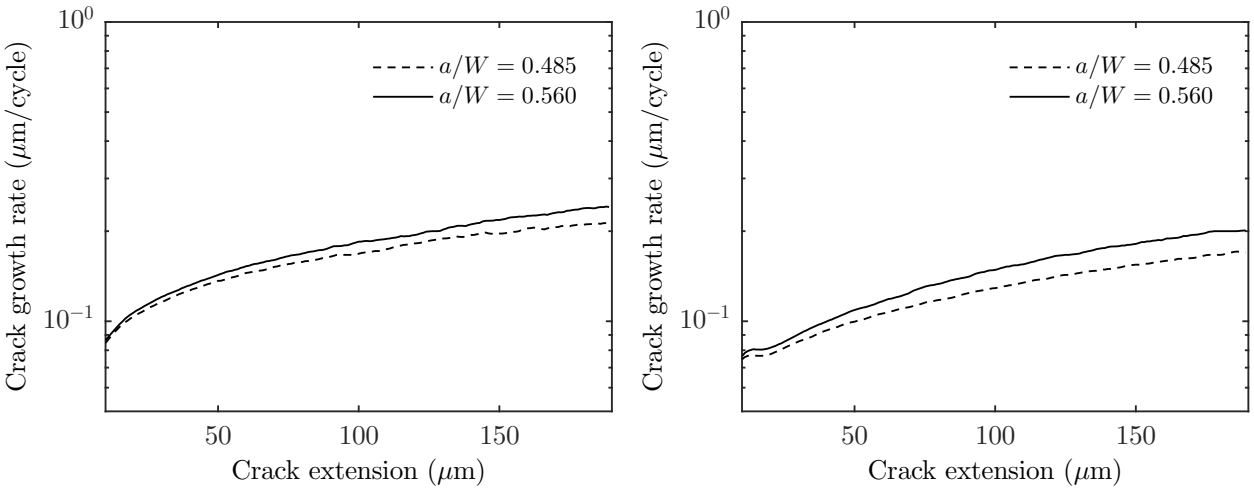

Figure 5.17. Predicted crack growth rates for computations with $C_f = 20$ MPa·mm and $\Delta K = 9.2$ MPa$\sqrt{\text{m}}$ at two different initial crack lengths. (a) $f = 0.33$ Hz. (b) $f = 0.05$ Hz.

0.05 Hz. The predicted crack growth rates are indeed somewhat dependent on the initial a/W value for $f = 0.05$ Hz, while the dependence is reduced for $f = 0.33$ Hz.

An alternate way to introduce rate dependence into the cohesive zone is through the monotonic traction separation law. This can be done by scaling the cohesive strength parameter $\sigma_{\text{max},0}$ instead of the reference damage energy by the ratios $R_{0.05}$ and $R_{5.0}$. Based on the interpretation of $\sigma_{\text{max},0}$ as setting the stiffness of the CZM, this creates a situation where the effective stiffness of the bulk material and the stiffness of the CZM share the same rate dependence. Using this approach, the computations predict essentially the same crack growth rates as shown in Figure 5.16. This is investigated further in Appendix C.

5.4 Discussion

The key outcome of this study is the transition from acceleration-dominated behavior at high rate sensitivities (low creep exponents) to retardation-dominated behavior at low rate-sensitivities (high creep exponents). Higher creep exponents are associated with larger accumulated viscoplastic strains near the crack tip, seen in Figure 5.8. The resulting compressive residual stresses disturb the traction distribution ahead of the crack tip, as indicated

by Figure 5.7. This in turn leads to suppressed damage accumulation and crack growth retardation. The value of the creep exponent corresponding to the transition between net acceleration and retardation is on the order of $m = 5.0$ to $m = 7.0$ for the load frequencies considered here.

The numerical predictions indicate that the rate sensitivity is the main material parameter influencing whether post-OL retardation occurs. The CZM parameters, which would in general need to be calibrated to the constant-amplitude crack growth rates for a particular material, did not affect the trends in the post-OL crack growth rates. The main effect of altering these parameters was suppressing the magnitude of both the acceleration and retardation at higher values of the threshold σ_f and the reference damage energy C_f. Higher values of these parameters correspond to lower constant-amplitude crack growth rates. These trends were similarly independent of strain hardening, although only isotropic hardening was considered in this study.

The computations provide insight into experimentally-measured crack extension following OLs in Alloy 617. The creep exponent for Alloy 617 of $m = 5.6$ is in the range of values where a close competition between post-OL acceleration and retardation was observed in the parametric study. This close competition does indeed occur in the fatigue crack growth experiments. The trend toward more acceleration following OL blocks at higher baseline ΔK is also present in both the computations and experiments.

The computations with OLs also help to explain an apparent contradiction in the experimental crack growth data for Alloy 617. Based on crack extension experiments under constant load, Alloy 617 has been described as creep-ductile [17], meaning that substantial viscoplastic deformation accompanies crack extension [5]. On the other hand, the fatigue crack growth experiments with OLs reported here demonstrate behavior more characteristic of brittle materials [20]: the possibility of acceleration-dominated behavior for OL blocks, as well as the lack of retardation after a single OL seen in the computations. As a result, classical OL models that assume retardation occurs as the crack grows through the OL-induced plastic zone [7], [44], [51] cannot be applied to this material. The parameters in such a model could be fit to a case where retardation does occur (e.g., Figure 5.1a), but the prediction would fail at a different applied load (e.g., Figure 5.1c). Most of these models

also do not account for the acceleration that occurs immediately after the OL(s), which is significant in the experiments with OL blocks. On the other hand, the model predictions in this study do reflect the trends in the experiments, without performing any calibration beyond the constant-amplitude crack growth results.

This observation is relevant to structural materials beyond Alloy 617. Many solid solution strengthened alloys, as well as pure metals, have a creep exponent in the range of $m = 5.0$ to $m = 7.0$, particularly at temperatures and stresses where dislocation climb is a dominant deformation mechanism [213]. These materials are therefore expected to show a close competition between acceleration and retardation after OLs, similar to Alloy 617. More experimental studies on high-temperature fatigue crack growth under transient loads would help to further understand this phenomenon.

Although the trends in the computations are similar to the experiments, the shape of the predicted crack extension curves differs from those observed experimentally. In particular, both the acceleration and retardation are more pronounced in the experiments. There are several possible reasons for this. A known difficulty with power law viscoplasticity models is that they can overestimate the stress and underestimate the viscoplastic deformation close to the crack tip [81], [215]. Accounting for this phenomenon using a double power law [88] or hyperbolic sine [215] creep model may remedy this issue. With increased crack-tip viscoplastic strain, the model would likely predict more pronounced retardation. It is also possible that some cavitation damage is induced during the OLs, which could enhance the crack growth acceleration [81]. Some cavitation has been observed at higher loads at the frequency of interest ($f = 0.33$ Hz) [15]. This is not accounted for in the model. Using a more complex fatigue damage model could also improve predictions. One common approach is to use a power law damage evolution equation rather than the linear relationship in Eq. (2.25) [88], [118]. This adds one additional fitting parameter to the CZM formulation. A formal calibration procedure involving, for example, an optimization algorithm and sensitivity analysis with the CZM parameters could further enhance this study. Here, the values for the CZM parameters were estimated by comparison with the emperimentally-measured crack growth rates. Overall, however, the qualitative agreement between model and exper-

iment regarding the trends in acceleration and retardation across different load magnitudes is encouraging.

A further limitation related to the OL computations is that the OLs were applied before the crack growth rates reached fully steady-state conditions. This ensured reasonable computational expense while computing a sufficient amount of crack extension to capture the post-OL acceleration and retardation. One possible solution to this limitation could involve using a numerical scheme where the model state after constant-amplitude loading just prior to OL application is stored and used as input to subsequent computations. Adaptive remeshing may also aid in computing larger amounts of crack extension with reasonable computational expense [119].

The results pertaining to constant-amplitude crack growth at different frequencies indicate that incorporating rate dependence into the CZM damage formulation based on the rate dependence in the bulk material brings the predicted crack growth rates at all load frequencies into closer agreement. This supports the idea that crack growth at all frequencies is closely associated with cyclic viscoplasticity at the loads of interest. Also, instead of the *ad hoc* adjustments to the CZM parameters based on the effective stress in the bulk material, a rate dependent CZM formulation could be used. An example of this approach is the work of Landis et al. [216], who used a rate-dependent CZM to model monotonic fracture of elastic-viscoplastic materials. Abraham et al. [123] used a similar rate-dependent CZM formulation to study thermomechanical fatigue in superalloys.

This study is also restricted to cases where crack growth is dominated by cyclic (fatigue) mechanisms, motivated by the experiments for Alloy 617 showing cycle-by-cycle crack growth at the load ranges and frequencies of interest [15]. The experimental and numerical results showed that it is possible for acceleration-dominated post-OL crack growth to occur in ductile materials, *without* the presence of time-dependent damage mechanisms. However, it would be important to extend the model to account for time-dependent processes like cavitation and oxidation, which contribute to high-temperature crack extension in many materials. Using a more detailed viscoplasticity model may also enable better agreement between computations and experiments. One improvement particularly relevant for fatigue crack growth is considering kinematic hardening, which can also introduce further rate dependence [217].

The results of this study indicate that using less rate-sensitive materials could enhance damage tolerance in applications where load transients are expected to be significant. However, there are additional complications that must be considered. Most importantly, highly creep-resistant alloys, such as Alloy 718, can often sustain higher crack-tip stresses over a longer period of time. As a result, time- and stress-dependent damage mechanisms, particularly grain boundary oxidation, are activated [29], [218]. In these cases, a potentially complex interplay between viscoplastic deformation, stress relaxation, grain boundary cavitation, dynamic embrittlement due to oxygen diffusion, stress-assisted grain boundary oxidation, and other time-dependent mechanisms may need to be considered [5]. Extending the current study by using one of these physically-based damage models in the CZM could help elucidate situations that may enhance enhance particular aspects of the OL response. Especially when these time-dependent damage mechanisms are activated, more complex loading waveforms containing hold times or multi-level block loading, should also be investigated. Oxide-induced crack closure and its influence on crack growth rates can also be an important consideration [66].

Although it was not the focus of this study, an interesting observation is that the computed steady-state crack growth rates depend non-monotonically on the material rate sensitivity. For example, in Figure 5.6, for the same applied load, the steady-state crack growth rate is highest for $m = 7.0$ and the lowest for $m = 5.0$. This contrasts with the trend for crack growth rates following OLs, with retardation becoming more significant with increasing creep exponent. This is conceptually similar to numerical results from Nielsen et al. [219], who used a steady-state numerical scheme to investigate the macroscopic fracture toughness for slow- and fast-growing cracks in rate-sensitive materials. The results showed a similar non-monotonic relationship: increased rate sensitivity increased the macroscopic toughness for slow cracks but decreased the macroscopic toughness for fast-growing cracks.

Finally, in general, the current study supports evidence that the material rate sensitivity is relevant to a variety of damage processes, including crack growth under monotonic loading [219], [220] and void growth and coalescence [214], [221], [222]. For example, Reboul et al. [214] found that the maximum accumulated plastic strain in a unit cell model containing a void increased with decreasing rate sensitivity. Similarly, in the current study, the accumu-

lated viscoplastic strain ahead of the crack tip increased for higher creep exponents (lower rate sensitivity). In the context of void growth, the increased plastic strain decreased the critical void volume fraction at which localization occurred. The authors in [214] also found that including isotropic strain hardening in the material response did not affect the trends of localization and void coalescence with respect to the rate sensitivity. This is again similar to the post-OL crack growth rates in the current study.

5.5 Conclusions

This study combined computations and experiments to investigate high-temperature fatigue crack growth following OLs. The finite element computations used a power-law viscoplasticity model for deformation in the bulk material and an irreversible cohesive zone model for material degradation ahead of the crack tip. A parametric study was first conducted to assess the influence of the material parameters on post-OL fatigue crack growth. The following conclusions are drawn from the parametric study:

- Post-OL crack growth rates depend strongly on the creep exponent m. Materials with low creep exponents (high rate sensitivity) show net acceleration. Materials with high creep exponent (low rate sensitivity) show net retardation.
- A transition between acceleration and retardation-dominated behavior occurs at creep exponent values characteristic of many solid solution strengthened alloys, including Alloy 617.
- Crack growth retardation is associated with higher local viscoplastic strain near the crack tip relative to the rest of the viscoplastic zone. This enhances compressive residual stress ahead of the crack tip, which disturbs the traction distribution.
- Strain hardening and the CZM damage parameters influence the magnitude of post-overload acceleration and retardation but not the trends with respect to the rate sensitivity.

The model was then applied to fatigue crack growth experiments on Alloy 617 at 800°C. The model was first calibrated to the crack growth rates from constant-amplitude loading

experiments at $f = 0.33$ Hz and applied to the experiments with OLs. The following conclusions are drawn from the experiments and the calibrated model:

- A single OL does not measurably affect crack growth rates.
- Blocks of 20 OLs can cause an acceleration-dominated or retardation-dominated response, depending on the baseline stress intensity factor range.
- Based on the parametric study, the creep exponent for Alloy 617 at 800°C is close to the transition between net acceleration and net retardation. This is in agreement with the close competition between acceleration and retardation observed in the experiments.
- The calibrated finite element model shows good agreement with the trends observed in the experiments, although the model predicts less severe acceleration and retardation than observed in the experiments.
- For Alloy 617 and similar materials, conventional overload models that assume crack growth retardation may be non-conservative.

6. TRANSIENT CREEP-FATIGUE CRACK GROWTH IN CREEP-BRITTLE MATERIALS: APPLICATION TO ALLOY 718

A version of this chapter is in preparation for submission to *Journal of Applied Mechanics* [223]: J.D. Pribe, H.E. Ostergaard, T. Siegmund, J.J. Kruzic, "Transient creep-fatigue crack growth in creep-brittle materials: Application to Alloy 718," *J Appl Mech*, In preparation.

6.1 Introduction

Alloy 718 is a precipitation-hardened alloy used in applications that require temperatures up to 650°C due to its good combination of toughness, strength, and creep resistance [21], [22]. Applications include gas turbine engines and nuclear power plants as well as other aerospace and nuclear applications frequently involving aggressive environments [21], [22], [25], [27]. In such applications, components are typically subjected to a combination of cyclic and sustained loads [29]. These loading waveforms also include load transients like OLs and hold times at multiple load levels. These transients arise due to both design loads (e.g., aircraft takeoff-cruise-landing cycles and load following requirements in power generation) and load excursions (e.g., turbulence) [13], [25], [34], [224]. Understanding crack growth following load transients is therefore important for predicting component lifetimes and determining inspection intervals in a damage-tolerant design approach [26], [34].

A large number of experimental studies have investigated steady-state crack extension in polycrystalline Alloy 718 under various mechanical and environmental conditions [22], [32], [225]. In general, these studies have successfully correlated crack growth rates with the stress intensity factor K for sustained loading and constant-amplitude cyclic loading [4], [22], [23], [77], [226]. This indicates that crack-tip conditions are uniquely described by K under these loading conditions. In the context of time-dependent fracture mechanics, Alloy 718 can be classified as a creep-brittle material: crack growth rates are sufficiently high, and the material is sufficiently resistant to creep deformation, that the viscoplastic zone grows with the advancing crack tip [5].

The specifics of the crack growth mechanism depend strongly on characteristics of the applied loading and the environment. The current study considers crack extension in polycrystalline Alloy 718 at 650°C in an air environment. Here, environmental damage due to preferential oxygen intrusion along grain boundaries ahead of the crack tip is significant [29], [32], [224], [227], [228]. The importance of environmental damage is demonstrated by significantly lower crack growth rates for tests in a vacuum environment compared with tests in air, particularly under sustained loading [29], [32], [224]. During cyclic loading in air, environmental damage causes crack growth behavior to depend strongly on the loading frequency [23]. Below a loading frequency of about $f = 0.01$ to 0.1 Hz, time-dependent environmental damage is dominant, indicated by a fully intergranular crack path [4], [22], [29]. Cyclic crack growth rates have been correlated with the maximum cyclic stress intensity factor $K_{\max}$ in this situation [77], [229]. At frequencies above $f \approx 1.0$ Hz, cycle-dependent fatigue damage is dominant, and the crack path is transgranular [4], [22]. In this case, cyclic crack growth rates have been correlated with the cyclic stress intensity factor range [225], [229]. Crack growth rates tend to increase with decreasing frequency, as the environmental damage mechanism becomes more dominant [225]. The high crack growth rates under sustained loads and low-frequency cyclic loading in air are due to oxygen-induced grain boundary embrittlement, but the precise mechanism is disputed [218], [230]. Some studies suggest that oxides form on the grain boundaries and subsequently crack, typically referred to as a stress-assisted grain boundary oxidation [31], [231]. Others suggest that elemental oxygen ingress lowers grain boundary cohesion through a dynamic embrittlement mechanism, leading to brittle failure before oxides can form [231]–[233]. Regardless of the active mechanism, a tensile stress on the grain boundary enhances the damage process [31], [230].

Several experimental studies have also investigated crack growth following OLs in polycrystalline Alloy 718 at 650°C. The loading waveforms have generally been inspired by aircraft turbine engine load spectra [26]. This includes sustained loads interrupted by an OL with a hold time at higher load [34] and trapezoidal waveforms with an OL prior to the hold-time portion of the cycle [25], [30], [33]. In each case, crack growth retardation occurred in the experiments. For sustained loads, a delay effect was observed following unloading from the OL back to the initial sustained load for both of the OL ratios that were considered

(1.2 and 1.5) [34]. The OL ratio was found to be the main factor influencing the amount of retardation, with longer delay times and the possibility of crack arrest being observed for OL ratio 1.5. For a trapezoidal waveform, the OL eliminated the detrimental effect of the hold time, so long as OL ratios above approximately 1.2 were considered [30], [33]. Similar results have been observed for other precipitation-hardened, creep-brittle alloys [26], [208], [210].

Explanations and phenomenological models for post-OL retardation have followed well-known approaches for rate-independent materials, especially the Willenborg model for crack growth following OLs [44]. This involves defining an effective stress intensity factor or load ratio during crack extension through the OL viscoplastic zone, based on compressive residual stress generated by the OL. Adding one or more fitting parameters to this basic framework of the Willenborg model has provided reasonable agreement with experiments [26], [33], [34], [48]. This approach has the advantage of being straightforward to apply in design situations, without requiring computationally-expensive simulations [26]. However, a key challenge is that a variety of different waveforms containing OLs may be relevant for realistic load spectra. Recalibrating the model or adding more fitting parameters may be necessary to capture the specific characteristics of crack growth retardation associated with each waveform [48]. Finite element and strip yield models are two approaches that enable consideration of arbitrary waveforms. Several studies have used these methods to analyze crack-tip fields in bodies with stationary cracks subjected to trapezoidal waveforms containing OLs. These have demonstrated reduced stresses ahead of the crack tip during the hold time after the OL [25], [30], [83]. Bouvard et al. [88] considered OLs during 5-Hz cyclic loading of a single-crystal Ni-based superalloy. These authors used finite element computations with a cohesive zone model that accounted for both cyclic and time-dependent damage. The computations predicted crack growth retardation that became more significant with increasing number of OLs. However, these results were not compared with specific experiments, and trends with respect to different waveforms and OL ratios were not investigated. This approach has also been applied to describe damage due to dynamic embrittlement, grain boundary sliding, and thermomechanical fatigue [89], [123], [124].

In the current study, finite element computations were conducted that combined a viscoplasticity model for the bulk material and a CZM to describe material degradation and crack extension. The computations could thereby predict crack extension and the crack-tip fields for various waveforms containing OLs. The viscoplasticity model is based on the Kocks-Mecking formalism [105], [106], [110]. Using this formulation, the computations account for dislocation storage and dynamic recovery in the evolving crack-tip viscoplastic zone. These processes are considered to be relevant since the viscoplastic zone is contained near the crack tip in creep-brittle materials like Alloy 718. In this situation, details of the hardening process when viscoplastic deformation is activated are expected to influence the crack-tip fields as the crack extends. Formulations based on the Kocks-Mecking approach have also been previously applied to precipitation-hardened materials like Alloy 718 [97], [106], [234], [235]. The model included the influence of hardening due to plastic strain gradients through the inclusion of GNDs [85], [93], [97]. The CZM captured subcritical material degradation through the use of a phenomenological stress- and time-dependent damage evolution equation [88], [89]. This was chosen based on the observed stress and time dependence of the environmentally-enhanced intergranular damage and crack extension in Alloy 718 [31], [32], [224].

The following research questions are addressed in this study:

- How do OLs affect crack extension when time-dependent damage is significant?
- How can these results help interpret experiments on Alloy 718 and similar creep-brittle materials?
- What is the role of dynamic recovery and hardening due to GNDs on these outcomes?

To address these questions, the model was first calibrated to experimentally-determined steady-state crack growth rates for polycrystalline Alloy 718 at 650°C in laboratory air. Subsequent computations considered three different waveforms containing OLs: cyclic loading with OLs, sustained loading interrupted by an OL, and a trapezoidal waveform with an OL prior to the hold time in each cycle. The last two waveforms allow comparisons with the experiments of Nicholas et al. [47], Weerasooriya and Nicholas [33], and Ponnelle et al. [30].

To investigate the role of dynamic recovery and GNDs, separate computations neglecting each mechanism were conducted for both steady-state and post-OL crack extension. These were compared with the predictions from computations with the full SGKM model.

6.2 Model description

The model geometry consisted of a symmetric modified boundary layer model similar to Chapter 3 and shown in Figure 6.1. This approach is justified for Alloy 718 since viscoplastic strains are confined to a region closely surrounding the crack tip, and small-scale creep conditions are applicable [203]. Displacements corresponding to the mode I stress intensity factor were applied to the outer nodes of the model [145]. Symmetry was enforced about the crack plane along the bottom of the model. The point $x = 0$ corresponds to the initial crack tip. The boundary layer model consisted of 9244 linear plane strain elements in the bulk material and 246 cohesive elements along the crack line ahead of the initial crack tip. The radius of the modified boundary layer model was $R_{\mathrm{MBL}} = 20.0$ mm; the maximum crack extension was $\Delta a_{\max} = 222$ μm; and the element size in the fine-meshed region was 1.0 μm. The predicted crack extension agreed with computations using a smaller element size of 0.5 μm, and this element size resolved the active cohesive zone. To ensure post-OL crack extension and crack-tip fields could be analyzed in detail, larger element sizes were not considered. Computations were terminated when the crack reached the end of the refined mesh region.

This study used the SGKM model described in Section 2.1.2 for deformation in the bulk material. The irreversible CZM described in Section 2.2.1 was used for the cohesive elements. Stress- and time-dependent damage in the CZM was described by the Rabotnov-Kachanov-type damage formulation in Eq. (2.26). Rate-independent fatigue damage was not considered.

6.2.1 Model parameters

The viscoplasticity parameters of the SGKM model are given in Table 6.1 and approximate the behavior of Alloy 718 at 650°C, following [97]. The elastic properties were $E = 165$

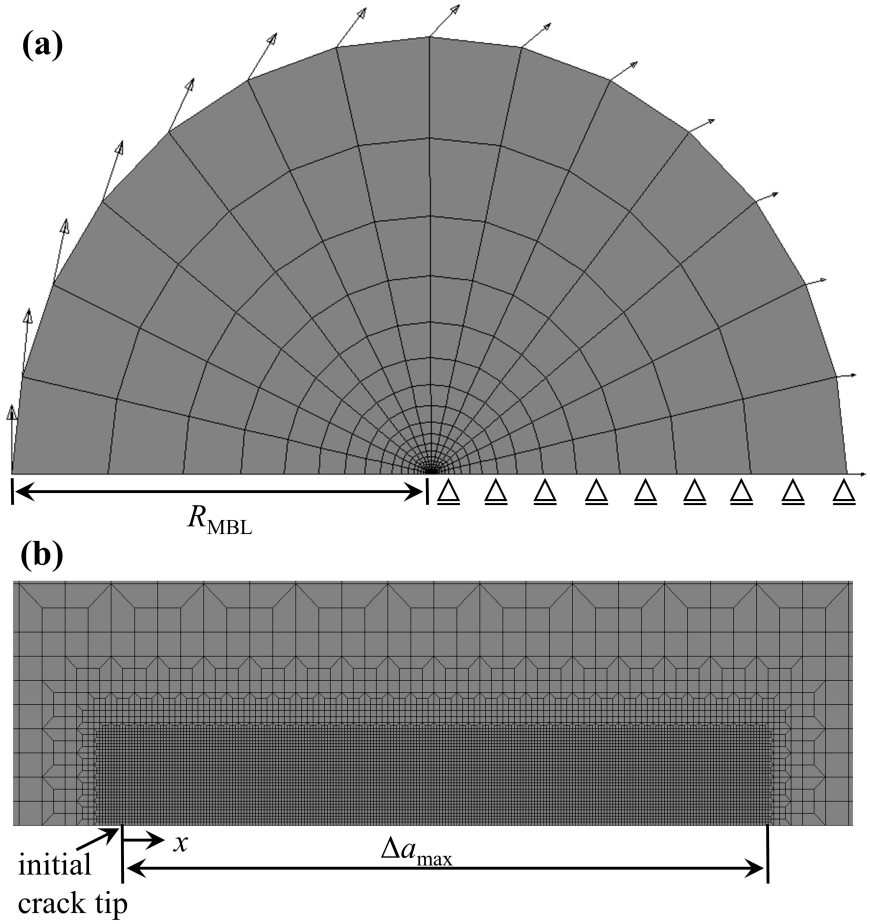

Figure 6.1. (a) Global mesh with displacement boundary conditions. (b) Refined crack-tip mesh.

Table 6.1. Property values for SGKM model.

σ_0 (MPa)	m	n	k_1 (mm^{-1})	k_{20}	M	α	b (nm)	$\dot{\varepsilon}_0$ (s^{-1})	ρ_0 (mm^{-2})
779	25	5	8×10^5	28.29	1.73	0.3	0.25	0.001	10^5

GPa and $\nu = 0.3$. In [97], the elastic-viscoplastic properties were chosen based on the work of Iyer and Lissendon [236]. Strengthening associated with precipitation hardening from the γ'' and γ' phases is accounted for within σ_0 [106]. The parameters associated with dislocation evolution, as well as an initial dislocation density ρ_0, were chosen within a reasonable range from references [105]–[107], [110].

In the cohesive zone, the parameters $\sigma_{\text{max},0}$ and δ_0 were interpreted as setting the stiffness of the CZM. These were set to $\sigma_{\text{max},0} = 10^4$ MPa and $\delta_0 = 0.002$ mm, as in Chapter 5. In the time-dependent damage formulation, the traction threshold was set to $T_c = 1200$ MPa (or approximately $1.54\sigma_0$) based on the analysis in [31] of stresses where stress-assisted intergranular oxidation becomes significant for nickel oxides. The remaining time-dependent damage parameters (C_c and r) were calibrated using experimentally-measured steady-state crack growth rates. Waveforms containing OLs were studied using the calibrated model. Specific characteristics of these waveforms are presented in subsequent sections.

6.3 Results

The model was first calibrated using the results of crack growth experiments on polycrystalline Alloy 718 compact tension specimens specimens at 650°C in laboratory air. The experiments used sustained loading and constant-amplitude cyclic loading waveforms. The cyclic loading was conducted at a frequency of $f = 0.1$ Hz and a load ratio of $R = K_{\text{max}}/K_{\text{min}} = 0.5$. More information on the experimental procedure can be found in [90]. Figure 6.2 shows the measured time-dependent crack growth rates $\mathrm{d}a/\mathrm{d}t$ together with the predicted values from the calibrated model. Crack growth rates are shown as a function of the stress intensity factor K for sustained loading and the maximum stress intensity factor K_{max} for cyclic loading. To calibrate the model, the damage exponent r was chosen such that the predicted slope of the $\mathrm{d}a/\mathrm{d}t$ versus K curve agreed with the experiments. The parameter C was chosen

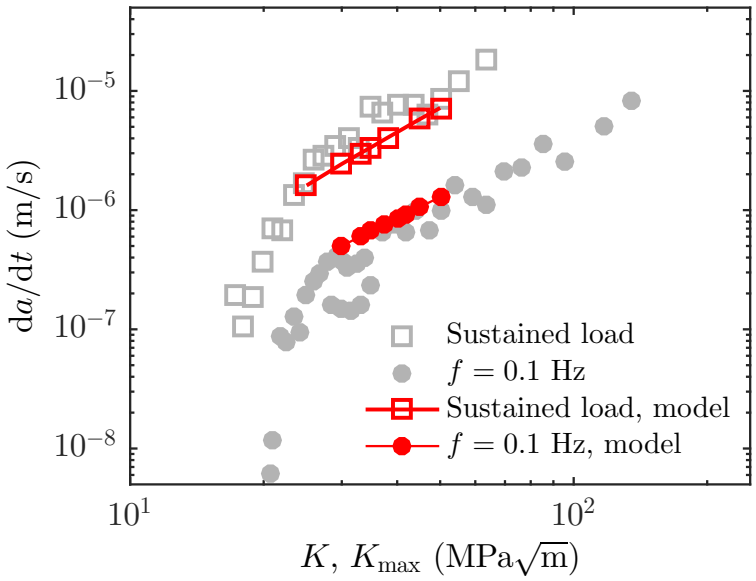

Figure 6.2. Time-dependent crack growth rates $\mathrm{d}a/\mathrm{d}t$ as a function of the stress intensity factor K for sustained loading and the maximum stress intensity factor $K_{\max}$ for constant-amplitude cyclic loading (double log scale). Results are shown for experiments and the calibrated model. Experiments conducted by H.E. Ostergaard.

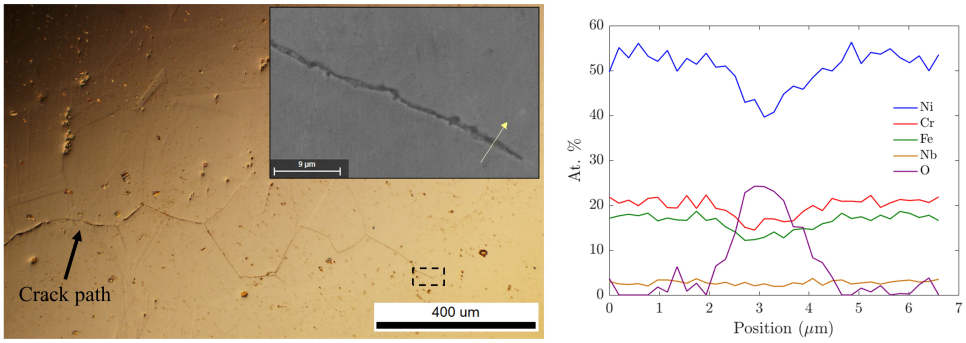

Figure 6.3. Damaged grain boundary in an Alloy 718 specimen subjected to cyclic loading. (a) Optical micrograph of the crack profile, with an enlarged SEM micrograph shown in the inset. (b) EDS line scan along the arrow in the inset in (a), demonstrating oxidation damage.

such that the numerical values of the crack growth rates aligned with the experiments. This process resulted in estimates of $r = 4.5$ and $C_c = 3500$ MPa·s$^{1/r}$, with $T_c = 1200$ MPa as noted in Section 6.2.1. The calibrated model shows good agreement with the experimentally-measured crack growth rates for both sustained loading and cyclic loading. This indicates that, in all cases considered here, time-dependent damage is dominant. Further evidence for time-dependent oxygen-drive crack growth is found in observations of fully-intergranular crack paths in the experimental samples. For example, Figure 6.3 shows a grain boundary demonstrating oxidation damage in a specimen subjected to cyclic loading. Next, the calibrated model was used to investigate several different waveforms containing OLs.

6.3.1 Overloads during cyclic loading

The model was next applied to the case of OLs during cyclic loading, with the loading waveform shown in Figure 6.4. The loading frequency $f = 0.1$ Hz and load ratio $R = 0.5$ were maintained during constant-amplitude loading and the OL cycles. A range of OL ratios between $R_{\text{OL}} = K_{\text{OL}}/K_{\text{max}} = 1.1$ and 1.5 were considered, with $K_{\text{max}} = 35.0$ MPa$\sqrt{\text{m}}$. Figure 6.5 shows the predicted crack extension for computations considering 1 and 3 OLs at five different OL ratios. The model predicts crack growth retardation occurs in all cases. The OL-induced retardation persists over a larger number of cycles for higher OL ratios.

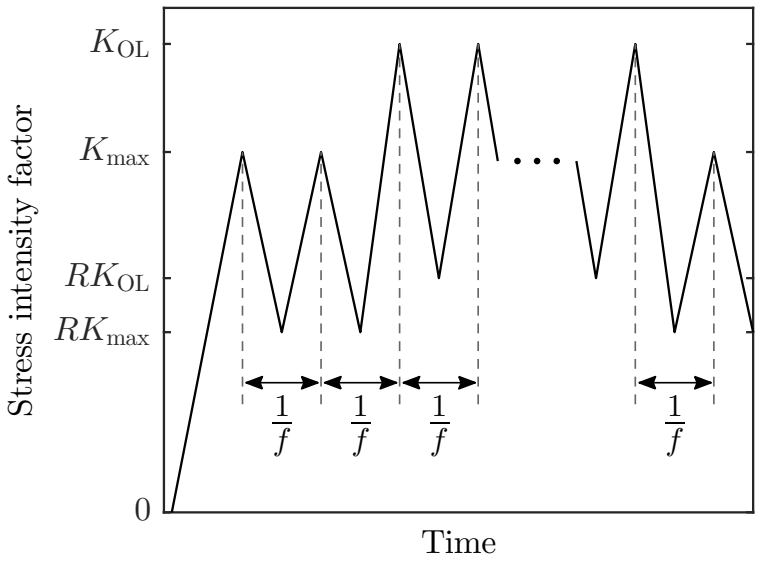

Figure 6.4. Schematic of the loading waveform for cyclic loading with OLs. The cyclic frequency f and load ratio R were constant for all cycles, including the OLs.

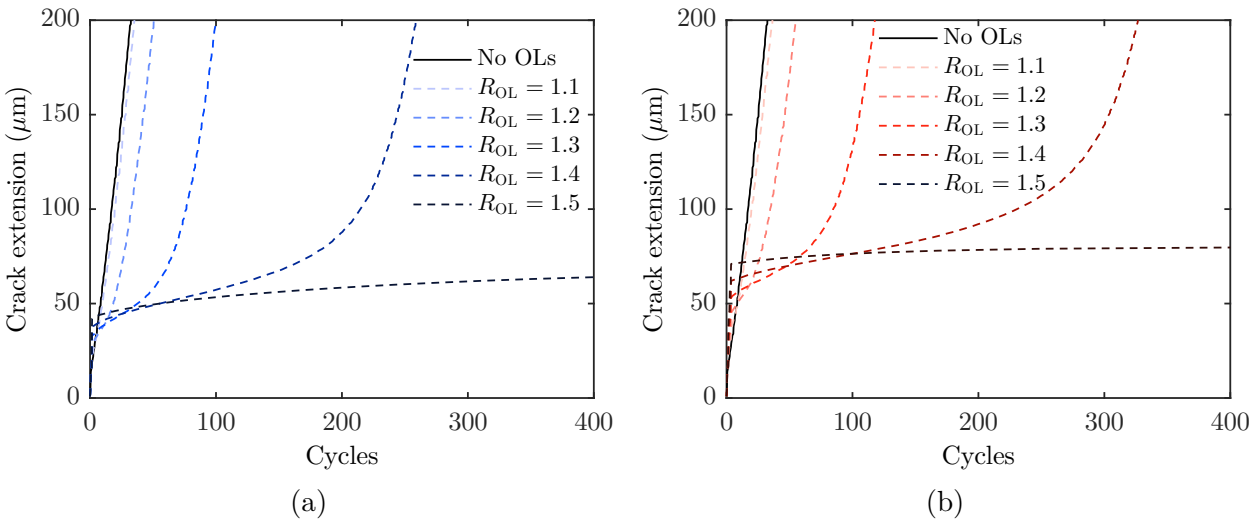

Figure 6.5. Predicted crack crack extension for cyclic loading with OLs at several OL ratios. (a) 1 OL and (b) 3 OLs. For both cases, the crack arrests in the computation with $R_{\mathrm{OL}} = 1.5$.

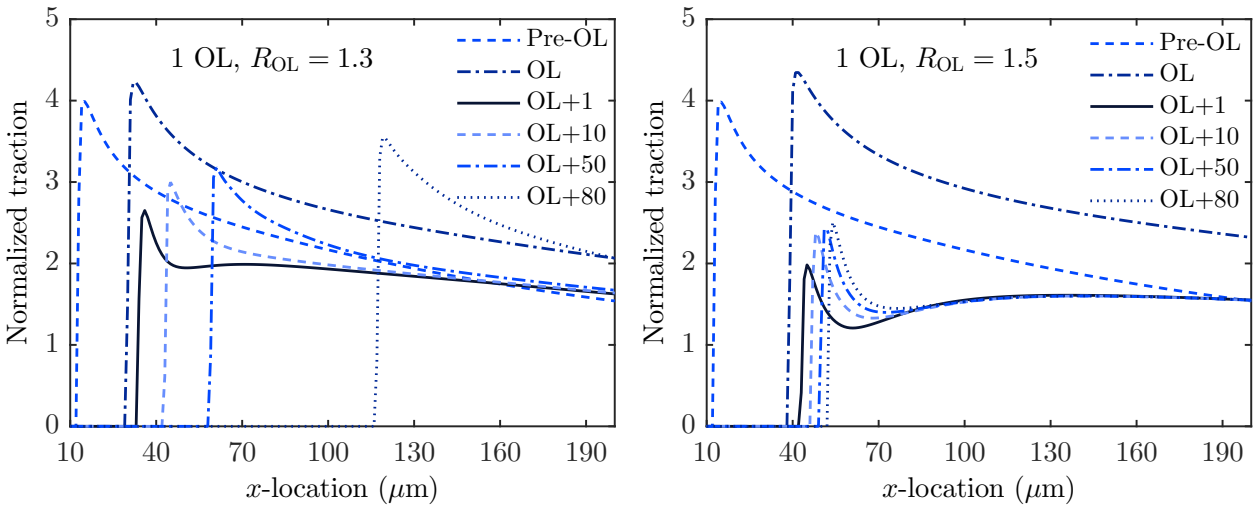

Figure 6.6. Predicted traction distributions in the cohesive zone normalized by the reference stress σ_0 for computations with 1 OL. (a) $R_{OL} = 1.3$, (b) $R_{OL} = 1.5$. Distributions are shown at maximum load during six different cycles: constant-amplitude loading before the OL; the OL cycle; and 1, 20, 50, and 80 cycles after the OL.

Retardation becomes especially significant above an OL ratio of about $R_{OL} = 1.2$. In all cases, applying multiple OLs causes stronger retardation compared to a single OL. For $R_{OL} = 1.5$, the crack arrests after a small amount of crack growth following the OL(s). Arrest occurs at a total crack extension of 67 μm for 1 OL and 80 μm for 3 OLs.

Figure 6.6 shows the computed traction distributions ahead of the crack tip at maximum load during several different cycles for computations with a single OL and OL ratios of 1.3 and 1.5. During crack growth before the OL, the traction distribution follows the form typically observed for elastic-plastic and elastic-viscoplastic solids. Following the OL, the traction magnitude is lower near the crack tip, and the shape of the distribution significantly changes. Most prominently, there is a clear local minimum in the traction beyond the crack tip. Crack growth retardation occurs as the crack extends through the region surrounding this local minimum. For $R_{OL} = 1.3$, the local minimum is seen during the first cycle after the OL. The traction distribution gradually returns toward the shape of the steady-state distribution in subsequent cycles, and the steady-state crack growth rate is recovered. For $R_{OL} = 1.5$, the overall magnitude of the traction is reduced over a larger region compared

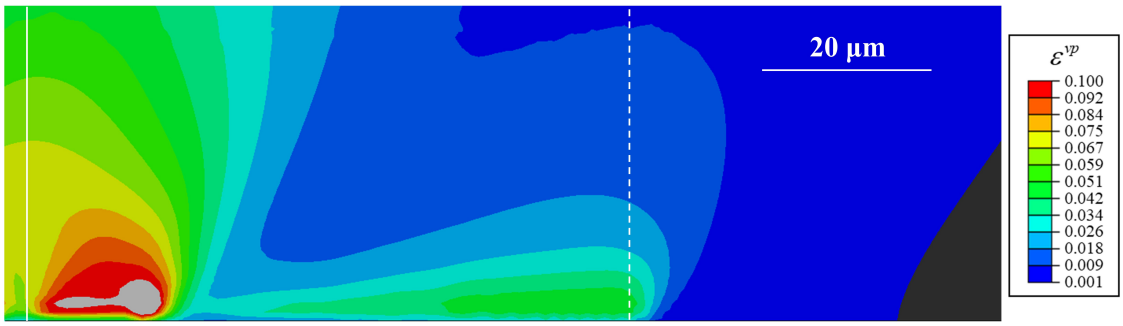

Figure 6.7. Equivalent plastic strain contours for cyclic loading at $K_{\max} = 35.0$ MPa$\sqrt{\text{m}}$ with 1 OL and $R_{\text{OL}} = 1.3$. Contours are shown on the undeformed mesh at maximum load in the 70th cycle after the OL. The solid line marks the location of the crack tip at the beginning of the OL cycle. The dashed line marks the current location of the crack tip.

to the case of $R_{\text{OL}} = 1.3$. The local minimum in the traction is also more pronounced, and it persists over a larger number of cycles. Crack extension only continues through the region that was damaged during the OL. The traction beyond this damaged region is not sufficient to cause further damage evolution. This ultimately results in crack arrest.

Figure 6.7 shows accumulated viscoplastic strain contours at maximum load 70 cycles after the OL for $R_{\text{OL}} = 1.3$. During steady-state crack growth, the viscoplastic zone advances with the growing crack and is contained near the crack tip, consistent with creep-brittle behavior. There is a clear increase in the viscoplastic strain near the crack tip when the OL was applied. The higher viscoplastic strain magnitude persists over the increment in crack extension during the OL. More significant viscoplastic deformation near the crack tip during the OL substantially alters the crack-tip fields in subsequent cycles. The highly-deformed region near the crack tip undergoes significant unloading, as seen in the suppressed post-OL tractions in Figure 6.6. These changes in the crack-tip fields cause the post-OL retardation observed in Figure 6.5. As crack extension continues, the steady-state viscoplastic zone gradually reforms.

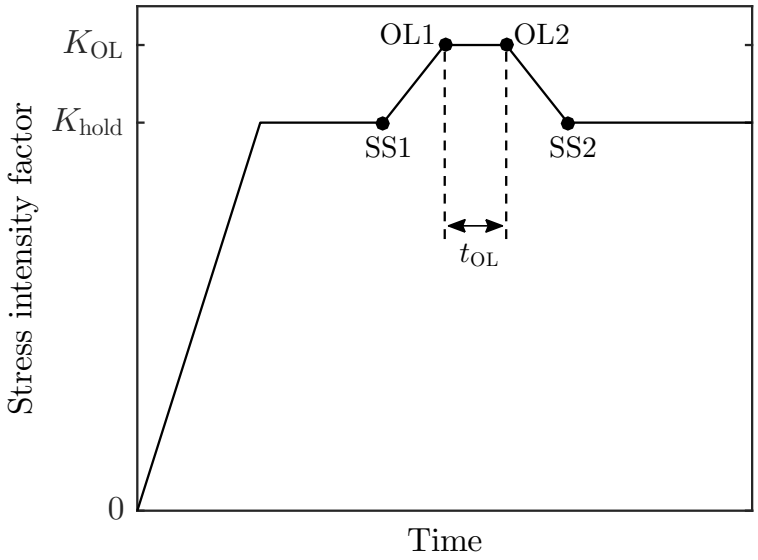

Figure 6.8. Waveform used for sustained loading computations with OLs. In all cases, $K_{hold} = 30.0$ MPa$\sqrt{\text{m}}$. The labeled points are used for subsequent figures with traction distributions.

6.3.2 Overloads during sustained loading

Sustained loading interrupted by an OL is now considered. The waveform used in these computations is shown in Figure 6.8. All computations began with a 10-second hold time at K_{hold} to minimize interactions between the OL viscoplastic zone and the viscoplastic zone associated with crack growth initiation. Regardless of the OL ratio, the ramp time while applying and removing the OL was 5 s. The OL load level was sustained for a hold time $t_{OL} = 0$ or 5 s. The load then returned to K_{hold} at the same loading rate for the remainder of the computation. A range of overload ratios between $R_{OL} = 1.1$ and 1.5 was considered.

Figure 6.9 shows crack extension for several OL ratios, with OL hold times of $t_{OL} = 0$ and 5 s. Crack extension for sustained loading with $K = K_{hold}$ is included for comparison. Crack growth retardation occurs in all cases. Adding a hold time at the OL load level of $t_{OL} = 5$ s enhances the crack growth retardation, especially for high OL ratios. For both $t_{OL} = 0$ and $t_{OL} = 5$ s, the retardation drastically increases at OL ratios above approximately 1.2. At high OL ratios, there is a substantial period of time following the OL where almost no crack growth occurs. The shape of the post-OL crack extension curves also changes for $R_{OL} = 1.4$ with $t_{OL} = 0$ and for both $R_{OL} = 1.35$ and 1.4 with $t_{OL} = 5$ s. Upon the resumption

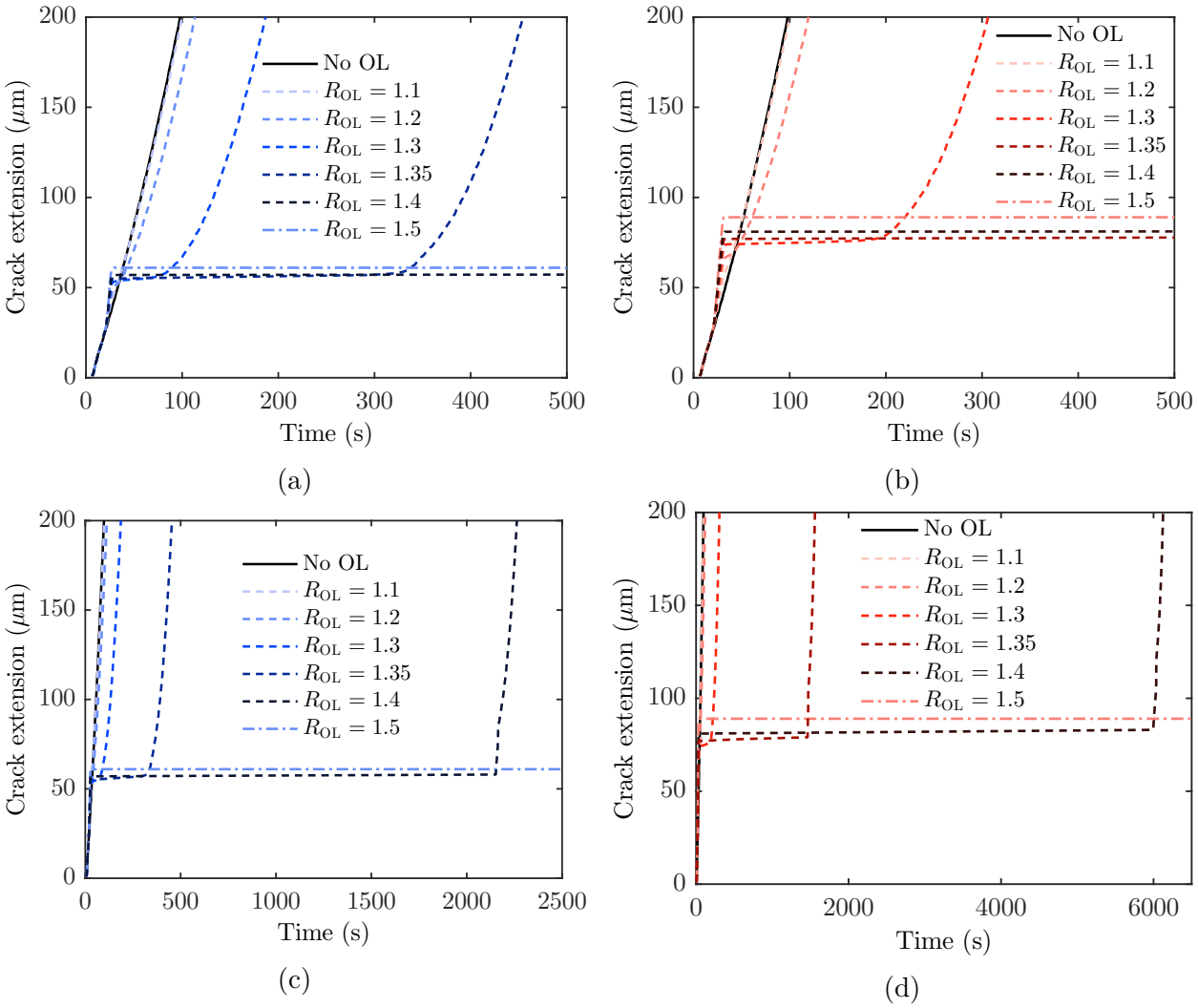

Figure 6.9. Predicted crack crack extension for sustained loading with OLs and several OL ratios. (a) $t_{OL} = 0$ and (b) $t_{OL} = 5$ s. For both cases, the computations with $R_{OL} = 1.5$ do not predict further crack extension after the OL. (c) and (d) are widened versions of (a) and (b), respectively, to show continued crack extension for $R_{OL} = 1.4$.

of crack extension after the OL, several elements fail nearly simultaneously as shown by a sudden jump in the predicted crack extension for these cases in Figure 6.9c and d. For $R_{\mathrm{OL}} = 1.5$, no further crack extension occurs after the OL during computations extending to 20000 seconds with both $t_{\mathrm{OL}} = 0$ and $t_{\mathrm{OL}} = 5$ s. However, the model predicts that post-OL damage accumulation does continue in the elements ahead of the crack tip, albeit very slowly ($\dot{D} < 10^{-4}$ 1/s). The continued damage accumulation suggests that the crack may not fully arrest.

Figure 6.10 shows the traction distributions at various time points for three cases: $t_{\mathrm{OL}} = 0$ and $R_{\mathrm{OL}} = 1.3$, $t_{\mathrm{OL}} = 0$ and $R_{\mathrm{OL}} = 1.5$, and $t_{\mathrm{OL}} = 5$ s and $R_{\mathrm{OL}} = 1.3$. Similar to the case of cyclic loading, the traction distribution before the OL is typical of elastic-plastic and elastic-viscoplastic materials. An important feature of the traction distribution is the suppressed crack-tip stress concentration. Here, unloading after the OL reduces the traction ahead of the crack tip, but the pronounced local minimum seen following OLs during cyclic loading is not present. For higher OL ratios, the traction peak ahead of the crack tip is nearly eliminated, Figure 6.10b. The nearly flat traction distribution for high OL ratios helps to explain the sudden resumption of crack growth for $R_{\mathrm{OL}} = 1.4$ observed in Figure 6.9c and d. As the post-OL traction distribution becomes flatter, the damage evolution becomes nearly uniform over a region ahead of the crack tip. As a result, failure occurs nearly simultaneously in several elements when crack growth resumes. After crack growth resumes, the traction distribution returns toward the steady-state shape. For $R_{\mathrm{OL}} = 1.5$, the traction distribution is virtually unchanged during the subsequent hold at constant load due to the slow damage accumulation. The stress is also sufficiently low in the bulk material due to unloading following the OL to preclude further viscoplastic deformation.

6.3.3 Overloads with a trapezoidal waveform

A trapezoidal waveform with an OL applied before each hold time, as shown in Figure 6.11, is now considered. At the beginning of each cycle, the load was increased to $K_{\mathrm{OL}} = R_{\mathrm{OL}} K_{\mathrm{hold}}$. The load was then decreased to K_{hold}, held constant for a time of t_{hold}, and finally decreased to RK_{OL}. As indicated in Figure 6.11, the loading rates in the un-

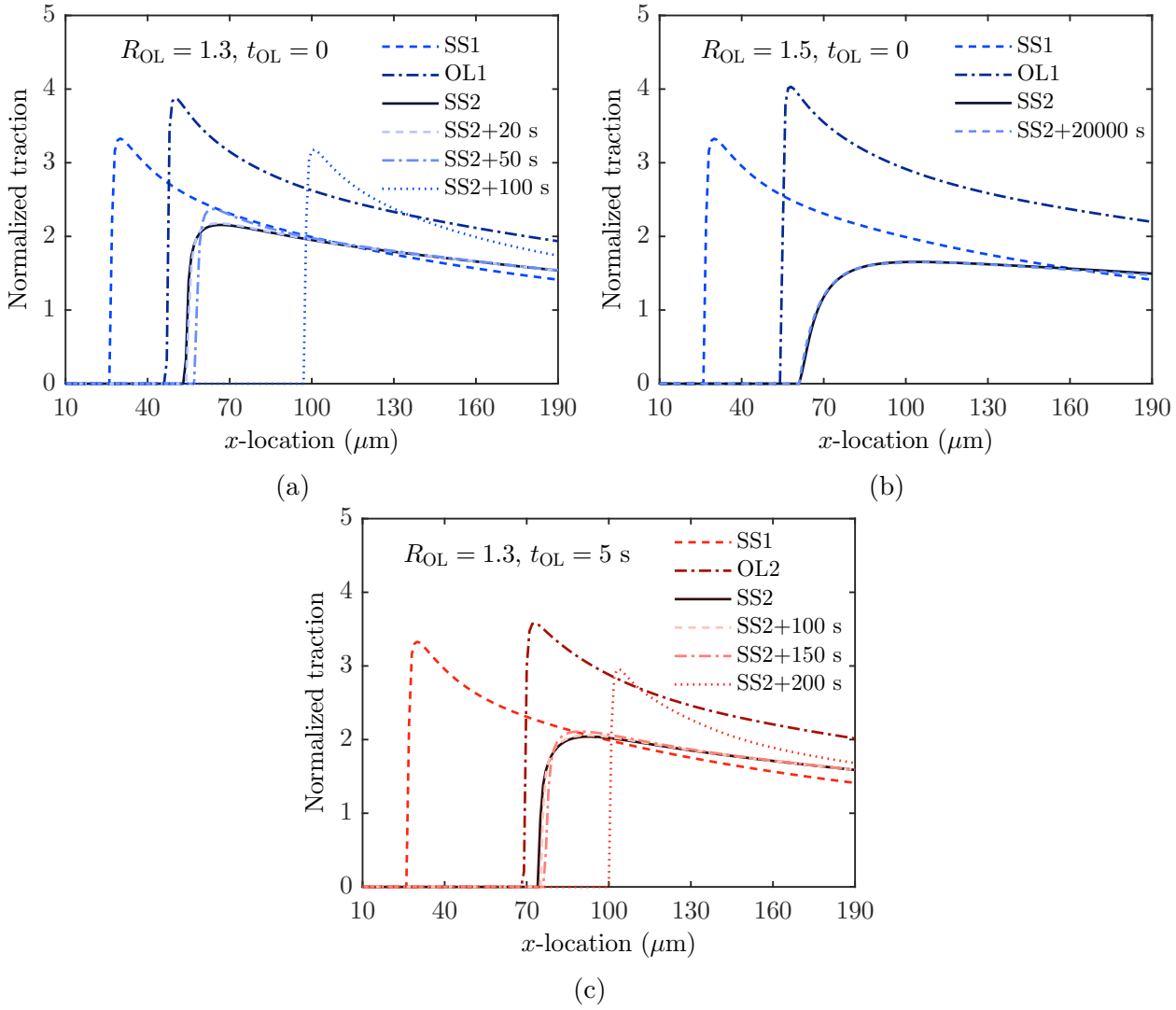

Figure 6.10. Predicted traction distributions in the cohesive zone normalized by the reference stress σ_0 for computations with sustained loading interrupted by an OL. (a) $t_{OL} = 0$ and $R_{OL} = 1.3$. (b) $t_{OL} = 0$ and $R_{OL} = 1.5$. (c) $t_{OL} = 5$ s and $R_{OL} = 1.3$ Distributions are shown at time points indicated in Figure 6.8, as well as additional time points following the return to steady-state loading at K_{hold} (i.e., after the point SS2).

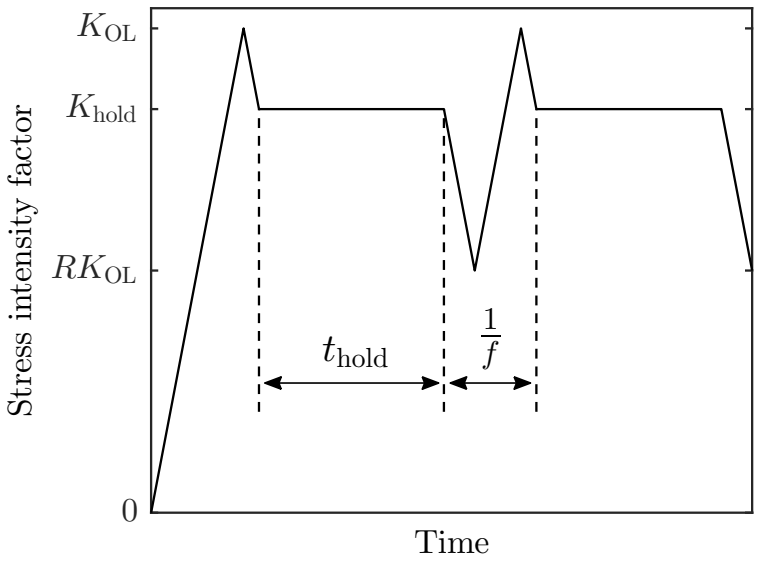

Figure 6.11. Waveform used for trapezoidal loading simulations with OLs. In all cases, the loading frequency was $f = 0.1$ Hz, the load ratio was $R = 0.5$, and $K_{\mathrm{hold}} = 30.0$ MPa$\sqrt{\mathrm{m}}$.

loading/reloading portions of each cycle matched the constant-amplitude cyclic loading with frequency $f = 0.1$ Hz. The computations used $K_{\mathrm{hold}} = 30$ MPa$\sqrt{\mathrm{m}}$ and a range of OL ratios between $R_{\mathrm{OL}} = 1.1$ and 1.5.

To investigate the influence of the OLs, two comparisons are relevant. The first is the cyclic crack growth rate $\mathrm{d}a/\mathrm{d}N$ for computations using constant-amplitude cyclic loading with $K_{\mathrm{max}} = K_{\mathrm{OL}}$. This represents the waveform shown in Figure 6.11 with the hold time removed. The second is a linear summation of this cyclic crack growth rate and the contribution of the hold time. The hold-time contribution was calculated as [33]

$$\left(\frac{\mathrm{d}a}{\mathrm{d}N}\right)_{\mathrm{hold}} = \frac{\mathrm{d}a}{\mathrm{d}t} t_{\mathrm{hold}} \tag{6.1}$$

with $\mathrm{d}a/\mathrm{d}t = 2.44 \times 10^{-6}$ m/s for $K_{\mathrm{hold}} = 30$ MPa$\sqrt{\mathrm{m}}$. This summation represents an upper bound on crack growth rates. It assumes there are no interaction effects between the OL and the subsequent hold time.

Figure 6.12 shows the predicted cyclic crack growth rates for this waveform with hold times of $t_{\mathrm{hold}} = 10$ s and 20 s and several OL ratios. The two comparisons described previ-

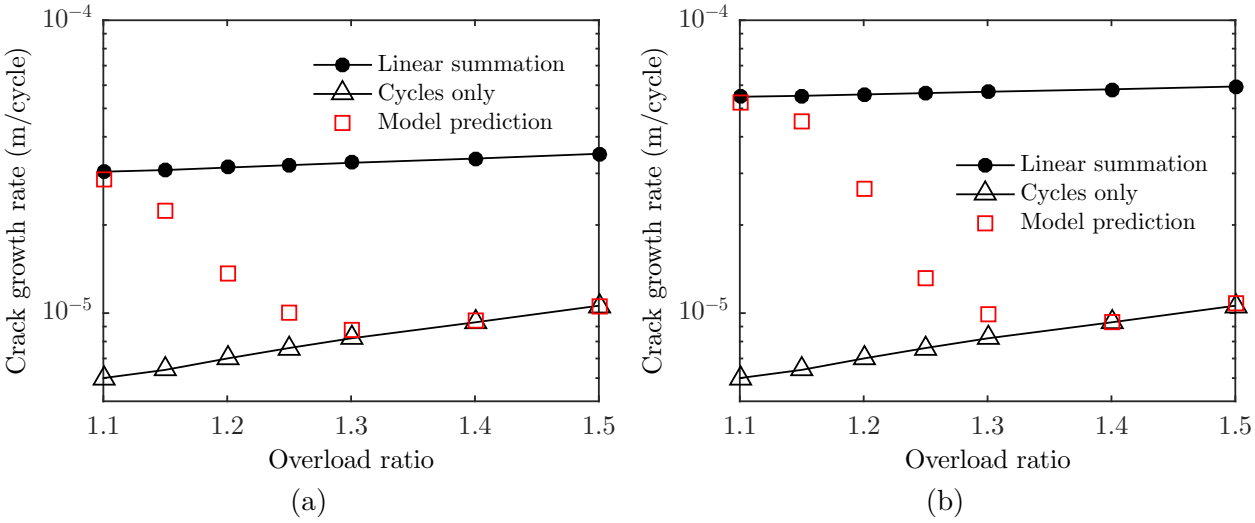

Figure 6.12. Predicted crack growth rates for the trapezoidal waveform as a function of the OL ratio with (a) $t_{\text{hold}} = 10$ s and (b) $t_{\text{hold}} = 20$ s. The linear summation and constant-amplitude crack growth rates are included for comparison. For higher OL ratios, the hold time contributes less to the crack growth rate.

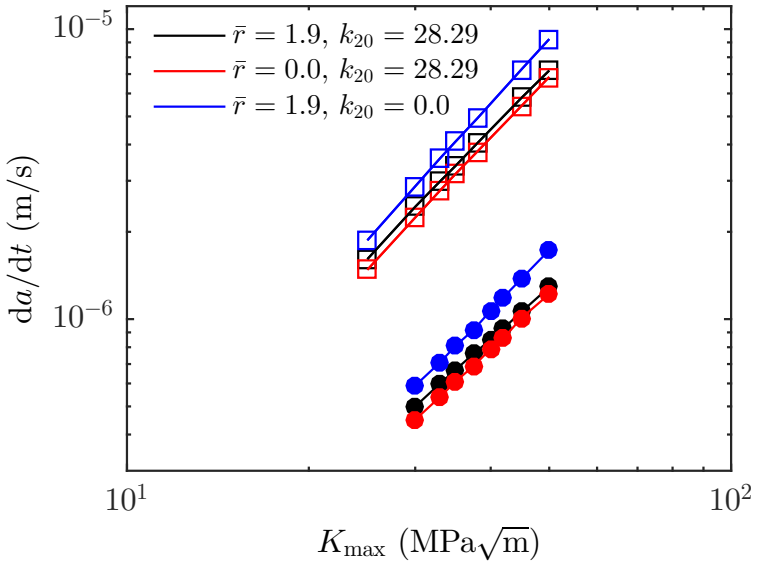

Figure 6.13. Predicted time-dependent crack growth rates $\mathrm{d}a/\mathrm{d}t$) as a function of the stress intensity factor using the full SGKM model (shown before in Figure 6.2); neglecting GNDs ($\bar{r} = 0.0$); and neglecting dynamic recovery ($k_{20} = 0.0$). Square symbols are for sustained loading; round symbols are for constant-amplitude cyclic loading with $f = 0.1$ Hz.

ously are also included in the figures as "Cycles only" and "Linear summation", respectively. For low OL ratios, the model predicts that the OLs only slightly reduce crack growth rates below the upper bound given by the linear summation. Increasing the OL ratio beyond approximately $R_{\mathrm{OL}} = 1.15$ begins to significantly reduce the crack growth rates. For $R_{\mathrm{OL}} = 1.3$, crack growth during the hold time is nearly eliminated for $t_{\mathrm{hold}} = 10$ s, but there is a greater increase in crack growth rates for $t_{\mathrm{hold}} = 20$ s. For $R_{\mathrm{OL}} \geq 1.3$, the predicted crack growth rates are nearly equal to the purely cyclic crack growth rates for both hold times. This indicates that the detrimental effect of the hold time is completely eliminated for high OL ratios.

6.3.4 Dynamic recovery and GNDs

Computations were conducted to separately investigate the roles of dynamic recovery and GNDs on steady-state and post-OL crack growth. Figure 6.13 shows the predicted steady-state crack growth rates for three cases: the original SGKM model, a modified model

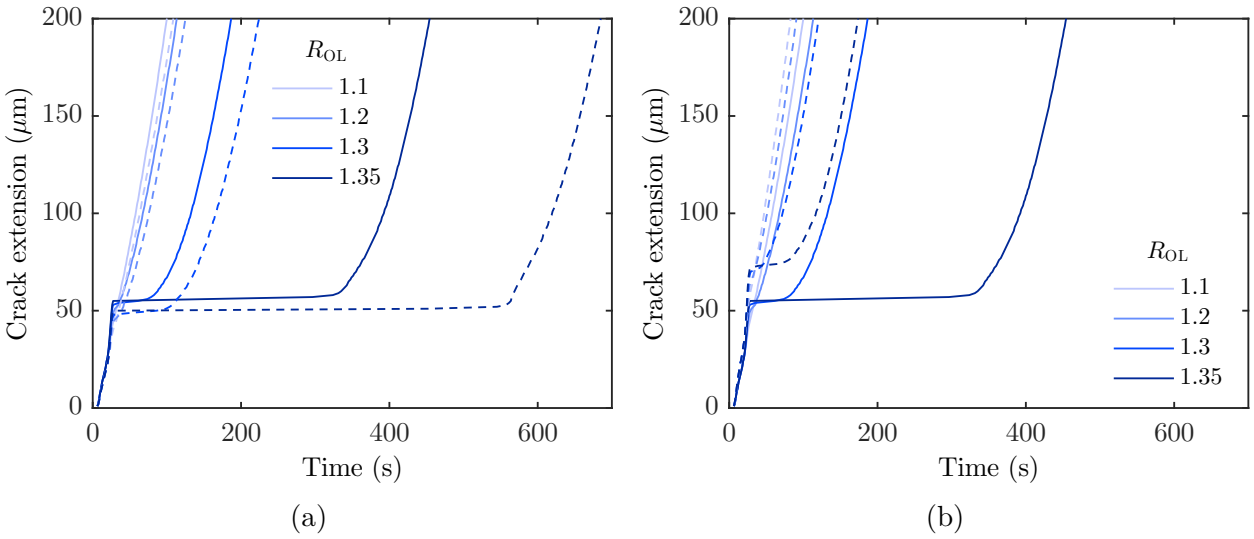

Figure 6.14. Predicted crack crack extension for sustained loading with OLs and several OL ratios investigating the influence of GNDs and dynamic recovery. Solid lines are predictions from the full SGKM model (shown before in Figure 6.9). Dashed lines are (a) $\bar{r} = 0.0$ (neglecting GNDs) and (b) $k_{20} = 0.0$ (neglecting dynamic recovery).

neglecting GNDs ($\bar{r} = 0.0$) but retaining dynamic recovery, and a modified model neglecting dynamic recovery ($k_{20} = 0.0$) but retaining GNDs. For each case, the computations considered sustained loading and constant-amplitude cyclic loading. The calibrated parameters were used in the CZM for all computations. The crack growth rates for the full SGKM model are the same as those shown in Figure 6.2. Neglecting GNDs leads to slightly lower predicted crack growth rates. Neglecting dynamic recovery leads to slightly higher predicted crack growth rates.

The role of GNDs and dynamic recovery in post-OL crack growth was investigated using the waveform described in Section 6.3.2. The crack extension predictions are shown in Figure 6.14 for OL ratios up to $R_{OL} = 1.35$ Both mechanisms significantly affect post-OL crack growth, especially for high OL ratios. Neglecting GNDs enhances the predicted retardation. The model predicts stronger crack-tip viscoplastic deformation and therefore lower tractions after the OL, leading to stronger retardation without hardening due to GNDs. Neglecting dynamic recovery has the opposite effect, as the predicted retardation is less significant. Dynamic recovery serves as a stress relaxation mechanism, enhancing the development of

Table 6.2. Delay time in seconds for sustained loading interrupted by an OL with several OL ratios, $t_{\text{hold}} = 0$, and $K_{\text{hold}} = 30$ MPa$\sqrt{\text{m}}$. Delay times are compared for the full SGKM model, the model neglecting GNDs, and the model neglecting dynamic recovery.

R_{OL}	1.1	1.2	1.3	1.35	1.4	1.45	1.5
$\bar{r} = 1.9$, $k_{20} = 28.29$	1.9	15.4	88.7	356.2	2166	8801	> 20000
$\bar{r} = 0.0$, $k_{20} = 28.29$	2.3	18.6	117.5	578.5	3003	12059	> 20000
$\bar{r} = 1.9$, $k_{20} = 0.0$	0.83	8.7	38.6	91.8	338.9	2021	9236

viscoplastic strain during the OL in the highly-stressed material near the crack tip. Neglecting dynamic recovery therefore allows higher stresses to develop at the crack tip, with less significant unloading after the OL.

To compare across all OL ratios, one useful metric is the delay time. The delay time is the difference in the time required for the crack to grow by a fixed amount for an OL case compared with sustained loading at K_{hold} [47]. The amount of crack extension was chosen as $\Delta a = 200.0$ μm since steady state crack growth had resumed by this point in all cases. Table 6.2 shows the predicted delay times for computations with a range of OL ratios. The delay time is recorded as > 20000 s for cases where no post-OL crack extension occurred in computations up to 20000 s, but the rate of damage evolution in the elements ahead of the crack tip was nonzero. The delay time is higher at all OL ratios for computations neglecting GNDs and lower at all OL ratios for computations neglecting dynamic recovery, consistent with the observations in Figure 6.14. As suggested by comparing across OL ratios in Figure 6.14, the differences in the predicted delay time become larger with increasing OL ratio. This further reinforces the roles of GNDs and dynamic recovery in post-OL crack extension, especially when there is substantial retardation.

6.4 Discussion

Crack extension predictions under three different types of waveforms containing OLs form the backbone of results generated in this study. The model predicts that, in general, OLs cause crack growth retardation in Alloy 718 and similar creep-brittle materials. In all

cases, the retardation depends strongly on the OL ratio. The delay effect rapidly increases above $R_{\mathrm{OL}} \approx 1.2$ for all waveforms. The highest OL ratio considered, $R_{\mathrm{OL}} = 1.5$, produces crack arrest for cyclic loading and long delay times (beyond 20000 s) for sustained loading. However, the shape of the post-OL crack extension curves differs for the cases of cyclic loading and sustained loading at OL ratios above $R_{\mathrm{OL}} = 1.2$. For cyclic loading, the model predicts that crack growth continues during the cycles immediately after the OL, and the crack growth rate gradually returns toward steady state. For sustained loading, the model predicts that there is a period of time after the OL where almost no crack growth occurs. For the trapezoidal waveform, OL ratios above approximately 1.3 eliminate the effect of the hold time on subsequent crack growth.

The predicted traction distributions (Figures 6.6 and 6.10) and accumulated plastic strain contours (Figure 6.7) during steady-state and post-OL crack growth provide further insight into the effects of OLs. Most importantly, these results demonstrate why Alloy 718 can be described as a creep-brittle material during steady-state crack growth but behaves like a ductile material following OLs. During steady-state crack growth, viscoplastic strains are small, and the viscoplastic zone is confined near the crack tip, consistent with the creep-brittle characterization. Overloads enhance the crack-tip viscoplastic strain. Significant unloading then occurs in the viscoplastically deformed material near the crack tip following OLs as shown in the traction distributions. The unloading is amplified by increasing the OL ratio. This leads to ductile post-OL behavior, with significant crack growth retardation.

The model predicts that GNDs and dynamic recovery both play a significant role in post-OL crack growth. Neglecting GNDs could render the model non-conservative for predicting crack growth following OLs. This is because, without GNDs, the model predicts only slightly reduced steady-state crack growth rates but significantly more retardation following OLs. This is similar to previous studies on OLs as well as crack growth transients due to material inhomogeneities in rate-independent materials characterized by a strain gradient plasticity model [129], [158]. On the other hand, the computations indicate that dynamic recovery is beneficial. Neglecting dynamic recovery has a somewhat larger effect than neglecting GNDs on the predicted steady-state crack growth rates, but this effect is again amplified in the case of OLs. Especially for high OL ratios (above $R_{\mathrm{OL}} \approx 1.2$), crack growth resumes substantially

sooner when dynamic recovery is neglected. Nonetheless, the overall trends remain the same, with the delay time increasing rapidly as the OL ratio increases. This further reinforces the strong influence of the OL ratio.

The observation that crack growth under cyclic loading at $f = 0.1$ Hz is due to a time- and stress-dependent mechanism associated with intergranular crack growth consistent with previous work [32]. At higher frequencies, crack growth due to fatigue can play a larger role and is typically indicated by transgranular crack growth [4], which was not observed here. The specific values of the damage evolution parameters were estimated by comparing the experimentally-measured crack growth rates with the values predicted from the model. A formal calibration procedure was not carried out. A least squares optimization procedure, for example, could enhance the parameter calibration, together with a detailed sensitivity analysis.

For crack growth following OLs, the model predictions overall show good qualitative agreement experimental studies. For example, Nicholas et al. [34], [47] considered sustained loading interrupted by OLs, similar to the waveform considered in Section 6.3.2. These authors observed crack arrest or delay times exceeding several hours in tests using an OL ratio of 1.5 and significant crack growth retardation, with delay times on the order of an hour before the resumption of crack growth, using an OL ratio of 1.2. The model similarly predicts lengthy delay times for $R_{\mathrm{OL}} = 1.5$. However, the model predicts these long delay times do not set in until OL ratios around 1.4. In addition, Nicholas et al. [34] did not observe a significant influence of the OL hold time on retardation. However, that study used much longer hold times than considered here, on the order of tens of minutes to hours, and it is possible that the influence of OL hold time predicted by the model would saturate for longer hold times. A larger domain would need to be used in the computations to study crack growth during and after long OL hold times. Due to the large amount of crack extension, such computations may need to use a full model of a fracture mechanics specimen. Otherwise, the stages in the crack extension predicted by the model for cases with substantial retardation are also similar to these experiments: there is a brief acceleration during the OL, followed by a period of time where virtually no crack extension occurs, followed by a rapid return to the steady-state crack growth rates when crack extension resumes. This contrasts with the

more gradual return to steady-state crack growth rates predicted for cyclic loading with OLs in cases where the crack did not arrest.

Weerasooriya and Nicholas [33] considered trapezoidal waveforms containing an OL, similar to the waveform considered in Section 6.3.3 but with a loading frequency of 1.0 Hz. These authors observed an increase in cyclic crack growth rates below OL ratios of about 1.1 due to increased damage during the hold time. For OL ratios above about 1.25, no crack advance occurred during the hold time. Ponnelle et al. [30] observed similar results with this waveform. Experiments with OL ratio 1.2 very nearly eliminated crack growth during the hold time. Experiments with OL ratio 1.5 fully eliminated crack growth during the hold time and, in some cases, produced crack growth rates slightly below the constant-amplitude loading experiments. These trends agree very well with the predictions for this waveform in the current study shown in Figure 6.12. Similar to the case of OLs during sustained loading, however, the model underpredicts the value of the threshold OL ratio where crack growth during the hold time is completely eliminated.

Crack branching induced by the OLs may provide an additional shielding mechanism beyond the increased viscoplastic strains, which was not considered in this study. This branching would reduce the effective driving force on the main crack as it grows through the OL-affected region. This mechanism is likely partially responsible for the more extensive retardation observed in the experiments at lower OL ratios in [30], [33], [34]. In experiments with a trapezoidal waveform at 550°C, Saarimaki et al. [27] observed crack branching for any OL ratio that was applied. The branching becoming more significant for higher OL ratios. A model that explicitly resolves the grain morphology, with cohesive elements placed along all grain boundaries, could account for intergranular crack branching. Advances in this direction include finite element computations with specialized grain elements [237] and crystal plasticity finite element models incorporating time-dependent grain boundary damage evolution [238]. A related phenomenon that may also be relevant is through-thickness curvature of the crack front [25].

On the other hand, the minimal retardation predicted at low OL ratios is qualitatively similar to the experimental results of Adair et al. [210]. In a study on IN100, another precipitation-hardened nickel-base superalloy, these authors observed crack growth acceler-

ation for cyclic OLs with $R_{OL} = 1.3$ at a temperature of 650°C in laboratory air. This behavior was attributed to the crack rapidly growing through a damaged region, characterized by more widespread oxidation induced by the OL, before the viscoplastic strain could cause significant retardation [210]. The enhanced damage can be thought of as an anti-shielding mechanism that counteracts the shielding associated with viscoplasticity and crack branching. The exact balance between these shielding and anti-shielding effects likely depends strongly on the material, microstructure, environment, and applied loads [230].

The traction distributions following OLs during hold-time loading, Figure 6.10, are similar to the crack-opening stress distributions observed in numerical studies of stationary cracks in Alloy 718. Ponnelle et al. [30] and Newman and Sullivan [83] showed substantially reduced crack-opening stress following OLs in a trapezoidal waveform. As in the current study, the stress distribution ahead of the crack tip became increasingly flat as the OL ratio increased [30]. These authors also observed a small region of compression that developed ahead of a stationary crack tip after the OL for OL ratio 1.5.

Another relevant situation involving transient crack growth rates is the period of time before steady-state crack growth rates set in for a given applied stress intensity factor. If this period of transient crack growth is significant, experiments beginning at different crack lengths but the same applied K would produce different crack growth rates [5]. Despite many analytical and numerical modeling efforts (e.g., [67], [72], [80], [203], [239]), the appropriate characterizing parameter for this situation is still unclear [5]. A detailed physical model of the relevant damage mechanisms could help in predicting the transient crack growth rates in this situation. Such a model could quantify the incubation time before the onset of crack growth, as well as the time period during which the kinetics of the relevant crack growth mechanism reach a steady state. Since the crack growth rates correlated with the stress intensity factor in this study, consistent with previous work on Alloy 718 [4], [23], [77], this stage of crack growth was not judged to be significant.

In the present study, a phenomenological approach was used to describe the stress- and time-dependent material separation and crack extension. Damage models based directly on the kinetics of relevant damage mechanisms at the crack tip could significantly enhance the work in this study [5], [24]. Particularly important mechanisms for Ni-base superalloys

at high temperatures in air environments include dynamic embrittlement due to elemental oxygen diffusion and stress-assisted grain boundary oxidation (SAGBO) [31], [205], [206], [230], [240]. Accurate models for stress-assisted oxygen diffusion and oxidation kinetics could, together with a crystal plasticity formulation, enable predictions of crack extension as a function of microstructure, alloy composition, loading waveform, and characteristics of deformation near the crack tip [231]. Using these models to investigate how OL-induced changes to the crack-tip stress state influence the dominant crack growth mechanisms could extend the results of the current study. For example, some observations of crack growth following OLs with a trapezoidal waveform have shown a mixed transgranular-intergranular crack path even for low-frequency loading [30]. In addition, the long delay times without any crack extension predicted for $R_{\mathrm{OL}} = 1.5$ may provide sufficient time for a protective oxide like chromia to form at the crack tip [29]. This could prevent further oxygen intrusion, leading to full crack arrest. One additional mechanism that may be important is compressive residual stresses that develop due to large transformation strains associated with the formation of oxides, particularly chromia [218], [241]. Ideally, numerical studies incorporating these physics-based damage and deformation models would be done in concert with specific experiments designed to probe the particular mechanisms of interest [5].

6.5 Conclusions

In this study, finite element computations were used to investigate post-OL crack growth in Alloy 718. The model described deformation in the bulk material using a strain gradient viscoplasticity model based on the Kocks-Mecking formalism. The formulation accounted for dislocation storage and dynamic recovery processes and the accumulation of GNDs. Material separation was described using an irreversible CZM with a phenomenological stress- and time-dependent damage evolution equation. The model was calibrated using steady-state crack growth rates from sustained loading and cyclic loading experiments on Alloy 718 at 650° C. Three different waveforms containing OLs were then considered: cyclic loading with 1 or 3 OLs, sustained loading interrupted by an OL, and a trapezoidal waveform with an

OL prior to the hold time. The observations related to OLs are likely relevant to other creep-brittle materials, where the viscoplastic zone grows with the advancing crack.

Key conclusions include the following:

- Steady-state crack growth rates for Alloy 718 under sustained loading and constant-amplitude cyclic loading at $f = 0.1$ Hz are both successfully captured using stress- and time-dependent damage and the SGKM viscoplasticity formulation.
- Overloads during cyclic loading and sustained loading cause crack growth retardation. This is associated with enhanced crack-tip viscoplastic strain during the OL and subsequent unloading and reduced traction ahead of the crack tip.
- The magnitude of the retardation depends strongly on the OL ratio, with crack arrest or delay times on the order of several hours occurring for OL ratios close to 1.5. This trend is in agreement with existing experimental evidence.
- Overloads applied in a trapezoidal waveform can suppress or eliminate the detrimental effect of hold times on crack growth. This depends on both the length of the hold time and the OL ratio. This trend also agrees with experiments.
- Neglecting GNDs that develop due to plastic strain gradients could lead to non-conservative predictions for crack growth following OLs, due to the higher predicted delay times in this case.
- Dynamic recovery is an important stress relaxation mechanism that enhances crack growth retardation following OLs.

7. SUMMARY AND CONCLUSIONS

This thesis advances knowledge of transient fatigue and creep crack growth in rate-independent and rate-dependent materials. Incremental finite element computations combined elastic-plastic or elastic-viscoplastic constitutive laws in the bulk material with an irreversible cohesive zone formulation to describe crack extension. The plasticity and viscoplasticity formulations accounted for hardening due to plastic strain gradients. Damage evolution equations accounted for material degradation due to rate-independent fatigue and time-dependent grain boundary embrittlement. The influence of plastic strain gradients and rate-dependent deformation on the predicted crack extension was investigated for cases where similitude is violated at the crack tip due to the applied loads or material inhomogeneity.

In Chapter 3 [129], computations investigated the role of hardening due to plastic strain gradients on fatigue crack growth in rate-independent materials. Crack extension was driven by fatigue damage evolution in the CZM. Accounting for plastic strain gradients did not influence the predicted steady-state crack growth rates under constant-amplitude loading. For the case of OLs, it was found that hardening due to plastic strain gradients significantly restricted plastic deformation near the crack tip in the OL plastic zone. Analysis of the crack-tip fields showed that the restricted plastic deformation led to higher maximum traction and reduced crack closure in subsequent cycles. As a result, computations accounting for plastic strain gradients predicted less significant post-OL retardation than computations with a classical plasticity model. However, the size of the OL-affected region was not influenced by hardening due to plastic strain gradients.

In Chapter 4 [158], rate-independent fatigue crack growth toward interfaces in bi-materials and multi-layered materials was investigated. The CZM with fatigue damage evolution described growth of the main crack perpendicular to the interface and separation along the interface itself. For bi-materials, computations identified the shielding or anti-shielding effects associated with the yield strength mismatch and weak interfaces. When the crack-tip plastic zone interacted with the interfaces, hardening due to plastic strain gradients was found to influence extension of both the main crack and the interface crack. Plastic strain gradients were also found to be significant when the plastic zone spread across a plastically-

soft interlayer within a plastically-hard matrix. Computations accounting for plastic strain gradients predicted crack penetration through the interlayer for a case where computations using a classical plasticity model predicted crack deflection into one of the interfaces.

In Chapter 5 [19], crack growth in power-law viscoplastic materials was investigated. Motivated by experiments on Alloy 617 at 800°C showing cycle-dependent transgranular crack growth at the loads of interest, material degradation was described based on fatigue damage evolution in the CZM. A parametric study demonstrated the important role of the material rate sensitivity in post-OL fatigue crack growth. The trends with respect to rate sensitivity (more acceleration for high rate sensitivity; more retardation for low rate sensitivity) were robust to changes in the underlying fatigue damage parameters. The fatigue damage parameters were subsequently calibrated using experimentally-measured steady-state crack growth rates for Alloy 617 at 800°C and a load frequency of 0.33 Hz. The crack extension predicted by the model showed good agreement with the trends observed in experiments on Alloy 617 including a single OL and a block of 20 OLs at different load magnitudes. Hardening due to plastic strain gradients was not found to influence steady-state or post-OL crack growth. Incorporating the viscoplastic rate dependence into the fatigue damage formulation for the calibrated model brings the predicted crack growth rates into closer agreement across different load frequencies.

In Chapter 6 [223], crack growth was investigated in viscoplastic materials described by a formulation based on the Kocks-Mecking approach. The viscoplasticity formulation accounted for dislocation storage and recovery processes in the evolving plastic zone ahead of the crack tip. Since experiments on Alloy 718 at 650°C demonstrated environmentally-enhanced grain boundary embrittlement, material degradation was described using a time- and stress-dependent damage formulation. The damage parameters were calibrated using experimentally-measured crack growth rates under sustained loading and constant-amplitude cyclic loading at a frequency of 0.1 Hz. Computations predicted crack growth retardation following OLs during cyclic loading, sustained loading, and trapezoidal loading waveforms. The retardation increased strongly with the OL ratio. The predicted crack extension for OLs in the sustained loading and trapezoidal loading waveforms showed good agreement with the trends observed in experiments on Alloy 718 at 650°C. Geometrically-necessary dislo-

cations induced by viscoplastic strain gradients influenced post-OL crack extension through restricted viscoplastic deformation near the crack tip. An important outcome of the applications to Alloy 617 and Alloy 718 is that, in each case, the model parameters were determined using only steady-state crack growth data. The correct trends in the post-OL behavior, based on experiments by collaborators (for Alloy 617) and experiments in the literature (for Alloy 718), were predicted without further modification to the model.

The results presented in Chapters 3–6 make it possible to address the research questions posed at the beginning of this thesis:

- *What role do plastic strain gradients play in predictions of fatigue crack growth under constant-amplitude and transient loading?* Hardening due to plastic strain gradients does not have a significant role in the constant-amplitude loading case. In the OL plastic zone, large plastic strain gradients develop near the crack tip. The restricted crack-tip plastic deformation leads to less post-OL crack growth retardation, compared to computations with a classical plasticity model.

- *How do the interface strength, yield strength mismatch, and plastic strain gradients control fatigue crack growth behavior in bimaterials?* The yield strength mismatch alone can have a shielding effect (for a plastically-soft-to-plastically-hard transition) or an anti-shielding effect (for a plastically-hard-to-plastically-soft transition). However, increasing the yield strength mismatch always enhances the shielding effect of a weak interface. Hardening due to plastic strain gradients restricts plastic deformation near the interface. Plastic strain gradients thereby influence crack growth rates for the main crack and interface crack and influence the critical conditions for crack bifurcation at the interface.

- *In a multilayered material, how does the size of a layer relative to the crack-tip plastic zone influence crack extension?* Interaction effects must be considered when the plastic zone spreads across an interlayer. Hardening due to plastic strain gradients becomes more significant due to constraint of the plastic zone in this situation, promoting crack penetration through the interlayer.

- *What is the influence of the material rate sensitivity on post-overload fatigue crack growth in creep-ductile materials like Alloy 617?* The computations indicate that the rate sensitivity (or creep exponent) strongly influences whether acceleration or retardation occurs following OLs. Low rate sensitivity is associated with higher local viscoplastic strain near the crack tip. Higher viscoplastic strains in turn disturb the steady-state crack tip fields and induce crack growth retardation. The transition between acceleration- and retardation-dominated behavior occurs over a range of rate sensitivity values characteristic of solid solution strengthened materials. The results are therefore relevant for Alloy 617 and similar materials undergoing crack growth by a cyclic fatigue mechanism.

- *What damage, hardening, and recovery mechanisms are relevant to steady-state and transient crack growth in creep-brittle materials like Alloy 718?* Crack growth under sustained loading and cyclic loading at $f = 0.1$ Hz is driven by stress- and time-dependent damage for Alloy 718. Damage is associated with environmental attack on the grain boundaries and is successfully captured in the CZM. Dynamic recovery is an important stress relaxation mechanism and reduces the traction ahead of the crack tip, especially following OLs. Computations accounting for only predict significantly less post-OL retardation

- *What insights do the computations provide into experimental results for crack growth following OLs in Alloy 617 and Alloy 718?* For Alloy 617, the numerical results demonstrate why OLs produce little to no crack growth retardation. The creep exponent for Alloy 617 lies very close to the transition value between acceleration- and retardation-dominated behavior predicted by the parametric study. In agreement with experiments, the computations subsequently predict a close competition between post-OL acceleration and retardation in Alloy 617. For Alloy 718, the computations demonstrate why steady-state crack growth is described as creep-brittle, but substantial crack growth retardation occurs following OLs. During OLs, the viscoplastic zone remains contained, but a strong viscoplastic strain concentration develops locally near the crack

tip. In agreement with experiments, the post-OL retardation depends strongly on the OL ratio through the unloading that occurs in the highly-deformed crack tip region.

- *For both Alloy 617 and Alloy 718, what role do plastic strain gradients play in steady-state and transient crack growth?* Hardening due to plastic strain gradients does not significantly influence either steady-state or post-OL fatigue crack growth in Alloy 617. For Alloy 718, plastic strain gradients play a similar role as in rate-independent materials. Specifically, development of GNDs in the viscoplastic zone during OLs leads to less crack growth retardation, compared with computations neglecting GNDs.

Put together, these results demonstrate the importance of material behavior deep inside the crack-tip plastic zone and its influence on the relevant material separation mechanisms in predicting transient crack growth rates. In the context of classical models for post-OL crack growth (e.g., Willenborg and Elber), this behavior determines the effective driving force on the crack as it grows through the OL plastic zone. Evolution of the effective driving force in turn determines the magnitude of crack growth retardation. Plastic strain gradients in rate-independent materials and the rate sensitivity in power-law viscoplastic materials were both found to significantly influence the plastic or viscoplastic strain magnitude close to the crack tip following OLs. Larger plastic or viscoplastic strain magnitudes produced larger changes in the crack-tip fields during subsequent cycles and led to more retardation. In the case of crack growth through a stress- and time-dependent mechanism, unloading in the highly-deformed material near the crack tip following an OL suppresses subsequent damage and crack extension.

The computations for rate-dependent materials in particular reinforce some of the challenges inherent in materials selection for high-temperature applications. An advantage of creep-ductile materials is that they typically cannot sustain high stresses for sufficiently long times to activate environmentally-enhanced damage mechanisms. However, the results of Chapter 5 indicate that the relatively high rate sensitivity characteristic of these materials can suppress or possibly eliminate the beneficial crack growth retardation that occurs following OLs in fatigue. On the other hand, creep-brittle materials generally experience higher steady-state crack growth rates under sustained loads and low-frequency cyclic loads due to

environmentally-enhanced damage. The trade-off here, based on the results of Chapter 6, is that OLs can cause significant crack growth retardation and even crack arrest, depending on the OL ratio. The results in this thesis can thereby aid in the design and materials selection for high-temperature components where transient loads are a significant concern.

REFERENCES

[1] T. L. Anderson, *Fracture Mechanics: Fundamentals and Applications*, 3rd ed. Boca Raton, FL: CRC Press, 2005.

[2] R. I. Stephens, A. S. Fatemi, R. R. Stephens, and H. O. Fuchs, *Metal Fatigue in Engineering*, 2nd ed. New York: John Wiley & Sons, 2001.

[3] R. O. Ritchie, "Mechanism of fatigue-crack propagation in ductile and brittle materials," *Int J Fract*, vol. 100, pp. 55–83, 1998. DOI: 10.1023/A:1018655917051.

[4] S. Floreen and R. H. Kane, "An investigation of the creep-fatigue-environment interaction in a Ni-base superalloy," *Fatigue Fract Eng Mater Struct*, vol. 2, no. 4, pp. 401–412, 1979. DOI: 10.1111/j.1460-2695.1979.tb01097.x.

[5] A. Saxena, "Creep and creep–fatigue crack growth," *Int J Fract*, vol. 191, no. 1-2, pp. 31–51, 2015. DOI: 10.1007/s10704-015-9994-4.

[6] M. Skorupa, "Load interaction effects during fatigue crack growth under variable amplitude loading - A literature review. Part I: Empirical trends," *Fatigue Fract Eng Mater Struct*, vol. 21, no. 8, pp. 987–1006, 1998. DOI: 10.1046/j.1460-2695.1998.00083.x.

[7] M. Skorupa, "Load interaction effects during fatigue crack growth under variable amplitude loading - A literature review. Part II: Qualitative interpretation," *Fatigue Fract Eng Mater Struct*, vol. 22, no. 10, pp. 905–926, 1999. DOI: 10.1046/j.1460-2695.1999.00158.x.

[8] R. Pippan, K. Flechsig, and F. O. Riemelmoser, "Fatigue crack propagation behavior in the vicinity of an interface between materials with different yield stresses," *Mater Sci Eng A*, vol. 283, no. 1-2, pp. 225–233, 2000. DOI: 10.1016/S0921-5093(00)00703-6.

[9] J. K. Wright, L. J. Carroll, C. Cabet, T. M. Lillo, J. K. Benz, J. A. Simpson, W. R. Lloyd, J. A. Chapman, and R. N. Wright, "Characterization of elevated temperature properties of heat exchanger and steam generator alloys," *Nucl Eng Des*, vol. 251, pp. 252–260, 2012. DOI: 10.1016/j.nucengdes.2011.10.034.

[10] R. N. Wright, "Updated Draft ASME Boiler and Pressure Vessel Code Case for Use of Alloy 617 for Construction of Nuclear Components for Section III Division 5," Idaho National Laboratory, Idaho Falls, Idaho, Tech. Rep., 2018.

[11] W. Ren and R. W. Swindeman, "A review on current status of Alloys 617 and 230 for Gen IV nuclear reactor internals and heat exchangers," *J Press Vessel Technol*, vol. 131, no. 4, p. 044 002, 2009. DOI: 10.1115/1.3121522.

[12] J. K. Benz, L. J. Carroll, J. K. Wright, R. N. Wright, and T. M. Lillo, "Threshold stress creep behavior of Alloy 617 at intermediate temperatures," *Metall Mater Trans A*, vol. 45, no. 7, pp. 3010–3022, 2014. DOI: 10.1007/s11661-014-2244-y.

[13] S. Mohanty, W. K. Soppet, S. Majumdar, and K. Natesan, "Thermal–mechanical stress analysis of pressurized water reactor pressure vessel with/without a preexisting crack under grid load following conditions," *Nucl Eng Des*, vol. 310, pp. 112–124, 2016. DOI: 10.1016/j.nucengdes.2016.09.020.

[14] A. Bosch and M. Vormwald, "Modeling short crack propagation under variable structural and thermal loadings," *Fatigue Fract Eng Mater Struct*, pp. 1652–1674, 2021. DOI: 10.1111/ffe.13447.

[15] D. A. Addison, J. D. Tucker, T. Siegmund, V. Tomar, and J. J. Kruzic, "Cyclic and time-dependent crack growth mechanisms in Alloy 617 at 800°C," *Mater Sci Eng A*, vol. 737, pp. 205–212, 2018. DOI: 10.1016/j.msea.2018.09.034.

[16] M. Rödig, H. Huthmann, and W. Hartnagel, "Fatigue and creep crack growth of alloy 800 and alloy 617 at high temperatures," *Mater High Temp*, vol. 10, no. 4, pp. 268–274, 1992. DOI: 10.1080/09603409.1992.11689429.

[17] S. S. Hsu, "Time-dependent crack growth in a heat-resistant alloy Inconel 617," *J Nucl Sci Technol*, vol. 30, no. 4, pp. 302–313, 1993. DOI: 10.1080/18811248.1993.9734487.

[18] D. A. Addison, "Time-Dependent Crack Growth Mechanisms in Alloy 617 at 800°C in Air," Master's Thesis, Oregon State University, 2017.

[19] J. D. Pribe, D. A. Addison, T. Siegmund, and J. J. Kruzic, "High-temperature fatigue crack growth under transient overloading: Application to Alloy 617," *Int J Fract*, Under minor revisions.

[20] R. Pippan, C. Bichler, B. Tabernig, and H. Weinhandl, "Overloads in ductile and brittle materials," *Fatigue Fract Eng Mater Struct*, vol. 28, no. 11, pp. 971–981, 2005. DOI: 10.1111/j.1460-2695.2005.00934.x.

[21] E. Hosseini and V. A. Popovich, "A review of mechanical properties of additively manufactured Inconel 718," *Addit Manuf*, vol. 30, p. 100 877, 2019. DOI: 10.1016/j.addma.2019.100877.

[22] H. Ghonem, T. Nicholas, and A. Pineau, "Elevated temperature fatigue crack growth in Alloy 718-Part I: Effects of mechanical variables," *Fatigue Fract Eng Mater Struct*, vol. 16, no. 5, pp. 565–576, 1993. DOI: 10.1111/j.1460-2695.1993.tb00767.x.

[23] M. Clavel and A. Pineau, "Frequency and wave-form effects on the fatigue crack growth behavior of Alloy 718 at 298 K and 823 K," *Metall Trans A*, vol. 9, no. 4, pp. 471–480, 1978. DOI: 10.1007/BF02646402.

[24] S. D. Antolovich, "Microstructural aspects of fatigue in Ni-base superalloys," *Philos Trans R Soc A*, vol. 373, p. 20 140 128, 2015, ISSN: 1364-503X. DOI: 10.1098/rsta.2014.0128.

[25] D. Gustafsson and E. Lundström, "High temperature fatigue crack growth behaviour of Inconel 718 under hold time and overload conditions," *Int J Fatigue*, vol. 48, pp. 178–186, 2013. DOI: 10.1016/j.ijfatigue.2012.10.018.

[26] R. H. Van Stone and D. C. Slavik, "Prediction of time-dependent crack growth with retardation effects in nickel base alloys," in *Fatigue Fract Mech 31st Vol ASTM STP 1389*, 1389, West Conshohocken, PA: ASTM International, 2000, pp. 405–426. DOI: 10.1520/STP14812S.

[27] J. Saarimäki, J. J. Moverare, R. Eriksson, and S. Johansson, "Influence of overloads on dwell time fatigue crack growth in Inconel 718," *Mater Sci Eng A*, vol. 612, pp. 398–405, 2014. DOI: 10.1016/j.msea.2014.06.068.

[28] K. Sadananda and P. Shahinian, "The effect of environment on the creep crack growth behavior several structural alloys," *Mater Sci Eng*, vol. 43, no. 2, pp. 159–168, 1980. DOI: 10.1016/0025-5416(80)90143-3.

[29] R. Molins, G. Hochstetter, J. C. Chassaigne, and E. Andrieu, "Oxidation effects on the fatigue crack growth behaviour of alloy 718 at high temperature," *Acta Mater*, vol. 45, no. 2, pp. 663–674, 1997. DOI: 10.1016/S1359-6454(96)00192-9.

[30] S. Ponnelle, B. Brethes, and A. Pineau, "High temperature fatigue crack growth rate in Inconel 718: Dwell effect annihilations," in *Eur Struct Integr Soc Temp Interact*, L. Remy and J. Petit, Eds., vol. 29, 2002, pp. 257–266. DOI: 10.1016/S1566-1369(02)80082-6.

[31] H. E. Evans, H. Y. Li, and P. Bowen, "A mechanism for stress-aided grain boundary oxidation ahead of cracks," *Scr Mater*, vol. 69, no. 2, pp. 179–182, 2013. DOI: 10.1016/j.scriptamat.2013.03.026.

[32] H. Ghonem, T. Nicholas, and A. Pineau, "Elevated temperature fatigue crack growth in Alloy 718-Part II: Effects of environmental and material variables," *Fatigue Fract Eng Mater Struct*, vol. 16, no. 6, pp. 577–590, 1993. DOI: 10.1111/j.1460-2695.1993.tb00103.x.

[33] T. Weerasooriya and T. Nicholas, "Overload effects in sustained-load crack growth in Inconel 718," in *Fract Mech Eighteenth Symp*, West Conshohocken, PA: ASTM International, 1988, pp. 181–191. DOI: 10.1520/STP23241S.

[34] T. Nicholas, G. K. Haritos, R. L. Hastie, and K. Harms, "The effects of overloads on sustained-load crack growth in a nickel-base superalloy: part I-analysis," *Theor Appl Fract Mech*, vol. 16, no. 1, pp. 35–49, 1991. DOI: 10.1016/0167-8442(91)90039-M.

[35] S. Suresh, Y. Sugimura, and E. K. Tschegg, "The growth of a fatigue crack approaching a perpendicularly-oriented, bimaterial interface," *Scr Metall Mater*, vol. 27, no. 9, pp. 1189–1194, 1992. DOI: 10.1016/0956-716X(92)90597-8.

[36] O. Kolednik, J. Zechner, and J. Predan, "Improvement of fatigue life by compliant and soft interlayers," *Scr Mater*, vol. 113, pp. 1–5, 2016. DOI: 10.1016/j.scriptamat.2015.10.021.

[37] M. C. Messner, A. J. Beaudoin, and R. H. Dodds, "Mesoscopic modeling of crack arrestor delamination in Al–Li: primary crack shielding and T-stress effect," *Int J Fract*, vol. 188, no. 2, pp. 229–249, 2014. DOI: 10.1007/s10704-014-9957-1.

[38] Y. Wei and J. W. Hutchinson, "Steady-state crack growth and work of fracture for solids characterized by strain gradient plasticity," *J Mech Phys Solids*, vol. 45, no. 8, pp. 1253–1273, 1997. DOI: 10.1016/S0022-5096(97)00018-5.

[39] S. Qu, Y. Huang, H. Jiang, C. Liu, P. D. Wu, and K. C. Hwang, "Fracture analysis in the conventional theory of mechanism-based strain gradient (CMSG) plasticity," *Int J Fract*, vol. 129, no. 3, pp. 199–220, 2004. DOI: 10.1023/B:FRAC.0000047786.40200.f8.

[40] E. Martínez-Pañeda and C. Betegón, "Modeling damage and fracture within strain-gradient plasticity," *Int J Solids Struct*, vol. 59, pp. 208–215, 2015. DOI: 10.1016/j.ijsolstr.2015.02.010.

[41] N. A. Fleck and J. W. Hutchinson, "Strain Gradient Plasticity," in *Adv Appl Mech*, vol. 33, Academic Press, 1997, pp. 295–361. DOI: 10.1016/S0065-2156(08)70388-0.

[42] P. Paris and F. Erdogan, "A critical analysis of crack propagation laws," *J Basic Eng*, vol. 85, no. 4, pp. 528–533, 1963. DOI: 10.1115/1.3656900.

[43] O. E. Wheeler, "Spectrum loading and crack growth," *J Basic Eng*, vol. 94, pp. 181–186, 1972.

[44] J. Willenborg, R. M. Engle, and H. A. Wood, "A crack growth retardation model using an effective stress concept," in *AFFDL TM-71-1-FBR*, 1971.

[45] J. P. Gallagher, "A generalized development of yield zone models," Air Force Flight Dynamics Laboratory, Wright-Patterson AFB, Tech. Rep., 1974.

[46] W. S. Johnson, "Multi-parameter yield zone model for predicting spectrum crack growth," in *Methods Model Predict Fatigue Crack Growth Under Random Loading, ASTM STP 748*, West Conshohocken, PA: ASTM International, 1981, pp. 85–102. DOI: 10.1520/STP28335S.

[47] T. Nicholas, G. Haritos, R. Hastie, and K. Harms, "The effects of overloads on sustained-load crack growth in a nickel-base superalloy: part II—experiments," *Theor Appl Fract Mech*, vol. 16, no. 1, pp. 51–62, 1991. DOI: 10.1016/0167-8442(91)90040-Q.

[48] V. M. Barker, W. Steven Johnson, B. S. Adair, S. D. Antolovich, and A. Staroselsky, "Load and temperature interaction modeling of fatigue crack growth in a Ni-base superalloy," *Int J Fatigue*, vol. 52, pp. 95–105, 2013. DOI: 10.1016/j.ijfatigue.2013.03.003.

[49] B. Yuen and F. Taheri, "Proposed modifications to the Wheeler retardation model for multiple overloading fatigue life prediction," *Int J Fatigue*, vol. 28, no. 12, pp. 1803–1819, 2006. DOI: 10.1016/j.ijfatigue.2005.12.007.

[50] X. Huang, M. Torgeir, and W. Cui, "An engineering model of fatigue crack growth under variable amplitude loading," *Int J Fatigue*, vol. 30, no. 1, pp. 2–10, 2008. DOI: 10.1016/j.ijfatigue.2007.03.004.

[51] W. Elber, "Fatigue crack closure under cyclic tension," *Eng Fract Mech*, vol. 2, no. 1, pp. 37–45, 1970. DOI: 10.1016/0013-7944(70)90028-7.

[52] K. Solanki, S. R. Daniewicz, and J. C. Newman, "Finite element analysis of plasticity-induced fatigue crack closure: An overview," *Eng Fract Mech*, vol. 71, no. 2, pp. 149–171, 2004. DOI: 10.1016/S0013-7944(03)00099-7.

[53] E. F. J. von Euw, R. W. Hertzberg, and R. Roberts, "Delay Effects in Fatigue Crack Propagation," in *Stress Anal Growth Cracks Proc 1971 Natl Symp Fract Mech Part 1, ASTM STP 513*, ASTM International, 1972, pp. 230–259. DOI: 10.1520/STP34123S.

[54] C. Bichler and R. Pippan, "Effect of single overloads in ductile metals: A reconsideration," *Eng Fract Mech*, vol. 74, no. 8, pp. 1344–1359, 2007. DOI: 10.1016/j.engfracmech.2006.06.011.

[55] R. Pippan and A. Hohenwarter, "Fatigue crack closure: a review of the physical phenomena," *Fatigue Fract Eng Mater Struct*, vol. 40, no. 4, pp. 471–495, 2017. DOI: 10.1111/ffe.12578.

[56] J. Newman, "Prediction of fatigue crack growth under variable-amplitude and spectrum loading using a closure model," in *Des Fatigue Fract Resist Struct ASTM STP 761*, P. Abelkis and C. Hudson, Eds., West Conshohocken, PA: ASTM International, 1982, pp. 255–277. DOI: 10.1520/STP28863S.

[57] S. Roychowdhury and R. H. Dodds, "A numerical investigation of 3-D small-scale yielding fatigue crack growth," *Eng Fract Mech*, vol. 70, no. 17, pp. 2363–2383, 2003. DOI: 10.1016/S0013-7944(03)00003-1.

[58] K. B. Cochran, R. H. Dodds, and K. D. Hjelmstad, "The role of strain ratcheting and mesh refinement in finite element analyses of plasticity induced crack closure," *Int J Fatigue*, vol. 33, no. 9, pp. 1205–1220, 2011. DOI: 10.1016/j.ijfatigue.2011.03.005.

[59] J. Newman, "A finite-element analysis of fatigue crack closure," in *Mech Crack Growth, ASTM STP 590*, West Conshohocken, PA: ASTM International, 1976, pp. 281–301. DOI: 10.1520/STP33952S.

[60] R. C. McClung and H. Sehitoglu, "On the finite element analysis of fatigue crack closure-1. Basic modeling issues," *Eng Fract Mech*, vol. 33, no. 2, pp. 237–252, 1989. DOI: 10.1016/0013-7944(89)90027-1.

[61] F. Jiang, Z. L. Deng, K. Zhao, and J. Sun, "Fatigue crack propagation normal to a plasticity mismatched bimaterial interface," *Mater Sci Eng A*, vol. 356, no. 1-2, pp. 258–266, 2003. DOI: 10.1016/S0921-5093(03)00142-4.

[62] K. S. Chan and J. Lankford, "The role of microstructural dissimilitude in fatigue and fracture of small cracks," *Acta Metall*, vol. 36, no. 1, pp. 193–206, 1988. DOI: 10.1016/0001-6160(88)90038-7.

[63] F. O. Riemelmoser and R. Pippan, "The J-integral at Dugdale cracks perpendicular to interfaces of materials with dissimilar yield stresses," *Int J Fract*, vol. 103, no. 4, pp. 397–418, 2000. DOI: 10.1023/A:1007605224764.

[64] N. K. Simha, F. D. Fischer, O. Kolednik, and C. R. Chen, "Inhomogeneity effects on the crack driving force in elastic and elastic-plastic materials," *J Mech Phys Solids*, vol. 51, no. 1, pp. 209–240, 2003. DOI: 10.1016/S0022-5096(02)00025-X.

[65] O. Kolednik, J. Predan, and F. D. Fischer, "Reprint of "Cracks in inhomogeneous materials: Comprehensive assessment using the configurational forces concept"," *Eng Fract Mech*, vol. 77, no. 18, pp. 3611–3624, 2010. DOI: 10.1016/j.engfracmech.2010.10.010.

[66] H. Riedel, *Fracture at High Temperatures*. Berlin: Springer-Verlag, 1987.

[67] T. C. Wang, C. F. Shih, and A. Needleman, "Crack growth by grain boundary cavitation in the transient and extensive creep regimes," *Int J Fract*, vol. 52, pp. 159–189, 1991. DOI: 10.1007/BF00034903.

[68] J. D. Landes and J. A. Begley, "A fracture mechanics approach to creep crack growth," in *Mechanics of Crack Growth, ASTM STP 590*, West Conshohocken, PA: ASTM International, 1976, pp. 128–148. DOI: 10.1520/STP33943S.

[69] J. L. Bassani and F. A. McClintock, "Creep relaxation of stress around a crack tip," *Int J Solids Struct*, vol. 17, no. 5, pp. 479–492, 1981. DOI: 10.1016/0020-7683(81)90055-X.

[70] J. W. Hutchinson, "Singular behaviour at the end of a tensile crack in a hardening material," *J Mech Phys Solids*, vol. 16, no. 1, pp. 13–31, 1968. DOI: 10.1016/0022-5096(68)90014-8.

[71] J. R. Rice and G. F. Rosengren, "Plane strain deformation near a crack tip in a power-law hardening material," *J Mech Phys Solids*, vol. 16, no. 1, pp. 1–12, 1968. DOI: 10.1016/0022-5096(68)90013-6.

[72] H. Riedel and J. R. Rice, "Tensile cracks in creeping solids," in *Fract Mech Twelfth Conf*, West Conshohocken, PA: ASTM International, 1980, pp. 112–130. DOI: 10.1520/STP36967S.

[73] A. Saxena, "Creep crack growth under non-steady-state conditions," in *Fract Mech Seventeenth Vol*, vol. 103, West Conshohocken, PA: ASTM International, 1986, pp. 185–201. DOI: 10.1520/STP17396S.

[74] J. L. Bassani, D. E. Hawk, and A. Saxena, "Evaluation of the C_t parameter for characterizing creep crack growth rate in the transient regime," in *Nonlinear Fract Mech Vol I Time-Dependent Fract*, West Conshohocken, PA: ASTM International, 1989, pp. 7–26. DOI: 10.1520/STP26768S.

[75] A. Saxena, "Creep crack growth in high temperature ductile materials," *Eng Fract Mech*, vol. 40, no. 4-5, pp. 721–736, 1991. DOI: 10.1016/0013-7944(91)90231-O.

[76] "ASTM E2760-19e1: Standard Test Method for Creep-Fatigue Crack Growth Testing," in, West Conshohocken, PA: ASTM International, 2019. DOI: 10.1520/E2760-19E01.

[77] P. Shahinian and K. Sadananda, "Effects of stress ratio and hold-time on fatigue crack growth in Alloy 718," *J Eng Mater Technol*, vol. 101, no. 3, p. 224, 1979. DOI: 10.1115/1.3443681.

[78] K. Sadananda and P. Shahinian, "Creep crack growth behavior of several structural alloys," *Metall Trans A*, vol. 14, no. 7, pp. 1467–1480, 1983. DOI: 10.1007/BF02664831.

[79] B. C. Hamilton, D. E. Hall, A. Saxena, and D. L. McDowell, "Creep crack growth behavior of aluminum alloy 2519: Part I—Experimental analysis," in *Elev Temp Eff Fatigue Fract ASTM STP 1297*, R. S. Piascik, R. P. Gangloff, and A. Saxena, Eds., West Conshohocken, PA: ASTM International, 1997, pp. 3–18. DOI: 10.1520/STP16314S.

[80] D. E. Hall, B. C. Hamilton, D. L. McDowell, and A. Saxena, "Creep crack growth behavior of aluminum alloy 2519: Part II—Numerical analysis," in *Elev Temp Eff Fatigue Fract ASTM STP 1297*, R. S. Piascik, R. P. Gangloff, and A. Saxena, Eds., West Conshohocken, PA: ASTM International, 1997, pp. 19–36. DOI: 10.1520/STP16315S.

[81] K. B. Yoon, A. Saxena, and D. L. McDowell, "Effect of cyclic overload on the crack growth behavior during hold period at elevated temperature," *Int J Fract*, vol. 59, no. 1, pp. 199–211, 1993. DOI: 10.1007/BF00012361.

[82] G. P. Potirniche, "A closure model for predicting crack growth under creep-fatigue loading," *Int J Fatigue*, vol. 125, pp. 58–71, 2019. DOI: 10.1016/j.ijfatigue.2019.03.029.

[83] J. C. Newman and R. Sullivan, "Strip-yield modeling of load-time-temperature effects on crack growth in engine materials," in *Proc ASME Turbo Expo 2020*, ASME, 2020, V10BT27A004.

[84] H. Sehitoglu and W. Sun, "The significance of crack closure under high temperature fatigue crack growth with hold periods," *Eng Fract Mech*, vol. 33, no. 3, pp. 371–388, 1989. DOI: 10.1016/0013-7944(89)90087-8.

[85] Y. Huang, S. Qu, K. C. Hwang, M. Li, and H. Gao, "A conventional theory of mechanism-based strain gradient plasticity," *Int J Plast*, vol. 20, no. 4-5, pp. 753–782, 2004. DOI: 10.1016/j.ijplas.2003.08.002.

[86] K. L. Roe and T. Siegmund, "An irreversible cohesive zone model for interface fatigue crack growth simulation," *Eng Fract Mech*, vol. 70, no. 2, pp. 209–232, 2003. DOI: 10.1016/S0013-7944(02)00034-6.

[87] B. Wang and T. Siegmund, "A numerical analysis of constraint effects in fatigue crack growth by use of an irreversible cohesive zone model," *Int J Fract*, vol. 132, no. 2, pp. 175–196, 2005. DOI: 10.1007/s10704-005-0627-1.

[88] J. L. Bouvard, J. L. Chaboche, F. Feyel, and F. Gallerneau, "A cohesive zone model for fatigue and creep-fatigue crack growth in single crystal superalloys," *Int J Fatigue*, vol. 31, no. 5, pp. 868–879, 2009. DOI: 10.1016/j.ijfatigue.2008.11.002.

[89] Y. Sun, K. Maciejewski, and H. Ghonem, "A damage-based cohesive zone model of intergranular crack growth in a nickel-based superalloy," *Int J Damage Mech*, vol. 22, no. 6, pp. 905–923, 2013. DOI: 10.1177/1056789512468917.

[90] T. Siegmund and J. Kruzic, "New Mechanistic Models of Creep-Fatigue Interactions for Gas Turbine Components - Final Report," National Energy Technology Laboratory, Pittsburgh, PA, Tech. Rep., 2018. DOI: 10.2172/1489645.

[91] N. A. Fleck, G. M. Muller, M. F. Ashby, and J. W. Hutchinson, "Strain gradient plasticity: Theory and experiment," *Acta Metall Mater*, vol. 42, no. 2, pp. 475–487, 1994. DOI: 10.1016/0956-7151(94)90502-9.

[92] A. Arsenlis and D. M. Parks, "Crystallographic aspects of geometrically-necessary and statistically-stored dislocation density," *Acta Mater*, vol. 47, no. 5, pp. 1597–1611, 1999. DOI: 10.1016/S1359-6454(99)00020-8.

[93] H. Gao, Y. Huang, W. D. Nix, and J. W. Hutchinson, "Mechanism-based strain gradient plasticity - I. Theory," *J Mech Phys Solids*, vol. 47, no. 6, pp. 1239–1263, 1999. DOI: 10.1016/S0022-5096(98)00103-3.

[94] W. D. Nix and H. Gao, "Indentation size effects in crystalline materials: A law for strain gradient plasticity," *J Mech Phys Solids*, vol. 46, no. 3, pp. 411–425, 1998. DOI: 10.1016/S0022-5096(97)00086-0.

[95] U. Komaragiri, S. Agnew, R. Gangloff, and M. Begley, "The role of macroscopic hardening and individual length-scales on crack tip stress elevation from phenomenological strain gradient plasticity," *J Mech Phys Solids*, vol. 56, no. 12, pp. 3527–3540, 2008. DOI: 10.1016/j.jmps.2008.08.007.

[96] E. Martínez-Pañeda, V. S. Deshpande, C. F. Niordson, and N. A. Fleck, "The role of plastic strain gradients in the crack growth resistance of metals," *J Mech Phys Solids*, vol. 126, pp. 136–150, 2019. DOI: 10.1016/j.jmps.2019.02.011.

[97] T. N. Nguyen, T. Siegmund, V. Tomar, and J. J. Kruzic, "Interaction of rate- and size-effect using a dislocation density based strain gradient viscoplasticity model," *J Mech Phys Solids*, vol. 109, pp. 1–21, 2017. DOI: 10.1016/j.jmps.2017.07.022.

[98] G. I. Taylor, "The mechanism of plastic deformation of crystals. Part I. Theoretical," *Proc R Soc A Math Phys Eng Sci*, vol. 145, no. 855, pp. 362–387, 1934. DOI: 10.1098/rspa.1934.0106.

[99] M. F. Ashby, "The deformation of plastically non-homogeneous materials," *Philos Mag*, vol. 21, no. 170, pp. 399–424, 1970. DOI: 10.1080/14786437008238426.

[100] J. F. Nye, "Some geometrical relations in dislocated crystals," *Acta Metall*, vol. 1, no. 2, pp. 153–162, 1953. DOI: 10.1016/0001-6160(53)90054-6.

[101] P. E. Seiler, T. Siegmund, Y. Zhang, V. Tomar, and J. J. Kruzic, "Stationary and propagating cracks in a strain gradient visco-plastic solid," *Int J Fract*, vol. 202, no. 1, pp. 111–125, 2016. DOI: 10.1007/s10704-016-0148-0.

[102] D. Systemes, *Abaqus Analysis 6.14 User's Guide*. Providence, RI: Dassault Systemes Simulia Corp., 2014.

[103] S. Qu, "A conventional theory of mechanism-based strain gradient plasticity," PhD thesis, University of Illinois at Urbana-Champaign, 2004.

[104] U. F. Kocks, "The relation between polycrystal deformation and single-crystal deformation," *Metall Mater Trans*, vol. 1, no. 5, pp. 1121–1143, 1970. DOI: 10.1007/BF02900224.

[105] H. Mecking and U. F. Kocks, "Kinetics of flow and strain-hardening," *Acta Metall*, vol. 29, no. 11, pp. 1865–1875, 1981. DOI: 10.1016/0001-6160(81)90112-7.

[106] Y. Estrin, "Dislocation-Density–Related Constitutive Modeling," in *Unified Const Laws Plast Deform*, Elsevier, 1996, pp. 69–106. DOI: 10.1016/B978-012425970-6/50003-5.

[107] U. F. Kocks and H. Mecking, "Physics and phenomenology of strain hardening: the FCC case," *Prog Mater Sci*, vol. 48, no. 3, pp. 171–273, 2003. DOI: 10.1016/S0079-6425(02)00003-8.

[108] U. F. Kocks, "Laws for work-hardening and low-temperature creep," *J Eng Mater Technol*, vol. 98, no. 1, pp. 76–85, 1976. DOI: 10.1115/1.3443340.

[109] P. S. Engels, C. Begau, S. Gupta, B. Schmaling, A. Ma, and A. Hartmaier, "Multiscale modeling of nanoindentation: From atomistic to continuum models," in *Nanomechanical Anal High Perform Mater Solid Mech its Appl Vol 203*, A. Tiwari, Ed., Dordrecht: Springer, 2014, pp. 285–322. DOI: 10.1007/978-94-007-6919-9_15.

[110] Y. Estrin and H. Mecking, "A unified phenomenological description of work hardening and creep based on one-parameter models," *Acta Metall*, vol. 32, no. 1, pp. 57–70, 1984. DOI: 10.1016/0001-6160(84)90202-5.

[111] D. S. Dugdale, "Yielding of steel sheets containing slits," *J Mech Phys Solids*, vol. 8, no. 2, pp. 100–104, 1960. DOI: 10.1016/0022-5096(60)90013-2.

[112] G. I. Barenblatt, "The mathematical theory of equilibrium cracks in brittle fracture," *Adv Appl Mech*, vol. 7, pp. 55–129, 1962. DOI: 10.1016/S0065-2156(08)70121-2.

[113] A. Needleman, "A continuum model for void nucleation by inclusion debonding," *J Appl Mech*, vol. 54, no. 3, p. 525, 1987. DOI: 10.1115/1.3173064.

[114] A. Needleman, "An analysis of decohesion along an imperfect interface," *Int J Fract*, vol. 42, no. 1, pp. 21–40, 1990. DOI: 10.1007/BF00018611.

[115] V. Tvergaard and J. W. Hutchinson, "The relation between crack growth resistance and fracture process parameters in elastic-plastic solids," *J Mech Phys Solids*, vol. 40, no. 6, pp. 1377–1397, 1992. DOI: 10.1016/0022-5096(92)90020-3.

[116] V. Tvergaard and J. W. Hutchinson, "Effect of strain-dependent cohesive zone model on predictions of crack growth resistance," *Int J Solids Struct*, vol. 33, pp. 3297–3308, 1996. DOI: 10.1016/0020-7683(95)00261-8.

[117] A. Needleman, "Some issues in cohesive surface modeling," *Procedia IUTAM*, vol. 10, pp. 221–246, 2014. DOI: 10.1016/j.piutam.2014.01.020.

[118] M. Kuna and S. Roth, "General remarks on cyclic cohesive zone models," *Int J Fract*, vol. 196, no. 1-2, pp. 147–167, 2015. DOI: 10.1007/s10704-015-0053-y.

[119] O. Nguyen, E. A. Repetto, M. Ortiz, and R. Radovitzky, "A cohesive model of fatigue crack growth," *Int J Fract*, vol. 110, no. 4, pp. 351–369, 2001. DOI: 10.1023/A:1010839522926.

[120] J. Lemaitre, *A Course on Damage Mechanics*. Berlin: Springer Berlin Heidelberg, 1992. DOI: 10.1007/978-3-662-02761-5.

[121] A. Ural, V. R. Krishnan, and K. D. Papoulia, "A cohesive zone model for fatigue crack growth allowing for crack retardation," *Int J Solids Struct*, vol. 46, no. 11-12, pp. 2453–2462, 2009. DOI: 10.1016/j.ijsolstr.2009.01.031.

[122] S. Roth, G. Hütter, and M. Kuna, "Simulation of fatigue crack growth with a cyclic cohesive zone model," *Int J Fract*, vol. 188, no. 1, pp. 23–45, 2014. DOI: 10.1007/s10704-014-9942-8.

[123] J. Abraham, S. Roth, and M. Kuna, "A cohesive zone model for thermomechanical fatigue," *Int J Fatigue*, vol. 136, p. 105 572, 2020. DOI: 10.1016/j.ijfatigue.2020.105572.

[124] K. Maciejewski, J. Dahal, Y. Sun, and H. Ghonem, "Creep-environment interactions in dwell-fatigue crack growth of nickel based superalloys," *Metall Mater Trans A*, vol. 45, no. 5, pp. 2508–2521, 2014. DOI: 10.1007/s11661-014-2199-z.

[125] X. P. Xu and A. Needleman, "Void nucleation by inclusion debonding in a crystal matrix," *Model Simul Mater Sci Eng*, vol. 1, no. 2, pp. 111–132, 1993. DOI: 10.1088/0965-0393/1/2/001.

[126] B. Wang and T. Siegmund, "Simulation of fatigue crack growth at plastically mismatched bi-material interfaces," *Int J Plast*, vol. 22, no. 9, pp. 1586–1609, 2006. DOI: 10.1016/j.ijplas.2005.09.004.

[127] J. Lemaitre, J. Sermage, and R. Desmorat, "A two scale damage concept applied to fatigue," *Int J Fract*, vol. 97, no. 1, pp. 67–81–81, 1999. DOI: 10.1023/A:1018641414428.

[128] Y. N. Rabotnov, *Creep problems in structural members*. Amsterdam: North-Holland, 1969.

[129] J. D. Pribe, T. Siegmund, V. Tomar, and J. J. Kruzic, "Plastic strain gradients and transient fatigue crack growth: A computational study," *Int J Fatigue*, vol. 120, pp. 283–293, 2019. DOI: 10.1016/j.ijfatigue.2018.11.020.

[130] T. Siegmund, "A numerical study of transient fatigue crack growth by use of an irreversible cohesive zone model," *Int J Fatigue*, vol. 26, no. 9, pp. 929–939, 2004. DOI: 10.1016/j.ijfatigue.2004.02.002.

[131] B. Wang and T. Siegmund, "Numerical simulation of constraint effects in fatigue crack growth," *Int J Fatigue*, vol. 27, no. 10-12, pp. 1328–1334, 2005. DOI: 10.1016/j.ijfatigue.2005.06.001.

[132] S. del Busto, C. Betegón, and E. Martínez-Pañeda, "A cohesive zone framework for environmentally assisted fatigue," *Eng Fract Mech*, vol. 185, pp. 210–226, 2017. DOI: 10.1016/j.engfracmech.2017.05.021.

[133] R. C. McClung, B. H. Thacker, and S. Roy, "Finite element visualization of crack closure in plane stress and plane strain," *Int J Fract*, vol. 50, pp. 27–49, 1991. DOI: 10.1007/BF00035167.

[134] E. Martínez-Pañeda and C. F. Niordson, "On fracture in finite strain gradient plasticity," *Int J Plast*, vol. 80, pp. 154–167, 2016. DOI: 10.1016/j.ijplas.2015.09.009.

[135] K. L. Nielsen, C. F. Niordson, and J. W. Hutchinson, "Strain gradient effects on steady state crack growth in rate-sensitive materials," *Eng Fract Mech*, vol. 96, pp. 61–71, 2012. DOI: 10.1016/j.engfracmech.2012.06.022.

[136] J. Gil Sevillano, "The effective threshold for fatigue crack propagation: a plastic size effect?" *Scr Mater*, vol. 44, no. 11, pp. 2661–2665, 2001. DOI: 10.1016/S1359-6462(01)00948-4.

[137] S. Brinckmann and T. Siegmund, "Computations of fatigue crack growth with strain gradient plasticity and an irreversible cohesive zone model," *Eng Fract Mech*, vol. 75, no. 8, pp. 2276–2294, 2008. DOI: 10.1016/j.engfracmech.2007.09.007.

[138] S. Brinckmann and T. Siegmund, "A cohesive zone model based on the micromechanics of dislocations," *Model Simul Mater Sci Eng*, vol. 16, no. 6, p. 065 003, 2008. DOI: 10.1088/0965-0393/16/6/065003.

[139] S. Suresh, "Micromechanisms of fatigue crack growth retardation following overloads," *Eng Fract Mech*, vol. 18, no. 3, pp. 577–593, 1983. DOI: 10.1016/0013-7944(83)90051-6.

[140] A. J. Wilkinson, G. Meaden, and D. J. Dingley, "High resolution mapping of strains and rotations using electron backscatter diffraction," *Mater Sci Technol*, vol. 22, no. 11, pp. 1271–1278, 2006. DOI: 10.1179/174328406X130966.

[141] E. Glaessgen, E. Saether, S. Smith, J. D. Hochhalter, V. Yamakov, and V. Gupta, "Modeling and characterization of damage processes in metallic materials," in *52nd AIAA/ASME/ASCE/AHS/ASC Struct Struct Dyn Mater Conf*, Reston, Virigina: American Institute of Aeronautics and Astronautics, 2011, pp. 1–16. DOI: 10.2514/6.2011-2177.

[142] A. T. Tucker, A. J. Wilkinson, M. B. Henderson, H. S. Ubhi, and J. W. Martin, "Measurement of fatigue crack plastic zones in fine grained materials using electron backscattered diffraction," *Mater Sci Technol*, vol. 16, no. 4, pp. 457–462, 2000. DOI: 10.1179/026708300101507910.

[143] R. I. Barabash, Y. Gao, Y. Sun, S. Y. Lee, H. Choo, P. K. Liaw, D. W. Brown, and G. E. Ice, "Neutron and X-ray diffraction studies and cohesive interface model of the fatigue crack deformation behavior," *Philos Mag Lett*, vol. 88, no. 8, pp. 553–565, 2008. DOI: 10.1080/09500830802311080.

[144] E. Salvati, H. Zhang, K. S. Fong, X. Song, and A. M. Korsunsky, "Separating plasticity-induced closure and residual stress contributions to fatigue crack retardation following an overload," *J Mech Phys Solids*, vol. 98, pp. 222–235, 2017. DOI: 10.1016/j.jmps.2016.10.001.

[145] M. L. Williams, "On the stress distribution at the base of a stationary crack," *J Appl Mech*, vol. 24, pp. 109–14, 1957.

[146] E. Martínez-Pañeda, S. del Busto, and C. Betegón, "Non-local plasticity effects on notch fracture mechanics," *Theor Appl Fract Mech*, vol. 92, pp. 276–287, 2017. DOI: 10.1016/j.tafmec.2017.09.007.

[147] J. R. Rice, "Mechanics of crack tip deformation and extension by fatigue," in *Fatigue Crack Propagation, ASTM STP 415*, ASTM International, 1967, pp. 247–309. DOI: 10.1520/STP47234S.

[148] L. P. Mikkelsen and S. Goutianos, "Suppressed plastic deformation at blunt crack-tips due to strain gradient effects," *Int J Solids Struct*, vol. 46, no. 25-26, pp. 4430–4436, 2009. DOI: 10.1016/j.ijsolstr.2009.09.001.

[149] V. S. Deshpande, A. Needleman, and E. van der Giessen, "Discrete dislocation modeling of fatigue crack propagation," *Acta Mater*, vol. 50, no. 4, pp. 831–846, 2002. DOI: 10.1016/S1359-6454(01)00377-9.

[150] A. K. Vasudevan, K. Sadananda, and G. Glinka, "Critical parameters for fatigue damage," *Int J Fatigue*, vol. 23, pp. 39–53, 2001. DOI: 10.1016/S0142-1123(01)00171-2.

[151] S. Daneshpour, J. Dyck, V. Ventzke, and N. Huber, "Crack retardation mechanism due to overload in base material and laser welds of Al alloys," *Int J Fatigue*, vol. 42, pp. 95–103, 2012. DOI: 10.1016/j.ijfatigue.2011.07.010.

[152] H. Jiang, Y. Huang, Z. Zhuang, and K. C. Hwang, "Fracture in mechanism-based strain gradient plasticity," *J Mech Phys Solids*, vol. 49, no. 5, pp. 979–993, 2001. DOI: 10.1016/S0022-5096(00)00070-3.

[153] N. A. Fleck, "Finite element analysis of plasticity-induced crack closure under plane strain conditions," *Eng Fract Mech*, vol. 25, no. 4, pp. 441–449, 1986. DOI: 10.1016/0013-7944(86)90258-4.

[154] Y. Jiang, M. Feng, and F. Ding, "A reexamination of plasticity-induced crack closure in fatigue crack propagation," *Int J Plast*, vol. 21, no. 9, pp. 1720–1740, 2005. DOI: 10.1016/j.ijplas.2004.11.005.

[155] V. S. Deshpande, A. Needleman, and E. van der Giessen, "Scaling of discrete dislocation predictions for near-threshold fatigue crack growth," *Acta Mater*, vol. 51, no. 15, pp. 4637–4651, 2003. DOI: 10.1016/S1359-6454(03)00302-1.

[156] W. A. Curtin, V. S. Deshpande, A. Needleman, E. van der Giessen, and M. Wallin, "Hybrid discrete dislocation models for fatigue crack growth," *Int J Fatigue*, vol. 32, pp. 1511–1520, 2010. DOI: 10.1016/j.ijfatigue.2009.10.015.

[157] Y. Wei, X. Qiu, and K. C. Hwang, "Steady-state crack growth and fracture work based on the theory of mechanism-based strain gradient plasticity," *Eng Fract Mech*, vol. 71, no. 1, pp. 107–125, 2004. DOI: 10.1016/S0013-7944(03)00065-1.

[158] J. D. Pribe, T. Siegmund, and J. J. Kruzic, "The roles of yield strength mismatch, interface strength, and plastic strain gradients in fatigue crack growth across interfaces," *Eng Fract Mech*, vol. 235, p. 107 072, 2020. DOI: 10.1016/j.engfracmech.2020.107072.

[159] D. Embury and O. Bouaziz, "Steel-based composites: Driving forces and classifications," *Annu Rev Mater Res*, vol. 40, no. 1, pp. 213–241, 2010. DOI: 10.1146/annurev-matsci-070909-104438.

[160] D. R. Lesuer, C. K. Syn, O. D. Sherby, J. Wadsworth, J. J. Lewandowski, and W. H. Hunt, "Mechanical behaviour of laminated metal composites," *Int Mater Rev*, vol. 41, no. 5, pp. 169–197, 1996. DOI: 10.1179/095066096790151204.

[161] M.-Y. He and J. W. Hutchinson, "Crack deflection at an interface between dissimilar elastic materials," *Int J Solids Struct*, vol. 25, no. 9, pp. 1053–1067, 1989. DOI: 10.1016/0020-7683(89)90021-8.

[162] M. Y. He, A. G. Evans, and J. W. Hutchinson, "Crack deflection at an interface between dissimilar elastic materials: Role of residual stresses," *Int J Solids Struct*, vol. 31, no. 24, pp. 3443–3455, 1994. DOI: 10.1016/0020-7683(94)90025-6.

[163] J. P. Parmigiani and M. D. Thouless, "The roles of toughness and cohesive strength on crack deflection at interfaces," *J Mech Phys Solids*, vol. 54, no. 2, pp. 266–287, 2006. DOI: 10.1016/j.jmps.2005.09.002.

[164] J. Li, "Debonding of the interface as 'crack arrestor'," *Int J Fract*, vol. 105, no. 1, pp. 57–79, 2000. DOI: 10.1023/A:1007603809972.

[165] T. Siegmund, N. A. Fleck, and A. Needleman, "Dynamic crack growth across an interface," *Int J Fract*, vol. 85, no. 1989, pp. 381–402, 1997. DOI: 10.1023/A:1007460509387.

[166] Y. Sugimura, L. Grondin, and S. Suresh, "Fatigue crack growth at arbitrary angles to bimaterial interfaces," *Scr Metall Mater*, vol. 33, no. 12, pp. 2007–2012, 1995. DOI: 10.1016/0956-716X(95)00442-X.

[167] M. R. Joyce, S. Syngellakis, and P. A. S. Reed, "Fatigue crack initiation and early growth in a multiphase Al alloy included in a multilayer material system," *Mater Sci Technol*, vol. 20, no. 1, pp. 47–56, 2004. DOI: 10.1179/026708304225010389.

[168] Y. Sugimura, P. G. Lim, C. F. Shih, and S. Suresh, "Fracture normal to a bimaterial interface: Effects of plasticity on crack-tip shielding and amplification," *Acta Metall Mater*, vol. 43, no. 3, pp. 1157–1169, 1995. DOI: 10.1016/0956-7151(94)00295-S.

[169] O. Kolednik, J. Predan, N. Gubeljak, and D. F. Fischer, "Modeling fatigue crack growth in a bimaterial specimen with the configurational forces concept," *Mater Sci Eng A*, vol. 519, no. 1-2, pp. 172–183, 2009. DOI: 10.1016/j.msea.2009.04.059.

[170] M. Sistaninia and O. Kolednik, "Effect of a single soft interlayer on the crack driving force," *Eng Fract Mech*, vol. 130, pp. 21–41, 2014. DOI: 10.1016/j.engfracmech.2014.02.026.

[171] W. Ochensberger and O. Kolednik, "Overload effect revisited - Investigation by use of configurational forces," *Int J Fatigue*, vol. 83, pp. 161–173, 2016. DOI: 10.1016/j.ijfatigue.2015.10.010.

[172] M. Alam, J. P. Parmigiani, and J. J. Kruzic, "An experimental assessment of methods to predict crack deflection at an interface," *Eng Fract Mech*, vol. 181, pp. 116–129, 2017. DOI: 10.1016/j.engfracmech.2017.05.013.

[173] S. Groh, S. Olarnrithinun, W. A. Curtin, A. Needleman, V. S. Deshpande, and E. van der Giessen, "Fatigue crack growth from a cracked elastic particle into a ductile matrix," *Philos Mag*, vol. 88, no. 30-32, pp. 3565–3583, 2008. DOI: 10.1080/14786430802320127.

[174] J. J. Kruzic, J. M. McNaney, R. M. Cannon, and R. O. Ritchie, "Effects of plastic constraint on the cyclic and static fatigue behavior of metal/ceramic layered structures," *Mech Mater*, vol. 36, no. 1-2, pp. 57–72, 2004. DOI: 10.1016/S0167-6636(03)00031-0.

[175] S. Brinckmann and E. van der Giessen, "A fatigue crack initiation model incorporating discrete dislocation plasticity and surface roughness," *Int J Fract*, vol. 148, no. 2, pp. 155–167, 2007. DOI: 10.1007/s10704-008-9190-x.

[176] S. Suresh, *Fatigue of Materials*, 2nd. Cambridge: Cambridge University Press, 1998. DOI: 10.1017/CBO9780511806575.

[177] S. Lu, A. Laborda, R. Cook, Y. Zhang, R. Verbickas, and P. A. S. Reed, "A numerical study of crack shielding/anti-shielding in layered architectures," *Int J Fatigue*, vol. 124, pp. 503–519, 2019. DOI: 10.1016/j.ijfatigue.2019.03.030.

[178] M. Sistaninia and O. Kolednik, "Improving strength and toughness of materials by utilizing spatial variations of the yield stress," *Acta Mater*, vol. 122, pp. 207–219, 2017. DOI: 10.1016/j.actamat.2016.09.044.

[179] R. Moresco and E. Bittencourt, "Numerical study of fatigue crack growth considering an elastic–plastic layer in mixed-mode loading," *Int J Fract*, vol. 221, no. 1, pp. 39–52, 2019. DOI: 10.1007/s10704-019-00402-9.

[180] V. S. Deshpande, A. Needleman, and E. van der Giessen, "A discrete dislocation analysis of near-threshold fatigue crack growth," *Acta Mater*, vol. 49, no. 16, pp. 3189–3203, 2001. DOI: 10.1016/S1359-6454(01)00220-8.

[181] R. B. Sills and M. D. Thouless, "The effect of cohesive-law parameters on mixed-mode fracture," *Eng Fract Mech*, vol. 109, pp. 353–368, 2013. DOI: 10.1016/j.engfracmech.2012.06.006.

[182] J. Lankford, T. S. Cook, and G. P. Sheldon, "Fatigue microcrack growth in a nickel-base superalloy," *Int J Fract*, vol. 17, no. 2, pp. 143–155, 1981. DOI: 10.1007/BF00053517.

[183] S. Alkan and H. Sehitoglu, "Nonuniqueness of the fatigue threshold," *Int J Fatigue*, vol. 104, pp. 309–321, 2017. DOI: 10.1016/j.ijfatigue.2017.07.027.

[184] A. Tambat and G. Subbarayan, "Simulations of arbitrary crack path deflection at a material interface in layered structures," *Eng Fract Mech*, vol. 141, pp. 124–139, 2015. DOI: 10.1016/j.engfracmech.2015.04.034.

[185] M. R. Joyce, P. A. S. Reed, and S. Syngellakis, "Numerical modelling of crack shielding and deflection in a multi-layered material system," *Mater Sci Eng A*, vol. 342, no. 1-2, pp. 11–22, 2003. DOI: 10.1016/S0921-5093(02)00279-4.

[186] N. Moës, J. Dolbow, and T. Belytschko, "A finite element method for crack growth without remeshing," *Int J Numer Methods Eng*, vol. 46, no. 1, pp. 131–150, 1999. DOI: 10.1002/(SICI)1097-0207(19990910)46:1<131::AID-NME726>3.0.CO;2-J.

[187] K. E. Aifantis, W. A. Soer, J. T. M. De Hosson, and J. R. Willis, "Interfaces within strain gradient plasticity: Theory and experiments," *Acta Mater*, vol. 54, no. 19, pp. 5077–5085, 2006. DOI: 10.1016/j.actamat.2006.06.040.

[188] A. Saxena and J. D. Landes, "Characterization of creep crack growth in metals," in *Fract 84*, 1984, pp. 3977–3988. DOI: 10.1016/B978-1-4832-8440-8.50419-1.

[189] H. Riedel, "Creep crack growth," in *Fracture Mechanics: Perspectives and Directions (Twentieth Symposium), ASTM STP 1020*, R. P. Wei and R. P. Gangloff, Eds., West Conshohocken, PA: ASTM International, 1989, pp. 101–126. DOI: 10.1520/STP18822S.

[190] A. Saxena and S. B. Narasimhachary, "Accounting for crack tip cyclic plasticity and creep reversal in estimating (Ct)avg during creep-fatigue crack growth," *Fatigue Fract Eng Mater Struct*, vol. 42, no. 9, pp. 2053–2060, 2019. DOI: 10.1111/ffe.13081.

[191] H. Riedel, "Crack-tip stress fields and crack growth under creep-fatigue conditions," in *Elastic-Plastic Fract Second Symp Vol I—Inelastic Crack Anal ASTM STP 803*, C. F. Shih and J. P. Gudas, Eds., West Conshohocken, PA: ASTM International, 1983, pp. I–505–I–520. DOI: 10.1520/stp37312s.

[192] F. Z. Li, A. Needleman, and C. F. Shih, "Characterization of near tip stress and deformation fields in creeping solids," *Int J Fract*, vol. 36, no. 3, pp. 163–186, 1988. DOI: 10.1007/BF00035098.

[193] C. Y. Hui and H. Riedel, "The asymptotic stress and strain field near the tip of a growing crack under creep conditions," *Int J Fract*, vol. 17, no. 4, pp. 409–425, 1981. DOI: 10.1007/BF00036192.

[194] D. E. Hawk and J. L. Bassani, "Transient crack growth under creep conditions," *J Mech Phys Solids*, vol. 34, no. 3, pp. 191–212, 1986. DOI: 10.1016/0022-5096(86)90018-9.

[195] J. C. Sung and J. Y. Liou, "Transient crack growth in a viscoplastic solid," *Eng Fract Mech*, vol. 46, no. 3, pp. 399–411, 1993. DOI: 10.1016/0013-7944(93)90233-I.

[196] D. R. Hayhurst, P. R. Brown, and C. J. Morrison, "The role of continuum damage in creep crack growth," *Philos Trans R Soc London Ser A, Math Phys Sci*, vol. 311, no. 1516, pp. 131–158, 1984.

[197] K. Saanouni, J. L. Chaboche, and C. Bathias, "On the creep crack growth prediction by a local approach," *Eng Fract Mech*, vol. 25, no. 5-6, pp. 677–691, 1986. DOI: 10.1016/0013-7944(86)90032-9.

[198] R. P. Skelton, "Damage factors and upper bounds for interactive creep-fatigue crack growth," *Mater High Temp*, vol. 25, no. 4, pp. 231–245, 2008. DOI: 10.3184/096034008X386049.

[199] J.-F. Wen and S.-T. Tu, "A multiaxial creep-damage model for creep crack growth considering cavity growth and microcrack interaction," *Eng Fract Mech*, vol. 123, pp. 197–210, 2014. DOI: 10.1016/j.engfracmech.2014.03.001.

[200] H. Jing, D. Su, L. Xu, L. Zhao, Y. Han, and R. Sun, "Finite element simulation of creep-fatigue crack growth behavior for P91 steel at 625°C considering creep-fatigue interaction," *Int J Fatigue*, vol. 98, pp. 41–52, 2017. DOI: 10.1016/j.ijfatigue.2017.01.004.

[201] L. G. Zhao and J. Tong, "A viscoplastic study of crack-tip deformation and crack growth in a nickel-based superalloy at elevated temperature," *J Mech Phys Solids*, vol. 56, no. 12, pp. 3363–3378, 2008. DOI: 10.1016/j.jmps.2008.09.006.

[202] J. Tong, L. G. Zhao, and B. Lin, "Ratchetting strain as a driving force for fatigue crack growth," *Int J Fatigue*, vol. 46, pp. 49–57, 2013. DOI: 10.1016/j.ijfatigue.2012.01.003.

[203] F. Z. Li, A. Needleman, and C. F. Shih, "Creep crack growth by grain boundary cavitation: crack tip fields and crack growth rates under transient conditions," *Int J Fract*, vol. 38, no. 4, pp. 241–273, 1988. DOI: 10.1007/BF00019803.

[204] J.-F. Wen, A. Srivastava, A. A. Benzerga, S.-T. Tu, and A. Needleman, "Creep crack growth by grain boundary cavitation under monotonic and cyclic loading," *J Mech Phys Solids*, vol. 108, pp. 68–84, 2017. DOI: 10.1016/j.jmps.2017.07.018.

[205] J.-F. Wen, Y. Liu, A. Srivastava, A. A. Benzerga, S.-T. Tu, and A. Needleman, "Environmentally enhanced creep crack growth by grain boundary cavitation under cyclic loading," *Acta Mater*, vol. 153, pp. 136–146, 2018. DOI: 10.1016/j.actamat.2018.04.034.

[206] R. J. Kashinga, L. G. Zhao, V. V. Silberschmidt, R. Jiang, and P. A. S. Reed, "A diffusion-based approach for modelling crack tip behaviour under fatigue-oxidation conditions," *Int J Fract*, vol. 213, no. 2, pp. 157–170, 2018. DOI: 10.1007/s10704-018-0311-x.

[207] K. Sadananda, A. K. Vasudevan, R. L. Holtz, and E. U. Lee, "Analysis of overload effects and related phenomena," *Int J Fatigue*, vol. 21, S233–S246, 1999. DOI: 10.1016/S0142-1123(99)00094-8.

[208] A. E. Gemma, "Hold-time effect of a single overload on crack retardation at elevated temperature," *Eng Fract Mech*, vol. 11, no. 4, pp. 763–774, 1979. DOI: 10.1016/0013-7944(79)90135-8.

[209] D. E. Macha, "Fatigue crack growth retardation behavior of IN-100 at elevated temperature," *Eng Fract Mech*, vol. 12, no. 1, pp. 1–11, 1979. DOI: 10.1016/0013-7944(79)90060-2.

[210] B. S. Adair, W. S. Johnson, S. D. Antolovich, and A. Staroselsky, "Temperature and load interaction effects on the fatigue crack growth rate and fracture surface morphology of IN100 superalloy," *Fatigue Fract Mech 38th Vol*, vol. 9, no. 4, pp. 254–277, 2012. DOI: 10.1520/stp49551t.

[211] X. Chen, M. A. Sokolov, S. Sham, D. L. Erdman III, J. T. Busby, K. Mo, and J. F. Stubbins, "Experimental and modeling results of creep–fatigue life of Inconel 617 and Haynes 230 at 850°C," *J Nucl Mater*, vol. 432, no. 1-3, pp. 94–101, 2013. DOI: 10.1016/j.jnucmat.2012.08.040.

[212] Y. Zhang, D. P. Mohanty, P. E. Seiler, T. Siegmund, J. J. Kruzic, and V. Tomar, "High temperature indentation based property measurements of IN-617," *Int J Plast*, vol. 96, pp. 264–281, 2017. DOI: 10.1016/j.ijplas.2017.05.007.

[213] O. D. Sherby and P. M. Burke, "Mechanical behavior of crystalline solids at elevated temperature," *Prog Mater Sci*, vol. 13, no. C, pp. 323–390, 1968. DOI: 10.1016/0079-6425(68)90024-8.

[214] J. Reboul, A. Srivastava, S. Osovski, and G. Vadillo, "Influence of strain rate sensitivity on localization and void coalescence," *Int J Plast*, vol. 125, pp. 265–279, 2019. DOI: 10.1016/j.ijplas.2019.09.007.

[215] J. L. Bassani, "Cracks in materials with hyperbolic-sine-law creep behavior," in *Elastic-Plastic Fract Second Symp Vol I—Inelastic Crack Anal ASTM STP 803*, West Conshohocken, PA: ASTM International, 1983, pp. I–532–I–550. DOI: 10.1520/STP37314S.

[216] C. M. Landis, T. Pardoen, and J. W. Hutchinson, "Crack velocity dependent toughness in rate dependent materials," *Mech Mater*, vol. 32, no. 11, pp. 663–678, 2000. DOI: 10.1016/S0167-6636(00)00031-4.

[217] J. L. Chaboche, "A review of some plasticity and viscoplasticity constitutive theories," *Int J Plast*, vol. 24, no. 10, pp. 1642–1693, 2008. DOI: 10.1016/j.ijplas.2008.03.009.

[218] K. S. Chan, "A grain boundary fracture model for predicting dynamic embrittlement and oxidation-induced cracking in superalloys," *Metall Mater Trans A*, vol. 46, no. 6, pp. 2491–2505, 2015. DOI: 10.1007/s11661-015-2860-1.

[219] K. L. Nielsen and C. F. Niordson, "Rate sensitivity of mixed mode interface toughness of dissimilar metallic materials: Studied at steady state," *Int J Solids Struct*, vol. 49, no. 3-4, pp. 576–583, 2012. DOI: 10.1016/j.ijsolstr.2011.11.001.

[220] L. B. Freund and J. W. Hutchinson, "High strain-rate crack growth in rate-dependent plastic solids," *J Mech Phys Solids*, vol. 33, no. 2, pp. 169–191, 1985. DOI: 10.1016/0022-5096(85)90029-8.

[221] B. Budiansky, J. W. Hutchinson, and S. Slutsky, "Void growth and collapse in viscous solids," in *Mech Solids*, Pergamon Press Ltd., 1982, pp. 13–45. DOI: 10.1016/b978-0-08-025443-2.50009-4.

[222] A. Srivastava and A. Needleman, "Void growth versus void collapse in a creeping single crystal," *J Mech Phys Solids*, vol. 61, no. 5, pp. 1169–1184, 2013. DOI: 10.1016/j.jmps.2013.01.006.

[223] J. D. Pribe, H. E. Ostergaard, T. Siegmund, and J. J. Kruzic, "Transient creep-fatigue crack growth in creep-brittle materials: Application to Alloy 718," *J Appl Mech*, In preparation.

[224] A. Pineau, D. L. McDowell, E. P. Busso, and S. D. Antolovich, "Failure of metals II: Fatigue," *Acta Mater*, vol. 107, pp. 484–507, 2016. DOI: 10.1016/j.actamat.2015.05.050.

[225] D. G. Leo Prakash, M. J. Walsh, D. Maclachlan, and A. M. Korsunsky, "Crack growth micro-mechanisms in the IN718 alloy under the combined influence of fatigue, creep and oxidation," *Int J Fatigue*, vol. 31, no. 11-12, pp. 1966–1977, 2009. DOI: 10.1016/j.ijfatigue.2009.01.023.

[226] E. Lundström, K. Simonsson, D. Gustafsson, and T. Månsson, "A load history dependent model for fatigue crack propagation in Inconel 718 under hold time conditions," *Eng Fract Mech*, vol. 118, pp. 17–30, 2014. DOI: 10.1016/j.engfracmech.2014.02.005.

[227] T. Weerasooriya, "Effect of frequency on fatigue crack growth rate of Inconel 718 at high temperature," in *Fract Mech Ninet Symp ASTM STP 969*, T. A. Cruse, Ed., Philadelphia, 1988, pp. 907–923. DOI: 10.1520/stp33112s.

[228] E. Andrieu, R. Molins, H. Ghonem, and A. Pineau, "Intergranular crack tip oxidation mechanism in a nickel-based superalloy," *Mater Sci Eng A*, vol. 154, no. 1, pp. 21–28, 1992. DOI: 10.1016/0921-5093(92)90358-8.

[229] F. Antunes, J. Ferreira, C. Branco, and J. Byme, "High temperature fatigue crack growth in Inconel 718," *Mater High Temp*, vol. 17, no. 4, pp. 439–448, 2000. DOI: 10.1179/mht.2000.058.

[230] R. Jiang and P. A. S. Reed, "Critical assessment 21: Oxygen-assisted fatigue crack propagation in turbine disc superalloys," *Mater Sci Technol*, vol. 32, no. 5, pp. 401–406, 2016. DOI: 10.1080/02670836.2016.1148227.

[231] R. Jiang, Y. D. Song, and P. A. Reed, "Fatigue crack growth mechanisms in powder metallurgy Ni-based superalloys—A review," *Int J Fatigue*, vol. 141, p. 105 887, 2020. DOI: 10.1016/j.ijfatigue.2020.105887.

[232] J. A. Pfaendtner and C. J. McMahon Jr., "Oxygen-induced intergranular cracking of a Ni-base alloy at elevated temperatures - An example of dynamic embrittlement," *Acta Mater*, vol. 49, no. 16, pp. 3369–3377, 2001. DOI: 10.1016/S1359-6454(01)00005-2.

[233] U. Krupp, "Dynamic embrittlement — Time–dependent quasi–brittle intergranular fracture at high temperatures," *Int Mater Rev*, vol. 50, no. 2, pp. 83–97, 2005. DOI: 10.1179/174328005X14320.

[234] J. A. del Valle, A. C. Picasso, and R. Romero, "Work-hardening in Inconel X-750: Study of stage II," *Acta Mater*, vol. 46, no. 6, pp. 1981–1988, 1998. DOI: 10.1016/S1359-6454(97)00425-4.

[235] A. Simar, Y. Bréchet, B. de Meester, A. Denquin, and T. Pardoen, "Sequential modeling of local precipitation, strength and strain hardening in friction stir welds of an aluminum alloy 6005A-T6," *Acta Mater*, vol. 55, pp. 6133–6143, 2007. DOI: 10.1016/j.actamat.2007.07.012.

[236] S. K. Iyer and C. J. Lissenden, "Multiaxial constitutive model accounting for the strength-differential in Inconel 718," *Int J Plast*, vol. 19, pp. 2055–2081, 2003. DOI: 10.1016/S0749-6419(03)00059-7.

[237] P. R. Onck and E. van der Giessen, "Microstructural modelling of creep crack growth from a blunted crack," *Int J Fract*, vol. 92, no. 4, pp. 373–399, 1998. DOI: 10.1023/A:1007584732405.

[238] V. T. Phan, X. Zhang, Y. Li, and C. Oskay, "Microscale modeling of creep deformation and rupture in Nickel-based superalloy IN 617 at high temperature," *Mech Mater*, vol. 114, pp. 215–227, 2017. DOI: 10.1016/j.mechmat.2017.08.008.

[239] J. L. Bassani and D. E. Hawk, "Influence of damage on crack-tip fields under small-scale-creep conditions," *Int J Fract*, vol. 42, no. 2, pp. 157–172, 1993. DOI: 10.1007/BF00018384.

[240] J. L. Evans, "Method for comparing the crack tip kinetics during creep-fatigue loading of nickel-base superalloys," *Mater Sci Eng A*, vol. 528, pp. 5306–5308, 2011. DOI: 10.1016/j.msea.2011.03.044.

[241] K. S. Chan, "Time-dependent crack growth thresholds of Ni-base superalloys," *Metall Mater Trans A*, vol. 45, no. 8, pp. 3454–3466, 2014. DOI: 10.1007/s11661-014-2271-8.

[242] E. A. de Souza Neto, D. Peric, and D. R. J. Owen, *Computational Methods for Plasticity: Theory and applications*, 1st. Chichester, UK: John Wiley & Sons, Ltd, 2008. DOI: 10.1002/9780470694626.

[243] A. F. Bower, *EN2340: Computational Methods in Solid Mechanics lecture notes*, 2017.

A. INTEGRATION OF CMSG-VP CONSTITUTIVE MODEL

The UMAT implementation of the CMSG-vp constitutive model follows standard approaches for integrating viscoplastic models using a predictor-corrector algorithm [102], [242]. It is based in part on the original CMSG implementation of [85] and the viscoplasticity algorithm of [243]. The main improvement of the new implementation is to ensure the quadratic convergence rate of the Newton-Raphson iterations. The original implementation did not fully account for strain hardening when calculating the correction term during each iteration. The algorithm consists of five steps:

1. Calculate the viscoplastic strain gradient increment.
2. Calculate the elastic predictor stress.
3. Calculate the viscoplastic strain increment
4. Update the stress using the calculated viscoplastic strain increment.
5. Calculate the material Jacobian.

First, the variables used in the subroutine are defined. Values of any variable at the start of the current increment are denoted with subscript n. Values at the end of the current increment are denoted with subscript $n+1$. The stress and strain tensors ($\boldsymbol{\sigma} = \sigma_{ij}$ and $\boldsymbol{\varepsilon} = \varepsilon_{ij}$) are stored as vectors using Voigt notation. In 3 dimensions, the representations are:

$$\boldsymbol{\sigma} = \begin{Bmatrix} \sigma_{11} \\ \sigma_{22} \\ \sigma_{33} \\ \sigma_{23} \\ \sigma_{13} \\ \sigma_{12} \end{Bmatrix}, \quad \boldsymbol{\varepsilon} = \begin{Bmatrix} \varepsilon_{11} \\ \varepsilon_{22} \\ \varepsilon_{33} \\ 2\varepsilon_{23} \\ 2\varepsilon_{13} \\ 2\varepsilon_{12} \end{Bmatrix} \tag{A.1}$$

For plane strain problems, these are:

$$\boldsymbol{\sigma} = \begin{Bmatrix} \sigma_{11} \\ \sigma_{22} \\ \sigma_{33} \\ \sigma_{12} \end{Bmatrix}, \quad \boldsymbol{\varepsilon} = \begin{Bmatrix} \varepsilon_{11} \\ \varepsilon_{22} \\ \varepsilon_{33} = 0 \\ 2\varepsilon_{12} \end{Bmatrix} \tag{A.2}$$

Elastic strains are denoted with a superscript e, and viscoplastic strains are denoted with a superscript vp. The deviatoric stress is given by $\boldsymbol{S} = \boldsymbol{\sigma} - \operatorname{tr}\boldsymbol{\sigma}/3$. The deviatoric strain is given by $\boldsymbol{e} = \boldsymbol{\varepsilon} - \operatorname{tr}\boldsymbol{\varepsilon}/3$. Also, two fourth-order tensors require definitions as matrices: the (symmetric) fourth-order identity tensor $\mathbb{I}$ and the outer product of the second-order identity tensor with itself $\boldsymbol{I} \otimes \boldsymbol{I} = \delta_{ij}\delta_{kl}$. In 3 dimensions, these are:

$$\mathbb{I} = \begin{bmatrix} 1 & 0 & 0 & 0 & 0 & 0 \\ 0 & 1 & 0 & 0 & 0 & 0 \\ 0 & 0 & 1 & 0 & 0 & 0 \\ 0 & 0 & 0 & 0.5 & 0 & 0 \\ 0 & 0 & 0 & 0 & 0.5 & 0 \\ 0 & 0 & 0 & 0 & 0 & 0.5 \end{bmatrix}, \quad \boldsymbol{I} \otimes \boldsymbol{I} = \begin{bmatrix} 1 & 1 & 1 & 0 & 0 & 0 \\ 1 & 1 & 1 & 0 & 0 & 0 \\ 1 & 1 & 1 & 0 & 0 & 0 \\ 0 & 0 & 0 & 0 & 0 & 0 \\ 0 & 0 & 0 & 0 & 0 & 0 \\ 0 & 0 & 0 & 0 & 0 & 0 \end{bmatrix} \tag{A.3}$$

For plane strain problems, these are:

$$\mathbb{I} = \begin{bmatrix} 1 & 0 & 0 & 0 \\ 0 & 1 & 0 & 0 \\ 0 & 0 & 1 & 0 \\ 0 & 0 & 0 & 0.5 \end{bmatrix}, \quad \boldsymbol{I} \otimes \boldsymbol{I} = \begin{bmatrix} 1 & 1 & 1 & 0 \\ 1 & 1 & 1 & 0 \\ 1 & 1 & 1 & 0 \\ 0 & 0 & 0 & 0 \end{bmatrix} \tag{A.4}$$

Finally, several useful relations are obtained from elasticity. The linear elastic stiffness tensor is $\mathbb{D}^e = 2G\left(\mathbb{I} - \frac{1}{3}\boldsymbol{I} \otimes \boldsymbol{I}\right) + K\boldsymbol{I} \otimes \boldsymbol{I}$. The stress-strain relationship, expressed in terms of the deviatoric and volumetric elastic strain components, is $\boldsymbol{\sigma} = 2G\boldsymbol{e}^e + 3K \operatorname{tr}\boldsymbol{\varepsilon}^e\mathbb{I}$. This can be separated into the deviatoric stress, $\boldsymbol{S} = 2G\boldsymbol{e}^e$, and the trace of the stress tensor,

$\operatorname{tr}\boldsymbol{\sigma} = 3K \operatorname{tr}\boldsymbol{\varepsilon}^e$. The von Mises effective stress and strain are $\bar{\sigma} = \sqrt{\frac{3}{2}\boldsymbol{S} : \boldsymbol{S}}$ and $\bar{\varepsilon} = \sqrt{\frac{2}{3}\boldsymbol{e} : \boldsymbol{e}}$. The effective stress and effective elastic strain are related by $\bar{\sigma} = 3G\bar{\varepsilon}^e$

A.1 Viscoplastic strain gradient increment

The effective viscoplastic strain gradient increment is calculated from the viscoplastic strain increment in the previous time step. This is because the viscoplastic strain increment at all integration points is required, which is not available for the current time step. Following Huang et al. [85], [103], a sub-element is constructed from the four integration points of a quadrilateral element. The components of the viscoplastic strain gradient are then determined using the shape function derivatives in the sub-element. Standard bilinear shape functions are used in the sub-element. In local coordinates, these are given by

$$N_1(\xi,\eta) = \frac{1}{4}(1-\xi)(1-\eta) \tag{A.5}$$

$$N_2(\xi,\eta) = \frac{1}{4}(1+\xi)(1-\eta) \tag{A.6}$$

$$N_3(\xi,\eta) = \frac{1}{4}(1-\xi)(1+\eta) \tag{A.7}$$

$$N_4(\xi,\eta) = \frac{1}{4}(1+\xi)(1+\eta). \tag{A.8}$$

The coordinate mapping and viscoplastic strain increment interpolation are given by

$$x = \sum_{i=1}^{4} N_i(\xi,\eta)\, x_i, \quad y = \sum_{i=1}^{4} N_i(\xi,\eta)\, y_i \tag{A.9}$$

$$\Delta\boldsymbol{\varepsilon}^{vp} = \sum_{i=1}^{4} N_i(\xi,\eta)\, \Delta\boldsymbol{\varepsilon}_i^{vp} \tag{A.10}$$

The derivatives of the shape functions with respect to the global coordinates are given by

$$\begin{Bmatrix} \dfrac{\partial N_i}{\partial x} \\ \dfrac{\partial N_i}{\partial y} \end{Bmatrix} = \mathbf{J}^{-1} \begin{Bmatrix} \dfrac{\partial N_i}{\partial \xi} \\ \dfrac{\partial N_i}{\partial \eta} \end{Bmatrix}, \tag{A.11}$$

where the Jacobian matrix $\mathbf{J}$ is

$$\mathbf{J} = \begin{bmatrix} \dfrac{\partial x}{\partial \xi} & \dfrac{\partial y}{\partial \xi} \\ \dfrac{\partial x}{\partial \eta} & \dfrac{\partial y}{\partial \eta} \end{bmatrix} \tag{A.12}$$

In plane strain, the nonzero components of the viscoplastic strain gradient increment are given in terms of the shape function derivatives by [103]

$$\Delta\eta^{vp}_{111} = \sum_{i=1}^{4} \frac{\partial N_i}{\partial x} \left(\Delta\varepsilon^{vp}_{11}\right)_i \tag{A.13}$$

$$\Delta\eta^{vp}_{112} = 2\sum_{i=1}^{4} \frac{\partial N_i}{\partial x} \left(\Delta\varepsilon^{vp}_{12}\right)_i - \sum_{i=1}^{4} \frac{\partial N_i}{\partial y} \left(\Delta\varepsilon^{vp}_{11}\right)_i \tag{A.14}$$

$$\Delta\eta^{vp}_{121} = \sum_{i=1}^{4} \frac{\partial N_i}{\partial y} \left(\Delta\varepsilon^{vp}_{11}\right)_i \tag{A.15}$$

$$\Delta\eta^{vp}_{122} = \sum_{i=1}^{4} \frac{\partial N_i}{\partial x} \left(\Delta\varepsilon^{vp}_{22}\right)_i \tag{A.16}$$

$$\Delta\eta^{vp}_{133} = -\sum_{i=1}^{4} \frac{\partial N_i}{\partial x} \left(\Delta\varepsilon^{vp}_{11} + \Delta\varepsilon^{vp}_{22}\right)_i \tag{A.17}$$

$$\Delta\eta^{vp}_{211} = \sum_{i=1}^{4} \frac{\partial N_i}{\partial y} \left(\Delta\varepsilon^{vp}_{11}\right)_i \tag{A.18}$$

$$\Delta\eta^{vp}_{212} = \sum_{i=1}^{4} \frac{\partial N_i}{\partial x} \left(\Delta\varepsilon^{vp}_{22}\right)_i \tag{A.19}$$

$$\Delta\eta^{vp}_{221} = 2\sum_{i=1}^{4} \frac{\partial N_i}{\partial y} \left(\Delta\varepsilon^{vp}_{12}\right)_i - \sum_{i=1}^{4} \frac{\partial N_i}{\partial x} \left(\Delta\varepsilon^{vp}_{22}\right)_i \tag{A.20}$$

$$\Delta\eta^{vp}_{222} = \sum_{i=1}^{4} \frac{\partial N_i}{\partial y} \left(\Delta\varepsilon^{vp}_{22}\right)_i \tag{A.21}$$

$$\Delta\eta^{vp}_{233} = -\sum_{i=1}^{4} \frac{\partial N_i}{\partial y} \left(\Delta\varepsilon^{vp}_{11} + \Delta\varepsilon^{vp}_{22}\right)_i \tag{A.22}$$

$$\Delta\eta^{vp}_{313} = -\sum_{i=1}^{4} \frac{\partial N_i}{\partial x} \left(\Delta\varepsilon^{vp}_{11} + \Delta\varepsilon^{vp}_{22}\right)_i \tag{A.23}$$

$$\Delta\eta^{vp}_{323} = -\sum_{i=1}^{4} \frac{\partial N_i}{\partial y} \left(\Delta\varepsilon^{vp}_{11} + \Delta\varepsilon^{vp}_{22}\right)_i \tag{A.24}$$

$$\Delta\eta^{vp}_{331} = \sum_{i=1}^{4} \frac{\partial N_i}{\partial x} \left(\Delta\varepsilon^{vp}_{11} + \Delta\varepsilon^{vp}_{22}\right)_i \tag{A.25}$$

$$\Delta\eta^{vp}_{332} = \sum_{i=1}^{4} \frac{\partial N_i}{\partial y} \left(\Delta\varepsilon^{vp}_{11} + \Delta\varepsilon^{vp}_{22}\right)_i \tag{A.26}$$

A.2 Elastic predictor stress and strain

The predictor stress and strain are computed based on the assumption that the strain increment is entirely elastic (i.e., the viscoplastic strain increment is zero). Predictor quantities are denoted using a superscript $*$. The predictor elastic strain is

$$\boldsymbol{\varepsilon}^{\mathrm{e}*} = \boldsymbol{\varepsilon}_n^e + \Delta\boldsymbol{\varepsilon}. \tag{A.27}$$

From the stress-strain relationship, the volumetric predictor stress is

$$\frac{\operatorname{tr}\boldsymbol{\sigma}^*}{3} = K \operatorname{tr}\boldsymbol{\varepsilon}^{\mathrm{e}*} \tag{A.28}$$

Similarly, the deviatoric predictor stress is

$$\boldsymbol{S}^* = \boldsymbol{S}_n + 2G\Delta\boldsymbol{e}. \tag{A.29}$$

Calculating $\boldsymbol{S}^*$ requires the deviatoric stress at the start of the increment and the deviatoric strain increment, which are given by

$$\boldsymbol{S}_n = \boldsymbol{\sigma}_n - \frac{\operatorname{tr}\boldsymbol{\sigma}_n}{3}\boldsymbol{I}, \quad \Delta\boldsymbol{e} = \Delta\boldsymbol{\varepsilon} - \frac{\operatorname{tr}\Delta\boldsymbol{\varepsilon}}{3}\boldsymbol{I}. \tag{A.30}$$

In the numerical implementation, the factor of 2 is removed from the engineering shear strain components when calculating the deviatoric strain. For later use, it is also helpful to write down the deviatoric predictor stress in terms of only the elastic predictor strain:

$$\boldsymbol{S}^* = 2G\boldsymbol{e}^{\mathrm{e}*} = 2G\left(\boldsymbol{\varepsilon}^{\mathrm{e}*} - \frac{\operatorname{tr}\boldsymbol{\varepsilon}^{\mathrm{e}*}}{3}\boldsymbol{I}\right). \tag{A.31}$$

The effective predictor stress $\bar{\sigma}^*$ is then calculated from the deviatoric predictor stress:

$$\bar{\sigma}^* = \sqrt{\frac{3}{2}\boldsymbol{S}^* : \boldsymbol{S}^*}. \tag{A.32}$$

For the rate-independent CMSG model, the effective strain increment is also needed:

$$\Delta\bar{\varepsilon} = \sqrt{\frac{2}{3}\Delta\boldsymbol{e} : \Delta\boldsymbol{e}}. \tag{A.33}$$

A.3 Viscoplastic strain increment

The backward Euler method is used to solve the constitutive law for the viscoplastic strain increment. Here, all quantities are expressed as their values at the end of the increment (besides the viscoplastic strain gradient, which is only available at the start of the increment):

$$\Delta\varepsilon^{vp} = \Delta\varepsilon_0 \left(\frac{\bar{\sigma}_{n+1}}{\sigma_{\text{flow}}\left(\varepsilon^{vp}_{n+1}, \eta^{vp}\right)} \right)^m, \tag{A.34}$$

where $\Delta\varepsilon_0 = \dot{\varepsilon}_0 \Delta t$. For the rate-independent CMSG, $\Delta\varepsilon_0$ is replaced by $\Delta\bar{\varepsilon}$. Next, all quantities in Eq. (A.34) are expressed in terms of $\Delta\varepsilon^{vp}$. First, the flow stress is

$$\sigma_{\text{flow}}\left(\varepsilon^{vp}_{n+1}, \eta^{vp}\right) = \sigma_Y \sqrt{\left(1 + \frac{E\left(\varepsilon^{vp}_n + \Delta\varepsilon^{vp}\right)}{\sigma_Y}\right)^{2N} + l\eta^{vp}} \tag{A.35}$$

Expressing the updated effective stress $\bar{\sigma}_{n+1}$ in terms of the viscoplastic strain increment requires an equation for the updated deviatoric stress $\boldsymbol{S}_{n+1}$. This is found from the relationship between the deviatoric stress and the deviatoric elastic strain increment:

$$\begin{aligned}
\boldsymbol{S}_{n+1} =& \boldsymbol{S}_n + 2G\Delta\boldsymbol{e}^e \\
=& \boldsymbol{S}_n + 2G\Delta\boldsymbol{e} - 2G\Delta\boldsymbol{e}^{vp} \\
=& \boldsymbol{S}^* - 2G\Delta\boldsymbol{e}^{vp} \\
=& \boldsymbol{S}^* - 2G\left(\frac{3\boldsymbol{S}_{n+1}}{2\bar{\sigma}_{n+1}}\Delta\varepsilon^{vp}\right).
\end{aligned} \tag{A.36}$$

The last step follows from the standard associativity rule and the incompressibility of plastic deformation (i.e., $\operatorname{tr}\varepsilon^{vp} = 0$):

$$\Delta\boldsymbol{\varepsilon}^{vp} = \Delta\boldsymbol{e}^{vp} = \frac{3\boldsymbol{S}_{n+1}}{2\bar{\sigma}_{n+1}}\Delta\varepsilon^{vp} \tag{A.37}$$

Taking the dot product of Eq. (A.36) with itself and simplifying the result gives

$$\bar{\sigma}_{n+1} = \bar{\sigma}^* - 3G\Delta\varepsilon^{vp}, \tag{A.38}$$

which expresses $\bar{\sigma}_{n+1}$ in terms of known quantities and $\Delta\varepsilon^{vp}$. Equation (A.36) can also be used to show that the $\boldsymbol{S}^*$ and the $\boldsymbol{S}_{n+1}$ are co-linear [242]:

$$\frac{\boldsymbol{S}_{n+1}}{\bar{\sigma}_{n+1}} = \frac{\boldsymbol{S}^*}{\bar{\sigma}^*}. \tag{A.39}$$

Substituting Eq. (A.38) into Eq. (A.34) gives

$$\bar{\sigma}^* - 3G\Delta\varepsilon^{vp} - \left(\frac{\Delta\varepsilon^{vp}}{\Delta\varepsilon_0}\right)^{1/m} \sigma_{\text{flow}}\left(\varepsilon^{vp}_{n+1}, \eta^{vp}\right) = 0. \tag{A.40}$$

For large m, this equation approaches the corresponding one for rate-independent plasticity. To simplify notation, the arguments are dropped from σ_{flow} in the subsequent derivations. Equation (A.40) is solved for $\Delta\varepsilon^{vp}$ using Newton's method:

$$\Delta\varepsilon^{vp}_{\text{new}} = \Delta\varepsilon^{vp}_{\text{old}} - \frac{f\left(\Delta\varepsilon^{vp}_{\text{old}}\right)}{f'\left(\Delta\varepsilon^{vp}_{\text{old}}\right)}, \tag{A.41}$$

where the function $f\left(\Delta\varepsilon^{vp}\right)$ is given by Eq. (A.40), and "old" and "new" refer to successive approximations of $\Delta\varepsilon^{vp}$. Differentiating Eq. (A.40) gives:

$$f'\left(\Delta\varepsilon^{vp}\right) = -3G - \left(\frac{\Delta\varepsilon^{vp}}{\Delta\varepsilon_0}\right)^{1/m} \left(\frac{\sigma_{\text{flow}}}{m\Delta\varepsilon^{vp}} + \frac{\mathrm{d}\sigma_{\text{flow}}}{\mathrm{d}\Delta\varepsilon^{vp}}\right) \tag{A.42}$$

where

$$\frac{\mathrm{d}\sigma_{\text{flow}}}{\mathrm{d}\Delta\varepsilon^{vp}} = \frac{NE\sigma_Y\left(1 + \frac{E\left(\varepsilon^{vp}_n + \Delta\varepsilon^{vp}\right)}{\sigma_Y}\right)^{2N-1}}{\sigma_{\text{flow}}}. \tag{A.43}$$

For later use, it is convenient to define

$$\begin{aligned} H =& \frac{\mathrm{d}}{\mathrm{d}\Delta\varepsilon^{vp}} \left[\left(\frac{\Delta\varepsilon^{vp}}{\Delta\varepsilon_0} \right)^{1/m} \sigma_{\text{flow}} \right] \\ =& \left(\frac{\Delta\varepsilon^{vp}}{\Delta\varepsilon_0} \right)^{1/m} \left(\frac{\sigma_{\text{flow}}}{m\Delta\varepsilon^{vp}} + \frac{\mathrm{d}\sigma_{\text{flow}}}{\mathrm{d}\Delta\varepsilon^{vp}} \right) \end{aligned} \tag{A.44}$$

allowing Eq. (A.42) to be written as

$$f'\left(\Delta\varepsilon^{vp}\right) = -3G - H. \tag{A.45}$$

For large m, this simplifies to $H \approx \mathrm{d}\sigma_{\text{flow}}/\mathrm{d}\Delta\varepsilon^{vp}$, which is simply the slope of the rate-independent strain hardening curve.

A.4 Stress update

With the viscoplastic strain increment in hand, the updated stress $\boldsymbol{\sigma}_{n+1}$ can be computed. From Eq. (A.36), the updated deviatoric stress is

$$\boldsymbol{S}_{n+1} = \left(1 - \frac{3G\Delta\varepsilon^{vp}}{\bar{\sigma}^*} \right) \boldsymbol{S}^* \tag{A.46}$$

Since the viscoplastic strain is purely deviatoric, the updated trace of the stress is $\operatorname{tr}\boldsymbol{\sigma}_{n+1} = \operatorname{tr}\boldsymbol{\sigma}^*$. The updated stress tensor is then

$$\boldsymbol{\sigma}_{n+1} = \boldsymbol{S}_{n+1} + \frac{\operatorname{tr}\boldsymbol{\sigma}_{n+1}}{3}\boldsymbol{I}. \tag{A.47}$$

A.5 Material Jacobian

The material Jacobian is required since the UMAT is implemented within an implicit finite element algorithm. The approach here follows Ch. 7 of [242]. Abaqus requires the material Jacobian $\mathbb{D}$ in the form

$$\mathbb{D} = \frac{\partial\Delta\boldsymbol{\sigma}}{\partial\Delta\boldsymbol{\varepsilon}}. \tag{A.48}$$

For the current model, $\partial\Delta\boldsymbol{\sigma}/\partial\Delta\boldsymbol{\varepsilon} = \partial\boldsymbol{\sigma}_{n+1}/\partial\boldsymbol{\varepsilon}_{n+1}$. Also, the elastic predictor strain can be expressed as $\boldsymbol{\varepsilon}^{\mathrm{e}*} = \boldsymbol{\varepsilon}_n^e + \Delta\boldsymbol{\varepsilon} = \boldsymbol{\varepsilon}_{n+1} - \boldsymbol{\varepsilon}_n^{vp}$. The updated stress $\boldsymbol{\sigma}_{n+1}$ can therefore be written as a function of the elastic predictor strain $\boldsymbol{\varepsilon}^{\mathrm{e}*}$, and the material Jacobian becomes

$$\mathbb{D} = \frac{\partial\boldsymbol{\sigma}_{n+1}}{\partial\boldsymbol{\varepsilon}^{\mathrm{e}*}}. \tag{A.49}$$

The updated stress must now be written in terms of the elastic predictor strain. To this end, Eqs. (A.46) and (A.31) are combined to express the updated deviatoric stress as

$$\begin{aligned}\boldsymbol{S}_{n+1} =& \left(1 - \frac{3G\Delta\varepsilon^{vp}}{\bar{\sigma}^*}\right)\boldsymbol{S}^* \\ =& 2G\left(1 - \frac{3G\Delta\varepsilon^{vp}}{\bar{\sigma}^*}\right)\boldsymbol{e}^{\mathrm{e}*}\end{aligned} \tag{A.50}$$

The updated stress from Eq. (A.47) then becomes

$$\begin{aligned}\boldsymbol{\sigma}_{n+1} =& 2G\left(1 - \frac{3G\Delta\varepsilon^{vp}}{\bar{\sigma}^*}\right)\boldsymbol{e}^{\mathrm{e}*} + K\,\mathrm{tr}\,\boldsymbol{\varepsilon}^{\mathrm{e}*} \\ =& 2G\boldsymbol{e}^{\mathrm{e}*} + K\,\mathrm{tr}\,\boldsymbol{\varepsilon}^{\mathrm{e}*} - \left(1 - \frac{3G\Delta\varepsilon^{vp}}{\bar{\sigma}^*}\right)\boldsymbol{e}^{\mathrm{e}*}\end{aligned} \tag{A.51}$$

The first two terms are simply the stress-strain relationship in terms of the strain predictor, so the updated stress can be written as

$$\boldsymbol{\sigma}_{n+1} = \left[\mathbb{D}^e - \frac{6G^2\Delta\varepsilon^{vp}}{\bar{\sigma}^*}\mathbb{I}_d\right] : \boldsymbol{\varepsilon}^{\mathrm{e}*}, \tag{A.52}$$

where the deviatoric identity tensor $\mathbb{I}_d = \mathbb{I} - \frac{1}{3}\boldsymbol{I}\otimes\boldsymbol{I}$ was defined to simplify the notation. Differentiating this equation using the chain and product rules gives

$$\frac{\partial\boldsymbol{\sigma}_{n+1}}{\partial\boldsymbol{\varepsilon}^{\mathrm{e}*}} = \mathbb{D}^e - \frac{6G^2\Delta\varepsilon^{vp}}{\bar{\sigma}^*}\mathbb{I}_d - \frac{6G^2}{\bar{\sigma}^*}\boldsymbol{e}^{\mathrm{e}*}\otimes\frac{\partial\Delta\varepsilon^{vp}}{\partial\boldsymbol{\varepsilon}^{\mathrm{e}*}} + \frac{6G^2\Delta\varepsilon^{vp}}{\bar{\sigma}^{*2}}\boldsymbol{e}^{\mathrm{e}*}\otimes\frac{\partial\bar{\sigma}^*}{\partial\boldsymbol{\varepsilon}^{\mathrm{e}*}} \tag{A.53}$$

The two derivatives with respect to the elastic predictor strain are unknown. The quantity $\frac{\partial \Delta\varepsilon^{vp}}{\partial \boldsymbol{\varepsilon}^{e*}}$ is found by differentiating the implicit function in Eq. (A.40):

$$\begin{aligned} 0 &= \frac{\partial \bar{\sigma}^*}{\partial \boldsymbol{\varepsilon}^{e*}} - 3G\frac{\partial \Delta\varepsilon^{vp}}{\partial \boldsymbol{\varepsilon}^{e*}} - \frac{\partial}{\partial \boldsymbol{\varepsilon}^{e*}}\left[\left(\frac{\Delta\varepsilon^{vp}}{\Delta\varepsilon_0}\right)^{1/m}\sigma_{\text{flow}}\right] \\ &= 3G\frac{\boldsymbol{S}^*}{\bar{\sigma}^*} - 3G\frac{\partial \Delta\varepsilon^{vp}}{\partial \boldsymbol{\varepsilon}^{e*}} - H\frac{\partial \Delta\varepsilon^{vp}}{\partial \boldsymbol{\varepsilon}^{e*}} \\ \implies \frac{\partial \Delta\varepsilon^{vp}}{\partial \boldsymbol{\varepsilon}^{e*}} &= \frac{3G}{3G+H}\frac{\boldsymbol{S}^*}{\bar{\sigma}^*}. \end{aligned} \tag{A.54}$$

The quantity $\frac{\partial \bar{\sigma}^*}{\partial \boldsymbol{\varepsilon}^{e*}}$ is found by using the chain rule and differentiating Eqs. (A.32) and (A.31):

$$\begin{aligned} \frac{\partial \bar{\sigma}^*}{\partial \boldsymbol{\varepsilon}^{e*}} =& \frac{\partial \bar{\sigma}^*}{\partial \boldsymbol{S}^*} : \frac{\partial \boldsymbol{S}^*}{\partial \boldsymbol{\varepsilon}^{e*}} \\ =& \left[\frac{1}{2\sqrt{\frac{3}{2}\boldsymbol{S}^* : \boldsymbol{S}^*}}\frac{3}{2}\left(\mathbb{I} : \boldsymbol{S}^* + \boldsymbol{S}^* : \mathbb{I}\right)\right] : [2G\mathbb{I}_d : \mathbb{I}] \\ =& \left[\frac{3\boldsymbol{S}^*}{2\bar{\sigma}^*}\right] : [2G\mathbb{I}_d] \\ =& 3G\frac{\boldsymbol{S}^*}{\bar{\sigma}^*} \end{aligned} \tag{A.55}$$

Substituting these results into the material Jacobian gives

$$\mathbb{D} = 2G\left(1 - \frac{3G}{\bar{\sigma}^*}\Delta\varepsilon^{vp}\right)\mathbb{I}_d - \frac{9G^2}{\bar{\sigma}^{*2}}\left(\frac{\Delta\varepsilon^{vp}}{\bar{\sigma}^*} - \frac{1}{3G+H}\right)\boldsymbol{S}^* \otimes \boldsymbol{S}^* + K\boldsymbol{I} \otimes \boldsymbol{I}. \tag{A.56}$$

This is equivalent to the approach from the Abaqus Analysis User Guide [102], which results in the equation

$$\mathbb{D} = Q\mathbb{I} - R\boldsymbol{S}_{n+1} \otimes \boldsymbol{S}_{n+1} + \left(K - \frac{1}{3}Q\right)\boldsymbol{I} \otimes \boldsymbol{I}, \tag{A.57}$$

where

$$Q = 2G\frac{\bar{\sigma}_{n+1}}{\bar{\sigma}^*}, \quad R = \frac{9G^2}{\bar{\sigma}_{n+1}^2}\left[\frac{\bar{\sigma}_{n+1} - H\Delta\varepsilon^{vp}}{\bar{\sigma}^*\left(3G+H\right)}\right]. \tag{A.58}$$

The equivalence of Eqs. (A.56) and (A.57) can be verified using the identity $\frac{\boldsymbol{S}_{n+1}}{\bar{\sigma}_{n+1}} = \frac{\boldsymbol{S}^*}{\bar{\sigma}^*}$ and the definition of the deviatoric identity tensor $\mathbb{I}_d = \mathbb{I} - \frac{1}{3}\boldsymbol{I} \otimes \boldsymbol{I}$.

B. INTEGRATION OF SGKM CONSTITUTIVE MODEL

The SGKM constitutive model is integrated within the same framework as the CMSG-vp model. The key differences involve determining the viscoplastic strain increment and the material Jacobian. These parts of the algorithm are described here. The UMAT implementation is based in part on the original implementation of [97]. As in the new implementation of the CMSG model, the quadratic rate of convergence of the Newton-Raphson iterations is recovered.

B.1 Viscoplastic strain increment

For the SGKM model, there are two internal state variables that must be calculated in this step: the viscoplastic strain and the SSD density. To avoid solving a system of equations, the increment in SSD density $\Delta\rho_S$ is expressed in terms of the viscoplastic strain increment $\Delta\varepsilon^{vp}$. The resulting equation is then solved for the viscoplastic strain increment using the backward Euler method.

The equations for $\Delta\varepsilon^{vp}$ and $\Delta\rho_S$ are the following, with all other parameters expressed using their values at the end of the increment:

$$\begin{aligned}
\Delta\varepsilon^{vp} &= \Delta\varepsilon_0 \left(\frac{\bar{\sigma}_{n+1}}{\sigma_{\text{flow}}\left(\varepsilon^{vp}_{n+1}, \rho_{S,n+1}, \rho_G\right)} \right)^m = \Delta\varepsilon_0 \left(\frac{\bar{\sigma}_{n+1}}{\sigma_0 + M\alpha Gb\sqrt{\rho_{S,n+1} + \rho_G}} \right)^m \\
\Delta\rho_S &= M \left[k_1 \sqrt{\rho_{S,n+1} + \rho_G} - k_{20} \left(\frac{\Delta\varepsilon^{vp}}{\Delta\varepsilon_0} \right)^{-1/n} \rho_{S,n+1} \right] \Delta\varepsilon^{vp}
\end{aligned} \tag{B.1}$$

From Appendix A, the updated effective stress is given by

$$\bar{\sigma}_{n+1} = \bar{\sigma}^* - 3G\Delta\varepsilon^{vp}. \tag{B.2}$$

Substituting Eq. (B.2) into the first part of Eq. (B.1) gives

$$\begin{aligned}
&\left(\frac{\Delta\varepsilon_0}{\Delta\varepsilon^{vp}}\right)^{1/m}\left(\bar{\sigma}^* - 3G\Delta\varepsilon^{vp}\right) - \sigma_{\text{flow}}\left(\varepsilon^{vp}_{n+1}, \rho_{S,n+1}, \rho_G\right) = 0 \\
\implies &\left(\frac{\Delta\varepsilon_0}{\Delta\varepsilon^{vp}}\right)^{1/m}\left(\bar{\sigma}^* - 3G\Delta\varepsilon^{vp}\right) - \sigma_0 - M\alpha Gb\sqrt{\rho_{S,n} + \Delta\rho_S + \rho_G} = 0 \\
\implies &\Delta\rho_S = \left[\frac{\left(\Delta\varepsilon_0/\Delta\varepsilon_p\right)^{1/m}\left(\bar{\sigma}^* - 3G\Delta\varepsilon_p\right) - \sigma_0}{M\alpha Gb}\right]^2 - \rho_{S,n} - \rho_G
\end{aligned} \tag{B.3}$$

This gives an equation for the SSD increment in terms of the viscoplastic strain increment and known quantities. Now the only unknown in the second part of Eq. (B.1) is $\Delta\varepsilon^{vp}$. This equation can be rearranged slightly to allow for a solution with Newton's method:

$$f\left(\Delta\varepsilon^{vp}\right) = \Delta\rho_S - M\left[k_1\sqrt{\rho_{S,n} + \Delta\rho_S + \rho_G} - k_{20}\left(\frac{\Delta\varepsilon_p}{\Delta\varepsilon_0}\right)^{-1/n}\left(\rho_{S,n} + \Delta\rho_S\right)\right]\Delta\varepsilon_p = 0, \tag{B.4}$$

where $\Delta\rho_S$ is given by Eq. (B.3). The derivative is also needed; this is given by

$$\begin{aligned}
f'\left(\Delta\varepsilon^{vp}\right) = &- Mk_1\sqrt{\rho_{S,n} + \Delta\rho_S + \rho_G} + \frac{1}{n}\left[Mk_{20}\left(\frac{\Delta\varepsilon^{vp}}{\Delta\varepsilon_0}\right)^{-1/n}\left(\rho_{S,n} + \Delta\rho_S\right)(n-1)\right] + \\
&\frac{\mathrm{d}\Delta\rho_S}{\mathrm{d}\Delta\varepsilon^{vp}}\left[1 + Mk_{20}\left(\frac{\Delta\varepsilon^{vp}}{\Delta\varepsilon_0}\right)^{-1/n}\Delta\varepsilon^{vp} - \frac{Mk_1\Delta\varepsilon^{vp}}{2\sqrt{\rho_{S,n} + \Delta\rho_S + \rho_G}}\right]
\end{aligned} \tag{B.5}$$

where

$$\begin{aligned}
\frac{\mathrm{d}\Delta\rho_S}{\mathrm{d}\Delta\varepsilon^{vp}} = &\frac{1}{M^2\alpha^2G^2b^2m}\left[2\left(\frac{\Delta\varepsilon_0}{\Delta\varepsilon^{vp}}\right)^{1/m}\left(\Delta\varepsilon^{vp}\right)^{-1-1/m}\left(3G\left(m-1\right)\Delta\varepsilon^{vp} + \bar{\sigma}^*\right)\right] \\
&\left[3G\Delta\varepsilon_0^{1/m}\Delta\varepsilon^{vp} + \left(\Delta\varepsilon^{vp}\right)^{1/m}\sigma_0 - \Delta\varepsilon_0^{1/m}\bar{\sigma}^*\right]
\end{aligned} \tag{B.6}$$

This can be simplified by defining

$$\rho^+ = Mk_1\sqrt{\rho_{S,n} + \Delta\rho_S + \rho_G}, \quad \rho^- = Mk_{20}\left(\frac{\Delta\varepsilon^{vp}}{\Delta\varepsilon_0}\right)^{-1/n}\left(\rho_{S,n} + \Delta\rho_S\right), \tag{B.7}$$

so the Newton's method equations are now

$$f\left(\Delta\varepsilon^{vp}\right) = \Delta\rho_s - \rho^+\Delta\varepsilon^{vp} + \rho^-\Delta\varepsilon^{vp} \tag{B.8}$$

and

$$f'\left(\Delta\varepsilon^{vp}\right) = -\rho^+ + \frac{\rho^-\left(n-1\right)}{n} + \frac{\mathrm{d}\Delta\rho_S}{\mathrm{d}\Delta\varepsilon^{vp}}\left[1 + \frac{\rho^-\Delta\varepsilon^{vp}}{\rho_{S,n}+\Delta\rho_S} - \frac{\rho^+\Delta\varepsilon^{vp}}{2\left(\rho_{S,n}+\Delta\rho_S+\rho_G\right)}\right]. \tag{B.9}$$

After solving for $\Delta\varepsilon^{vp}$, the SSD increment is calculated from Eq. (B.3), and the stress update proceeds as in Appendix A.

Convergence is fastest if the initial guess for the viscoplastic strain increment is chosen as $\dot{\varepsilon}_n^{vp}\Delta t$. However, due to the rate dependence in the dynamic recovery term, there may be two local minima for the objective function, Eq. (B.8) (essentially, the total change in dislocation density can be achieved by a small *or* large viscoplastic strain increment in some cases). Therefore, after convergence is achieved, the code checks that

$$\Delta\varepsilon^{vp} = \Delta\varepsilon_0\left(\frac{\bar{\sigma}_{n+1}}{\sigma_{\mathrm{flow,n+1}}}\right)^m. \tag{B.10}$$

If this equation is not satisfied, the iteration is restarted with an initial guess of

$$\Delta\varepsilon_0\left(\frac{\bar{\sigma}^*}{\sigma_{\mathrm{flow,n}}}\right)^m. \tag{B.11}$$

If the algorithm still does not converge, the increment is restarted with a smaller time increment.

B.2 Material Jacobian

The approach to calculating the material Jacobian is the same as in Appendix A. First, the material Jacobian is written in terms of the updated stress and the elastic predictor strain:

$$\frac{\partial\Delta\boldsymbol{\sigma}}{\partial\Delta\boldsymbol{\varepsilon}} = \frac{\partial\boldsymbol{\sigma}_{n+1}}{\partial\boldsymbol{\varepsilon}^{\mathrm{e}*}}. \tag{B.12}$$

As before, the updated stress as a function of the elastic predictor strain is

$$\boldsymbol{\sigma}_{n+1} = \left[\mathbb{D}^{\mathrm{e}} - \frac{6G^2\Delta\varepsilon^{vp}}{\bar{\sigma}^*}\mathbb{I}_d\right] : \boldsymbol{\varepsilon}^{\mathrm{e}*}. \tag{B.13}$$

Differentiating this equation and using the relationship $\boldsymbol{S}^* = 2G\mathrm{e}^{\mathrm{e}*}$ gives

$$\frac{\partial\boldsymbol{\sigma}_{n+1}}{\partial\boldsymbol{\varepsilon}^{\mathrm{e}*}} = \mathbb{D}^{\mathrm{e}} - \frac{6G^2\Delta\varepsilon^{vp}}{\bar{\sigma}^*}\mathbb{I}_d - \frac{3G}{\bar{\sigma}^*}\boldsymbol{S}^* \otimes \frac{\partial\Delta\varepsilon^{vp}}{\partial\boldsymbol{\varepsilon}^{\mathrm{e}*}} + \frac{3G\Delta\varepsilon^{vp}}{\bar{\sigma}^{*2}}\boldsymbol{S}^* \otimes \frac{\partial\bar{\sigma}^*}{\partial\boldsymbol{\varepsilon}^{\mathrm{e}*}}. \tag{B.14}$$

As before, the quantity $\frac{\partial\bar{\sigma}^*}{\partial\boldsymbol{\varepsilon}^{\mathrm{e}*}}$ is given by

$$\frac{\partial\bar{\sigma}^*}{\partial\boldsymbol{\varepsilon}^{\mathrm{e}*}} = 3G\frac{\boldsymbol{S}^*}{\bar{\sigma}^*}. \tag{B.15}$$

The quantity $\frac{\partial\Delta\varepsilon^{vp}}{\partial\boldsymbol{\varepsilon}^{\mathrm{e}*}}$ is found by differentiating the implicit function in Eq. (B.8):

$$\begin{aligned} 0 &= \frac{\partial}{\partial\boldsymbol{\varepsilon}^{\mathrm{e}*}}\left(\Delta\rho_S - \rho^+\Delta\varepsilon^{vp} + \rho^-\Delta\varepsilon^{9}\right) \\ &= \frac{\partial\Delta\rho_S}{\partial\boldsymbol{\varepsilon}^{\mathrm{e}*}} - \Delta\varepsilon^{vp}\frac{\partial\rho^+}{\partial\boldsymbol{\varepsilon}^{\mathrm{e}*}} - \rho^+\frac{\partial\Delta\varepsilon^{vp}}{\partial\boldsymbol{\varepsilon}^{\mathrm{e}*}} + \Delta\varepsilon^{vp}\frac{\partial\rho^-}{\partial\boldsymbol{\varepsilon}^{\mathrm{e}*}} + \rho^-\frac{\partial\Delta\varepsilon^{vp}}{\partial\boldsymbol{\varepsilon}^{\mathrm{e}*}}, \end{aligned} \tag{B.16}$$

where

$$\begin{aligned} \frac{\partial\rho^+}{\partial\boldsymbol{\varepsilon}^{\mathrm{e}*}} &= \frac{Mk_1}{2\sqrt{\rho_{S,n} + \Delta\rho_S + \rho_G}}\frac{\partial\Delta\rho_S}{\partial\boldsymbol{\varepsilon}^{\mathrm{e}*}} \\ &= \frac{\rho^+}{2\left(\rho_{S,n} + \Delta\rho_S + \rho_G\right)}\frac{\partial\Delta\rho_S}{\partial\boldsymbol{\varepsilon}^{\mathrm{e}*}} \end{aligned} \tag{B.17}$$

and

$$\begin{aligned} \frac{\partial\rho^-}{\partial\boldsymbol{\varepsilon}^{\mathrm{e}*}} &= -\frac{1}{n}\left[Mk_{20}\left(\frac{\Delta\varepsilon^{vp}}{\Delta\varepsilon_0}\right)^{-1/n}\Delta\varepsilon^{vp^{-1}}\left(\rho_{S,n} + \Delta\rho_S\right)\right]\frac{\partial\Delta\varepsilon^{vp}}{\partial\boldsymbol{\varepsilon}^{\mathrm{e}*}} + Mk_{20}\left(\frac{\Delta\varepsilon^{vp}}{\Delta\varepsilon_0}\right)^{-1/n}\frac{\partial\Delta\rho_S}{\partial\boldsymbol{\varepsilon}^{\mathrm{e}*}} \\ &= \frac{-\rho^-}{n\Delta\varepsilon^{vp}}\frac{\partial\Delta\varepsilon^{vp}}{\partial\boldsymbol{\varepsilon}^{\mathrm{e}*}} + \frac{\rho^-}{\rho_{S,n} + \Delta\rho_S}\frac{\partial\Delta\rho_S}{\partial\boldsymbol{\varepsilon}^{\mathrm{e}*}}. \end{aligned} \tag{B.18}$$

Combining this with Eq. (B.16) gives

$$\begin{aligned} 0 &= \frac{\partial \Delta\rho_S}{\partial \boldsymbol{\varepsilon}^{\mathrm{e}*}} \left(1 - \frac{\rho^+ \Delta\varepsilon^{vp}}{2\left(\rho_{S,n} + \Delta\rho_S + \rho_G\right)} + \frac{\rho^- \Delta\varepsilon^{vp}}{\rho_{S,n} + \Delta\rho_S}\right) + \frac{\partial \Delta\varepsilon^{vp}}{\partial \boldsymbol{\varepsilon}^{\mathrm{e}*}} \left(\rho^- - \frac{\rho^-}{n} - \rho^+\right) \\ &= C_1 \frac{\partial \Delta\rho_S}{\partial \boldsymbol{\varepsilon}^{\mathrm{e}*}} + C_2 \frac{\partial \Delta\varepsilon^{vp}}{\partial \boldsymbol{\varepsilon}^{\mathrm{e}*}} \end{aligned} \tag{B.19}$$

where the notation has been simplified by defining two constants:

$$\begin{aligned} C_1 &= 1 - \frac{\rho^+ \Delta\varepsilon^{vp}}{2\left(\rho_{S,n} + \Delta\rho_S + \rho_G\right)} + \frac{\rho^- \Delta\varepsilon^{vp}}{\rho_{S,n} + \Delta\rho_S} \\ C_2 &= \rho^- - \frac{\rho^-}{n} - \rho^+. \end{aligned} \tag{B.20}$$

The remaining unknown is $\partial \Delta\rho_S / \partial \boldsymbol{\varepsilon}^{\mathrm{e}*}$, which comes from differentiating Eq. (B.3):

$$\frac{\partial \Delta\rho_S}{\partial \boldsymbol{\varepsilon}^{\mathrm{e}*}} = C_3 \left[\bar{\sigma}^* \frac{\partial \Delta\varepsilon^{vp}}{\partial \boldsymbol{\varepsilon}^{\mathrm{e}*}} + 3G\Delta\varepsilon^{vp}\left(m-1\right)\frac{\partial \Delta\varepsilon^{vp}}{\partial \boldsymbol{\varepsilon}^{\mathrm{e}*}} - 3Gm\Delta\varepsilon^{vp}\frac{\boldsymbol{S}^*}{\bar{\sigma}^*}\right]. \tag{B.21}$$

This required use of Eq. (B.15) to differentiate $\bar{\sigma}^*$. Another constant was also defined to simplify the equation further:

$$C_3 = \frac{2\left(\frac{\Delta\varepsilon_0}{\Delta\varepsilon^{vp}}\right)^{1/m} \Delta\varepsilon^{vp^{-1-1/m}}}{M^2\alpha^2 G^2 b^2 m}\left[3G\Delta\varepsilon_0^{1/m}\Delta\varepsilon^{vp} + \Delta\varepsilon^{vp^{1/m}}\sigma_0 - \Delta\varepsilon_0^{1/m}\bar{\sigma}^*\right]. \tag{B.22}$$

Substituting this into Eq. (B.19) gives

$$\begin{aligned} 0 &= C_1 C_3 \left[\bar{\sigma}^* \frac{\partial \Delta\varepsilon^{vp}}{\partial \boldsymbol{\varepsilon}^{\mathrm{e}*}} + 3G\Delta\varepsilon^{vp}\left(m-1\right)\frac{\partial \Delta\varepsilon^{vp}}{\partial \boldsymbol{\varepsilon}^{\mathrm{e}*}} - 3Gm\Delta\varepsilon^{vp}\frac{\boldsymbol{S}^*}{\bar{\sigma}^*}\right] + C_2 \frac{\partial \Delta\varepsilon^{vp}}{\partial \boldsymbol{\varepsilon}^{\mathrm{e}*}} \\ \implies \frac{\partial \Delta\varepsilon^{vp}}{\partial \boldsymbol{\varepsilon}^{\mathrm{e}*}} &= \frac{3C_1C_3Gm\Delta\varepsilon^{vp}}{\left(C_1C_3\bar{\sigma}^* + 3C_1C_3\Delta\varepsilon^{vp}\left(m-1\right) + C_2\right)\bar{\sigma}^*}\frac{\boldsymbol{S}^*}{\bar{\sigma}^*}. \end{aligned} \tag{B.23}$$

After substituting Eqs. (B.15) and (B.23) into Eq. (B.14), the material Jacobian becomes

$$\begin{aligned} \frac{\partial \boldsymbol{\sigma}_{n+1}}{\partial \boldsymbol{\varepsilon}^{\mathrm{e}*}} = \mathbb{D}^{\mathrm{e}} &- \frac{6G^2\Delta\varepsilon^{vp}}{\bar{\sigma}^*}\mathbb{I}_d - \frac{9G^2C_1C_3m\Delta\varepsilon^{vp}}{\left(C_1C_3\bar{\sigma}^* + 3C_1C_3\Delta\varepsilon^{vp}\left(m-1\right) + C_2\right)\bar{\sigma}^{*2}}\boldsymbol{S}^* \otimes \boldsymbol{S}^* \\ &+ \frac{9G^2\Delta\varepsilon^{vp}}{\bar{\sigma}^{*3}}\boldsymbol{S}^* \otimes \boldsymbol{S}^*. \end{aligned} \tag{B.24}$$

This can also be written in the form from the Abaqus Analysis User Guide [102]:

$$\mathbb{D} = Q\mathbb{I} - R\boldsymbol{S}_{n+1} \otimes \boldsymbol{S}_{n+1} + \left(K - \frac{1}{3}Q\right)\boldsymbol{I} \otimes \boldsymbol{I}, \tag{B.25}$$

where

$$Q = 2G\frac{\bar{\sigma}_{n+1}}{\bar{\sigma}^*} \tag{B.26}$$

and the last two terms in Eq. (B.24) combine to give

$$R = \frac{9G^2\Delta\varepsilon^{vp}}{\bar{\sigma}_{n+1}^2}\left[\frac{C_1C_3m}{C_1C_3\bar{\sigma}^* + 3C_1C_3\Delta\varepsilon^{vp}(m-1) + C_2} - \frac{1}{\bar{\sigma}^*}\right]. \tag{B.27}$$

C. FURTHER ANALYSIS OF THE COHESIVE ZONE PARAMETERS IN COMPUTATIONS AT MULTIPLE LOAD FREQUENCIES FOR ALLOY 617

In Section 5.3.3, the reference damage energy C_f was scaled based on the rate dependence of the bulk material in order to fit the steady-state crack growth rates at different frequencies. This is not the only parameter in the CZM formulation that could be scaled in this way. Another option is to scale the stiffness of the CZM through the cohesive strength $\sigma_{\max,0}$ based on the argument that the relationship between the effective stiffness in the bulk material and the CZM should be the same for each loading frequency. The predicted crack growth rates were found to be virtually identical to those in Figure 5.16.

This can be interpreted as follows. The bulk material and the CZM are essentially two springs in series, each of which will experience the same normal stress [117]. Unlike a monotonic CZM, the stress is not limited by the initial cohesive strength, which is interpreted as setting the stiffness of the CZM as in [88], [89]. Instead, the stress is mainly controlled by the viscoplastic response of the bulk material to the applied loading. This leads to a situation where the stress distribution does not depend on the initial cohesive strength parameter, except very close to the crack tip. This is illustrated in Figure C.1a through traction distributions during steady-state crack growth for $f = 0.05$ Hz. The traction distributions are nearly identical, regardless of whether the scaling factor $R_{0.05}$ is applied to C_f or $\sigma_{\max,0}$. In the context of damage evolution, it is important to note that the separation Δ_n corresponding to a particular traction is decreased when the stiffness of the CZM is increased. Therefore, increasing $\sigma_{\max,0}$ by a particular scaling factor reduces $\dot{\Delta}_n$ by the same scaling factor due to the stiffer CZM. This in turn reduces the fatigue damage increment in an equivalent way to scaling the C_f parameter directly.

This idea is further supported by additional computations at $f = 0.33$ Hz with scaled values of C_f and $\sigma_{\max,0}$. Based on the previous observations, this should not alter the crack growth rates. Figure C.1b shows that this is indeed the case. The predicted crack extension for constant-amplitude loading and blocks of 20 OLs are nearly identical across each property set as long as the product of $\sigma_{\max,0}$ and C_f is constant.

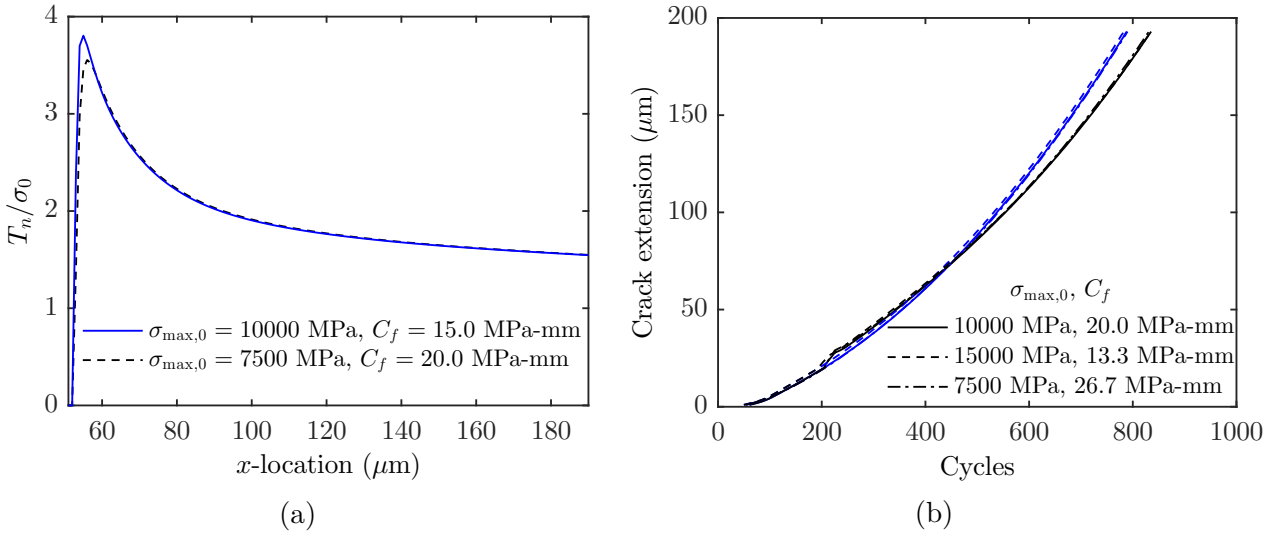

Figure C.1. (a) Predicted traction distributions for $f = 0.05$ Hz with two sets of CZM parameters that produce the same crack growth rates. (b) Predicted crack extension for $f = 0.33$ Hz with the original calibrated model and two other sets of CZM parameters with constant $C_f\sigma_{\max,0}$.

These results seem to indicate that the calibration approach is reasonable. In particular, similar results are attained as long as the value of the cohesive strength (and, in turn, the stiffness of the CZM) is set within an acceptable range: it should be high enough that the compliance of the cohesive zone does not restrict plasticity in the bulk material, but also low enough that it allows the traction and damage distributions to become fully-developed. The damage parameters can then be calibrated given this choice of the CZM stiffness. As noted in Section 5.4, these ideas could be investigated in more detail by using an explicitly rate dependent CZM [216].

There are two caveats that could require further investigation. First, the calibrated threshold $\sigma_f = 100$ MPa was relatively small compared to the actual tractions observed ahead of the crack tip in this case. The appropriate scaling of C_f and $\sigma_{\max,0}$ may be affected by higher values of this parameter, as well as by using a more complex damage evolution law like in [88]. Second, in rate-independent materials, the higher traction near the crack tip observed at higher cohesive strengths will likely trigger more plastic deformation. This could be especially pronounced during OLs. In the model for Alloy 617, this effect was mitigated by the relatively high rate sensitivity.

VITA

Joshua Pribe was born in Indianapolis, Indiana, on May 21, 1994, and he grew up in St. Louis, Missouri. He completed his undergraduate degree in Mechanical Engineering at Missouri University of Science and Technology in May 2016. He began his PhD at the Purdue School of Mechanical Engineering in August 2016, working with Professor Thomas Siegmund. In addition to his research at Purdue, Joshua taught a section of the Mechanics of Materials undergraduate course during the Fall 2019 and Summer 2020 semesters. He also spent two months working with Professor Jamie Kruzic's group at UNSW-Sydney in 2018. Following completion of his PhD, Joshua will begin a postdoctoral position at the NASA Langley Research Center.